Geosciences and engineering : a publication of the University of Miskolc

1. évf. 1. sz. / 2012

Bánhidi Olivér Studying the Interference Effects Occurring in the Course of Analysis of Environmental Samples in ICP-AES Spectrometry Using a Spectrometer with Axial View	5-12
Bánhidi Olivér The Importance and Essence of the Validation Procedure of Instrumental Analytical Methods Dealing with the Determination of the Chemical Composition and Speciation of Environmental Samples	13-20
Baracza Mátyás Krisztián Dimensional Model Studies of Modern Landfills	21-28
Bobok Elemér Comparison of Geothermal Energy Production Technologies	29-35
Bobok Elemér - Szarka Zoltán Determination of the Temperature Distribution in the Circulating Drilling Fluid	37-47
Bódi Tibor Gas Flow in the Nano Pore Channels of Tight and Non Conventional Gas Storage Formations	49-63
Gilicz András - Bódi Tibor Measurement of Porosity and Gas Permeability of Tight Rocks by the Pulse Decay Method	65-74
Pintér Ákos - Bódi Tibor Determination of Capillary Pressure and Relative Permeability Curves with a Novel Ultra Rock Centrifuge	75-86
Csuhanics Balázs - Debreczeni Ákos Introduction of New Measuring Devices for the Rock Mechanics Laboratory and the First Measurement Experiences	87-91
Dabasi-Halász Zsuzsanna - Hegyi-Kéri Ágnes The Effects of Black, Brown and Green Revitalizing Investments on the Labour Market and Economy	93-101
Darabos Enikő Analysis of Precipitation Groups and Related Water Level Peak Times in the Bükk Mountains	103-111
Debreczeni Ákos Some Remarks on the Failure Curves of Rocks	113-119
Gombkötő Imre - Nagy Sándor Evaluation of Separation Processes and its Practical Significance	121-127
Hartai Éva Potential of CO2 Geological Storage in Porous Sedimentary Formations in North Hungary	129-138
Havasi István - Ferenc Marcell Application of (Generic Mapping Tools) Software for Volume Computation in Mining Industry	139-145
Kadenczki Lajos - Stefánné Szopkó Henrietta Adaptation and Extension of Sulfonamide and Other Antibiotics Determination by Solid-Phase Extraction Followed by Liquid Chromatography and Mass Spectrometry	147-157

Kompár László - Szűcs Péter - Palcsu László - Deák József Determination of Natural Groundwater Recharge with the Help pf Groundwater Modeling and Tritium Field Measurements [Teljes szöveg (PDF)]	159-165
Kujbus Attila Hungarian Geothermal Energy in the Common Vision of the European Renewable Energy [Teljes szöveg (PDF)]	167-176
Ladányi Gábor **- Sümegi István** Bucket and Cutting Tooth Developments for the Bucket Wheel Excavators of Mátra Power Station LLC [Teljes szöveg (PDF)]	177-186
Lakatos István **- Lakatos-Szabó Julianna - Bódi Tibor - Vágó Árpád - Szentes Gabriella** Reservoir Conformance Enhancement in Gas Fields Using Microemulsions [Teljes szöveg (PDF)]	187-204
Mádai Viktor Examination of Utilization of Gyöngyösoroszi Flotation Tailing Material as Aggregate for Concrete [Teljes szöveg (PDF)]	205-216
Molnár József Expected Cement Corrosion Problems in Underground Carbon-dioxide Disposal [Teljes szöveg (PDF)]	217-222
Mucsi Gábor - Csőke Barnabás Power Plant Fly Ash as a Valuable Raw Material [Teljes szöveg (PDF)]	223-236
Mucsi Gábor - Csőke Barnabás - Zsolt István - Garamvölgyi Ernő Preliminary Investigation of Using Cathoderay-tube Waste to Produce Glassfoam [Teljes szöveg (PDF)]	237-245
Nagy Sándor **- Mádainé Üveges Valéria - Boros Éva - Szűcs István** Investigation of the Solid Waste of a Small Town for the Production of RDF [Teljes szöveg (PDF)]	247-254
Németh Norbert **- Kasó Attila - Földessy János** Sphalerite Indications in the Aggtelek Mts [Teljes szöveg (PDF)]	255-260
Németh Norbert Geological Observations in the Cserehát, Between Irota and Gadna [Teljes szöveg (PDF)]	261-269
Pethő Gábor Frequency Domain Electromagnetic Investigation on Elongated Conductivity Structures [Teljes szöveg (PDF)]	271-282
Takács Gábor **- Ladányi Gábor** Calculation of Gearbox Torques Considering Inertial Effects [Teljes szöveg (PDF)]	283-291
Turzo Zoltán - Takács Gábor Nodal Analysis of a Geothermal Well Produced by an ESP Pump [Teljes szöveg (PDF)]	293-302
Tihanyi László **- Szunyog István** The Effects of Weather Changes on Natural Gas Consumption [Teljes szöveg (PDF)]	303-314
Tóth Anikó Nóra Geothermal Energy Production and Utilization in Hungary [Teljes szöveg (PDF)]	315-319
Tóth Anikó Nóra Heat Losses in a Geothermal Reservoir [Teljes szöveg (PDF)]	321-327
Takács Gábor **- Turzo Zoltán** Description of the Production Conditions of a Geothermal Well Using Nodal Analysis Techniques [Teljes szöveg (PDF)]	329-336
Virág Zoltán **- Szirbik Sándor** Examination of an Optimized Replaceable Cutting Tooth of Excavator [Teljes szöveg (PDF)]	337-342

Geosciences and Engineering, Vol. 1, No. 1 (2012), pp. 5–12.

STUDYING THE INTERFERENCE EFFECTS OCCURRING IN THE COURSE OF ANALYSIS OF ENVIRONMENTAL SAMPLES IN ICP-AES SPECTROMETRY USING A SPECTROMETER WITH AXIAL VIEW

OLIVÉR BÁNHIDI
University of Miskolc, Institute of Chemistry
3515 Miskolc-Egyetemváros, Hungary
akmbo@uni-miskolc.hu

Abstract
The analysis of overwhelming part of environmental samples is usually performed by application of ICP-AES spectrometry. So that the possible most accurate analytical results could be obtained, the study of different interference effects has a key importance in the course of developing and validating analytical methods aiming at the analysis of environmental samples using ICP-AES spectrometry.

1. Introduction

ICP-AES spectrometry has been a wide-spread, favorable analytical method for decades, and therefore it has been used extensively for the elementary analysis of different kind of environmental samples. The reason for this fact is that ICP-AES spectrometry has some very important advantages, comparing with other instrumental analytical methods. It makes possible the determination of almost 75–80 elements, with favorable detection power in most cases. Another important feature of the method is that the calibration function, i.e. the relationship between the concentration of an element to be analyzed in the solution and that of the measured line intensity is linear, or at least close to that through several magnitudes. It is also well-known that relatively few interference effects exist in ICP-EAS, but it does not mean that this method is free from interferences. Therefore in the course of developing new analytical methods applying ICP-AES or in the course of analysis of samples having no information about the type of matrices, care must be taken of the possible interferences [1, 2].

According to the literature two types of interferences can be encountered; the first type of these effects is related to the plasma and the other one is related to the samples introduction [3]. The most frequent effects in the first group are the so-called spectral interferences, which include the spectra overlapping and the effect of different molecular bands. Most of them are well-known and thoroughly studied. In most cases they can be relatively easily eliminated, a suitable other analyte line must be selected. Most of the modern ICP spectrometers are equipped with some kind of CCD detector, which makes the line-selection simple.

The other type of interferences is related to the sample introduction and therefore it has an influence usually on all the analytical lines and frequently causes changes in the background too. Its presence is reflected in the deterioration of the performance characteristics such as the detection power, accuracy, and it may produce sudden changes in the signal either. Basically the chemical composition of the sample and the chemicals used in the course of the sample preparation are responsible for its occurrence, because they have a strong effect on the physical characteristics of the solution, such as surface tension, viscosity etc. These parameters influence the phenomena of forming and evaporation of liquid droplets and, as a consequence of that, the efficiency of the sample introduction and

long-time behavior of the sample introduction device. Although, the general laws and rules of these phenomena are well-known because of their thoroughful investigation, the real environmental samples have such a diverse chemical composition, and their sample preparation procedure may demand such different methods, that there are no uniform, general rules for predicting the occurrence of such effects. So each different new sample and sample preparation procedure needs a careful study before the routinely application, so that the possible most confident analytical results could be achieved.

The aim of this work is to study the effect of some frequent matrices and chemicals used in the sample preparation procedure on the some performance characteristics.

2. The matrices and chemicals studied

Matrices. Though the environmental samples have diverse chemical composition, there are certain components that frequently can be found at a high concentration in these kinds of samples, therefore it may be useful to know their influence on the ICP analysis. Two metallic elements were chosen, aluminium and calcium. It was because they may be present at a higher concentration in different minerals, soils, rocks. Both of them were applied at a concentration of 1,000 mg/dm^3. The Ca was in the solution in the form of $Ca(NO_3)_2$ and the solution contained besides the salt, nitric acid at a concentration of 10 g/dm^3. The Al solution had a rather high Na level, as it contained 4000 mg/dm^3 $NaNO_3$ and nitric acid at a concentration of 40 g/dm^3.

Chemicals used in the sample preparation procedure. There are numerous methods to dissolve samples. Besides methods that totally dissolve the samples, there are ones that only partially dissolve them. The later are the so-called extraction methods, which are also standardized. One of the most frequently used extraction agents is the ammonium-acetate with pH of 4.5. We applied it at a concentration of 0.1 mol/dm^3, which can be obtained by dilution from the standardized 1 mol/dm^3 solution. Most rocks and minerals contain silicon in some form. If silicon is to be determined, the sample preparation procedure should include the addition of hydro-fluoric acid, so that the silicon could be dissolved. On the other hand, the hydrofluoric acid is dangerous for the torch, spray chamber and that of the torch, as they are made of glass and silica. So that these parts could not be damaged, boric acid should be added to the solution before the analysis in such cases. Boric acid forms fluoroboric acid (HBF_4) with the free HF, therefore, it is also interesting to know, what matrix effect may be expected in the presence of HBF_4. That is why HBF_4 at a concentration of 10 g/dm^3 was chosen for a second chemical to be studied.

All these four solutions were used as a kind of blank solutions and each of them was spiked with a known quantities of a multi-element certified reference material solution (Merck Ltd., CertiPUR IV multielement solution, with 23 elements, each of them at a concentration of 1,000 mg/dm^3), so that the analyte concentration was 5 mg/dm^3 for each element studied. Distilled water containing 10 g/dm^3 nitric acid was used as reference blank solution, and an aqueous spiked standard, at an analyze concentration of 5 mg/dm^3 was used as reference standard solution.

3. The spectrometer and the measuring conditions

In the course of the measurements 720 OE ICP spectrometer, manufactured by the Varian Inc. (at present belongs to Agilent) was used. Its main features can be found in *Table 1*.

Table 1

Features of the ICP spectrometer used in the course of experiments

Type of viewing the plasma:	Axial
The frequency of the generator:	40 MHz
The RF performance applied on the torch:	900–1500 W, adjustable by the software
Type of the optical system:	Double monochromatic with Echelle gratings
Type of detector:	Two-dimension CCD
Wavelength range:	160–780 nm
Primary sample introduction system:	Pneumatic (K-type) nebulizer
Secondary sample introduction system:	Ultrasonic nebulizer
Controlling software:	ICP Expert II (under Microsoft Windows XP OS)

Though the CRM solution used to spike the solutions contained 23 elements, only three of them were studied here: Ba, Cd and Pb. As the optical system makes possible the simultaneous multi elemental analysis, i.e. any of the lines in the range of 160–780 nm can be chosen and more 100 than lines can be measured at the same time, three lines were selected for each element to be studied. During the line selection care was taken that both atomic and ionic lines should be chosen and they should be suitable for trace analysis, i.e. they should be among the most sensitive lines of the chosen element. Ba was an exception as it does not have a sensitive atomic line because of its low ionisation energy. The spectral characteristics of the selected lines are presented in *Table 2.*

Table 2

The characteristics of the selected spectral lines

Element	**Ionization energy [eV]**	**Type of the line**	**Wavelength [nm]**
Ba	5.21	Ionic	233.527
Ba		Ionic	455.404
Ba		Ionic	493.407
Cd	8.99	Ionic	214.440
Cd		Ionic	226.502
Cd		Atomic	228.802
Pb	7.42	Ionic	182.143
Pb		Atomic	217.000
Pb		Ionic	220.353

4. Results and their discussion

The reference blank and the reference standard solutions were also used as calibration samples. Ten replicates were measured and then averaged for each measured line in case of each solution. The length of the integration time was 5 s. In case of each matrix the blank solution was measured, and then it was followed by the (spiked) standard. After each pair of solutions the reference blank solution was re-measured, so that all the traces of the previous pair of solutions could be washed out. From the measured intensities the standard deviation of the blank solution, the net peak intensity of the spiked samples and finally the detection limit values have been calculated.

The detection limit values were calculated by the following formula:

$$DL = \frac{3^{*}SD_{IBL}}{I_{Std}} * C_{Std}$$

where DL the detection limit [mg/dm^3]
SD_{IBL} standard deviation of the intensity of the blank solution [a.u.]
I_{Std} background corrected net intensity of the standard [a.u.]
C_{Std} the concentration of the analyte in the standard solution [mg/dm^3].

No spectral interferences could be noticed on any of the studied spectral lines, as it can be seen in *Figure 1, 2* and *3,* where the studied lines and their spectral environment can be seen.

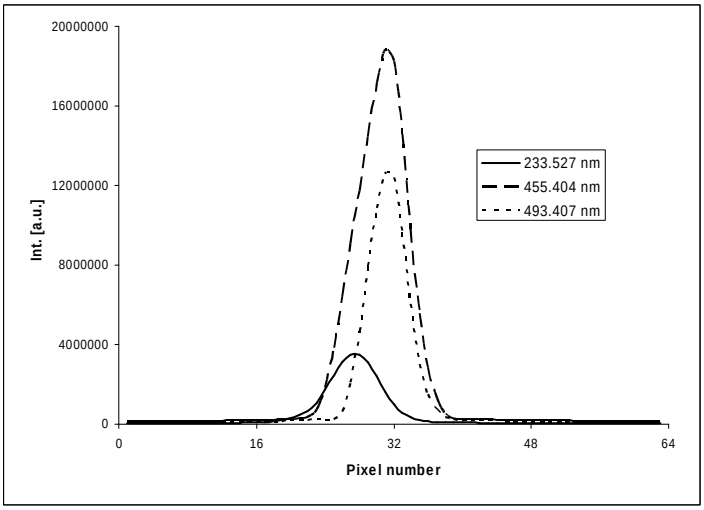

Figure 1: The spectral environment of the selected Ba lines

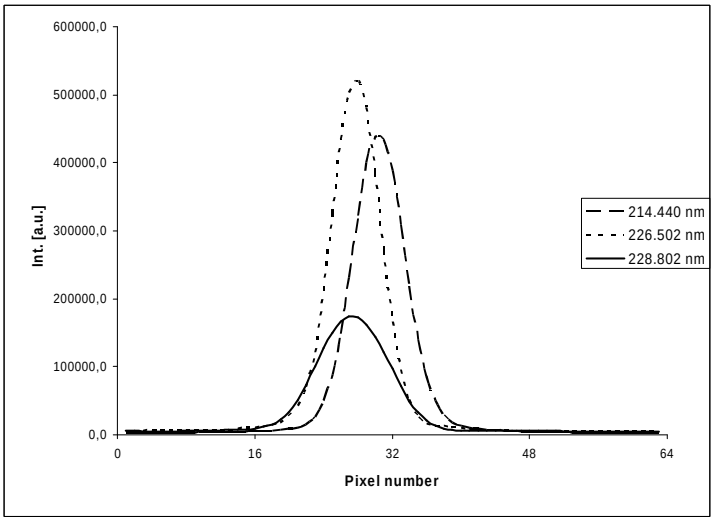

Figure 2: The spectral environment of the selected Cd lines

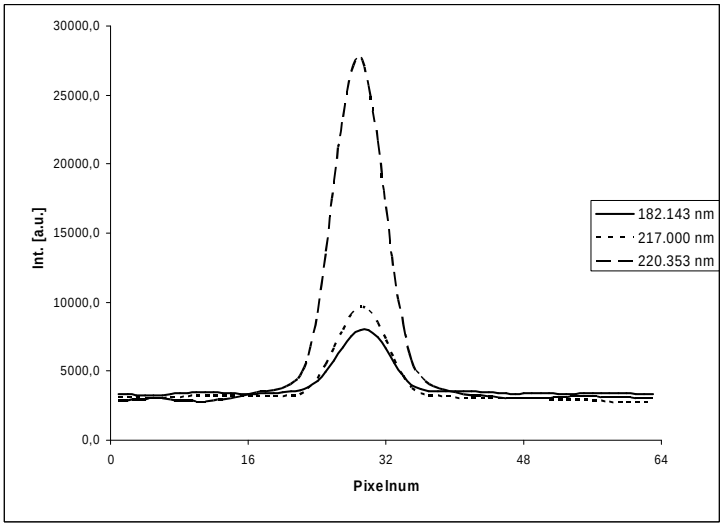

Figure 3: The spectral environment of the selected Pb lines

In these figures the data obtained by measuring the spiked solution containing fluoroboric acid matrix are presented.

So that the data could be evaluated more easily, the peak values of standards were divided by the peak values and of the reference standard, which did not contain any matrix. Similarly the calculated detection limits were divided by the detection limit measured with the reference standard solution, which was eventually an aqueous solution without any specific matrices. The results are presented in *Table 3* and *Table 4*.

Table 3

Relative peak intensities (related to the matrix-free aqueous standard)

	Ba lines [nm]			**Cd lines [nm]**			**Pb lines [nm]**		
Matrix	233.527	455.404	493.407	214.440	226.502	228.802	182.143	217.000	220.353
Ca	0.8412	0.7873	0.7598	0.8870	0.8522	0.8945	0.8485	0.8059	0.8444
NH_4Ac	0.8668	0.9897	0.9375	0.9431	0.8492	0.9076	0.9246	0.9070	0.9353
Al	0.7015	0.7300	0.6498	0.8622	0.7362	0.8052	0.7660	0.7210	0.7665
HBF_4	0.7407	0.8810	0.7886	0.8273	0.6602	0.7798	0.7095	0.7378	0.7525

Table 4

Relative detection limits (related to the aqueous matrix-free standard)

	Ba lines [nm]			**Cd lines [nm]**			**Pb lines [nm]**		
Matrix	233.527	455.404	493.407	214.440	226.502	228.802	182.143	217.000	220.353
Ca	0.8915	0.9897	2.0725	1.2315	1.0757	1.0844	1.1707	1.8834	1.2471
NH_4Ac	1.5602	0.9836	2.1606	0.9333	1.1972	1.4505	0.8122	0.9744	1.0552
Al	1.2115	1.0902	1.9406	2.1110	0.8653	1.0026	1.6496	1.4724	2.8709
HBF_4	1.2528	1.1298	1.9002	0.9394	1.4261	1.8114	3.9621	1.6462	2.6647

Reduction of the peak signal. Looking at *Table 3*, it can be noticed that each of the matrices decreased the net peak signal compared with that of measured in the matrix-free solution. It also can be seen that there are no substantial differences in the decrease, they are more or less uniform at all the lines studied.

Obviously, it does not mean that there are no differences among the effects of the different matrices. The data presented in the table suggest that it is the ammonium-acetate that has the lowest effect on the signal. The highest reduction occurred is about 15%, and there are only 2 lines where the decrease exceeds 10%. On the other hand it can be stated that it is the fluoroboric acid that has the highest impact on the signal, the smallest value it caused is approximately 12% and the largest one is about 34%.

Changes of the detection power. As the aim of the analysis in case of environmental samples to determine elements, whose concentration may be very low, the detection power of the analytical methods applied to this field is a parameter of key-importance. The detection power is characterised by the detection limit values. That's why the possible effects of matrices on their value are also very important. According to the formula used to calculate the detection limits, the result depends on both the net peak intensity and that of the standard deviation of the background. With the same net peak intensity value the higher is the standard deviation, the higher is the calculated detection limit, and consequently, the poorer is the detection power.

Looking at *Table 4* it can be stated that there are no huge changes in most cases and in some cases where the ratio is smaller than 1, i.e. the detection limit in that matrix is somewhat better than that of measured in the matrix-free solution. Nevertheless, it should be mentioned that in the analytical practice there are often cases where a much higher matrix concentration has to be encountered, and in these conditions poorer detection power

can be expected by all means. Regarding the different matrices it can be stated that fluoroboric acid has the highest impact on the detection limit values, it has a great influence on all of the studied lead lines, producing the largest increase of the values. From the solutions studied, the one containing Ca has perhaps the lowest effect on the results. Looking at the effects on a specific spectral line, there are two cases worth mentioning. The first thing is, that both aluminium and fluoroboric acid cause a strong decrease in the detection power at all of the lead lines. It seems to be a specific effect, though no such influence could be expected based upon the data presented in *Table 1*. Probably some kind of chemical interference might be responsible for that.

The other interesting case is the 493.407 nm Ba line. Each of the studied matrices decreased the detection power at about 50%. As only one Ba line is affected among the three lines, it suggests that this is not a physical effect but it must be some kind of spectroscopic effect, which influences the transition probability and by that the emission intensity, which may be the real reason.

There is one question left concerning these interferences, how they could be eliminated, or what is to be done if such effects may be encountered.

Normally, it is not possible to eliminate these effects, because the matrices themselves cannot be removed from the solution. It means that the analyst should take into account their effect in the course of method-development and during the analysis.

The reduced peak intensities may lead to false results if the calibration is based upon matrix-free calibration standards, therefore – in agreement with the literature data [4, 5] – it is inevitable to use matrix-matched calibration standards if any serious matrix effect may be encountered.

The poorer detection ability usually increases the lowest quantity of the determination, in other words, in such cases the limit of the quantitative analysis becomes higher, and the method is less sensitive in the presence of the matrix producing the interference.

5. Summary

In this paper the physical interference effects of 4 matrices on 9 spectral lines of three elements important from view of environment, such as Ba, Pb and Sr, were studied in the course of ICP-AES analysis. Because of the influence of the matrices both signal depression and deterioration of the detection power could be obtained. Regarding the signal depression it can be stated that the fluoroboric acid has the largest effect on the signal, while no substantial differences could be obtained among the lines studied.

As for as the detection power, again the fluoroboric acid produces the greatest influence. Among the spectral lines all the lead lines are sensitive both fluoroboric acid and aluminium and the 493.407 nm Ba line is almost uniformly influenced by each of the matrices.

"Acknowledgement: This work was carried out as part of the TÁMOP-4.2.1.B-10/2/KONV-2010-0001 project in the framework of the New Hungarian Development Plan. The realization of this project is supported by the European Union, co-financed by the European Social Fund."

REFERENCES

[1] Todoli, J. M.–Mermet, J. M.: *Spectrochim*. Acta 54B, (1999) 985.
[2] Todoli J. M.–Gras, L.–Hermandis, V.–Mora, J.: *J. A. A. Spectrom*. 17, (2002), 142.
[3] Záray, GY.–Co-Workers: *Az elemanalitika korszerű módszerei.* Akadémiai Kiadó, Budapest, 2006.
[4] Varna, A.: *Handbook of inductively coupled plasma atomic emission spectroscopy.* CRC Press, USA, 1991.
[5] De Boer, I. L. M.–Velterop, M.: *Fres. J. Anal*. Chem. 356, (1996), 363.

Geosciences and Engineering, Vol. 1, No. 1 (2012), pp. 13–20.

THE IMPORTANCE AND ESSENCE OF THE VALIDATION PROCEDURE OF INSTRUMENTAL ANALYTICAL METHODS DEALING WITH THE DETERMINATION OF THE CHEMICAL COMPOSITION AND SPECIATION OF ENVIRONMENTAL SAMPLES

OLIVÉR BÁNHIDI
University of Miskolc, Institute of Chemistry
3515 Miskolc–Egyetemváros, Hungary
akmbo@uni-miskolc.hu

Abstract
The validation of the instrumental analytical methods has a key importance so that the possibly most reliable chemical information could be provided. As some kind of wet chemical sample preparation is always involved in these methods, therefore the validation procedure should cover the checking both the measurement conditions and that of the sample preparation. In this paper the important points of validation of a possible analytical method using wet chemical sample preparation and ICP-AES spectrometry for the analysis of environmental samples will be discussed.

1. Introduction

The role of the measurements among them the analytical chemical measurements in the engineering is of key importance. The research, design and production are all based on measurement results. Similarly many actions and legal decisions of the local and government authorities are related to some kind of measurements. That is why it is essential that the measurement results, which form the base of so many things should be the possible most reliable and accurate. This importance is reflected in the fact that in Hungary there is a special law concerning the measurements [1]. In the European Union has a special committee, the European Committee for Standardisation which deals with measurements. Besides that EU has an Institute for Reference Materials and Measurements and an organisation, the European cooperation for Accreditation, which aims at harmonizing the activity of the testing and calibration laboratories, so that a possible uniform measurement practice could be wide-spread in the Union. The laboratory accreditation is performed according to the requirements of the MSZ EN ISO 17025 standard. This standard also declares the concept and general principles of the validation procedure of the so-called non-standardised methods. Obviously, it does not cover specific details of any given specific non-standardised method. As most of the instrumental methods applied in the chemical analysis are in the phase of rapid development, most of them have not been standardised. According the above-mentioned standard and that of the principles of the Good Laboratory Practice [2] each non-standardised measuring method has to be validated. In case of standardised methods these checks had been performed during the standardisation process.

Each measurement is eventually a comparison, i.e. comparison with the measurement unit. The different measurements can be divided into two groups. The measurement methods in the first group make a direct comparison, e.g. the comparison with the measurement unit of length. The methods that can be found in the second group perform an indirect comparison, i.e. the measured property is not directly compared, but a property, which is strongly related to the one to be measured, is being compared in the course of the measurement process. These are the so-called relative, or indirect measuring methods. Obviously, these are usually much more complicated than those in the first group.

Unfortunately, most of the instrumental methods applied in the chemical analysis belong to the second group. Because of the fact of relative measurements, the use and application of different reference materials both during calibration and checking the so-called performance characteristics of the methods have a key importance. Special care must be taken when methods with wet sample preparation procedures are considered. There are several sources of errors which have to be encountered in the course of such procedures. Complete or partial dissolution of the sample either directly or following a fusion procedure is involved in these methods. During fusion and dissolution analyte-losses may occur and/or analyte may get into the sample solution from the labware used from the chemicals applied. The wet chemical procedures applied during the sample preparation often determine the chemical form of the components to be measured. So that the most accurate measurement results could be provided, care must be taken that the analyte should be in the same chemical form both in the samples and in the standards used in the course of the calibration.

In the followings some important points of the wet chemical sample preparation procedures for ICP-AES analysis and those of the ICP-AES measurements will be discussed.

2. Important points of the wet chemical sample preparation

The wet chemical preparation of the samples is often a complicated procedure including several steps. Each of these steps has to be carefully examined in the course of the validation procedure, so that all the possible regular effects could be recognised and corrected. It must be noticed that although the key importance of the sample preparation is well-known, it is not always examined and tested according to its importance in the course of the validation procedure. Almost all the performance characteristics determined in the course of the validation process are related to the measurements. In our opinion the sample preparation is as important as the measurement therefore careful attention must be paid to that by the validation process.

The first step is – after weighing the sample using an analytical balance – taking it into solution. The dissolution often includes fusion or the application of microwave power. In most cases it is necessary to achieve the complete dissolution for reliable results. The first thing that has to be checked during the validation is whether the dissolution is complete. It must be mentioned that there are methods, where the aim is to determine the partially dissolved concentration of the analyte, in this case there is no reason to check how complete the dissolution is. The chemicals used to dissolve the samples always have some contaminants; the question is their concentration, which should be well below the concentration level expected for the analyte. The chemicals most frequently used for sample preparation are hydrochloric acid and nitric acid. In *Figure 1* some contaminants of high purity hydrochloric and nitric acid can be seen. It can be noticed that both acids have a rather high Mg contents, due to the fact that they are available in bottles made of glass.

If Mg is expected in the sample at a very low concentration, then some kind of purification of the acids to be applied (e.g. distillation using an apparatus made of silica, or ion exchange procedure etc.) is necessary before they can be used during the preparation procedure. The water used in the procedures must also be pure. The modern appliances

utilizing the reverse osmotic technology are able to produce water, which has contaminants only at a very low concentration, in addition to that its quality can be easily monitored by measuring the electric conductivity.

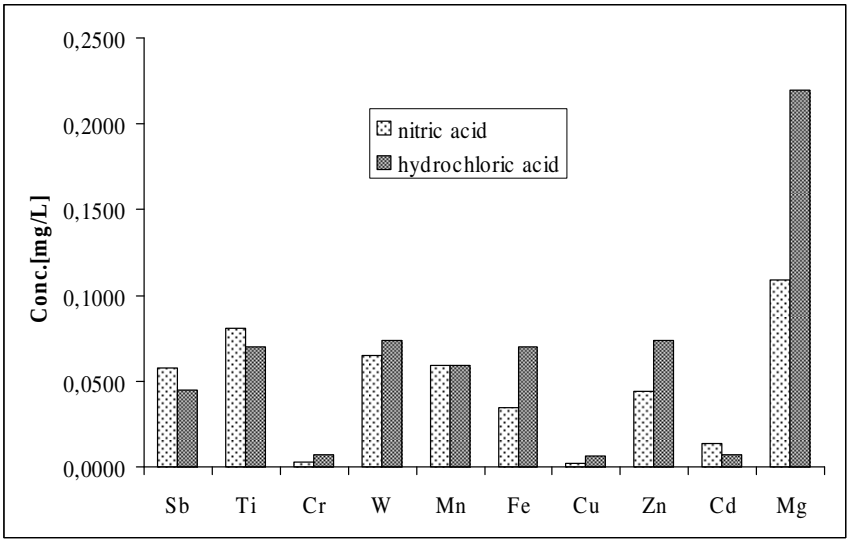

Figure 1: Contaminants found in high-purity nitric acid and hydrochloric acid

Besides the chemicals special care must be taken of the labware used in the fusion and dissolution processes. It is a well-known fact that most chemicals attack not only the sample to be dissolved, but the dishes, in that the processes take place, may cause contamination [3, 4, 5, 6]. Similarly the material of different crucibles applied in the course of fusion processes dissolve more or less in the fusion-mixtures. By careful selection of the labware a reasonable low contaminant concentration can be achieved. Nevertheless, in case of trace analytical methods the possible concentration of the contaminants must be determined by all means, and if it is comparable to the analyte concentration to be measured, a solution with the same contaminant levels must be applied as a blank solution. On the other hand, not only contaminants may get into the sample solution, but especially in case of volatile analytes material loss may be experienced. The material loss can be prevented by applying special equipment, which ensures that the volatile components cannot leave the apparatus. In the validation procedure the method also has to be checked for the possible analyte-loss.

3. Important points of the measurements

ICP-AES spectrometry requires usually simple sample preparation procedures provided only the elementary composition is needed, i.e. no speciation information is expected. After the dissolution have completed, the procedure is normally finished by making up the solution into a fixed volume in a volumetric flask. The calibration of the volumetric labware may also be relevant in some cases. As ICP spectrometry is a relative measuring method, the instrument has to be calibrated prior to the analysis. So that the calibration

could be performed a suitable series of reference solutions is needed. This solution series should be made of certified reference solutions. Regarding preparation of the calibration standard solutions the following problems might be encountered.

The best results can be achieved when the calibration standards are the solutions of certified reference materials with the possibly closest chemical composition to the samples. The sample preparation must be the same both for the standards and for the samples. Unfortunately carefully analysed certified reference materials are available just a few type of environmental samples.

Frequently one cannot find suitable standards, and in this case the standards must be prepared from one- or multi-element stock solutions, and normally the above-written principle concerning the preparation can no longer be expected to be fulfilled and in many cases somewhat poorer accuracy may be expected. Nevertheless, care must be taken that the calibration solutions should contain all the chemicals applied during the sample preparation at the same concentration they can be found in the sample solutions. If the calibration solutions are prepared from stock solutions, the main components of the samples have to be added to them at the same concentration level. That is the so-called matrix-matching. It usually requires the use of concentrated stock solutions and these solutions also have to be checked for the possible contaminants. In *Figure 2* the contaminants of Cu and Fe solutions (the concentration is 20 g/dm^3 in both cases) can be seen.

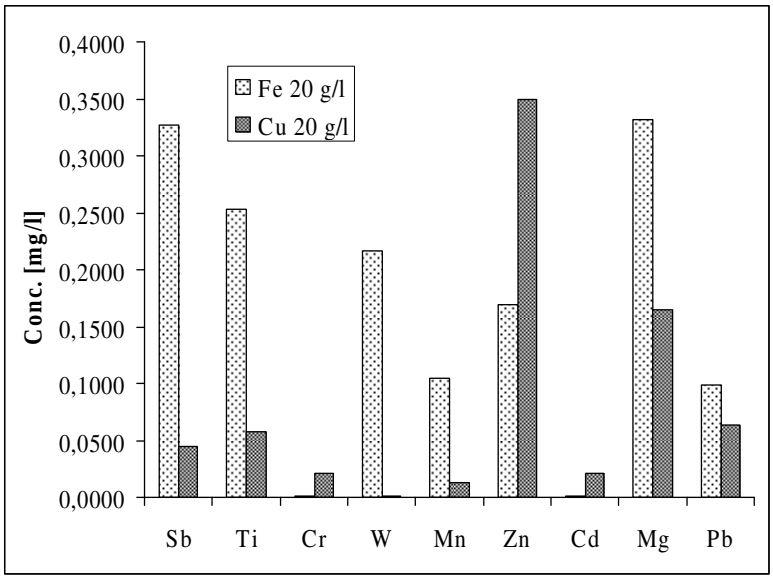

Figure 2: Some contaminants of concentrated high purity Cu and Fe stock solutions

4. Determination of the performance characteristics

The calibration procedure is followed by the determination of the performance characteristics of the measurement. Regarding the trace analytical methods, the detection power is probably one of the most important performance characteristics. It is important to mention that the detection limit values provided by the instrument manufacturers and used

for comparison purposes in the literature have been performed in dilute aqueous solutions, containing only some little acid. In the analytical practice these values cannot be used in many cases or can only be used with caution because of the effect of the matrix. Depending on the composition and concentration of the matrix, the real detection limit values may even be 10 times higher than those of determined in aqueous solutions. Therefore, it is essential that in the course of the validation procedure the detection limit values should be measured in solutions with the same matrix composition as the samples had. In *Figure 3* the spectral environment of the 220.353 nm lead line is presented using 5 mg/l concentration lead with increasing copper concentration applying ICP-AES spectrometry. Regarding the Figure it can be noticed that the spectral background is increasing with increasing copper concentration. This clearly shows the deterioration of the detection power. On the other hand, it also can be seen that beside the increasing background, the peak of the lead line decreases with higher copper concentration, which means further deterioration of the detection power. In *Table 1* the calculated background equivalent concentration values are presented as the function of copper concentration.

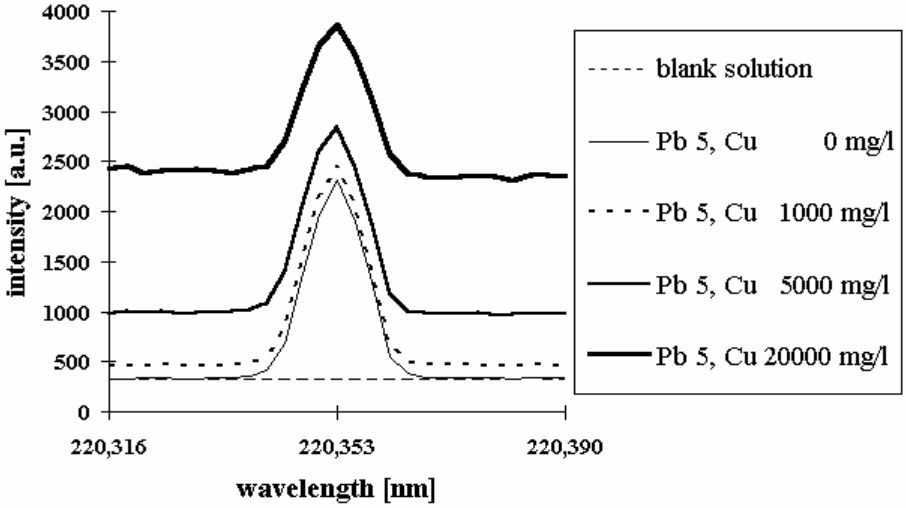

Figure 3: The spectral environment of the 220.353 nm lead line using 5 mg/l lead solution and ICP spectrometry

Table 1
Background equivalent values measured on the 220.353 nm lead line by ICP spectrometry, as the function of the copper concentration

Copper [mg/l]	BEQ for Pb
0	0,714
1000	1,125
5000	2,78
20 000	8,00

The data of *Table 1* also can be seen in *Figure 4*. Looking at this figure it can be stated that an excellent linear function can be established between the rising copper concentration and that of the BEQ values. It also can be noticed, that the detection power is eight times poorer at 20 000 mg/l copper concentration than in copper-free aqueous solution.

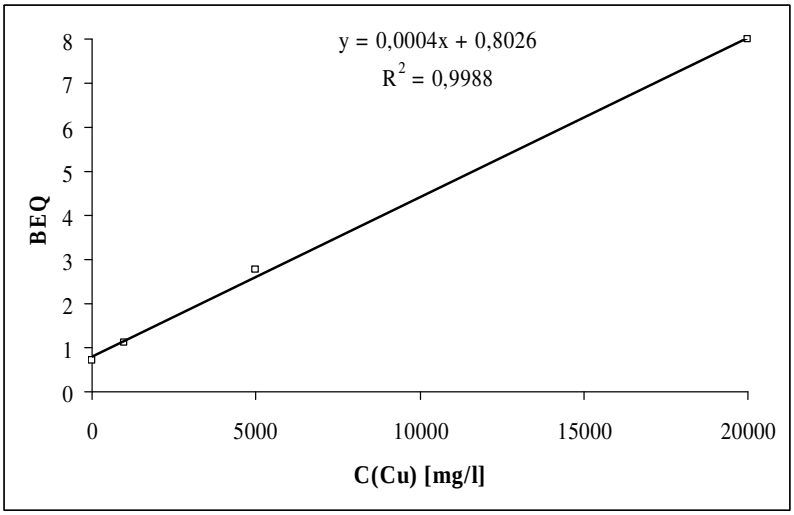

Figure 4: The background equivalent concentration measured on the 220.353 nm lead line using ICP-AES spectrometry as the function of copper concentration in the solution

Another important performance characteristic of an analytical method is the repeatability, which may have different interpretations in case of a method with wet chemical sample preparation. On one hand it may mean the repeatability of the measurement, which means the measurement of the same sample solution. This characterizes rather the instrument – i.e. the ICP-spectrometer – than the method. On the other hand repeatability may also mean the repeatability of the measurement, when more than one sample solution – usually 3 or 5 – prepared from the same sample have been measured. In both cases the repeatability is characterized by the standard deviation calculated from the measurements. In the latter case the random errors of both the sample preparation and the measurements are included in the resulting value, while in the first case only the effect of the measurement determines the value. In our opinion only the latter case provides reliable values, which may characterise the method being validated.

The concept of reproducibility is rather close to that of the repeatability. The main difference is that repeatability applies to the case when almost all conditions are unchanged, while reproducibility covers the cases when one or more conditions have been changed. As it involves those important cases when samples taken from the same lot of the material being tested by different laboratories and in that way it provides information what extent of deviations in the results can be expected, it has to be determined during the validation by all means.

One of the questions with key importance is that how close the measuring results may be to the – unknown – real value of the analyte concentration. It is the accuracy that can answer this question. In the course of the validation it is determined by measuring at least one or more certified reference materials, with chemical composition close to the samples going to be analysed. In lack of certified reference materials, real information can be provided only with big difficulties.

According to the principles of the Good laboratory Practice, all the regular effects have to be recognized and corrected in the course of the method development, so that only the so-called random effects could influence the measurement results. It is the measurement uncertainty that gives information about the extent of the random effects therefore it also has to be determined. When the measurement uncertainty is determined in the course of the validation, all the possible sources of random errors must be estimated and taken into account.

The resulting total uncertainty must be calculated and it is usually converted into the form of confidence intervals.

Last but not least, the possible interference effects also have to be checked. In case of ICP-AES spectrometry mainly spectral, physical and sometimes chemical interferences have to be encountered.

There are some other performance characteristics playing only minor role such as linearity, analytical working range etc. Because of their minor importance they are not discussed here now.

5. Summary

In this paper the specific features and requirements of the validation procedure in case of instrumental analytical chemical methods has been discussed. Special emphasis was laid to the role and importance of the wet chemical sample preparation, as most of the environmental samples are analysed by methods using such preparation procedures. It was mentioned that special care has to be taken of checking the completeness of the dissolution, the possible contaminants originating partially from the labware, partially from the water and chemicals applied. The role of the certified reference materials was also discussed. As for as the determination of the performance characteristics of the methods, the importance of determining the real detection power was also emphasized. The specific feature of the repeatability was also discussed. From the above information it can be seen that validation of an analytical chemical method is a complex procedure and it involves a tedious amount of work, but as it has a key importance, it should be performed in case of each non-standardised method.

"Acknowledgement: The described work was carried out as part of the TÁMOP-4.2.1.B-10/2/KONV-2010-0001 project in the framework of the New Hungarian Development Plan. The realization of this project is supported by the European Union, co-financed by the European Social Fund."

REFERENCES

[1] 1991. évi XLV. *Törvény a mérésügyről*. Measuring act No. XLV, 1991.
[2] OECD Environmental Health and Safety, Publications, *OECD Principles of Good Laboratory Practice* (Revised in 1997), (OECD) 1, 1998.
[3] Ernyei, L.–Bezúr: XXXVI. *Proceedings of magyar színképelemző vándorgyűlés és IX. magyar molekulaspektroszkópiai konferencia*. 24–27 august, 1993. Lillafüred, Hungary, 181.
[4] Csikkelné Szolnoki, A.: *Proceedings of XXXVIII. magyar színképelemző vándorgyűlés és XI. magyar moilekulaspektrozkópiai konferencia*.10–12 July, Paks, Hungary, 51.
[5] Záray, Gy.–Co-Workers: *Az elemanalitika korszerű módszerei.* Akadémiai Kiadó, Budapest, 2006.
[6] Varna, A.: *Handbook of inductively coupled plasma atomic emission spectroscopy.* CRC Press, USA, 1991.

Geosciences and Engineering, Vol. 1, No. 1 (2012), pp. 21–28.

3 DIMENSIONAL MODEL STUDIES OF MODERN LANDFILLS

MÁTYÁS KRISZTIÁN BARACZA–ÁKOS GYULAI
University of Miskolc, Department of Geophysics
3515 Miskolc-Egyetemváros, Hungary
baracza@uni-miskolc.hu, gfgyulai@uni-miskolc.hu

Abstract
Nowadays most of the waste is being taken to waste sites. The aim is to provide such a final disposal of waste that any harmful components could not get into its environment. In order to avoid the pollution from the waste site the suitable isolation of the landfills has to be ensured. Identifying leaks in landfill liners is an essential part of waste management. A geo electrical 3-D Forward Modeling has been carried out to detect and locate leaks in the geomembrane liner used in landfill to prevent environment from leachate contamination. The principle of the geo electrical leak location is to place a voltage across the geomembrane liner and measure the resultant electrical potentials. To investigate the performance of the mobile leak detection method a landfill was simulated using a 3-D Forward Modeling program. the Pole-Pole and Pole-Dipole arrangements were utilized. The results accurately show the position of the leaks.

1. Introduction

Containment of municipal and hazardous waste materials in modern landfills is frequently achieved thorough lining the structure with a low permeability geosynthetic membrane or "geomembrane", commonly made of plastics like high density polyethylene (HDPE). The function of geomembrane liner is to prevent percolate flow to the environment. These materials, which arrive to the landfills on rolls, are deployed in strips and then welded together to form a continuous coverage (Szabó, 2001). This coverage is typically coated by either a geotextilie and a drainage layer or sand type protection materials. Strict construction quality assurance is applied during the construction of the geomembrane to ensure that the number of penetrating holes and other imperfections in the geomembrane are reduced to an acceptable value. Many of leaks occurred at T-joints, patches and at the seams in highly-stressed areas such as the base of the side slope (Szabó, 2008). Locating leaks in geomembrane after installation is an essential element to ensure that the lined facility is functioning as designed. Conventional non destructive testing methods, such as air channel testing for double track seams, spark tests or vacuum box testing for extrusion seams have been used to detect punctures. However, these methods are not practically applicable to the complete geomembrane surface, especially under the filling operation of waste site.

Some geophysical electrical arrangement closely related to the direct current electrical resistivity method is capable of accurately locating leaks in the geomembrane after the waste cover is placed over the liner. The geoelectrical techniques exploit the insulating properties of geomembrane and are able to locate the holes under the protective soil or waste covered geomembrane. In the practice these methods are not damage the liner.

There are two geoelectrical ways to control the integrity of geomembrane. The one of them is the pre built-in electrode system, and the other is the mobile measuring system (Frangos, 1997, Kovács, KBFI-Triász Kft., 2007). The permanent system is a widely used measurement all of the word. This pre built-in system consists of electrical nodes with electrodes, which are installed under the construction of the geomembrane liner system.

These nodes are connected to an external panel which is used to systematically energies the nodes by mean a resistivity meter and to monitor the sub grade response, automatically performing a resistivity survey of the entire area. There are measurement systems which are measure the soil moisture changes beneath the geomembrane liner (Metolabor AG., 2004).

In the application of the mobile system, there were only trial measurements, caused by the difficult data processing and measurement implementation. In this paper I preferate the mobile system instead of using the previously built-in permanent electrode monitoring system. The mobile electrical leak location is working on the top of the waste body without any pre built-in electrodes, detects electrical leak paths through the geomembrane liner caused by water or moisture in holes through the geomembrane.

Taking physical features of surface geoelectrical exploration into consideration as a basis in my investigations, I have utilized a 3-Dimensional Finite Difference (3-D FD) Forward Modeling solution of the governing equations for this potential equation problem. This research work allow to show and separate of possible occurring liner defects. The results are seems to be promising and effective way to locate the damages for repair.

2. Principle of geoelectrical model-experiments

The geoelectrical leak location method is based on the impression of voltage across the geomembrane and the detection of the exact place where electrical current flows through the geomembrane *(Figure 1).*

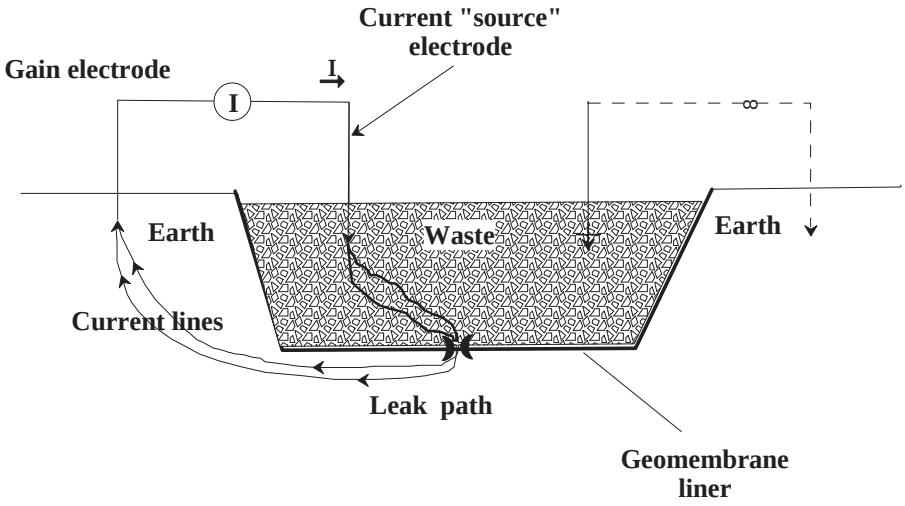

Figure 1: Configuration of electric leak location technique for landfills

A voltage is connected to an electrode placed on the top of the waste body and to a second electrode placed in earth ground. When no leak or leaks are present, the voltage impressed across the liner, produces a very low and a relatively uniform voltage distribution in the material above the surface of the wastebody. If a hole is present in the geomembrane liner, conductive fluids passing through the hole will allow a much larger

and more significant current in order to flow through the hole, produce localized anomalous area of high current density at the leak. The increase in the current density at the location of the hole forms an electrical anomaly that can be mapped to detect the position of the hole. The voltage produced by the voltage source will be divided approximately according to the resistance of waste R_H , the resistance of drainage layer cushion R_{TSZ}, the resistance of geomembrane R_{SZ}, the resistance of the earth R_T and the contact resistance of the source electrodes R_+; R_-. The equivalent electrical circuit is illustrated schematically in *Figure 2*.

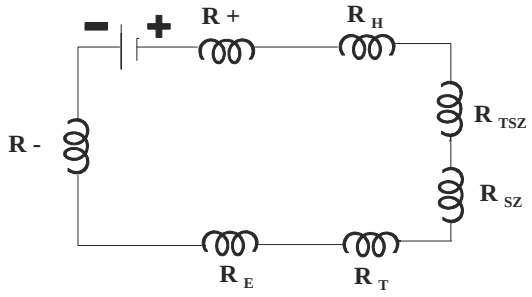

Figure 2: Electrical analogue of resistance circuit for geoelectrical leak location

Using Ohm's Law (U = IR), the current flow (I) produced by a given voltage (U) can be calculated from the relationship:

$$I = \frac{U}{R_+ + R_H + R_{TSZ} + R_{SZ} + R_T + R_E + R_-}$$

In my 3-Dimensional Forward Modeling work I've calculated with two types of electrode arrangement. The first is the Pole-Pole arrangement, and the other is the Pole-Dipole arrangement. *Figure 3* shows the Pole-Pole arrangement.

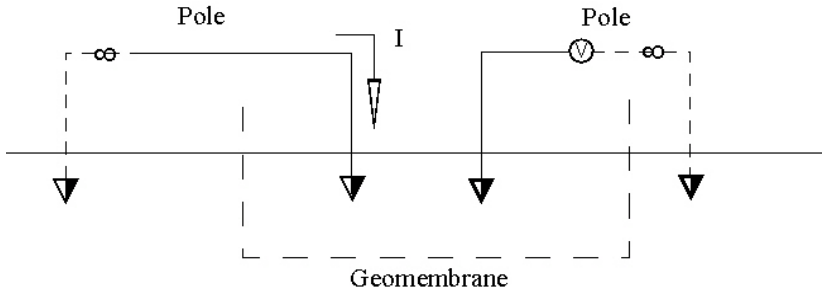

Figure 3: Scheme representation of Pole-Pole electrode arrangement

With Pole-Pole configuration one of the current electrode is locate inside the isolated area and the other electrode of the pair, locate outside of the geomembrane at a quasi infinite point. In this arrangement one of the potential electrode (reference electrode) locate on the top of the isolated area, the other of the potential electrode pair is fixed in the infinite

distance from the other potential electrode. The potential distribution is sampled by a moving electrode across the measuring grid and sense the potential difference it.

With Pole-Dipole configuration one of the current electrode locate inside isolated area and the other electrode of the pair locate outside of the geomembrane, as shown on the *Figure 4*. To locate a leak or leaks, an electrical current is applied to the waste. The potential (measurement) electrodes are located inside the measured isolated area.

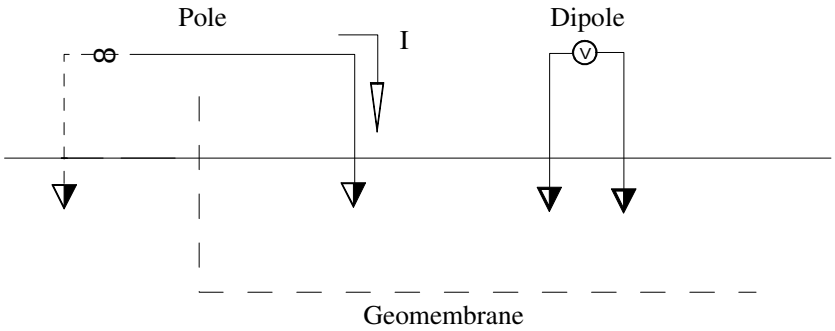

Figure 4: Scheme representation of Pole-Dipole electrode arrangement

In this paper I preferate the mobile method of geoelectrical measurements like the permanent pre built-in electrode system. Electrical leak location on the top of the waste body seems to be promising and gives an effective way to locate the damage for repair. The results can show sharp position of the leak, after the mathematical operations.

3. Applied models in 3-D FD modeling

The available 3-D FD Forward Modelling program permits of investigation of deposits combined with features of such a waste that has optional horizontal range, three-dimensional inhomogeneous with arbitrary resistivity and geometry in a general sense. The notation of arbitrary is valid for such ordinary physical properties, which are experienced normally in case of waste disposal.

The finite difference direct problem solution's subroutine was developed by Professor K. Spitzer in Geophysical Institute of Mining Academy of Freiberg (Spitzer, 1995). The maximum numbers of x-y horizontal and z vertical direction grid elements are 73 and 39, respectively. By means of the software grid-independent electrode positioning can be achieved, i.e. transmitters and receivers, and the potential values can be obtained in arbitrary points of x-y-z space. The program determines potential values (as a final result) that have been turning out in electrical field induced by electrode array according to the actual set. For the interpretation of results I applied numerical modeling outcomes received from Á. Gyulai with the help of other finite difference program (Gyulai, 1997).

In this paper I've calculated with 5 m thicknesses of waste. I used the Pole-Dipole, Pole-pole electrode arrays in order to achieve deep penetration and detection ability. The relation between the magnitude of the noise and the magnitude of the leak signal is often called the signal-noise ratio. This signal-noise ratio can also suffer from much larger noise, what cause by poor electrode contact or too dry soil surface. With the mathematical formu-

lation of normalizing can able to get better signal-noise ratio, indicate more accurately the position of the leak.

The results are related to two basic models:

1.1. The leak-free model (model-1) was formed by internal waste area with 200m * 200m, in which a waste layer with 5m of thickness and 50 Ωm of apparent resistivity was calculated. The waste thickness can be considered as a cultivated deposit. Under the waste body locate the perip material (uncontaminated) with 20 Ωm of apparent resistivity, separated from the waste with geomembrane. The apparent resistivity of geomembrane is 50 000 Ωm, as the *Figure 5* is shown.

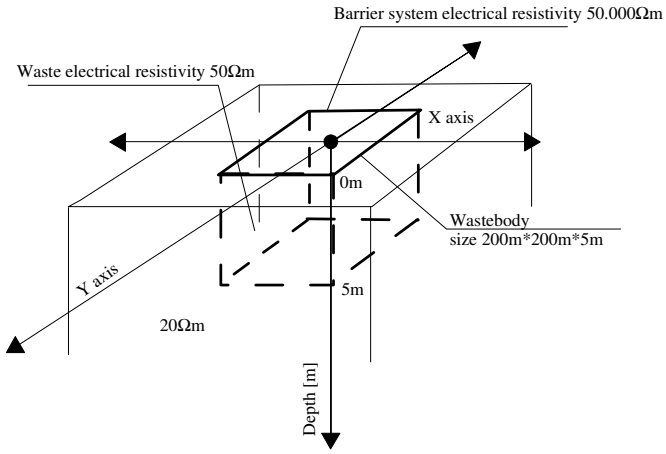

Figure 5: Leak free model

1.2. The other model (model-2) including a leak is different from model-1. There is a 2m *0.4m sized leak with 0,1 Ωm apparent resistivity at the centre of the coordinate-system, as the *Figure 6* shows.

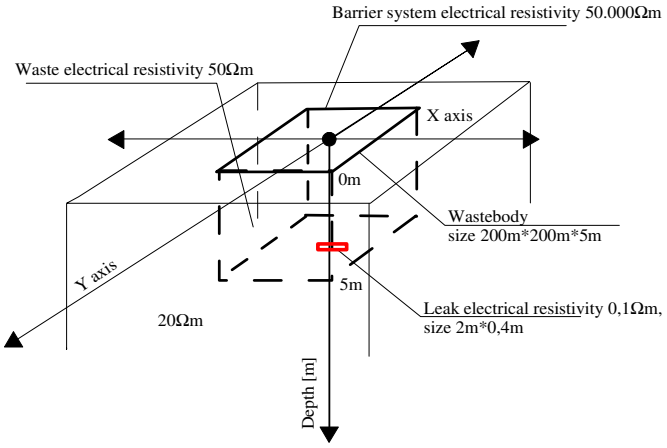

Figure 6: Model with a leak

4. Results

For the better demonstration of the results I've applied the mathematical formulation of normalizing. A contour map calculated from model-1 and model-2 excited potential values normalized to each other, which shown in the Figure 7. The potential distribution anomaly appears as a pattern of concentric circles centered on the leak. The leak with the size of 2m x 0.4m is located on the centre, as shown. For this figure I've utilized the Pole-Pole electrode array. The current source was located at (X = –40; Y = 0; Z = 0) point in the Cartesian coordinate-system. The receiver was at (X = –6000; Y = –6000; Z = 0) point in the distance of quasi-infinity. The contour map is indicating the leak at the centre leak. On the centre of the leak, the deviation from the leak free model's potential value is – 6%.

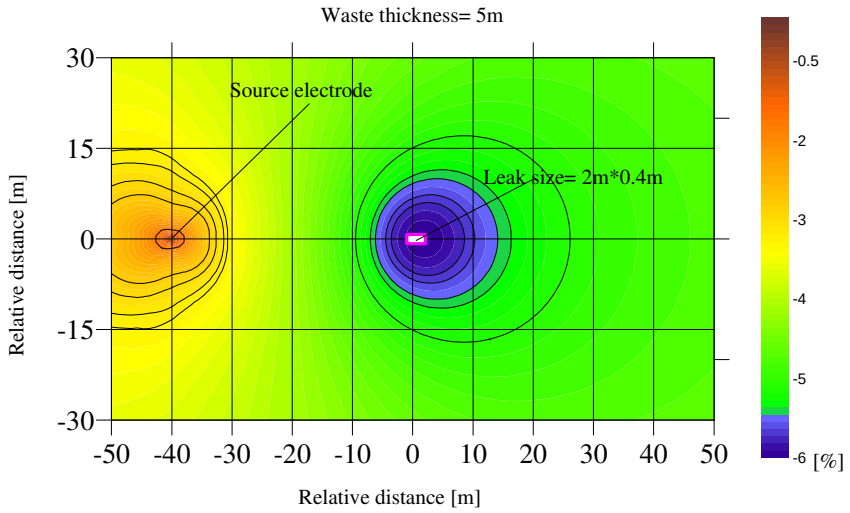

Figure 7: Normalized potential distribution map of Pole-Pole arrangement (zoomed map)

With Pole-Dipole configuration, a leak anomaly generated as a characteristic bipolar anomaly as the *Figure 8* shown.

Along the grid line, this is an anomaly that change from background to positive (or negative anomaly, it is depends from the normalizing mathematical method) values, then drops through zero to negative (or positive) values before returning to background levels. The values are plotted around the two extremum. The location of the leak is determined by locating the inflexion point between the maximum and minimum peak to peak value.

The calculated apparent resistivity values from the potential distribution values give the next figure. In Figure 9 right next to the leak with centre position of x = 40m, y = 0m, z = 0 m the distortion of apparent resistivity can be noticed. The midpoint of an imaginary line between extreme values of the symmetric positioned two anomalies signs the location of the leak.

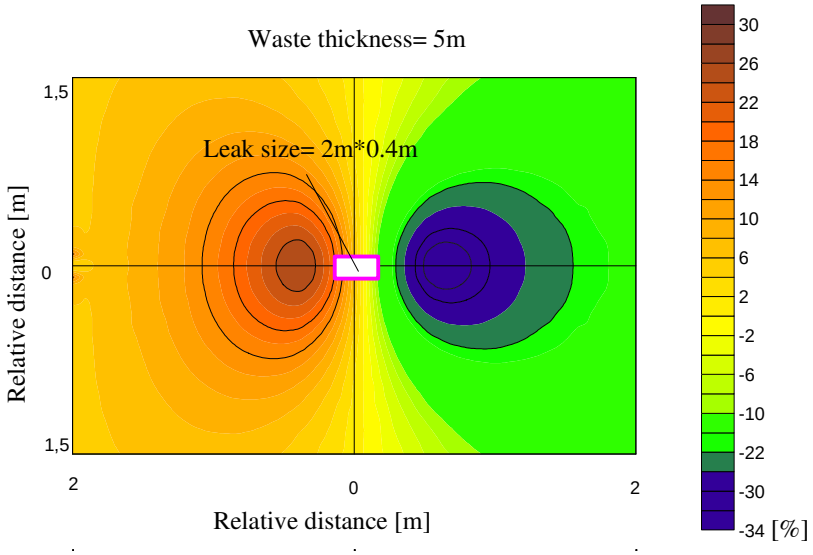

Figure 8: Normalized potential distribution map of Pole-Dipole arrangement (zoomed map)

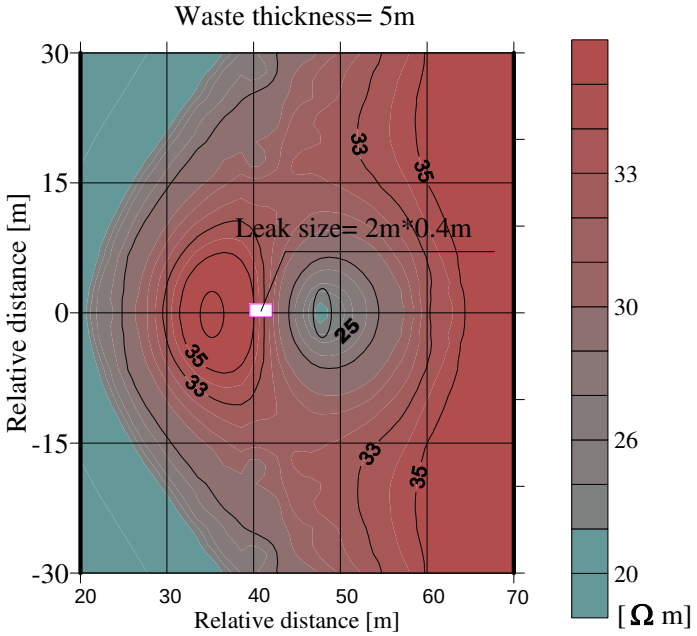

Figure 9: Apparent resistivity distribution map of Pole-Dipole electrode array

5. Conclusions

On the score of above presented figures it can be declared that in the case of overlaying by waste with 5m average thickness the defects in geomembrane system of waste site well-separated geoelectrically from surroundings can be confidently distinguished from the average values of potential distribution measured above deposits.

The applied 3-D FD Forward Modeling program helped me to simulate the values of potential distribution, measured above a waste site constructed on the basis of a practical example. The adopted Pole-Pole and Pole-Dipole electrode arrays are suitable to locate leaks of liner thanks to powerful currents penetration ability. With the help of special normalizing mathematical formulation the defect-indication ability of the applied electrode arrays can be improved. I keep the testing the presented Forward Modeling method also in the field practice and to carry out measurements by another special electrode arrays applied in the geoelectrical practice (Szalai, Varga, Novák, Szarka, 2010).

I plan also to apply to the interpretation practice of geoelectrical leak location detecting methods, the 1.5 D inversion procedure (Gyulai, Ormos, 1999a).

Acknowledgement

This described work was carried out as part of the TÁMOP-4.2.1.B-10/2/KONV-2010-0001 project in the framework of the New Hungarian Development Plan. The realization of this project is supplied by the European Union, co-financed by the European Social Fund. The authors are also grateful for the support of the research team of the Department of Geophysics, University of Miskolc.

REFERENCES

[1] Szabó, I.: *Hulladékelhelyezés.* Miskolci Egyetemi Kiadó, Miskolc, 2001.
[2] Szabó, A.: *Hulladéklerakók lezárásának aktuális kérdései*. PhD-értekezés, Mikoviny Sámuel Földtudományi Doktori Iskola, Miskolc, 2008.
[3] Frangos, W., 1997: *Electrical detection of leaks in lined disposal ponds*. Geophysics 62, 1737–1744.
[4] Kovács, A.–KBFI-Triász Kft.: *Műanyag földműszigetelések ellenőrzése*. Mélyépítő Tükörkép Magazin, 2007/3.
[5] Metolabor AG.: *Dichtungskontrollsystem TAUPE für Mülldeponien I–II.* Forschungs-zentrum Karlsruhe in der Helmholtz-Gemeinschaft, 2004/10.
[6] Spitzer, K.: *A 3-D finite difference algorithm for DC resistivity modelling using conjugate gradient methods*. Geophysical Journal International, 1995, 123, 902–914.
[7] Gyulai, Á.: *Geoelektromos 3-D FD modellezési vizsgálatok*. T 019088 sz. OTKA-pályázat, II. Részjelentés,1997, 1–48.
[8] Szalai, S.–Varga, M.–Novák, A.–Szarka, L.: *A „Nem-konvencionális geoelektromos elrendezések"* című K 49604 sz. OTKA-projekt eredményeiből. Magyar Geofizika, 51. évf. (2010) 4. szám, 209–226.
[9] Gyulai, Á.–Ormos, T., 1999a: *A new procedure for the interpretation of VES data: 1.5-D simultaneous inversion method*. Journal of Applied Geophysics, 41, 1–17.

Geoscienses and Engineering, Vol. 1, No. 1 (2012), pp. 29–35.

COMPARISON OF GEOTHERMAL ENERGY PRODUCTION TECHNOLOGIES

ELEMÉR BOBOK
Department of Petroleum and Natural Gas Engineering, University of Miskolc
3515 Miskolc-Egyetemváros, Hungary
boboke@kfgi.uni-miskolc.hu

Abstract
Geothermal energy production technologies of direct use are compared. The doublet-technology obtains the best recovery factor for hydrothermal systems. The ground source heat pumps fitted to shallow borehole heat exchangers are rapidly spreading because of their obvious advantages. There are further opportunities for further innovative technologies.

1. Introduction

Geothermal energy production and utilization has grown remarkably worldwide in the recent years. A coherent view can be obtained about the development of the geothermal industry from the general survey of the International Geothermal Association. It is composed from the individual country reports made in uniform point of view for the fifth World Geothermal Congress, held in Bali, Indonesia in 2010. Bertain [1] held the general report on the geothermal power production. Lund [3] presented the state of the direct use of geothermal energy. It can be ascertained a definitive progress on both fields. The installed capacity of the geothermal power plants has grown linearly from year to year. The growth of the direct use is more rapid: the thermal power predicted for 2020 was achieved in 2010. The development seems to be exponential in consequence of the fast worldwide spreading of the ground source heat pumps.

2. International and Hungarian background

The capacity of the installed geothermal power plants at the end of 2005 and 2010 years are shown in *Table 1*. The growth is convicting in the number of the concerned countries, the installed capacities of the power plants and the produced energy.

Table 1

Electricity production

Year	2005	2010
Number of countries	22	24
Installed capacity MW	8933	10 715
Produced energy GWh	55 709	67 246

The growth is more rapid in the direct use in number of countries, installed capacity of the world and the produced energy. *Table 2* shows these data.

Table 2

Direct heat use

Year	2005	2010
Number of countries	72	78
Installed capacity MW	28 268	50 583
Produced energy GWh	273 372	438 071

Table 3

Top 5. electricity producers

Country	Installed capacity MW	Produced energy GWh
USA	3060	19 000
Philippines	1904	10 311
Indonesia	1197	9600
Mexico	958	7047
Italy	843	5520

The list of the most important countries in direct use is rearranged last years. Sweden joined up to China and the USA while Iceland and Hungary are superseded from the leading position. Especially remarkable the Swedish advance as a result of the fast spreading of the ground source heat pumps.

Table 4

Top 5 direct users

Country	Installed capacity MW_t	Produced energy GWh
China	3700	12 800
Sweden	3840	10 000
USA	9000	9700
Turkey	1500	6900
Iceland	1850	6800

Favorable natural conditions of Hungary are well known. The average value of the terrestrial heat flow is 97 mW/m^2, the average geothermal gradient is 0,048 $^oC/m$. There are huge porous and permeable sandstone aquifers mainly in the Southeastern part in the Great Hungarian Plain, in the Dráva-trench and in the Little Hungarian Plain. The whole extension of these aquifers is more than 40 000 km^2. The well-known deep karst in Zala county and the promising deep carboniferous reservoirs in Northern Hungary are containing substantial geothermal reserves. In addition, the energy of the shallow rock layers can be utilized by ground source heat pumps in the whole area of Hungary considering the above mentioned reservoirs, the economically recoverable geothermal reserves of Hungary can be estimated as 455 000 PJ [2]. This amount of geothermal energy is contained both in the reservoir rock and its pore system filled by water. It is obvious, that the whole energy

content of the reservoir cannot be recovered. The applied production technology determines what part of the reserve can be recovered.

Hungary's geothermal energy reserves are qualified as low enthalpy reserves. This name suggest an opinion whereas of these reserves are limited because of the restricted feasibility of the utilization.

Although electricity generation is technically feasible from low enthalpy resources (< 120 ^{o}C), there is an efficiency thus an economical limit of the resource temperature for power generation. Low enthalpy resources can be used more economically for direct heat utilization.

The usual temperature range of a heating system is 55–80 ^{o}C. These heating temperature requirements can be fitted to the low enthalpy geothermal resource temperatures. In the other hand, Hungary's primary energy consumption for heating is 435 PJ/year, which is 40% of Hungary's whole primary energy demand. This important section of the Hungarian energy market can be matched the significant geothermal potential of the country.

Nowadays the Hungarian geothermal energy production capacity is based on 778 production wells. Their possible total mass flow rate is 5880 kg/s. The thermal power capacity belongs to this mass flow rate which is

$$P = \sum_{i=1}^{n} m_i c_v \left(T_i - T_o \right) \tag{2.1}$$

where m_i is the mass flow rate and T_i is the wellhead temperature of the well, c_w is the specific heat capacity of the water, n is the number of the wells, T_0 is the annual mean temperature at the surface. The obtained thermal power potential is 1785 MW. In spite of this the effective produced annual mean thermal power is 654,6 MW (Tóth, [5]). The reasons of the difference between the potential and the produced power are the seasonality of the energy consumption and the mass flow decrease as the reservoir pressure decreases. It can be recognized that geothermal energy production and utilization has promising outlook in Hungary.

3. Geothermal energy production technologies

The currently applied geothermal energy production technologies in Hungary can be categorized into two major classes. One of them is the thermal water production from deep hydrothermal systems. The other class is geothermal energy production from shallow, near-surface formations by borehole heat exchangers and ground source heat pumps without thermal water recovery. Appearance of the ground source heat pumps considerably changed both the theoretical and the technical ideas of the energy recovery. Using heat pumps it becomes possible to recover the energy content of rock domains having lower temperature than the surroundings. The utilizable part of the geothermal energy belongs to the temperature range which is higher than the surroundings. This is the so-called exergy. The energy content of the domain having a lower temperature than the surroundings cannot utilizable according to the classical thermodynamics. This is the so-called anergy. The heat pump transforms the anergy to exergy, via input of mechanical work thus the non-utilizable part of energy can be recovered.

In the initial period of geothermal energy production, the natural flow of thermal water by resulted of elastic expansion of the reservoir fluid was almost exclusive. In this case the flow in the well starts by pumping until the whole tubing was filled by hot water. Because of this the bottomhole pressure becomes lower. The pressure decrease induces the elastic expansion of the reservoir fluid flowing to the well and rising through the tubing to the surface. After this well flow becomes self-supporting, while the separation of dissolved gases helps to maintain the flow. Gradually the wellhead pressure decreases, tends to the atmospheric pressure when the flow is stopped.

The bottomhole pressure can be lowered substantially applying a submersible pump in the well. Thus the elastic expansion of the reservoir fluid becomes more intensive; the reservoir can be expelled greater amount of thermal water, the thermal power of the well increases. It is obvious that increasing the flow rate fewer wells need to be drilled to lowering the implementation costs.

A geothermal energy production system which consists of a production well, a heat exchanger and a reinjection well, where all the produced and cooled geothermal water is returned the reservoir is the so-called doublet system. A doublet system is a more complex construction; it has greater implementation and operating costs than an elastic expansion system.

The advantages of a doublet system counterbalance plentifully the increased costs. The reservoir fluid cannot decrease because of the steady reinjection. For the same reason the reservoir pressure doesn't decrease. The rock matrix of the reservoir is flushed continuously, thus the thermal energy content of the rock can be recovered too. The limit of the recovered geothermal energy is the cooling of the reservoir. To choose this temperature limit is a reasonable but an arbitrary decision. An additional benefit is that no environmental pollution occurs. It is a frequently encountered issue in this technology that in order to achieve an effective reinjection into porous rocks the technological requirements must be rigorously followed so as to avoid the decrease of permeability. In fractured carboniferous reservoirs the short-circuiting between production and reinjection wells must be eliminated.

4. Comparison of the thermal water production technologies

In the following it will be compared several thermal water production technologies: the flowing well, the submersible pumping and the doublet method. The base of the comparison is the attained recovery factor simple lumped-parameter model is chosen for the calculations. Consider part of a porous sandstone reservoir of unit balk volume it is the same for all cases.

Its porosity ϕ = 0,18, temperature T = 80 ^{o}C. The density of rock matrix ρ_r = 2400 kg/m^3, while water density ρ_w = 971 kg/m^3. Specific heat capacities of the rock c_r = 0,87 KJ/kg ^{o}C and of the water c_w = 4,19 KJ/kg ^{o}C. The annual mean surface temperature T_0 = 10,5 ^{o}C. In this case the exergy of the water-saturated sandstone of unit bulk volume is

$$e_1 = \left[(1-\varphi)\rho_r c_r + \varphi\rho_w c_w\right](T - T_0) = 169\,890 \text{ KJ/m}^3 . \qquad (2.2)$$

Herein the exergy of the rock is e_{1r} = 118995 KJ/m^3 while the exergy of the water is e_{1w} = 50 895 KJ/m^3. The recoverable mass of water from this part of reservoir of unit bulk volume is

$$m_w = \varphi\beta\rho_w\left(p_1 - p_2\right) \tag{2.3}$$

where the isothermal compressibility of water is $\beta = 4,68\cdot10^{-8}\,\mathrm{m}^2/\mathrm{N}$. The pressure p_1 refers to the initial state of the reservoir, while p_2 refers to the final state of production. The typical pressure difference obtained in the Upper-Pannonian aged sandstone reservoirs is $p_1 - p_2 = 3\cdot10^5\,\mathrm{N/m}^2$. Thus the water mass expelled by elastic expansion m_w = 2.45 kg/m^3. The recoverable exergy by the flowing well is

$$\varepsilon_{uf} = m_w c_w\left(T - T_0\right) = 713\ \mathrm{KJ/m}^3. \tag{2.4}$$

This is only 0,42 percent of the exergy content of the reservoir.

Applying artificial lift by built in a submersible pump into the well it can be attained even $30\cdot10^5\,\frac{\mathrm{N}}{\mathrm{m}^2}$ bottomhole pressure decrease. This depression gives a possibility to recover water of 24,5 kg/m^3. Thus the recoverable exergy from the unit volume reservoir-part by pumping $e_p = 7130\ \mathrm{KJ/m}^3$. This is 4,2 percent of the whole exergy content of the reservoir.

Operating a doublet it can be allowed to recover the energy both of the water and the rock cooling the reservoir from the initial temperature T_1 to the arbitrary chosen final temperature T_2. Let be T_2 = 60 °C. Thus the recoverable energy

$$e_d = \left[\left(1-\varphi\right)\rho_r c_r + \varphi\rho_w c_w\right]\left(T_1 - T_2\right) = 44880\ \mathrm{KJ/m}^3. \tag{2.5}$$

This value is far greater than the recoverable energy by pumping. It can be recovered 28,8 percent of the exergy content of the reservoir. The effectiveness of the production technology by reinjection is obvious.

The recovery factor of flowing well method is 0,42 percent, it can increase to 4,2 percent by submersible pumps, while the doublet operation can attain 28,8 percent.

We shall note that the introduced comparison is based on a very simple lumped-parameter reservoir model. The obtained differences in recovery factors are so large, that a more sophisticated simulation seems to be unnecessary for this analysis.

5. Geothermal energy production by ground source heat pumps

Geothermal energy production by ground source heat pumps contrasts strikingly with thermal water production not just theoretical base, production technology and equipments, but also its resources. The ground source heat pumps use as heat source another depth and temperature interval than hydrothermal systems. The rapidly spreading ground source heat

pumps are fitted to shallow downhole heat exchangers which supply heat at a moderate temperature. The heat pump transformed the recovered energy to a greater temperature. The produced energy can be applied for floor and wall heating at least 50–55 ^{o}C. Currently these facilities exceeded the level of family houses. Largest Hungarian system are based on more than 180 borehole heat exchangers, attained the 1 MW thermal power.

Geothermal energy can also be produced from deep borehole heat exchangers (DBHE). This recommendation occurred as a possibility of utilization of dry holes i.e. the unsuccessful hydrocarbon prospecting wells. To drill a well directly for implementation of a deep borehole heat exchanger is cannot be economical. The produced thermal power of a DBHE decreases rapidly after an initial performance state and tends asymptotically to an equilibrium value. For example a DBHE having a depth of 2000 m across a formation with average heat conductivity of 2 W/mK, produces steadily thermal power of 300 kW only. The drilling and completion costs such a well can be about 250–300 million HUF. A shallow borehole heat exchanger of 110 m can be produced at least 3 kW. Thus the 300 kW thermal power of the DBHE can be replaced by the thermal power of 100 shallow borehole heat exchangers. The whole cost of the latter is 50 million HUF only. This cost is even less than the reforming of a dry hole to DBHE. Geothermal energy can be produced less specific cost per KW from shallow, than deep borehole.

It can be operated complex systems producing water and applying heat pumps to recover energy from the produced water simultaneously. The processing heat of the mineral water bottling plant in Zalaszentgrót is provided from the mineral water of 33 ^{o}C.

The abandoned and flooded underground mine workings constitute low enthalpy geothermal reservoirs. The utilization of mine water applying geothermal heat pumps is a promising idea. The geometry of the workings and the site-specific geological, hydrogeological conditions are known and well documented. The water is easily accessible through the shafts or can be tapped by shallow wells. The heat transfer area between the tunnel wall and the water is large enough, and the natural supply of the mine water allows a sustainable operation of the energy production. In spite of this, there are a few known projects as Malolepszy [4] reports it. The most promising Hungarian site is the abandoned copper mine in Recsk flooded by warm water of 55 ^{o}C [6].

There are many settlements in Hungary, for example Eger, where mild water is mixed to the drinking water network. Its value in use increases cooling the water by heat pump, the exploited heat can be utilized energetically.

An original two-stage geothermal heating system is elaborated for de-icing of the inclined main road of the underground nuclear waste deposit in Bátaapáti [7]. The intake air is warmed up to 16–17 ^{o}C along the large heat transfer surface of the working. Air-water heat pumps heat the circulated water in the floor-heating pipe network. To use the warmed up ventilated air as geothermal heat carrying fluid is a new solution.

It can be utilized the geothermal energy of hot water co-produced with oil from reservoirs. Their water content can be more than 90 percent. Before reinjection it can be suitable to cool this water by heat pump.

At last but not least the energetically used thermal water contains substantial amount of energy. In many cases the waste water temperature is even $T_2 = 60$ ^{o}C. Its energy can be utilized applying a heat pump to re-heat a secondary fluid circuit to the original temperature T_1, while the primary fluid is cooled down to temperature T_3. Since the utilized temperature difference increases from $T_1 - T_2$ to $T_1 - T_3$, the efficiency of the system increases. The

heating can be performed by less water production and reinjection. Inventive engineers can be attain further original and efficient internationally remarkable solutions.

6. Conclusions

Geothermal energy production can be realized by various technologies according to the site-specific natural and technical conditions. Amongst these there is no a generally best production technology for all possible cases. The necessity of reinjection is motivated only the point of view of environmental protection, but it obtains the best recovery factor amongst the water production technologies. An important aspect of feasibility that the site of the hydrothermal resource and the implemented utilization system let be close to one another. The co-location isn't so rigorous for district heating systems. In spite of this there is no such constraint in the case of ground source heat pumps. A borehole heat exchanger can be implemented practically everywhere. There are new ideas to utilize the rest energy content of the waste thermal waters, or to produce energy from the abandoned flooded mine workings.

"Acknowledgement: This work was carried out as part of the TÁMOP-4.2.1.B-10/2/KONV-2010-0001 project in the framework of the New Hungarian Development Plan. The realization of this project is supported by the European Union, co-financed by the European Social Fund."

REFERENCES

[1] Bertani: *Geothermal power generation in the world.* 2005–2010. Update report 008 World Geothermal Congress, Bali, 2011.
[2] Bobok, E.: *Geothermal energy production (in Hungarian).* University textbook, Miskolc, 1997.
[3] Lund, J.–Freeston, D.–Boyd, T.: *Direct utilization of geothermal energy* 2010. Worldwide Review, 007 World Geothermal Congress, Bali, 2011.
[4] Malolepszy, Z.: *Man-made low temperature geothermal reservoirs in abandoned workings of underground mines international.* Geothermal Conference Reykjavik, S13, Paper 083, 2003, 23–29.
[5] Tóth, A.: *Hungarian Country Update 2005–2009.* 0125 World Geothermal Congress, Bali, 2010.
[6] Tóth, A.: *Geothermal potential of an abandoned copper mine.* Transactions of GRC, 35, 2011, 540–546.
[7] Tóth, A.: *Geothermal deicing in a mine tunnel. Proc.* of 36th Stanford Geothermal Reservoir Workshop, 2012.

Geosciences and Engineering, Vol. 1, No. 1 (2012), pp. 37–47.

DETERMINATION OF THE TEMPERATURE DISTRIBUTION IN THE CIRCULATING DRILLING FLUID

ZOLTÁN SZARKA–ELEMÉR BOBOK
Department of Petroleum and Natural Gas Engineering, University of Miskolc
3515 Miskolc-Egyetemváros, Hungary
boboke@kfgi.uni-miskolc.hu

Abstract
An analytical mathematical model is developed to calculate the temperature distribution of the circulating drilling fluid in the drillpipe and the annulus. The obtained formulas are valid for forward circulation. Influence of geothermal, geometrical and performance variables are investigated.

1. Introduction

The knowledge of the temperature distribution in the circulating drilling fluid has a great importance to design drilling operations. Determination of the maximum allowable pumping rate, design of cementing program, calculation of thermal stresses in casing strings, logging tool design need to modeling the borehole heat transfer process. It is especially necessary for drilling geothermal wells, where significant heat transfer occurs. Fluid temperature is influenced by many variables: the depth, the elapsed time, mass flow rate and material properties of the drilling fluid, thermal properties and temperature distribution of the surrounding rocks. Although direct temperature measurements can be made at a given depth and time within drilling operations, without the heat transfer model we cannot predict temperatures for arbitrary performance states. Flow and heat transfer in drilling operations is a complex simultaneous interaction between the circulating flow and the surrounding rock mass around the borehole. The temperature of the flowing fluid in the drill pipe and the annulus is lower than the undisturbed rock temperature. This temperature-inhomogenity induces a radial heat flux toward the borehole. It must be noted that the upper section of the borehole the fluid is warmer than the rock, thus the heat flux is directed radially outward.

The drilling fluid is heated by the surrounding rock which is cooled. The heat transfer process is a time-depending phenomenon during the drilling history. An analytical mathematical model is elaborated to describe this transient heat transfer. It makes possible to calculate temperature profiles for entire wellbore and to investigate the influence of the main performance parameters.

Two types of mathematical models, analytical and numerical, have emerged for determination the circulating fluid temperature. Their theoretical bases are the same: the balance equations of mass, momentum and energy. The initial and boundary conditions, the material properties are obviously the same. The definitive difference between the two models is the different ways to solve the equations. Applying analytical solutions the obtained differential equations are integrated in closed form as mathematical analytic functions. In order to easy integration some simplifying assumptions can be made. Analytic functions can give information about the system behavior even for lack of detailed calculations. Numerical models use some time and space stepping procedure, the solution is obtained by a generated table or a graph. Numerical techniques are suitable to consider more realistic models of greater complexity, at the cost of extended amount of calculations.

Many early models assumed constant temperatures of the flowing fluid as Edvardson et al (1962). Others used experimentally determined approximate correlations as Dowdle and Cobb (1975). A sophisticated analytical model was made by Boldizsár (1958) neglecting the thermal resistance of the multiple casing string. Raymond's first numerical model (1969) has included the transient response of the flow for the initial short-time period.

The present model is an analytical approach, in which the unnecessary simplifications are avoided; a rigorous analytical treatment is applied as far as it is possible within reasonable limits. The temperature distribution is determined along the depth both in the drilling pipe and the annulus. Influencing factors: flow rate, well completion, elapsed time and geothermal conditions of the surrounding rock are investigated.

2. Formulation of the problem

The so-called forward circulation system is investigated, where the drilling fluid flows down in the drillpipe and back up in the annulus.

The thermal interaction between the drilling fluid and the formation is considered axisymmetric. In accordance to the system's geometry a cylindrical coordinate system is chosen. Its z-axis is coaxial with the drillpipe, directing downward. The origin z = 0 is at the surface.

At the depth of z a suitable chosen control volume is taken in order to write the balance equation of the internal energy. The control volume is coaxial with the borehole. Its boundaries consist of a cylindrical surface of radius R_∞ and two horizontal parallel planes of distance dz between them. The radius R_∞ belongs to the location of the undisturbed formation temperature T_∞. The temperature difference between the formation and the drilling fluid induces a radial heat flux through several elements of the wellbore. The control volume is shown in *Figure 1*. It is convenient to separate it into four sub-systems: the flowing fluid in the drillpipe and the annulus, the well completion and the formation.

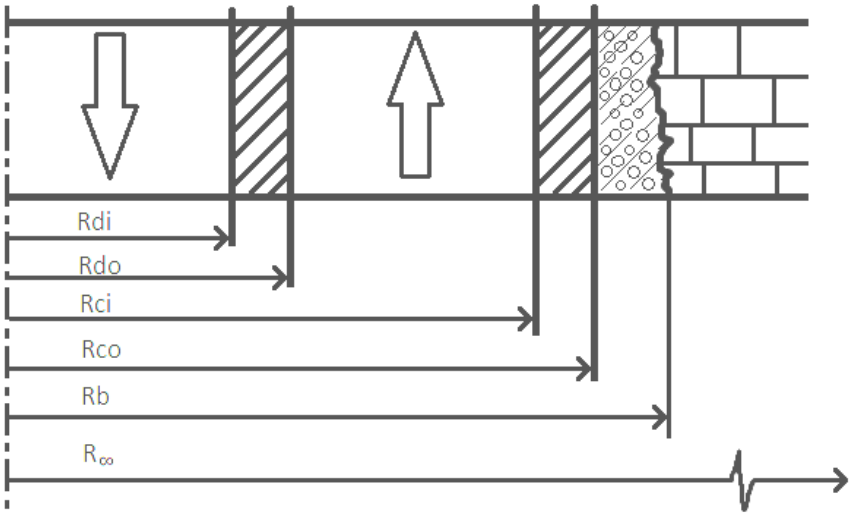

Figure 1: Elementary control surface

In the downward flow through the drillpipe the forced convection is the dominant mechanism of the heat transfer. In the upward flow through the annulus there is a twofold forced convection on both surfaces of the annulus. The well completion may be a completed section of the borehole, but it may be an open hole where the only thermal resistance is simply the forced convection between the formation and drilling fluid. In the formation radial conduction is the definitive phenomenon. This heat flux crossing the boundaries of the sub-systems must be the same on both sides.

Before balance equations are written, some simplifying assumptions can be taken. The drilling fluid is considered incompressible. The flow is steady and turbulent both through the drillpipe and the annulus. It is well known that the velocity and temperature distribution becomes more uniform over the pipe cross section as the Reynolds number increases, while the average velocity tends to the hypothetical velocity distribution of a perfect fluid. Thus the cross-sectional average velocities and temperatures can be used in the balance equations. The steep temperature change near the pipe wall in the thermal boundary layer is replaced by an abrupt temperature drop between the solid wall and the flowing fluid. The axial component of the conductive heat flux in the fluid is negligible. The temperature field of the formation is considered to axisymmetric around the borehole. The rate of change of the temperature in the fluid is substantially greater than in the surrounding rock. Thus the transient heat transfer process can be considered to a slow temperature change of the huge heat capacity rock mass, while the thermal response of the tiny fluid filament in the borehole follows it instantaneously.

Thereafter the balance equation of the internal energy can be written for the drillpipe as follows.

$$\dot{m}cdT_D = 2\pi R_{Di} U_{Di} \left(T_A - T_D\right) dz \tag{1}$$

Where $\dot{m}$ is the mass flow rate of the fluid [kg/s], c is its specific heat capacity [J/kg ^oC]. U_{iv} is the overall heat transfer coefficient referring to the inner surface of the drillpipe [W/m^2 ^oC], T_D and T_A are the flowing fluid temperatures in the drillpipe and the annulus. The other notations are clearly shown in *Figure 1*.

The internal energy balance for the upflowing fluid in the annulus is

$$\dot{m}cdT_A = 2\pi R_{Ci} U_{Ci} \left(T_B - T_A\right) dz - 2\pi R_{Di} U_{Di} \left(T_A - T_D\right) dz \tag{2}$$

where U_{zi} is the overall heat transfer coefficient referring to the inner surface of the casing, T_B is the temperature of the cement sheet at the borehole radius R_B.

The heat fluxes at the boundary of the cement sheet and the surrounding rock are the same:

$$2\pi R_{Ci} U_{Ci} \left(T_B - T_A\right) = 2\pi k_R \frac{T_\infty - T_B}{f(t)} \tag{3}$$

where k_R is the heat conductivity of the rock [W/m ^oC], $T\infty$ is the undisturbed temperature of the rock at the given depth:

$$T_\infty = T_0 + \gamma z \tag{4}$$

T_0 is the surface temperature, γ is the geothermal gradient [°C/m], f(t) is the so-called transient heat conduction function, depending on the Fourier number and the quantity $\frac{R_{Ci}U_{Ci}}{k_R}$.

3. Solution

The balance equation (1) can be slightly modified:

$$\frac{dT_D}{dz} = \frac{T_A - T_D}{B} \tag{5}$$

where the quantity

$$B = \frac{\dot{m}c}{2\pi R_{Di}U_{Di}} \tag{6}$$

doesn't depends on the depth z.

Balance equations (1) and (2) are added, thus we get:

$$\dot{m}c\left(\frac{dT_A}{dz} + \frac{dT_D}{dz}\right) = 2\pi R_{Ci}U_{Ci}\left(T_B - T_A\right) \tag{7}$$

The temperature difference T_B-T_A can be expressed from (7)

$$T_B - T_A = \frac{\dot{m}c}{2\pi R_{Ci}U_{Ci}}\left(\frac{dT_A}{dz} + \frac{dT_D}{dz}\right) \tag{8}$$

Similarly $T_\infty - T_B$ is obtained from Eq. (3):

$$T_\infty - T_B = \frac{R_{Ci}U_{Ci}f(t)}{k_R}\left(T_B - T_A\right) \tag{9}$$

The sum of Eq. (8) and Eq. (9) obtains.

$$T_\infty - T_A = \left(\frac{\dot{m}c}{2\pi R_{Ci}U_{Ci}} + \frac{R_{Ci}U_{Ci}f(t)}{k_R}\cdot\frac{\dot{m}c}{2\pi R_{Ci}U_{Ci}}\right)\left(\frac{dT_A}{dz} + \frac{dT_D}{dz}\right) \tag{10}$$

After some simplification we get the expression

$$\frac{dT_A}{dz} + \frac{dT_D}{dz} = \frac{T_\infty - T_A}{A} \tag{11}$$

in which the so-called performance state coefficient

$$A = \frac{\dot{m}c\left(k_R + R_{Ci}U_{Ci}f\right)}{2\pi R_{Ci}U_{Ci}k_R} \tag{12}$$

seems to be independent of the depth z. Nevertheless A depends linearly on the circulating mass flow rate and the specific heat capacity of the drilling fluid. Thus at a given state of performance A can be considered constant. In the case of constant A the equation system is linear and an analytic solution can be obtained relative easily. However A has a weak dependence on depth, temperature and time.

In accordance to the well completion R_{Ci} and U_{Ci} changes in different depth intervals. Heat conductivity k_R can be replaced by its depth-averaged value. Heat transfer coefficient between flowing fluid and pipe wall depends on the viscosity, i.e. the temperature. In fluid-filled annular sections natural convection occurs. Its heat transfer coefficient depends on the temperature both directly and because of the viscosity-dependence indirectly too. The transient heat conduction function f depends on the Fourier-number, i.e. the time and the well completion. At a given time it can be taken to constant, thus we obtain different f values for different time-steps. Thus, however Eq. (11) has a slightly non-linear character, simple depth averaged material properties are suitable to determine temperature distributions.

Finally the differential equation system from pure mathematical point of view is

$$A\frac{dT_A}{dz} + A\frac{dT_D}{dz} = T_\infty - T_A \tag{13}$$

and

$$B\frac{dT_D}{dz} + T_D = T_A \tag{14}$$

Differentiating Eq. (14) by z, after substitution we obtain a second-order, linear, inhomogeneous differential equation with constant coefficient for T_s:

$$AB\frac{d^2T_D}{dz^2} - B\frac{dT_D}{dz} - T_D + T_0 + \gamma z = 0 \tag{15}$$

The homogeneous differential equation belonging to it is:

$$AB\frac{d^2T_D}{dz^2} - B\frac{dT_D}{dz} - T_D = 0 \tag{16}$$

Its characteristic equation is

$$AB\lambda^2 - B\lambda - 1 = 0 \tag{17}$$

The roots of the characteristic equation are:

$$\lambda_1 = \frac{1}{2A}\left(1+\sqrt{1+\frac{4A}{B}}\right) \tag{18}$$

and

$$\lambda_2 = \frac{1}{2A}\left(1-\sqrt{1+\frac{4A}{B}}\right) \tag{19}$$

Since both A and B are real, the solution of the homogeneous differential equation is obtained as

$$T_{D\,hom} = C_1 e^{\lambda_1 z} + C_2 e^{\lambda_2 z} \tag{20}$$

Since the right-hand side of the Eq. (15) is linear, a particular solution of it is looking for also in linear form:

$$T_{Dinh} = \alpha + \beta z \tag{21}$$

Substituting it into the Eq. (15), we get

$$T_{Dinh} = B\gamma - T_0 - \gamma z \tag{22}$$

Thus the general solution of Eq. (15) is the sum of Eqs. (20) and (22):

$$T_D = C_1 e^{\lambda_1 z} + C_2 e^{\lambda_2 z} + T_0 + \gamma z - B\gamma \tag{23}$$

The temperature distribution of the annular flow can be determined substituting Eq. (23) into Eq. (14).
Thus we get:

$$T_A = C_1\left(1+B\lambda_1\right)e^{\lambda_1 z} + C_2\left(1+B\lambda_2\right)e^{\lambda_2 z} + T_0 + \gamma z \tag{24}$$

The constant coefficients C_1 and C_2 can be determined satisfying the following boundary conditions: If z = 0, $T_D = T_e$. That is the drilling fluid temperature at the entrance in the drillpipe on the surface is T_e. The other is that the bottomhole temperatures both in the drillpipe and the annulus are the same. If z = H, $T_D(H) = T_A(H)$. Thus the following linear algebraic equation system is obtained

$$C_1 + C_2 = T_e - T_0 + B\gamma \tag{25}$$

and

$$C_1\lambda_1 e^{\lambda_1 H} + C_2\lambda_2 e^{\lambda_2 H} = -B\gamma \tag{26}$$

The roots of this equation system are

$$C_1 = \frac{D_1}{D}; \qquad C_2 = \frac{D_2}{D} \tag{27}$$

where

$$D = \lambda_2 e^{\lambda_2 H} - \lambda_1 e^{\lambda_1 H}$$

$$D_1 = \lambda_2 \left(T_e - T_0 + B\gamma\right) e^{\lambda_2 H} + \gamma \tag{28}$$

$$D_2 = -\lambda_1 \left(T_e - T_0 + B\gamma\right) e^{\lambda_2 H} - \gamma$$

Temperature distributions $T_D(z)$ and $T_A(z)$ can be determined by Eqs. (23) and (24). In order to calculate these it is necessary to evaluate the constants A and B. Both constants depend on the data of borehole geometry, drilling fluid properties, surrounding rock parameters and the data of performance. These are the following:

- borehole depth, drillpipe outer and inner diameters, drill bit size, the instantaneous completion of the borehole,
- entrance mud temperature, density, viscosity, specific heat capacity and heat conductivity of the mud,
- average density, heat conductivity, specific heat capacity of the rock, surface earth temperature, geothermal gradient,
- circulation mass flow rate, mud temperature at the entrance, elapsed time during drilling operation.

Knowing these data the overall heat transfer coefficients U_{Di} and U_{Ci}, the transient heat conduction function f(t) can be calculated in the well-known manner (WILLHITE, 1967). The transient heat transfer function has different values belonging successive steps of elapsed time.

Using the evaluated constants A and B temperature distributions is obtained from Eqs. (23) and (24). It is obvious that many independent variables influence temperature distributions in the borehole. This can be followed in the calculated temperature distribution diagrams.

4. Conclusions

Considerable observations can be made examining the calculated temperature distribution functions.

The temperature of the downward flow in the drillpipe increases monotonically. Bottomhole temperatures decrease as the mass flow rates increase. Temperature gradient of the downward flow at the bottomhole equals zero. These observations are demonstrated in *Figure 2.*

As the fluid turns upward at the bottomhole temperature increases until attains its maximum. The location of this maximum is obtained at hardly different depths as it is shown in *Figure 3*. It is remarkable that the annular temperature distribution differs greatly from the undisturbed natural geothermic temperature.

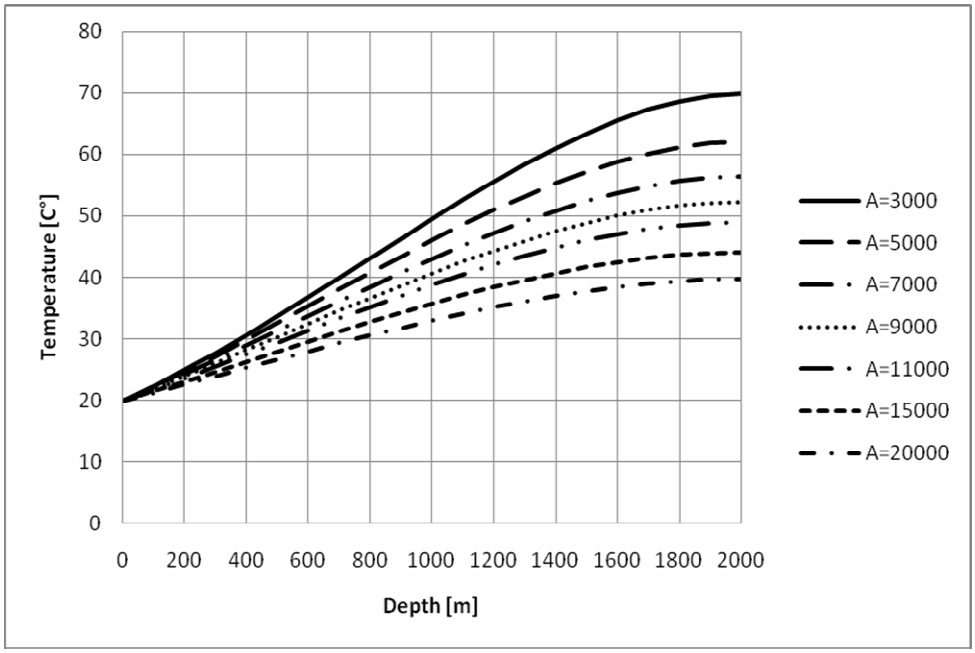

Figure 2: The temperature distribution in the drillpipe

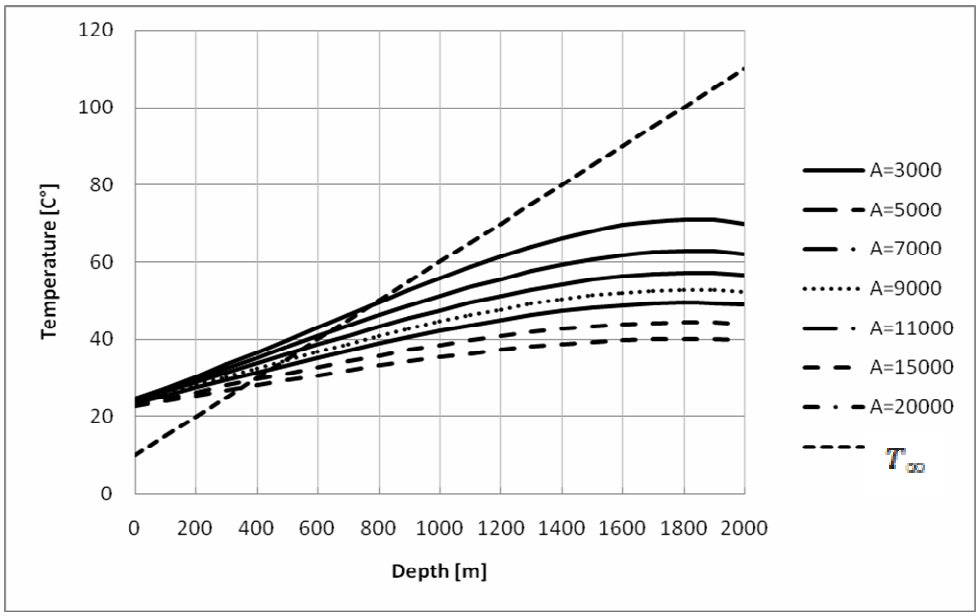

Figure 3: The temperature distribution in the annulus

Above this depth the temperature of the upflowing fluid decreases and converges to the downflowing fluid temperature as shown in *Figure 4*.

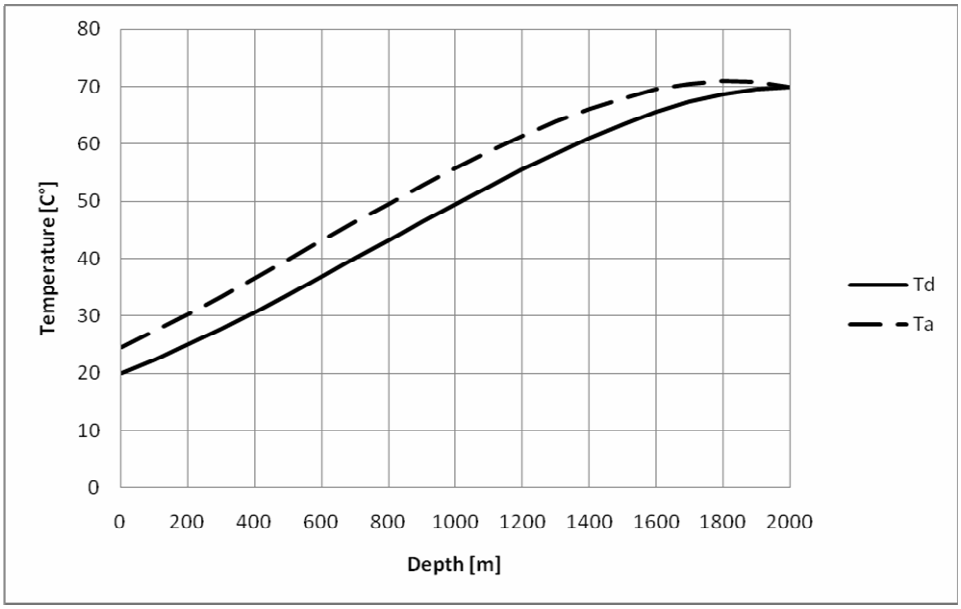

Figure 4: The temperature distribution in the drillpipe and in the annulus

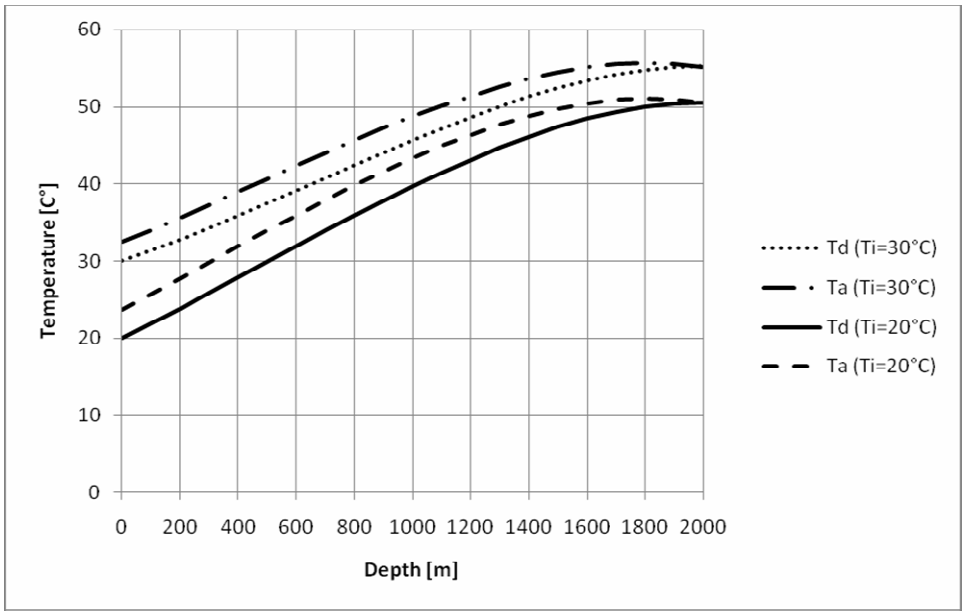

Figure 5: The effect of the injection temperature on the temperature distributions

Both the downflowing and the upflowing fluid temperature depend on the mass flow rate and the specific heat capacity of the circulating drilling fluid. As mass flow rate increases the fluid temperature decreases since the performance coefficients A and B are linear functions of the mass flow rate.

Bottomhole temperature is also influenced by the mass flow rate. Entrance temperature of the drilling fluid influences the bottomhole temperature especially at high mass flow rates. The change of the bottomhole temperature can be seen in *Figure 5*.

The introduced observations based on results of our mathematical model seem to have a general validity.

5. Summary

An analytical mathematical model is presented to predict the temperature distribution of the circulating drilling fluid both in the drillpipe and in the annulus. Calculations are referred to forward circulation. Many independent variables influence temperature distribution in the drillpipe and the annulus. Some of these are constant like rock properties geothermal gradient, borehole geometry, etc. Others change as performance parameters vary, e.g. mass flow rate, entrance fluid temperature, the elapsed time. The knowledge of the temperature distribution in the circulating drilling fluid can be applied in the design of different drilling operations.

LEGENDS

A	borehole performance state coefficient	[m]
B	drillpipe performance state coefficient	[m]
c	specific heat capacity	[J/kg °C]
C_1, C_2	constants of integration	[°C]
D	auxiliary variable	[m^{-1}]
D_1,D_2	auxiliary variables	[°C/m]
f	transient heat conduction function	[–]
H	bottomhole depth	[m]
k	heat conductivity	[W/m °C]
$\dot{m}$	mass flow rate	[kg/s]
R_{Di}	inner radius of the drillpipe	[m]
R_{Ci}	inner radius of the casing	[m]
R_B	radius of the borehole	[m]
R_∞	radius of the undisturbed temperature field	[m]
T	temperature	[°C]
T_A	drilling fluid temperature in the annulus	[°C]
T_D	drilling fluid temperature in the drillpipe	[°C]
T_0	surface temperature	[°C]
Te	drilling fluid temperature at the entrance	[°C]
T_∞	undisturbed rock temperature	[°C]
U_{Di}	overall heat transfer coefficient of the drillpipe	[W/m^2 °C]

U_{Ci}	overall heat transfer coefficient of the casing	[W/m^2 °C]
z	depth coordinate	[m]
α	auxiliary variable	[°C]
γ	geothermal gradient	[°C/m]
λ_1, λ_2	roots of the characteristic equation	[m^{-1}]

"Acknowledgement: This work was carried out as part of the TÁMOP-4.2.1.B-10/2/KONV-2010-0001 project in the framework of the New Hungarian Development Plan. The realization of this project is supported by the European Union, co-financed by the European Social Fund."

REFERENCES

[1] Boldizsár, T.: *The distribution of temperature in flowing wells*. American Journal of Science, 1958, 256.
[2] Dowdle, W. L.–Cobb, W. N.: *Static formation temperature from well log – an empirical method.* Journal of Petroleum Technology, 1975, 1326–1330.
[3] Edwardson, M. J. et al.: *Calculation of formation temperature disturbances caused by mud circulation.* Journal of Petroleum Technology, 1962, 416–426.
[4] Raymond, L. R.: *Temperature distribution in a circulating drilling fluid*. Journal of Petroleum Technology, 1969, 331–341.
[5] Tóth, A.: *Limits of heat extraction from dry holes*. Proc. 33th Workshop of Geothermal Reservoir Engineering, Stanford, 2008. SGP-TR-185, 417–423.
[6] Willhite, G. P.: *Overall heat transfer coefficients in steam and hot water injection wells*. Journal of Petroleum Technology, 1967, 607–615.

Geosciences and Engineering, Vol. 1, No. 1 (2012), pp. 49–63.

GAS FLOW IN THE NANO SIZE PORE CHANNELS OF TIGHT AND NON CONVENTIONAL GAS STORAGE FORMATIONS

TIBOR BÓDI
Research Institute of Applied Earth Sciences, University of Miskolc
3515 Miskolc-Egyetemváros, PO Box 2, Hungary
bodit@akki.hu

Abstract
Low permeability tight gas and shale gas fields cover an increasing percentage of gas production in the world. In the past years, the research of tight gas fields and non-conventional gas reservoirs has begun in Hungary as well. The productivity of these reservoirs mainly depends on the gas production capacity of the well drilled in the given formation, and on the stimulation possibility of the well. Considering economical aspects, the construction and maintenance costs of achieving adequate gas production are also important factors. Apart from well structure and well completion technology, the capacity of such hydrocarbon producing wells is mainly determined by the characteristics of the flow around the well, and by the permeability of the formation rock.

At the University of Miskolc – Research Institute of Applied Earth Sciences, petrophysical property measurements of several rock samples originating from non-conventional hydrocarbon reservoirs have been performed in the past years. Pore structure and wettability property measurements were also included in these examinations. As a result of these measurements, it became obvious that despite the measured decent porosity data of the rocks, the permeability values of the samples were very low, only a few micro- or nano-Darcies. According to our experiences, the very low permeability of the rocks can be attributed to the pore structure: there are many very small pore channels with nanometer size diameter. In the past period, several articles dealing with gas flow in nano-size pore channels were published. It was assessed that in pore channels of such size, apart from the regularly considered Darcy flow, many other factors occur, especially diffusion. Taking the previously mentioned facts and the results of our earlier measurements into account, the theoretical background of the flow processes occurring in non-conventional reservoirs are summarized in this study. The importance of non-Darcy flow in tight gas reservoirs, its effects on the productivity of the gas producing wells, are also described in this paper.

1. Introduction

Since the past two decades, an increasing share of the world's gas supply is being provided by low permeability "tight gas" and "shale gas" storage formations. Parallel with the intensification of gas production from these formations, more and more complex studies are being published on gas flow mechanisms in tight gas and shale gas deposits [3, 4, 6, 7]. Such reservoirs can typically be characterized by extremely low permeability rates ($k_g < 0.1$ mD and $k_g < 0.01$ mD). Low permeability is the consequence of the matrix structure of the formation rock, since the total pore volume is built up of micro- or even nanopore channels, with the average pore radii (r_{avg}) ranging from a few nanometers (10^{-9}) to a few micrometers (10^{-6}). Relying on the published literature, it can be said that flow in such pore channels is not or only to some extent characterized by Darcy flow model valid for conventional gas storage formations. Thus, Darcy's law, universal gas law and other

functional flow relations deriving from the "Continuity equation" for porous media are not, or only to some extent applicable in these cases. All the experts studying flow in nanopores agree that – besides Darcy flow – such flow types exhibit effects of the so-called "slip flow" (observed first by Klinkenberg) and diffusion type flow, mostly referred to as Knudsen flow.

F. Javadpour et al. [6] suggest that in case of non-conventional (shale gas and tight gas) storage formations, producing wells first reach larger fractures and larger pore channels, gradually extending to micro-fractures and micro- or even nanopores as well. After a certain production period the production of these wells will dominantly depend on the volume of gas flowing and being released in these micro- and nanopore channels.

Gas molecules in nanopore channels are located in the center of the channel with some of them adsorbed on the channel walls. Supposing that the pore channel wall contains kerogen, gas molecules might cover the surface of the kerogen materials as adsorbed gas and disperse in the kerogen materials as dissolved gas. During the flow, gas molecules in the center of the pore channel either move without slippage, showing laminar flow – Darcy flow – depending on pore channel size, average pressure of gas flow, average temperature of the flow and gas mean-free-path or they change to the diffusion type "slip flow" described by Knudsen, where, besides pressure difference, the movement of gas molecules is influenced by diffusion caused by concentration differences. When gas pressure drops inside the nanopore, volumetric gas concentration will drop as well, which leads to the desorption of formerly adsorbed gas molecules on the wall of the pore channels. As a result of desorption, the gas concentration will decrease on surface of the kerogen materials of wall of the pore channels, which triggers gas diffusion within the kerogen material and makes dissolved gas molecules move towards the pore channel. These transformations within the kerogen material may release new gas molecules as well.

Conclusively, in the case when the formation rocks contain kerogen, not only gas flow and gas diffusion occur, but also gas release as well.

If the rock does not contain kerogen, we have to reckon with Knudsen flow type and the presence of adsorbed gas along the nanopore walls. Thus, it seems obvious, that by estimating the productivity of tight gas reservoirs, we cannot disregard diffusion effects and Knudsen's slip flow.

In the published literature [3, 4, 6, 7], different authors select different approaches to discuss the questions of gas flow in nanopores. T. Ertekin et al. {[4] modify the b coefficient in Klinkenberg equation ($k_g = k_\infty (1 + b/\bar{p})$ }, referring to it as "dynamic slippage factor". In addition, they introduce a so-called "apparent slippage factor" to manage pore saturations and two-phase flow. F Javadpour et al. [7] introduces an "apparent permeability" (k_{app}) factor instead, to model flow in nanopore networks and determine the ratio of apparent permeability respective of Knudsen flow and Darcy permeability (k_{app}/k_D)).

F Chivan et al. [3] also calculate with an apparent permeability factor (k_{app}), though somewhat different from Javadpour's, and they develop a complex flow equation respective of both the Darcy and the Knudsen flow and the additional gas adsorption, to model the flow through nanopore networks. They prove, via detailed theoretical calculations, that it is convenient to consider Knudsen diffusion and gas desorption when evaluating the results of pulse decay permeability measurements performed on tight reservoir rocks.

It obviously follows from the above description, that in estimating the production capacity of non-conventional reservoir wells, and thus, of tight gas or shale gas formations, we have to calculate with Knudsen diffusion as well.

2. Gas flow in nanopores

In the case of gas flow through nanopores, we have to distinguish between Darcy flow – that can modelled with functional relations deriving from the so-called "continuum theory" –and Knudsen diffusion flow, where gas diffusion and gas adsorption have to be regarded.

To differentiate between the two types of flow, the Knudsen number K_n can be used, which is a dimensionless parameter. Based on Navier–Stokes equation, Javadpour et al. [1] suggested the following K_n value ranges to distinguish between the two flow types:

$K_n < 0.001$ for Darcy flow "no-slip" flow in the pore channels

$0.001 < K_n < 0.1$ for Knudsen diffusion "slip flow" in the pore channels.

N. G. Hadjiconstatinou [5] defines the Knudsen number with the following mathematical expression

$$K_n = \frac{\lambda}{d} \tag{1}$$

According to the published literature, the mean-free-path of gas can be calculated from the following equation

$$\lambda = \frac{k_B T}{\sqrt{2}\pi\delta^2 p} \tag{2}$$

F. Javadpour et al. [6] calls our attention to the inaccuracy of Eq. 2, which would result at high pressure in a gas mean-free-path shorter than the collision diameter – which is a physical nonsense. Alternatively they propose the following formula to describe gas flow through nanopores with respect to gas diffusion

$$q\rho = \varphi A D_K \frac{M}{RT}\frac{\Delta p}{L} \tag{3}$$

Eq. 3 gives the mass flow of flowing gas through porous medium, expressed in kg/s. Knudsen diffusion constant can be determined from the following equation

$$D_K = \frac{d}{3}\sqrt{\frac{8RT}{\pi M}} \tag{4}$$

Due to the complex structure of porous rocks, Knudsen diffusion constant for porous rock, $D_{K,pm}$ is best to be obtained from measurements. In the absence of such results, $D_{K,pm}$ can be approximated by the following equation

$$D_{K,pm} = \frac{\varphi}{\tau} D_K \tag{5}$$

When deriving Eq. 3, the authors primarily focused on diffusion flow, and calculated with a constant diffusion coefficient, neglecting the effect of viscosity and viscous flow. In order to eliminate this problem and correctly calculate K_{app}, consideration had to be given to the "no-slip" Darcy viscous flow as well.

Total mass flux (J) of a gas through a nanopore is the result of a combination of Knudsen diffusion and pressure forces, which can be described with the following expression

$$J = J_a + J_D \tag{6}$$

The mass flux of Knudsen diffusion, being the quotient of $q\rho$ mass flow and $A\phi$, cross-section of the flow, can be derived with the rearrangement of Eq. 3

$$J_D = \frac{q\rho}{\varphi A} = D_K \frac{M}{RT} \frac{\Delta p}{L} \tag{7}$$

The flux of laminar flow (Darcy flow), controlled by differential pressure in a circular pore channel, can be determined from Hagen-Poiseuille equation

$$J_a = \frac{\rho_{avg} r^2}{8\mu} \frac{\Delta p}{L} \tag{8}$$

In nanopore channels the boundary conditions for "no-slip" flow usually cannot be precisely defined [5, 6]. Slippage velocity, occurring along the wall of nanopores, makes the flow of gas smoother; i.e. in the case of slip flow the volumetric gas flow through the pore channel becomes larger than in the case of conventional flow. Brown et al. [2] introduced a theoretical dimensionless parameter, F, to account for slippage along pore channel walls, calculated as follows

$$F = 1 + \sqrt{\frac{8\pi RT}{M}} \frac{\mu}{p_{avg} r} \left(\frac{2}{\alpha} - 1 \right) \tag{9}$$

where α is tangential momentum accommodation coefficient, which signifies the part of gas molecules reflected diffusely from the pore channel wall relative to specular reflection.

Theoretically the value of α changes between 0 and 1, depending on the smoothness of the pore channel walls, the gas type, the pressure and temperature gradients. The exact value of α for a given formation rock type should be defined by way of experimental measurements. Brown et al. [2] developed Eq. 9 for low pressure flow through circular pore channels with relatively large diameter. In the case of tight shale/sand reservoirs, however we need a mathematical formulation of high pressure flow through nanopores. The basic physical effect will be the same, since the proportion of mean-free-path of flowing gas to

pore channel diameter (that is the Knudsen number) – which determines the occurrence of slip flow – will fall into the same order of magnitude.

Substituting Eqs. 7 and 8 into Eq. 9, we can obtain total mass flow flux as follows

$$J = D_K \frac{M}{RT}\frac{\Delta p}{L} + F\frac{\rho_{avg} r^2}{8\mu}\frac{\Delta p}{L} = \left(\frac{2r}{3}\frac{M}{RT}\sqrt{\frac{8RT}{\pi M}} + F\frac{\rho_{avg} r^2}{8\mu}\right)\frac{\Delta p}{L} \tag{10}$$

Let us describe volumetric flux for compressible gas flow by applying the modified form of Darcy's equation

$$\frac{q}{A} = \left(\frac{k_D \rho_{avg}}{\mu}\right)\frac{(p_1 - p_2)}{L} \tag{11}$$

Eq. 11 can be applied to determine the volumetric flux of gas flowing through porous medium in conventional gas reservoirs, supposing that pore channel size varies within a range of 0.1 and 1 10^{-4} m orders of magnitude.

The mathematical formula for volumetric flux in nanopores can be given by rearranging Eq. 11 in the following way

$$\frac{q}{A} = \left(\frac{2r}{3}\frac{M}{RT\rho_{avg}}\sqrt{\frac{8RT}{\pi M}} + F\frac{r^2}{8\mu}\right)\frac{(p_1 - p_2)}{L} \tag{12}$$

Comparing the above two equations (Eqs. 11 and 12), it can be observed that a new parameter, k_{app} (apparent permeability) is possible to be introduced. k_{app} can be defined as follows

$$k_{app} = \frac{2r}{3}\frac{\mu M}{RT\rho_{avg}^2}\sqrt{\frac{8RT}{\pi M}} + F\frac{r^2}{8\rho_{avg}} \tag{13}$$

As it is obvious from Eq. 13, apparent permeability is dependent not only on rock type and rock structure (size of pore channels, smoothness of the wall of pore channels, tortuosity etc.) but also on average temperature, average pressure of flow and fluid properties of the flowing gas. This is evident, since gas flow through nanopore network is substantially influenced by Knudsen diffusion.

In order to estimate the effects of Knudsen diffusion flow, the quotient of apparent permeability and Darcy permeability can be calculated by the following equation

$$\frac{k_{app}}{k_D} = \left[\frac{2}{3}\frac{\mu M}{RT\rho_{avg}^2}\sqrt{\frac{8RT}{\pi M}}\frac{8}{r} + \left[1 + \sqrt{\frac{8\pi RT}{M}}\frac{\mu}{p_{avg} r}\left(\frac{2}{\alpha} - 1\right)\right]\frac{1}{\rho_{avg}}\right]\frac{r^2}{8} \tag{14}$$

According to Eq. 14 the smaller the pore channel radius, the more remarkable the difference between k_{app} apparent permeability and k_D Darcy permeability will be. It can also be noticed that with lowering average pressure of flow, the same difference (i.e. between k_{app} apparent permeability and k_D Darcy permeability) will increase.

3. Laboratory experiments on rock samples derived from a Hungarian gas reservoir, with respect to flow mechanisms in pore channels

As reported in our earlier publications [1], the Research Institute of Applied Earth Sciences of the University of Miskolc joined a Hungarian research project to study non-conventional gas storage formations about five years ago. In the course of our research work, several routine laboratory experiments and special petrophysical measurements were performed, from assessing pore size distribution to determining the wettability properties of the given formation rock. For detailed descriptions see [1].

On the basis of our formerly recorded measurement results, a flow analysis for the studied rocks was accomplished, within the framework of an R & D project financed by TÁMOP. In the following, the results and databases used for the calculations are presented.

It is important to emphasize that during our analysis, the initial presumption was the presence of exclusive gas saturation in the pores; we neglected contingent flow mechanism problems occurring when the pore channels are to some extent (or fully) saturated with water, as a result of drilling and layer opening operations. Examining gas diffusion through partly or fully water-saturated formation rocks would require special laboratory measurements and further research work. By now, such results have not been published.

The evaluation was performed on a dataset obtained from the petrohysical measurements of samples derived from a production well (Well #1) of a Hungarian non-conventional gas formation. Well pressure and temperature profiles are represented in *Figure 1*.

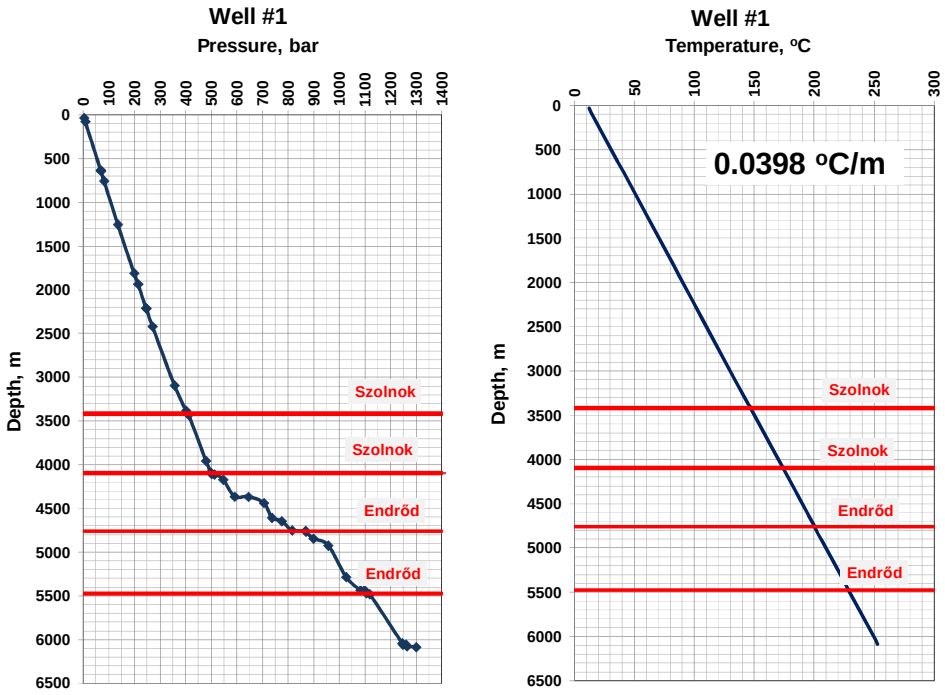

Figure 1

The left-side section of the *Figure 1* shows the pressure gradients measured during the drilling of the well (calculated from the applied mud density). The right-side section illustrates the temperature vs. the depth based on the average of geothermal gradients that were calculated from measured temperature data of the given well and adjacent wells. The average of geothermal gradients that we considered for our calculations is 0.0398 °C/m.

The above temperature gradient has been calculated from the following equation

$$T\left[°C\right] = \left(D - 1\right) \cdot t_{grad} + 11 \tag{15}$$

The numerical value 11 in Eq. 15 is the annual mean temperature in Hungary, measured at 1 m depth (subsurface).

In the figure, the depth intervals and formation strata from where the petrophysical measurement data originated were plotted with red color. *Table 1* represents some basic datasets of these measurement intervals, used in our further calculations.

The simplified gas compound required for our calculations was determined by analysis of gas samples derived from an adjacent well. Gas composition data applied for the calculations are shown in *Table 2*. Based on this gas composition, the average molecular weight (kg/kmol) and collision diameter (nm) for the gas compound was determined. The collision diameter is the shortest possible distance between the center of two colliding gas molecules. At the mass calculation, molecular mass of propane was used instead of the average molecular mass of ethane+ fraction (see *Table 2*).

Table 1

Average depth **m**	**Average pressure** **bar**	**Average temperature** **°C**	**Average porosity** **%**	**Average absolute permeability** **mD**	**Average pore radius** **μm**	**Average most frequent radius** **μm**
3413.04	406.3	146.7	8.54	0.16490	0.3918	0.2782
3422.24	409.6	147.1	11.08	0.36308	0.7023	0.4900
4090.38	497.9	173.6	6.96	0.07845	0.0996	0.0949
4099.52	499.7	174.0	7.03	0.00877	0.1231	0.1020
4758.58	868.3	200.2	7.48	0.03309	0.0131	0.0131
5474.34	1113.2	228.7	2.08	0.00585	0.0552	0.0393

Table 2

Component	**Composition mol %**	**Molecular mass kg/kmol**	**Collision Diameter nm**
Methane	75.402	16.04	0.400
Ethane+	10.265	44.09	0.520
Carbon dioxide	14.333	44.01	0.450
Calculated values		22.93	0.419

Using the data represented in *Tables 1* and *2*, and applying Eqs. 1 and 2, the mean-free-path of gas and the Knudsen number for the respective depth intervals were determined. The results, plotted against depth, can be seen in *Figures 2* and *3*.

In *Figure 2*, the collision diameter of the given gas compound is indicated with a red line. As it was mentioned before (see also in reference [6]), the functional relation given by Eq. 2 is not accurate enough, resulting is shorter mean-free-path of the gas than its collision diameter at high pressure and temperature flow. This problem can be clearly detected by studying Figure 2, where the studied depth intervals are all characterized by high pressure and temperature.

Figure 3 represents the calculated Knudsen numbers against depth. The Knudsen numbers for the studied depth intervals were determined by using the measured average pore diameter and the most frequent pore diameter of the rock samples. These data were calculated from the pore size distribution obtained by mercury injection porosity measurement of the rock samples. During the mercury-injection porosity measurements, a maximum pressure of 3500 bar was applied. In *Figure 3* we indicated the particular Knudsen number range where Knudsen diffusion flow should be respected with continuous and dashed red lines.

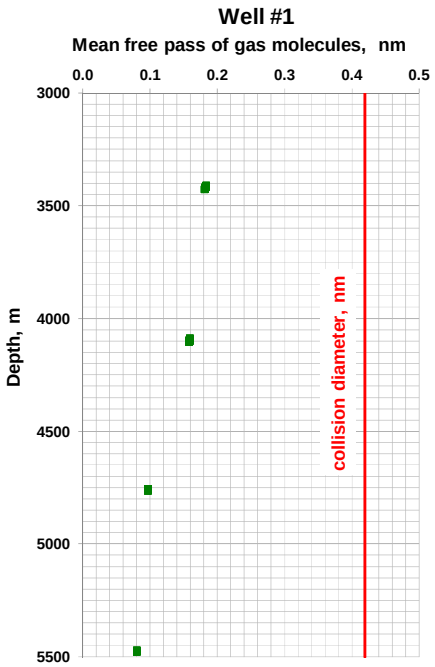

Figure 2

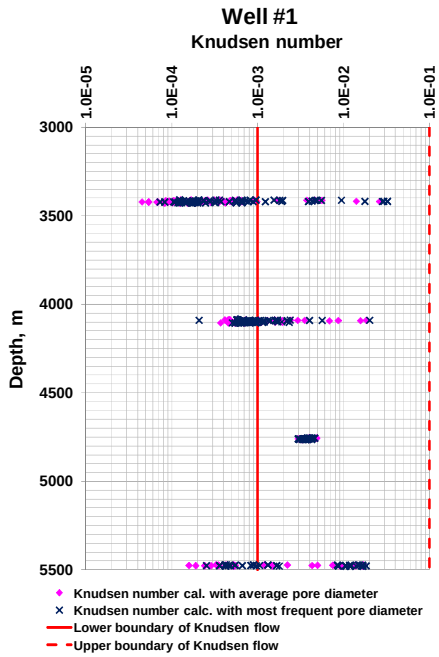

Figure 3

The two sets of results shown against depth values on *Figures 2* and *3* are detailed in *Figures 4* to *6* – using a special mode of representation. Here, starting from 0 meter on the horizontal axis, we represent the position of the rock samples subjected to petrophysical measurements in their respective depth intervals. The same indications are used as in *Figures 2* and *3*.

As it was mentioned earlier (see comments on *Figure 2*), it is impossible to use Eq. 2 for the studied depth intervals, because the high pressure and temperature of the flow in each case would result in shorter gas mean-free-path than the average collision diameter,

which is a physical nonsense. *Figure 4* also justifies this observation. When calculating the Knudsen numbers from Eq. 1, we used the gas mean-free-path data defined according to Eq. 2, which means that the numerical values represented in *Figures 3, 5* and *6* contain significant errors. Still, the conclusion can be drawn that each studied depth interval involves formation rock sections where Knudson-type diffusion flow needs to be considered. As it can be seen in the Figures, all samples taken from the interval of 4754.20–5462.95 m, and most of the ones taken from the 5470.26–5478.42 m interval, fall into the diffusion type flow regime.

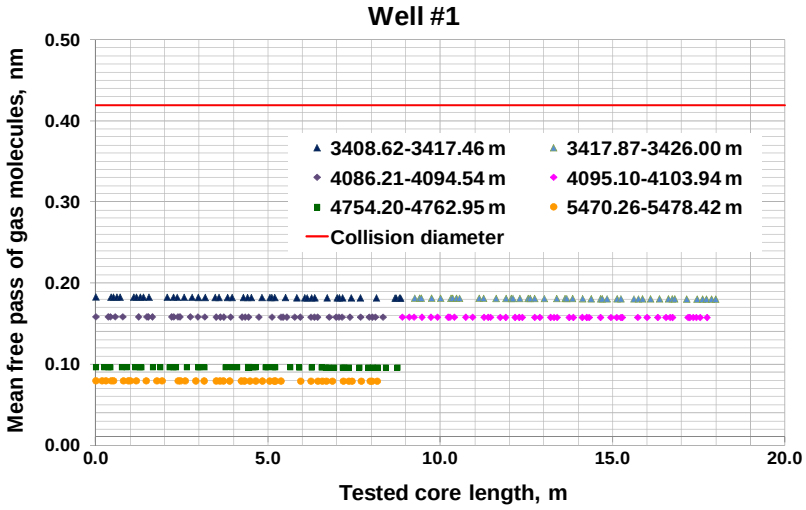

Figure 4

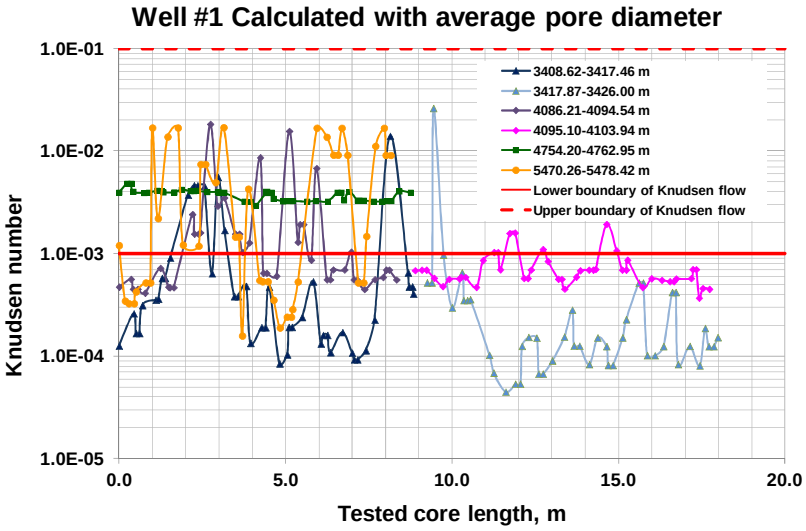

Figure 5

In the reviewed literature, no other mathematical formula applicable for the determination of mean-free-path of the gas was found. If consideration is given to the fact that the gas mean-free-path values in reality are ten times longer than the calculated data so that it exceeds the collision diameter, then Knudsen numbers – calculated according to Eq. 1 – will be cca. ten times larger too. On the basis of these theoretical considerations, it seems obvious that all of the studied rock samples composed mainly of nanopores and taken from the respective depth intervals, fall into the Knudsen diffusion flow regime.

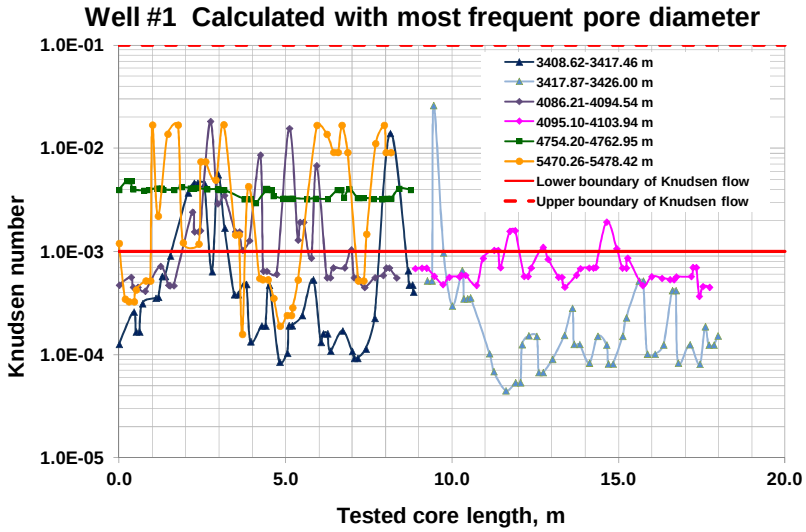

Figure 6

Based on the average parameters displayed in *Table 1*, the total mass flux of gas (using Eq. 10) and k_{app} (using Eq. 13) for each respective interval against depth were calculated. These plots are represented in *Figures 7* and *8*.

In order to apply Eqs. 10 and 13, further parameters have to be considered. One of them is the length or thickness L of the porous rock. Another parameter is Δp pressure difference or depression along L length. For purposes of our calculations, we have estimated L as 5 m and Δp as 100 bars.

Using the average temperature and pressure data for the respective intervals as indicated in *Table 1* and considering the given gas composition shown in Table 2, ρ_{avg} average gas density, p_{avg} average pressure and μ average gas viscosity were determined with the help of a special computer program, called STRAPP. STRAPP uses a modified Peng-Robinson equation of state to perform calculations.

By determining the F dimensionless parameter from Eq. 9, we have chosen 0.8 for α tangential momentum accommodation coefficient, relying on published data [7]. These additional parameters were used for the calculations, the results are represented in *Figures 7* and *8*.

Figure 7 shows the total mass flux of gas for each depth interval, determined by using average pore radius data (violet points) and most frequent pore radius data (blue points) against depth. As it can clearly be seen from the Figure, the total mass flux of gas,

respective of both Darcy and diffusion-type flow regimes, decreases in orders of magnitude along with increasing depth and with degrading formation rock parameters.

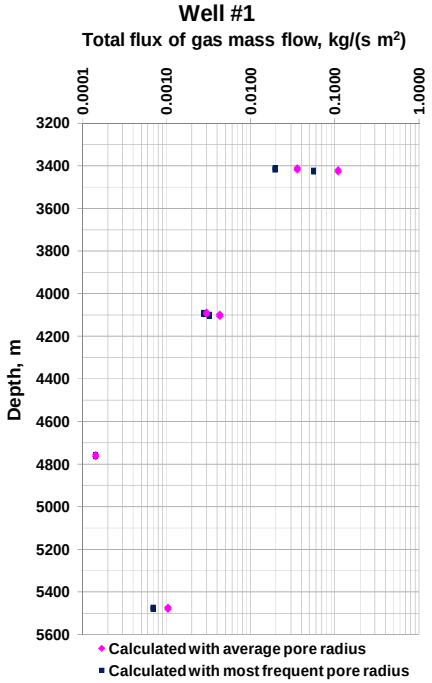

Figure 7

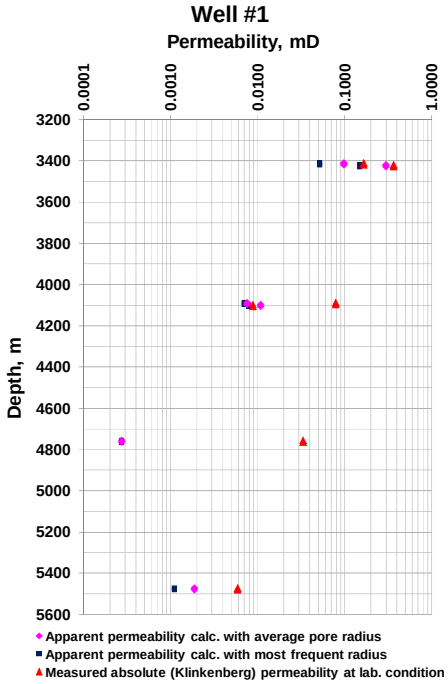

Figure 8

In *Figure 8,* just like in *Figure 7,* the apparent permeability rates calculated in two different ways from Eq. 13 are plotted against depth. Red points indicate k_{abs} permeabilities calculated from laboratory measurement results of the tested rock samples, and the average values of their respective Klinkenberg permeabilities. By average we mean the mathematical mean of measured and calculated results.

In Figure 8, it can be noticed that as depth increases and formation rock layers become tighter, apparent permeability rates become smaller, their decrease may even reach one order of magnitude. The same decreasing tendency is followed by the absolute permeability values of the tested rock samples for the respective depth intervals. It can also be concluded that absolute permeabilities, measured for each of the samples, are higher than the calculated apparent permeability for the same intervals. Relying on these observations, we suppose that apparent permeabilities – based on measurement data or calculated with respect to flowing gas properties, formation rock structure, flow pressure and temperature conditions, Darcy flow and Knudsen diffusion – are essential to be taken into account.

The application of absolute permeability data measured on the studied rock samples at laboratory conditions (1 bar, 20 °C) in hydrodynamical calculations, may lead to an overestimation of expected gas production of the wells.

In order to estimate the expected gas production of Well 1, a massive fracture at each depth interval was assumed. This assumption was taken to make gas production more

efficient. The parameters of these hypothetical fractures were the following: half-lengths of the fracture were x_f = 30 m, fracture height was h = 10 m; and with these, a surface area of $A = 4\, x_f\, h = 1200$ m^2 can be formed between the fracture and the formation rock. Assuming that we generate a depression of Δp = 100 bar in the fracture, which is effective along about L = 5 m wall thickness, the expected gas volume (expressed in normal cubic meter units) producible through the fracture can be determined with the following expression

$$q_g = \frac{JA\overline{\phi} \cdot 3600 \cdot 24}{M} \cdot 23.59 \tag{16}$$

The numerator in Eq. 16 shows the mass flux of the produced gas (expressed in kg/d units). Dividing this value with the molecular weight of the gas, the produced gas quantity expressed can be obtained in of kmol/d units. When determining the mole number of produced gas, the real cross section areas ($A\phi$) of the pore channels were only taken into account. Assuming that the volume of 1 kmol normal gas (15 °C, 1.01325 bar) is 23.59 m^3, Eq. 16 gives the expected production volume, expressed in nm^3/d, for the respective depth levels through the hypothetical fracture. The same calculation was used for each depth interval, determining the expected gas flow rate producible through the hypothetical fracture. The results can be seen in *Table 3*.

Table 3

Depth **m**	**Gas production (calculated with average pore radius)** **nm^3/d**	**Gas production (calculated with most frequent pore radius)** **nm^3/d**
3413.04	323917	176244
3422.24	1285273	656840
4090.38	22065	20551
4099.52	31997	24044
4758.58	1137	1135
5474.34	2290	1526

Since the total mass flux of flowing gas was determined by using two distinctive rock parameters (average pore radius and most frequent pore radius), the same double calculation method was used for attaining the expected gas production.

As it is obvious from *Table 3,* the two lowest of the studied depth intervals (4754.20–4762.95 m, 5470.26–5478.42 m) are likely to give very low (1137, 1135 m^3/d, 2290, 1526 m^3/d) gas flow rates, hence in these zones, more fractures or larger fracture would be required to achieve satisfactory production.

It is necessary to emphasize, though, that in determining the expected producing rates (as they are shown in *Table 3*), it was assumed that all pores, including nanopores as well, are exclusively filled with one-phase gas, without the presence of water. If the pore channels are partly or fully water-saturated, the gas production rates will be substantially lower than the indicated values.

As it sometimes occurs, primary water-saturation around the well-head zone or the fraction, or other water saturation resulting from drilling and fracturing operations may

completely block the gas from flowing into the fracture or into the well. In such cases, it is necessary to study gas flow through water-saturated pores and gas diffusion through water in nanopores. We consider such research work to be an essential issue in the future.

4. Summary

Using special petrophysical parameters, measured on rock samples taken from a particular production well of a non-conventional gas bearing formation in Hungary, we represented the flow mechanisms that take place at distinctive depth intervals, and we determined the expected volumes of gas producible via an artificially created fracture, assuming that the pore system is 100% gas saturated.

The following results can be concluded:

- The mathematical expression found in the published literature for determining the mean-free-path of gas (Eq. 2) cannot or can only to a limited extent be applied for storage formations like the Hungarian one, due to the high pressure and temperature flow of the corresponding depth intervals.
- It was proved that in the case of the studied deep tight reservoir rocks, diffusion effects cannot be disregarded. Even if 100% gas saturation in the formation rocks is assumed, we have to take Knudsen diffusion flow and "slip flow" into consideration.
- It was observed that absolute (Klinkenberg) gas permeability rates obtained from the results of laboratory gas permeability measurements are higher than apparent permeability rates respective of gas diffusion. This can be attributed to laboratory conditions, i. e. the displacing fluid (Nitrogen gas) and the measurement conditions (pressure, temperature) significantly differ from reservoir conditions.
- The calculation results presented in this paper are only approximate, because they reckon with the potentially most optimal reservoir conditions, assuming 100% gas saturation and neglecting even a minimal rate of water saturation.
- Based on our analysis, it seems essential to conduct in the future further theoretical and laboratory research on studying gas flow through fully or partly water-saturated nano-size pore channels.

List of symbols

A	total area of the porous rock surface, perpendicular to the flow direction, (m^2)
b	constant of the Klinkenberg gas permeability equation, (Pa)
d	average diameter of the pore channel, (m)
D	depth, (m)
D_K	Knudsen diffusion constant, (m^2/s)
$D_{K,pm}$	Knudsen diffusion constant for porous rock, (m^2/s)
F	theoretical dimensionless parameter to account for slippage along pore channel walls
J	total mass flux of gas flow, ($kg/(s\ m^2)$)
J_a	mass flux of gas controlled by differential pressure, ($kg/(s\ m^2)$)
J_D	mass flux for Knudsen diffusion, ($kg/(s\ m^2)$)

k_B Boltzmann constant ($1.3805\ 10^{-23}$ J/K)
k_g gas permeability, (mD)
k_D permeability of so-called Darcy flow, (m^2)
K_n Knudsen number
k_{app} apparent permeability, (mD)
k_D Darcy permeability, (mD)
k_∞ absolute permeability, Klinkenberg permeability of gas, (mD)
L length of the flow, (m)
M molecular weight of flowing and diffusive gas, (kg/mol)
p pressure, (Pa)
p_1 pressure at the inlet face of the pore channel, (Pa)
p_2 pressure at the outlet face of the pore channel, (Pa)
Δp depression or differential pressure along L length, (Pa)
q flow rate of gas through the cross section area A of the rock, (m^3/s)
q_g gas production for normal gas (15 °C, 1.01325 bar), (m^3/d)
r pore channel radius, (m)
R universal gas constant, 8.314 J/(mol K)
t_{grad} geothermal gradient, (°C/m)
T temperature, or average flow temperature, (K)
α tangential momentum accommodation coefficient
δ collision diameter, (m)
ϕ porosity of the rock, (–)
$\overline{\phi}$ average porosity of the rock, (–)
λ gas mean-free-path of gas, (m)
ρ average gas density at average flow pressure and temperature, (kg/m^3)
ρ_1 gas density at p_1 inlet pressure of the pore channel, (kg/m^3)
ρ_2 gas density at p_2 outlet pressure of the pore channel, (kg/m^3)
ρ_{avg} average density $\rho_{avg} = (\rho_1 + \rho_2)/2$ of gas flowing through the pore channel, at average flow pressure $p_{avg} = (p_1 + p_2)/2$, (kg/m^3)
τ tortuosity of the rock

"Acknowledgement: This work was carried out as part of the TÁMOP-4.2.1.B-10/2/KONV-2010-0001 project in the framework of the New Hungarian Development Plan. The realization of this project was supported by the European Union, co-financed by the European Social Fund."

REFERENCES

[1] Bódi, T.–Tóth, J.–Lakatos, I.–Jobbik, A.–Szabó, Gy.: *Nem-konvencionális szénhidrogéngáz előfordulások kőzeteinek petrofizikai vizsgálatai.* XXVII. Nemzetközi Olaj- és Gázipari Konferencia Hungary, Siófok, 2008. szeptember 16–19. CD A 04. 1–53.
[2] Brown, G. P.–Dinado, A.–Cheng, G. K.–Sherwood, T. K.: *The Flow of Gases in Pipes at Low Pressures*. Journal of Applied Physics, Vol. 17, October 1946, 802–813.

[3] Chivan, F.–Rai, C. S.–Sondergeld, C. H.: *Shale gas permeability and diffusivity inferred by improved formulation of relevant retention and transport mechanisms.* Transport Porous Media (2011) 86-925-944 DOI 10.1007/s11242-010-9665-x. Published online: 14 October 2010 Springer Science+ Business Media B.V. 2010.

[4] Ertekin, T.–King, G. R.–Schwerer,F. C.: *Dynamic gas slippage: A unique dual-mechanism approach to the flow of gas in tight formation.* SPE: Formation Evaluation, February 1986.

[5] Hadjiconstatinou, N. G.: *The limits of Navier-Stokes Theory and Kinetic extensions for describing small-scale gaseous hydrodynamics*. Physics of Fluids, vol. 18. No. 11. November 2006. 11301–11320.

[6] Javadpour, F.–Fisher, D.–Unsworth, M.: *Nanoscale gas flow in shale gas sediments.* Journal of Canadian Petroleum Technology, October 2007, Volume 46, No. 10.

[7] Javadpour, F.: *Nanopores and apparent permeability of gas flow in mudrocks (shales and siltstone).* Journal of Canadian Petroleum Technology, August 2009, Volume 48, No. 8.

Geosciences and Engineering, Vol. 1, No. 1 (2012), pp. 65–74.

MEASUREMENT OF POROSITY AND GAS PERMEABILITY OF TIGHT ROCKS BY THE PULSE DECAY METHOD

ANDRÁS GILICZ–TIBOR BÓDI
EON Földgáz Storage,
H-1051Budapest, Széchenyi István sqr. 7–8,
andras.gilicz@eon-foldgaz.com
Miskolc University, Applied Geo Science Research Institute,
H-3515 Miskolc-Egyetemváros, P.O.Box.2
bodit@akki.hu

Abstract
Due to rising gas demand there is an increasing focus towards unconventional tight and shale gas reservoirs, which contain by several order of magnitude more gas, than conventional reservoirs – although under more difficult circumstances. For production their key petrophysical parameters (porosity and permeability) have to be determined. The main difficulty is, that their permeability is low, typically in the nano and 0.1 mD range, therefore conventional steady state measurement techniques cannot be applied. For this type of measurements the so called pressure pulse decay method is used. In this technique a pressure wave propagates through the core. Its decline time is inversely proportional to permeability, whereas the final equilibrium pressure is characteristic for the porosity of the core. In the Applied Geo Science Research Institute of Miskolc University a unique apparatus was developed a few years ago, which can carry out the pulse decay technique on full diameter radial cores. Complete measurement technique and interpretation software was developed for this purpose. In laboratories worldwide however the conventional linear plug measurement is still used widespread, so it was decided to extend the existing interpretation software with the algorithms of the linear plug measurements to obtain a flexible tool, which can interpret both types of measurements with the same easiness. The extension took place by solving the governing partial differential equation of the measurement with linear geometry, and implement the solution into the existing software. The software developed simulates the measurement itself, so no simplifying assumptions are needed for evaluation. Practical examples show the applicability of the new tool.

1. Methodology

The scheme of the measurement is shown in *Figure 1.* As can be seen two vessels (V_1, V_2) are connected to the inlet and outlet face of the core having a pore volume of V_p. The whole system is filled up initially with gas or fluid all the valves being open. After equilibrium has been reached, Valve 1 is closed, and the pressure of the inlet vessel V_1 is increased slightly (c.5%). By opening Valve 1 the pressure difference between vessels V_1 and V_2 declines through the core. Decline is measured in time with a data acquisition system. Besides other input values this recording is used to evaluate the measurement for permeability and possibly porosity.

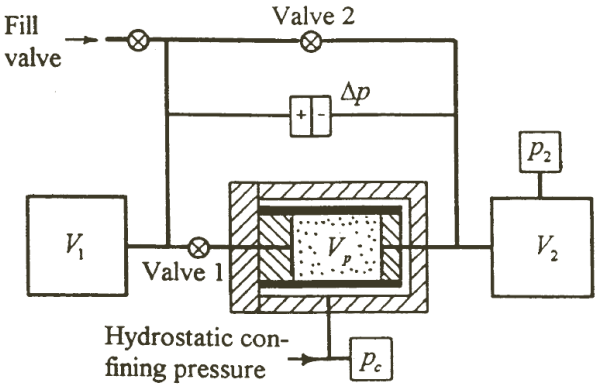

Figure 1

In the figure above a linear plug is visible. The corresponding laboratory equipment is shown in *Figure 2.* If the core plug is a full diameter whole core, the measurement principle is still the same, but the core holder is different. This is shown in *Figure 2* [1], the corresponding lab apparatus is depicted in *Figure 3*.

This core holder is slightly more complex than the conventional linear one but has several advantages [1]:

- The radial whole core is larger than the conventional linear plug, so it represents the reservoir more correctly.
- Radial flow takes place in the core, just like the flow in the vicinity of wells.
- Both porosity and permeability can be obtained from the same measurement simultaneously.
- The measurement is quick and easily reproducible, reproducibility is excellent.
- Core preparation works are simpler.
- The measurement can be carried out under reservoir conditions.
- Core load can be regulated in both axial and radial directions, so reservoir stress conditions can be simulated.

Description of the radial measurement method was described in an earlier paper [1]. It has to be noted however that this unique radial measurement technique is not widely used in laboratories worldwide; rather the conventional linear plug technique is used. So the idea came to develop a flexible tool, which combines the two measurement techniques, i.e. both radial and linear.

The physical development of such a device is however a complicated and costly task, which can be accomplished on longer term only, but the development of the software, was already possible, this paper describes this intermediate situation. So the problem to be solved was to extend the existing radial interpretation software with the conventional linear one.

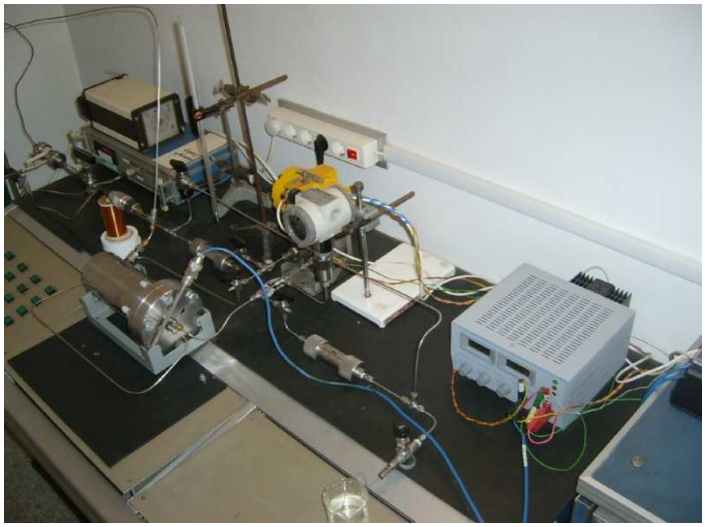

Figure 2

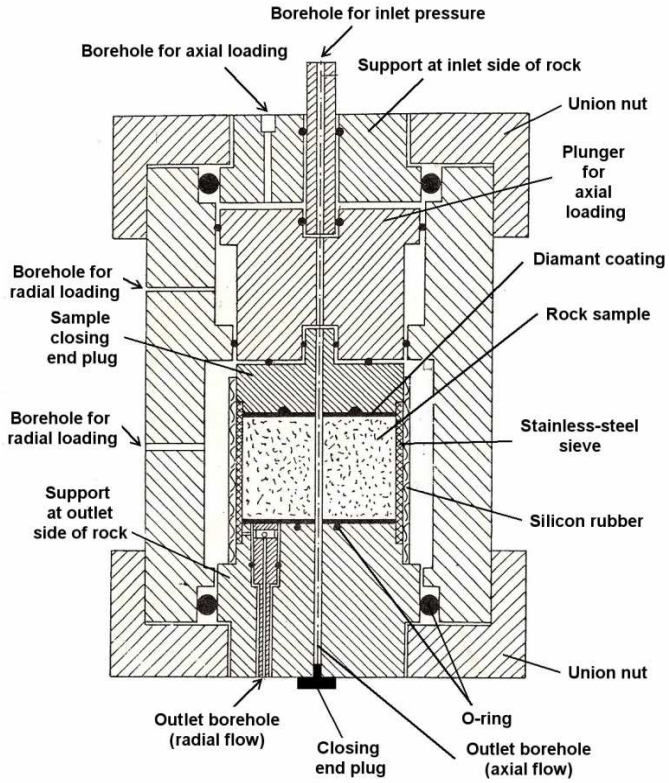

Figure 3

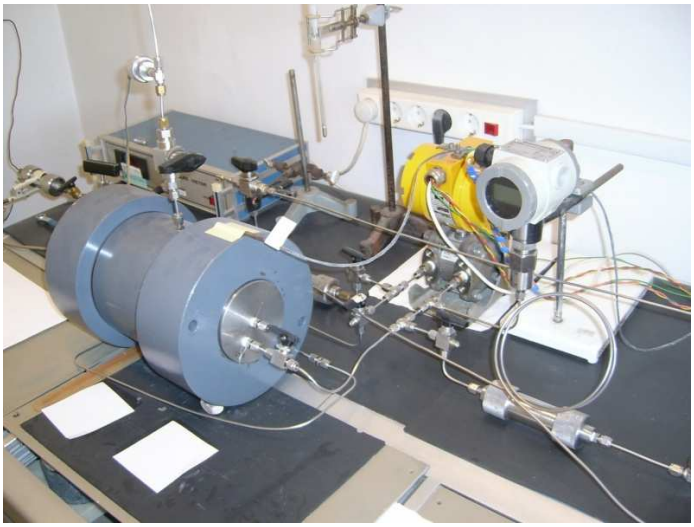

Figure 4

2. Evaluation, interpretation methods.

The radial pulse decay technique has been discussed in other papers already [1, 2], this is not the scope of this work. In this paper the linear pulse decay technique is discussed only. To evaluate a linear pulse decay measurement, Jones has proposed a technique [4]. According to his method the logarithm of the normalized pressure difference change is linear in time:

$$\ln\left(\frac{\Delta p}{\Delta p_0}\right) = b + m_1 \cdot t \tag{1}$$

Permeability can be calculated from the m_1 slope.

$$k_w = \frac{-m_1 \mu_w l\left(c_w + c_{v1}\right)}{A\left(\frac{1}{V_1} + \frac{1}{V_2}\right)} \tag{2}$$

So the principle of the Jones method is to depict measurement points according to Equation 2, and calculate permeability from the slope of the fitted straight line. As an example, *Figure 5*. depicts such an evaluation, which was carried out with water on a core sample of a tight, unconventional reservoir. Blue dots depict measurement points, whereas the blue line is fitted to the points.

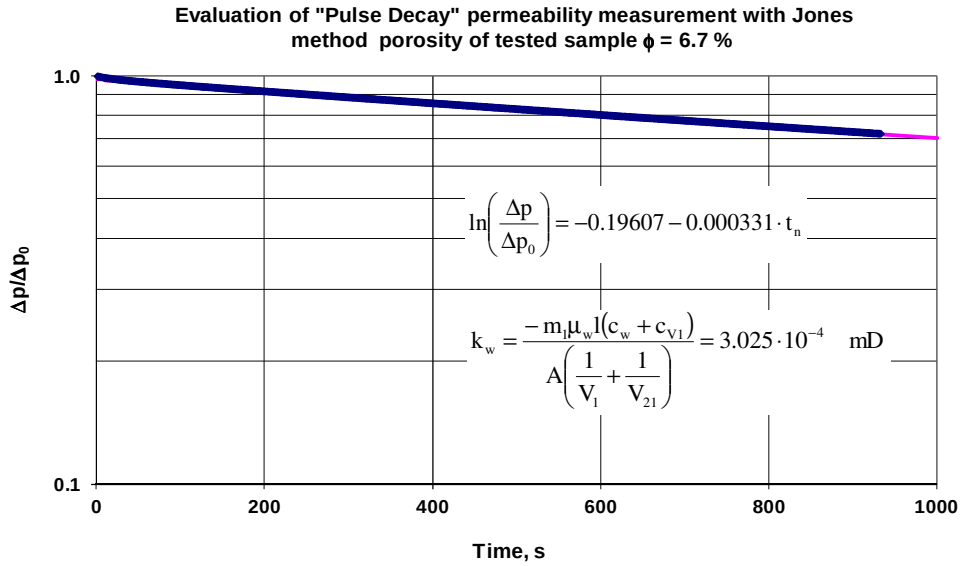

Figure 5

There is an other evaluation method also, where the mathematical model simulating the whole measurement is fitted to measurement points. Such a solution was published by Haskett et al [3]. Their solution however is full with dimensionless variables, conversion factors, etc. which makes it difficult to understand and apply, so it was decided to develop our own solution, which was called RIAES LPD.

The governing equation of flow within the linear core is the partial differential equation of hydraulic diffusivity:

$$\frac{\partial^2 P}{\partial x^2} = C\frac{\partial P}{\partial t} \tag{3}$$

where

$$P = p - p_{ini} \tag{4}$$

Initial conditions are:

$$p(x; t = -0) = p_{ini} \tag{5}$$

$$p_u(t = -0) = p_1 \tag{6}$$

$$p_d(t = -0) = p_2 \tag{7}$$

Boundary conditions are for x = 0, and t > 0

$$p_u(t) = p(x = 0;\ t)\ . \tag{8}$$

$$C_1\frac{dp_1}{dt} = \left.\frac{\partial p}{\partial x}\right|_{x=0} \tag{9}$$

where

$$C_1 = \frac{\mu c V_u}{kA} \tag{10}$$

i.e. for x = L, t > 0

$$p_d(t) = p(x = L; t) \tag{11}$$

$$C_2 \frac{dp_2}{dt} = -\left.\frac{\partial p}{\partial x}\right|_{x=L} \tag{12}$$

$$C_2 = \frac{\mu c V_d}{kA} \quad , \tag{13}$$

further

$$C = \frac{\varphi \mu c}{k} \quad . \tag{14}$$

In general $p_2 = p_{ini}$, but not necessarily. With this notation the solution can be given quite generally.

Equations 8 and 11 express pressure continuity between core ends and attached vessels, whereas equations 9 and 12 express mass balance, i.e. the rate of pressure change is proportional to in- and outlet fluxes of the core.

Equation 3 was solved via Laplace transform. The general solution is as follows:

$$P(x,t) = P_\infty + \frac{2}{C}\sum_{n=1}^{\infty} \frac{M_1 - M_2}{\alpha_n^2 \left[F_1 - F_2\right]} e^{-\frac{\alpha_n^2}{C} t} \tag{15}$$

where

$$M_1 = C_2 P_2 \cos(\alpha_n x) + C_1 P_1 \cos\left[\alpha_n (L - x)\right] \tag{16}$$

$$M_2 = \frac{C_1 C_2 \alpha_n}{C}\left[P_2 \sin(\alpha_n x) + P_1 \sin\left[\alpha_n (L - x)\right]\right] \tag{17}$$

$$F_1 = \left[\frac{L}{\alpha_n^2} - \frac{(C_1 + C_2)}{C\alpha_n^2} - \frac{C_1 C_2 L}{C^2}\right]\cos(\alpha_n L) \tag{18}$$

$$F_2 = \left[\frac{2}{\alpha_n^3} + \frac{(C_1 + C_2)L}{\alpha_n C}\right]\sin(\alpha_n L) \tag{19}$$

and α_n –s are the roots of the following transcendent equation:

$$\mathrm{tg}(\alpha_n L) = \frac{(C_1 + C_2) C \alpha_n}{C_1 C_2 \alpha_n^2 - C^2} \tag{20}$$

α_n –s can be calculated numerically.

Pressures of the vessels are measured at the in- and outlet end of the core (i.e. at x = 0, and x = L) so the mathematical solution has to be taken at these locations. Accordingly:

$$M_1\big|_{x=0} = C_2P_2 + C_1P_1\cos(\alpha_n L) \tag{21}$$

$$M_1\big|_{x=L} = C_2P_2\cos(\alpha_n L) + C_1P_1 \tag{22}$$

$$M_2\big|_{x=0} = \frac{C_1C_2\alpha_n}{C}P_1\sin(\alpha_n L) \tag{23}$$

$$M_2\big|_{x=L} = \frac{C_1C_2\alpha_n}{C}P_2\sin(\alpha_n L) \tag{24}$$

The above formulas were implemented into the software the graphical interface of the software is shown below in *Figure 6.*

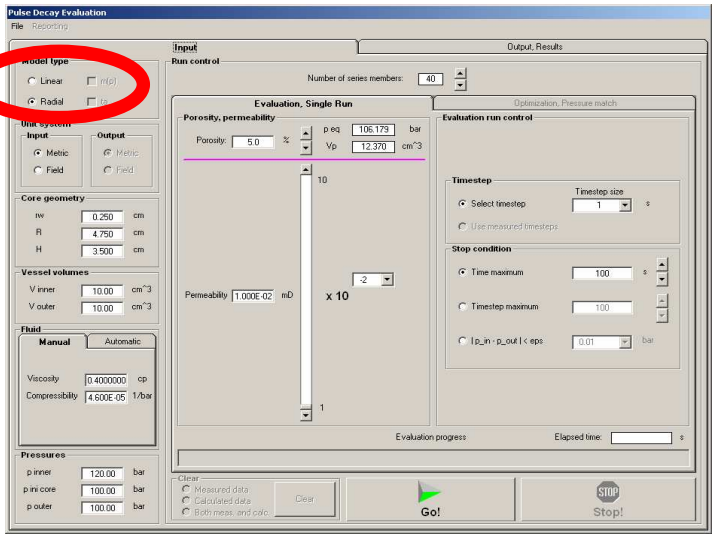

Figure 6

An example application with the new software is shown in *Figure 7.*

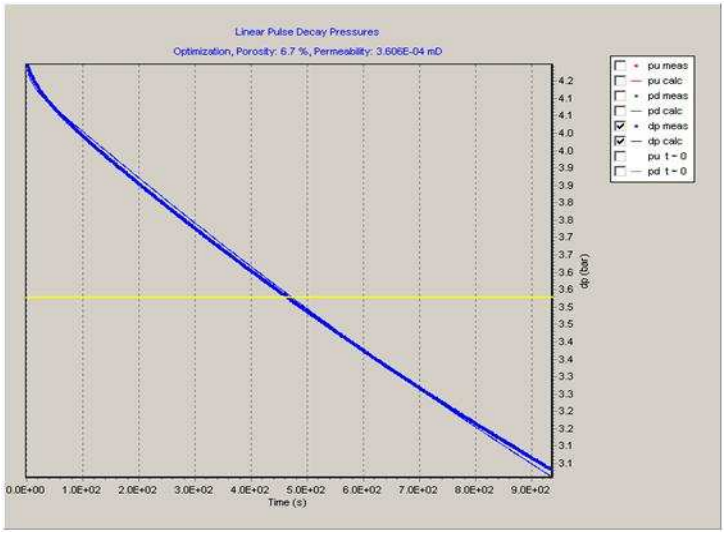

Figure 7

3. Conclusions

The pulse decay technique was used to determine the permeability of a core originating from a Hungarian unconventional gas reservoir. Measurements were done with water. Interpretation was done with both the Jones and our method, and results were compared. The comparison is shown *in Figure 8* and *Table 1*.

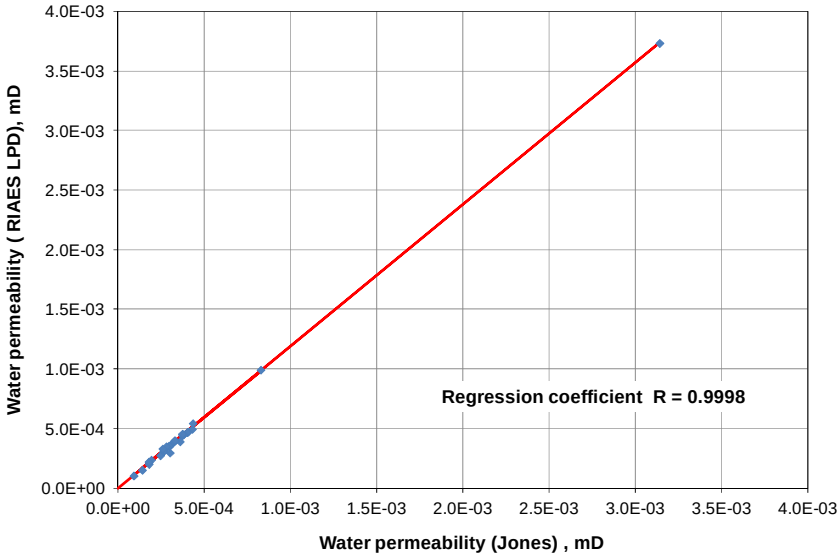

Figure 8

Table 1

Number	Porosity (%)	Permeability (Jones) (mD)	Permeability (AFKI) (mD)
1	6.700	3.025E-04	3.606E-04
2	5.900	4.326E-04	5.428E-04
3	4.100	4.284E-04	4.952E-04
4	7.400	4.041E-04	4.719E-04
5	6.900	2.652E-04	3.171E-04
6	6.700	3.999E-04	4.682E-04
7	6.100	3.295E-04	3.970E-04
8	6.600	1.385E-04	1.517E-04
9	6.500	2.994E-04	2.957E-04
10	3.800	8.979E-05	1.037E-04
11	6.900	3.579E-04	3.908E-04
12	6.700	1.780E-04	2.009E-04
13	6.600	2.437E-04	2.739E-04
14	3.400	2.787E-04	3.485E-04
15	6.400	3.221E-04	3.873E-04
16	6.200	3.788E-04	4.496E-04
17	7.000	3.720E-04	4.415E-04
18	6.900	3.263E-04	3.995E-04
19	6.400	2.623E-04	3.080E-04
20	6.400	2.960E-04	3.498E-04
21	7.500	8.259E-04	9.915E-04
22	7.000	3.707E-04	4.546E-04
23	8.100	3.138E-03	3.733E-03
24	6.900	2.571E-04	3.303E-04
25	6.200	1.764E-04	2.203E-04
26	6.200	2.941E-04	3.553E-04
27	6.400	2.239E-04	2.969E-04
28	6.600	1.916E-04	2.359E-04

The following conclusions can be drawn:

- There is a strong correlation between the two measurement methods.
- The Jones method slightly underestimates the values obtained by the numerical method. This is most probably because the Jones method has some limiting assumptions.
- In case of using water, porosity measurement was not possible unlike in the case of gas as a measurement medium.
- The two methods give consistent results in cases, when the straight line fit of the Jones method is easy and straightforward. If the match of the Jones line is good, than the match of the numerical model is good, and vice versa.

- In case of a linear fit there is some degree of freedom to fit the straight line, which however is not possible with the numerical method.
- The ideal medium for measurement is gas, not water, or any other fluid. Gas does not contaminate the core, there is a large compressibility contrast between the gas and the steel core holder, and the real reservoir fluid is also gas.

Nomenclature

Δp	pressure difference
Δp_0	pressure difference at t = 0
t	time
b	intersection
m_1	slope
μ	viscosity
l	length
A	cross section
c_w	isothermal compressibility of water
c_1	isothermal compressibility of the measurement system
V_1	volume of the inlet pressure
V_2	volume of the outlet vessel
c	compressibility
C	see eq. 14.
C_1	see eq. 10.
C_2	see eq. 13.
$F_{1, 2}$	see eq. 15.
k	permeability
M	numerator
$M_{1, 2}$	members in eq. 15.
P	$p-p_{ini}$
p	pressure
p_u	inlet pressure
p_d	outlet pressure
p_1	initial inlet pressure
p_2	initial outlet pressure
x	distance
V_u	inlet vessel volume
V_p	pore volume
V_d	outlet vessel volume

Greek letters

φ	porosity
μ	viscosity
α_n	positive roots of eqn. 20

"Acknowledgement: This works was carried out ad part of the TÁMOP-4.2.1.B-10/2/KONV-2010-0001project in t5he framework of the New Hungarian Development Plan. The realization of this project is supported by the European Union, co-financed by the European Social Fund."

REFERENCES

[1] Bódi, Tibor–Gilicz, András: *Tömött kőzetek porozitásának és gázpermeabilitásának egyidejű meghatározása a dinamikus nyomásváltozás mérésével*. XXVII. Nemzetközi Olaj- és Gézipari Konferencia Hungary, Siófok 2008. szeptember 16–19. CD A 06 1–40.

[2] Gilicz, András: *Application of the Pulse Decay Technique*. SPE 22688, presented at the 66th Annual Technical Conference and Exhibition of the SPE held in US Texas, Oct. 6–9, 1991.

[3] Haskett–Narahara: *A Method for Simultaneous Determination of Permeability and Porosity in Low Permeability Cores*. SPE Formation Evaluation, September 1988, 651–658.

[4] Jones, S. C.: *A Technique for Faster Pulse Decay Permeability Measurement in Tight Rock*. SPE Formation Evaluation, 1997 March.

[5] Serag El Din, et al.: *Whole Core Versus Plugs: Integratin Log and Core Data to Decrease Uncertainty in Petrophysical Interpretation and STOIP Calculations*. SPE 137679

Geosciences and Engineering, Vol. 1, No. 1 (2012), pp. 75–86.

DETERMINATION OF CAPILLARY PRESSURE AND RELATIVE PERMEABILITY CURVES WITH A NOVEL ULTRA ROCK CENTRIFUGE

ÁKOS PINTÉR–TIBOR BÓDI
Research Institute of Applied Earth Sciences, University of Miskolc
3515 Miskolc-Egyetemváros, Hungary
pinter@akki.hu, bodit@akki.hu

Abstract
Drainage capillary pressure curves were determined in water-gas system with new and modern ultra rock centrifuge (CoreTest URC-628 type of instrument). The measurements were performed on different porosity rocks. The shape of the capillary pressure curves was decent for the high porosity sandstone rocks. For this type of sample plugs, further measurements can be suggested, and more detailed examinations are planned to be performed by us in the near future (imbibition tests, usage of oil in the system). On the other hand, in the cases when the measurements were performed on low porosity, fissured rocks, the measurement proved to be less efficient. The small size of the pore volumes impaired the resolution of the measurement, the water left the rocks too early through the fissures, moreover in some cases, the rocks broke into pieces.

From the obtained data, the relative permeability values were also calculated with the Brooks–Corey method. These values were plotted vs. the water saturation. The adequacy of these relative permeability curves was investigated.

1. Introduction

The modern hydrocarbon production methods, especially the exploitation of the non-conventional hydrocarbon reservoirs, make the properties of the rock and the fluid necessary to be known. Capillary pressure and relative permeability curves are two of these features, the determination of these parameters are among the most difficult and elaborate petrophysical measurements.

This paper aims to describe capillary pressure curve measurements with a novel high speed ultra rock centrifuge, to evaluate the results of the measurements, and to make conclusions regarding its applicability.

2. Preliminaries

The theoretical background of capillary pressure curve measurements was summarized by Pirson [3]. He defines capillary pressure, P_c, as the differential pressure that exists between two fluid phases at their interface when they are distributed under static equilibrium within a porous material. When oil and water are the two fluids, the measurable physical properties of rocks and fluids can be calculated with the following equation:

$$P_c = \sigma \frac{2}{r} \cos\theta = gh(\rho_w - \rho_o) \tag{1}$$

Besides this relationship, P_c is a function of fluid saturation and of the direction of change of fluid saturation, whether we mean drainage or imbibition.

In practice, the capillary-pressure curve is inverted and plotted above the abscissa. The curve represents negative values of pressure for the wetting phase. Subtracting the capillary pressure from the pressure in the nonwetting phase, we can obtain the pressure in the wetting phase.

The capillary pressure of a reservoir rock sample can be measured by finding out how much pressure must be applied on a nonwetting fluid in order to reach a certain saturation in that fluid. If we assume that the largest capillary opening is circular, it's radius is r, the pressure needed for forcing the nonwetting fluid will be $\Delta P = (2\ \sigma \cos \theta)/r$. The nonwetting fluid starts to enter the core at this minimum pressure. Any capillary of smaller radius will require a higher pressure application. The minimum pressure can be referred to as the threshold pressure of the core.

Capillaries of smaller and smaller radii are reached by the nonwetting fluid as the driving pressure upon the nonwetting fluid is increased. If the capillaries of the rock sample are highly uniform in size, no excess pressure is required to saturate them in nonwetting fluid. In this case, the pressure applied vs. fluid saturation curve is very flat until the irreducible saturation is reached. On the other hand, if the capillaries are of very heterogeneous size, the capillary pressure curve is very steep.

The capillary pressure of a reservoir rock as a function of fluid saturation can be considered as a measure of capillary size distribution, which actually is a measure of the rock texture. For fine textured rock samples made up of small cemented closely packed grains, higher capillary pressure can be measured at a given saturation than for coarse textured rocks made up of large grains, poorly cemented and loosely packed.

From the capillary pressure curves, it is possible to calculate the average size of the pores making up a stated function of the total pore space. The average capillary radius r can be obtained from the following equation:

$$r = \frac{2\sigma \cos \theta}{P_c} \tag{2}$$

Assuming that the interfacial tension σ and the contact angle θ are known, we can get the results by solving this Eq. 2.

Since the centrifuge method for capillary pressure measurements was first introduced in 1945, the procedure became much faster, though somewhat more complex. The principle of it is to make use of a highly increased gravity drainage effect by submitting the saturated cores to variable multiplies of the acceleration of gravity, g, in a high-speed centrifuge. It is necessary that a centrifuge for capillary pressure measurement should run smoothly even when it is considerably out of balance. In order to fulfill this requirement, Hassler used a centerless rotor for his apparatus, suspended on a shaft flexible enough to bend while the rotor takes whatever center the constantly shifting liquid masses require. The damping forces required to avoid the damaging resonance vibration to which this type of construction normally gives rise are supplied by a rubber damping bearing below the rotor, consisting of a leather bearing enclosed in a metal cup surrounded by a ring of sponge rubber which is held in a steel ring. This bearing does not support any of the weight of the rotor, which is suspended from a ball bearing. The suspension represents a compromise between flexibility and strength; it consists of a rigid shaft provided with two universal

joints and the other hidden by the streamlined rotor cover. The rotor is driven at speeds up to 4000 rpm by a 1/8 hp variable speed a-c motor. There is motor provided with an adjustable centrifugal governor which actuates an electronic relay. The core is held in a metal container, which is provided with a graduated glass pipette to collect the liquid pulled from the core. Provision is made for four core holders on the rotor, and the pipettes are read by means of a stroboscope lamp operated by a contact device on the motor shaft. The contact device is provided with four contacts, and a selector switch enables any one of the four pipettes to be viewed as desired through the window. The speed of the centrifuge is obtained by measuring the voltage of a small a-c generator on the motor shaft. This tachometer is calibrated by means of stroboscope disk on the rotor. For capillary pressure measurements with the described apparatus, we have to saturate the extracted cores and place them in the core holders, after their dry and saturated weights have been recorded. Then we start the centrifuge and let it run at successively higher speeds, each being held constant at a chosen value until all the cores have attained equilibrium. This is indicated by no further increase of the quantity of liquid contained in the pipettes. Reaching equilibrium may take from a few minutes to ½ hr or more. Then, the quantity of liquid in each pipette should be read with the aid of the stroboscope and recorded before increasing the speed of the centrifuge. When the run is over, the cores are removed from the centrifuge and they are weighed in order to check the saturation determined from the last pipette reading.

In the following section, simplified theory for the computation of the capillary pressure is presented, which is sufficiently accurate for practical purposes.

As shown above, capillary pressure is a function of the fluid saturation along the core. Conversely, we might as well say that saturation is a function of capillary pressure: $S = S(P_c)$. For centrifuge measurements P_c is given by

$$P_c = a\rho h' \tag{3}$$

Keeping the centrifuge at a definite constant speed, the average saturation S_{avg} in the core can be obtained from the following relationship

$$S_{avg} = \frac{1}{L}\int_0^L S(P_c)dP_c = \frac{1}{a\rho L}\int_0^L S(h)dh \tag{4}$$

The following equation can be used:

$$a\rho L S_{avg} = \int_0^L S(h)dh \tag{5}$$

Derivating the terms of both sides with respect to L, we shall obtain

$$a\rho S_{avg} = S(L) \tag{6}$$

Thus we can calculate the saturation S(L) at the face of the core closest to the axis of rotation from the fluid density ρ, the average fluid saturation S_{avg}, and the acceleration a

produced at an average distance r of the core from the axis of the centrifuge rotor. Saturation S(L) corresponds to a capillary pressure $P_c = a\rho L$.

Assuming that the angular velocity ω or the speed of rotation in rpm is known, the acceleration a can be calculated:

$$a = \omega^2 r = \left(\frac{n}{120\pi}\right)^2 r \tag{7}$$

For our capillary pressure measurements, a CoreTest URC-628 Ultra Rock Centrifuge (see *Figure 1*) was used. This modern device is able to operate at up to 16500 rpm rotational speed. There are 3 buckets in a rotor, balanced, having a rock sample (1.5" diameter, maximum 2" length) in each of them. The effluent fluid is collected in so-called receiving tubes of the buckets. At the moment, our institute only has a rotor and a receiving tube set only for drainage capillary pressure curve determination tests.

Figure 1: The centrifuge used for our measurements

After selecting the rock samples to be measured, the petrophysical properties (helium and water porosity, nitrogen and brine permeability) of the rock samples have to be measured. The geometric data of the rocks (length, diameter) should also be known. Before the measurement, the samples have to be saturated with brine (until 100% saturation is reached), then a pre volume should be injected into the receiving tubes, finally the plug (~1.5 inch in diameter, maximum 2 inch in length) samples should be placed into the buckets of the rotor.

During the examination, the change of the fluid level shows the amount of the effluent fluid. The movement of the level is observed by a camera, and the whole system is connected to a computer. In the monitor screen, the movement of the fluid level can be seen as a movement of the peaks, in pixel units. Before the capillary pressure measurement, a calibration test was performed and the ml fluid / pixel unit ratio was determined, which data was used to calculate the amount of the effluent water.

Rotational speeds gradually increasing from 1000 rpm to 16000 rpm (between 1000 rpm and 5000 rpm, in 500 rpm steps, above 5000 rpm, in 1000 rpm steps) were used,

having a total of 20 rotational speed levels, 10 minutes of rotation on each speed level. A measurement took 3 hours and 50 minutes. The amount of the effluent water was read on the computer at each rotational speed level.

According to the users' manual [1], the capillary pressure can be calculated for each rotational speed with the following expression:

$$P_c = (0.1578 \cdot 10^{-6})\, \Delta\rho \left(R - \frac{1}{2} \right) hn^2 \tag{8}$$

The average saturation of the rock sample could be calculated for each rotational speed with the following equation:

$$S_{avg} = \left(\frac{V_{Ieff} - V_{IinjL}}{\text{Pore Volume}} \right) \cdot 100 \tag{9}$$

By obtaining these data, the capillary pressure curve can be plotted. Since we don't have the necessary inverted buckets to determine the imbibition curve, only the drainage curve could be determined of the rock samples.

After measuring and plotting the capillary pressure curves from the data obtained by the centrifuge and its software, we examined how the measured capillary pressure and water saturation data could be converted into relative permeability curves.

Several studies dealing with relative permeaiblity calculations had been checked, and it was found that two of them may be suitable for the needed data conversion. The other calculation methods demanded data which could not be determined with our instruments. The two possible methods were Corey's Model and the Brooks–Corey Model [2].

The Corey Model has limitations. It is only applicable if capillary pressure can be represented by the following equation:

$$\frac{1}{P_c^{\,2}} = C S_w^{\,*} \tag{10}$$

After plotting P_c^2 against S_w^*, we fould that the C factor is not constant in our case, thus the capillary pressure can not be represented by Eq. 10. The normalized wetting phase saturation S_w^* could be expressed as follows for the drainage case:

$$S_w^{\,*} = \frac{S_w - S_{wr}}{1 - S_{wr}} \tag{11}$$

Brooks and Corey modified the representation of capillary pressure function to a more general form,

$$P_c = p_e (S_w^{\,*})^{-1/\lambda} \tag{12}$$

In order to use the Brooks–Corey method, we tested whether Eq. 12 is valid for our measurement points.

The λ had to be determined since all other factors were known (we considered p_e the first measured capillary pressure value). Taking the logarithm of both sides of Eq. 12, we got the following equation:

$$\lg P_c = \lg p_e - \frac{1}{\lambda}(S_w^*) \tag{13}$$

which means if we plot lg S_w^* against lg P_c, it should be a linear function whose slope is $-(1/\lambda)$. We put our measurement data into Eq. 13 and an acceptable linear function could be plotted from them, which meant that the Brooks–Corey model is applicable for our measurement data (capillary pressure, water saturation) to be converted to relative permeability data with it. The λ could be obtained as the modulus of the reciprocal of the slope of the plotted linear function.

Thus, the calculation of the relative permeabilities with the Brooks–Corey method was available, which is described in the followings. According to Burdine's Model, the relative permeability of the wetting phase can be computed as follows:

$$k_{rw} = (\tau_{rw})^2 \frac{\int_0^{S_w} dS_w / (P_c)^2}{\int_0^1 dS_w / (P_c)^2} \tag{14}$$

In the same way, the relative permeabilities of the nonwetting phase can be expressed as follows:

$$k_{rnw} = (\tau_{rnw})^2 \frac{\int_{S_w}^1 dS_w / (P_c)^2}{\int_0^1 dS_w / (P_c)^2} \tag{15}$$

Substituting Eq. 2.12 into Eq. 2.14 and 2.15, with the assumption that $S_e = 0$, Brooks and Corey derived equations to calculate the wetting and nonwetting phase relative permeabilities as follows:

$$k_{rw} = (S_w^*)^{\frac{2+3\lambda}{\lambda}} \tag{16}$$

and

$$k_{rnw} = (1 - S_w^*)^2 \left[1 - (S_w^*)^{\frac{2+\lambda}{\lambda}} \right] \tag{17}$$

During our calculations, Eq. 16 and Eq. 17 were used to calculate the relative permeabilities of the phases. From these data, the relative permeability curves could be plotted against the water saturation.

3. Results and discussion

The high speed centrifuge was first used to determine drainage capillary curves for good porosity and permeability rock samples. These rock samples were of sandstone. The geometric data (length, diameter) of a representative sample from these sandstone plug samples is shown in *Table 1*. Our measurements on this kind of samples will be introduced upon this sample. The porosity and permeability data of this sample, which were measured earlier by us for other purposes, are also given there. From these data, the pore volume of the rock sample could be calculated.

Table 1

Petrophysical and geometric data of good porosity rock sample

Sample length (cm)	4.982
Sample diameter (cm)	3.478
Helium porosity (%)	11.34
Water porosity (%)	11.28
Nitrogen permeability (mD)	4.29
Water permeability (mD)	2.60
Pore volume (cm3)	5.34

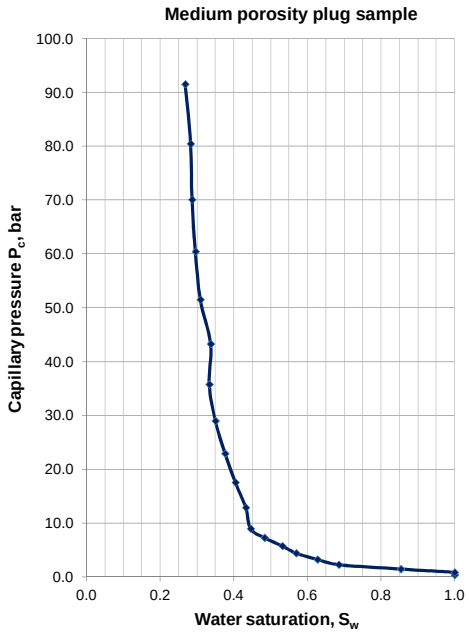

Figure 2: Capillary pressure drainage curve for medium porosity plug sample

After saturating the rock sample with water (100 percent water saturation is reached), the rotor of the centrifuge was assembled and the measurements were performed on this sample (with two other samples to keep the centrifuge in balance). The data of the measurement was then analyzed, and the drainage capillary pressure curve could be drawn up. It can be concluded that the measurements for this kind of rocks can be performed well, the shape of the drainage capillary pressure curve is adequate. Though, some of the rocks might break into pieces during the measurement due to the applied high rotational speed. The obtained capillary pressure curve for this rock sample, which was found the most representative curve for this kind of rocks, can be seen in *Figure 2*. The measurement points were connected by straight lines instead of fitting a curve on them.

The determined data was then compared with data for tight limestone rock samples. These rock samples were of the same size, but they had lower porosity and permeability, as can be seen in *Table 2,* where the data of the most representative sample of our tight limestone rocks are shown. Thus, the pore volume of these rock samples was also lower.

Table 2

Petrophysical and geometric data of lower porosity rock sample

Sample length (cm)	4.568
Sample diameter (cm)	3.772
Helium porosity (%)	2.92
Water porosity (%)	1.25
Nitrogen permeability (mD)	0.111
Water permeability (mD)	0.0027
Pore volume (cm3)	0.66

As it was expected, the smaller pore volume values resulted in a lower amount of effluent water. The volume of the collecting tubes is 12 cm^3. The camera can focus on 80 percent of this volume, so 9.6 cm^3 of volume change can be examined. 1 cm^3 of volume change is equal to ~100 pixel units on the screen of the computer, which means the device can not detect a volume change less than 0.01 cm^3. If the pore volume of a rock sample is only a few tenths of cm^3, the amount of effluent water will be even less. Thus he differences between the effluent water amount data measured for the different rotational speed levels will approach the resolution of the measurement, thus the shape of the capillary pressure curve will be not as good as it was for higher porosity rock samples, as can be seen in *Figure 3,* which is a representative capillary pressure curve figure for this kind of rock samples. The measurement points were connected by straight lines instead of fitting a curve on them. The fact that these kind of tight rock samples often have most of their pore volume in small cracks and fissures also makes the measurement more challenging, since in this case, the water leaves the sample at lower rotational speed, and then, the amount of the effluent water practically does not change, making the connate water saturation being reached only in a few rotational speed levels. A lower number of measurement points can also contribute to a less good capillary pressure curve. The rock samples also tended to break into pieces with a higher possibility. These phenomena were observed when we dealt with such tight and fissured limestone rock samples.

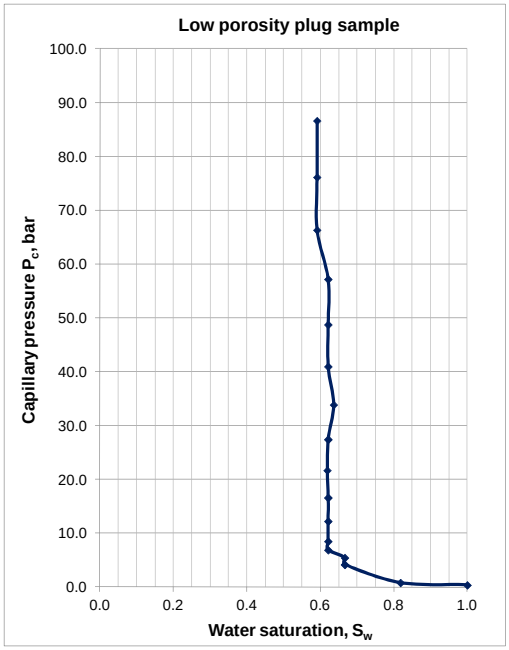

Figure 3: Capillary pressure drainage curve measured for a low porosity plug sample

After plotting the capillary pressure curves, the relative permeability curves were about to be determined from the data. First we tried to use the Corey method, but its limitations of usage wasn't fulfilled at our measurements. Thus, the Brooks–Corey method was used. λ was calculated from Eq. 12 by the procedure detailed earlier, and then the relative permeability data of the phases were calculated from Eq. 16 and Eq. 17. From the data obtained by this way, the relative permeability curves were plotted. We show the two representative relative permeability curves of the previously mentioned representative rock samples (a good porosity sandstone sample and a low porosity tight limestone sample), they can be seen in *Figures 4–5.* In *Figure 4,* a relative permeability curve can be seen for a good porosity and permeability sandstone rock sample. In *Figure 5,* a relative permeability curve can be seen for a low porosity and permeability, fissured limestone rock sample. The measurement points were connected by straight lines instead of fitting a curve on them. By comparing the two figures, it can obviously be seen that the shape of the curves are more adequate on *Figure 4,* i.e. a better curve could be plotted for a better porosity sample. This fact corresponded with our expectations. If the pore volume of the rock sample is higher and if there are less cracks, fissures inside it, the measurement can be carried out more properly, the data are more reliable, better capillary pressure and relative permeability curves can be plotted.

On the basis of our experiences, it can be concluded that in case of the sandstone samples, the determination of the capillary pressure and the relative permeability curves are relatively simple. On the other hand, for tight, fissured limestone reservoir rocks, the low permeability and the occurence of fissures made the measurement procedure more complicated.

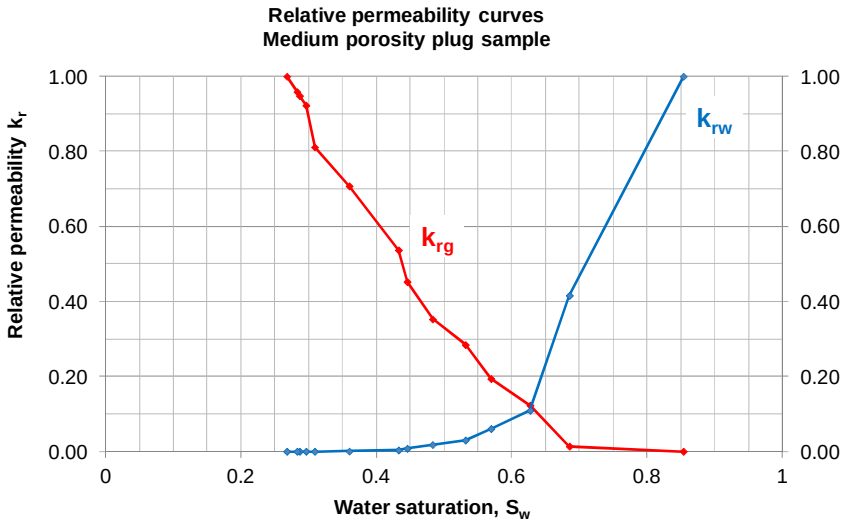

Figure 4: Relative permeability curves determined for low porosity rock sample

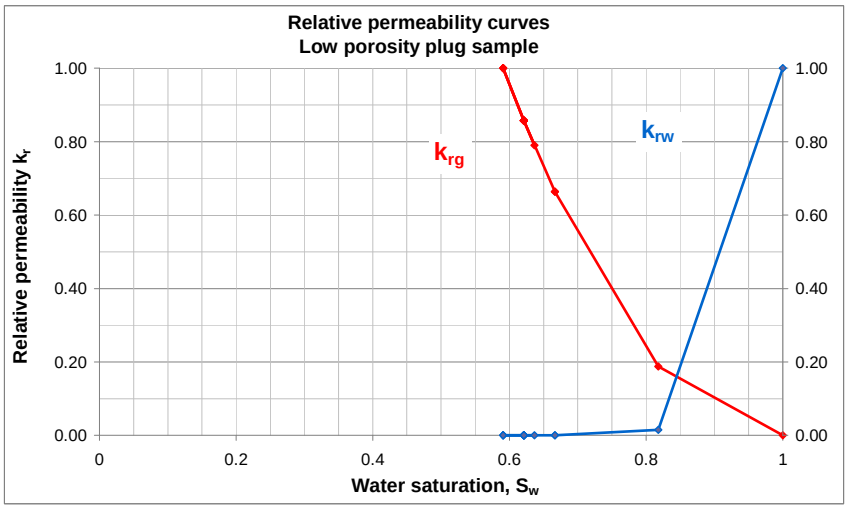

Figure 5: Relative permeability curves determined for medium porosity rock sample

The size of the rock samples, along with the low porosity, determines the pore volume of the rock samples. For our tight, fissured limestone samples, we had to deal with this problem. A small size of pore volume deters the preciseness of the measurement, the water saturation change is hard to be traced in this case, since it is close to the resolution of the measurement. If there are large fissures observable on the rock, it can happen that the whole pore volume leaves the rock sample through it before the first centrifuge speed gets settled, and then, no further water saturation change can be observed.

According to our experiences, before the measurement with the centrifuge, the petrophysical and geometrical properties (length, diameter, porosity, permeability, pore volume, fissures) of the rocks are important to be known to properly plan the examination.

4. Summary

Generally it can be said that this kind of measurement (with this new centrifuge) is suitable for obtaining capillary pressure curves for different type of rock samples. Good porosity sandstone rock samples and low porosity tight fissured limestone samples were tested with the device, and the measurement results were suitable to be evaluated, the capillary pressure against the water saturation could be plotted. With the good porosity samples, the determination of capillary pressure was relatively simple, while for the low porosity, fissured samples, some factors made the measurement and its evaluation more complicated.

From the obtained capillary pressure and water saturation measurement data, we tried to find a proper calculation method to convert them into relative permeability data. The Brooks–Corey model was found to be suitable to perform these calculations.

In the future, the imbibition curve of the capillary pressure curve is also about to be tested, this would require a development of our device. We also plan to compare this kind of measurement with other types of capillary pressure measurements.

List of symbols

a	the acceleration produced by rotation of centrifuge at an angular velocity ω
C	a constant used for calculations
g	acceleration of gravity, m/s^2;
h'	distance of any fluid element from core outlet where capillary pressure is zero owing to its contact with fluid of zero curvature in the measuring pipette
h	height above free water surface, m
k_{rw}	relative permeability of the wetting phase
k_{rnw}	relative permeability of the nonwetting phase
l	length of core plug, cm
L	the total length of the core
n	rotational speed, rpm.
P_c	capillary pressure, Pa
p_e	entry capillary pressure
r	capillary radius, m
R	centrifuge radius of rotation, cm (center of rotation to the bottom of the sample)
r_{avg}	average radial distance between the core samples and the rotational axis, m
rh	mean radius of rotation, (R–0.5h), cm;
S_{avg}	average fluid saturation
S_w	wetting phase saturation
S_{wr}	the residual saturation of the wetting phase
S_w^*	normalized wetting phase saturation
V_{Ieff}	incremental effluent tube volume, cm^3

V_{IinjL} initial ijected liquid volume, cm^3
V_p pore volume, cm^3
$\Delta\rho$ density difference between fluid phases, g/cm^3
θ contact angle of wetting phase measured through the liquid, rad;
λ pore size distribution index
ρ fluid density, g/cm^3
ρ_o density of oil, kg/m^3
ρ_w density of water, kg/m^3
σ interfacial tension, N/m
τ_{rw} tortuosity ratio of the wetting phase
τ_{rnw} tortuosity ratio of the nonwetting phase
ω angular velocity, radians per sec

"Acknowledgements: This work was carried out as part of the TÁMOP-4-2-1-B-10/2/KONV-2010-0001 project int he framework of the New Hungarian Development Plan. The realization of this project is supported by the European Union, co-financed by the European Social Fund."

REFERENCES

[1] CoreTest System Inc., *URC-628 Users manual, Ultra-rock centrifuge*, 2010, V2d
[2] Li, K.–Horne, R. N.: *Experimental Verification of Methods to Calculate Relative Permeability Using Capillary Pressure Data*, Society of Petroleum Engineers 76757, 2002.
[3] Pirson, S. J.: *Oil Reservoir Engineering*. McGraw–Hill Book Company, Inc., New York–Toronto–London, 1958, 372–382.

Geosciences and Engineering, Vol. 1, No. 1 (2012), pp. 87–91.

INTRODUCTION OF NEW MEASURING DEVICES FOR THE ROCK MECHANICS LABORATORY AND THE FIRST MEASUREMENT EXPERIENCES

BALÁZS CSUHANICS–ÁKOS DEBRECZENI
Institute of Mining and Geotechnical Engineering
University of Miskolc
3515 Miskolc-Egyetemváros
bgtcsub@uni-miskolc.hu ; bgtda@uni-miskolc.hu

Abstract
Carbon-dioxide injection into exhausted oil fields is in the scope of recent research. Rock mechanics have an important role in this research, since the primary stress field should be known for the sake of the borehole stability during CO_2 injection into deep level formations. The laboratory strength tests on intact rock cores are indispensable for the determination of the in situ measured primary rock stress. The development strategy of rock mechanics laboratory was based on these measuring needs. On the one hand the development involved a brand new Hottinger–Baldwin Messtechnik measuring system which was connected to the existing loading machines; on the other hand the latest Controls testing equipment developed originally for concrete and cement was adapted to the rock mechanical purposes.

1. Introduction

Loading machines represent the main measuring equipments in the rock mechanics Laboratory of the University of Miskolc. The oldest, still functioning loading machine with a 25 kN loading capacity, was manufactured in 1958 at the Materials Testing Equipment Facility in Budapest (Hungary). The loading machine with a 100 kN measuring limit was also manufactured at the Materials Testing Equipment Facility in Budapest, in the 60's. The third loading machine with a measuring limit of 1000 kN was manufactured in 1965 in Leipzig, in the former German Democratic Republic. This machine is adaptable for both tensile load and compression load. These loading machines have own displays (readers), however, their accuracy is often not satisfactory [1]. On the other hand, we measure usually not only forces, but also the displacements and pressure data. So that, the measuring the value–pairs and their readings and records should be carried out simultaneously. These conditions made the installation of a new measuring system highly essential.

The acquisition of the new measuring devices was performed by our Institute in several stages. In the first stage, the Hottinger Baldwin Messtechnik made load cells, the single-channel amplifiers and the additional inductive displacement transducers were purchased for the rock mechanics laboratory. During the second stage, the HBM made Quantum X data acquisition system, respectively QuantumX Assistant and Catman Easy measurement software were purchased for the new acquisition system.

The new rock mechanics laboratory was equipped with the Controls-made triaxial apparatus which has a 700 bar confining pressure capacity, the Hoek triaxial cells together with loading machines with 3000 kN, 250 kN and 15 kN loading capacity, furthermore a bending machine with a 150 kN loading capacity, as well as the control software, the Advantest 9 servo hydraulic testing unit and the Sercomp 7 automatic control console.

2. Materials and methods

The aim of the research was to install the automatic data acquisition systems for the both measuring units. To meet our requirements the automatic data acquisition systems had to match the following requirements:

- real time data acquisition with adjustable sampling frequency,
- easy-to-use database from measuring data with excellent file compatibility export feasibility,
- stable software environment during the measurements is required and
- data loss because of software error should be out of the question.

The former requirements can be evaluated with a large number of tests on rocks with dissimilar solidity. We carried out the tests on different rock types to study the behaviour of the devices in wide loading ranges. The numbers of tests with the different rock materials are enlisted in the following *Table 1*.

Table 1

Rock materials used for the tests

Rock material	**Number of tests**
andesite from Recsk	32
andesite from Mátraszentimre	25
30 days old concrete from Lasselsberger Knauf dry-batched concrete	46
concrete paving	20
total:	*123*

From the total 123 tests we carried out 66 tests with the HBM automatic data acquisition system connected to different, HBM-made load cells and 57 tests on the Controls system.

In case of the uniaxial measurements carried out with Hottinger system, 1000 kN and 470 kN capacity load cells were used. The Brazilian tensile tests were carried out with a 50 kN capacity load cell.

In case of 23 uniaxial compression tests, the axial deformations were measured with 3 inductive displacement inducers at an angle of 120° to each other.

The test types were the following:

- uniaxial compressive strength measuring:69 pieces (longitudinal deformation measuring on 23 samples),
- Brazilian tensile strength measuring: 54 pieces**.**

We performed our uniaxial compression tests with cylindrical, l/D (sample length/sample diameter) = 1.32…1.49 slimness samples. The uniaxial compression tests were complemented with longitudinal deformation measuring in order to determine Young's elastic modulus. In case of uniaxial compression tests that performed along of quasi-static loading ($\sigma_1 < \sigma_F$) the following equations are valid from the Hook's-law of elasticity with fair approach:

$$\sigma_2 = \sigma_3 = 0 \quad \text{and}$$

$$\varepsilon_1 = \frac{\sigma_1}{E}$$

hence:

$$E = \frac{\sigma_1}{\varepsilon_1}.$$

Relevant reference of the ISRM (International Rock Mechanics Association) contains the regulation of stress tests of the rocks [2, 3], therefore they are not detailed here. In the majority of the practical cases standard sized samples for tension tests could not be prepared. In such cases we determine tensile strength from indirect measuring, rather than with direct initial tension tests. We performed our Brazilian tensile strength tests with cylindrical, l/D = 0.36…0.8 slimness samples. Along with a vertical loading angle on axis of the sample body in normal plane, in surroundings of the sample body axis, the vertical stress is compression stress (σ_1), the horizontal stress is initial tension (σ_3). At the centre of the sample (at r = 0 positions), where failure starts, at hard rocks the σ_3 stress corresponds with tensile strength (σ_t), that is:

$$\sigma_t = -\sigma_3 = \frac{2F}{D\pi l}$$

where:

F: breaking power [N]
D: the diameter of the sample [mm]
l: the length of the sample [mm].

3. Results and discussion

During the test measuring with the automatic data acquisition systems we focused on the behaviour of the systems during the measuring. Accordingly the analyzed rock specimens were also chosen so as to demonstrate the diversified strength parameters.

3.1. Experiences about the Hottinger–Baldwin Messtechnik measuring equipment

The Quantum X-type universal amplifier from HBM made possible the real-time measuring data processing with catman®Easy evaluation PC software. With TEDS (Transducer Electronic Data Sheet) chips we sealed into the connectors of the force transducers and inductive displacement transducers, the "Plug and Play" connecting familiar from PC technology became available. The most important characteristics of these units are stored in the transducer for TEDS and can be read by the connected amplifier, which can then automatically adjust its settings to the connected transducer. Summarising, we experienced the followings in connection with the HBM system:

- compatible with components of former versions,
- simple connection between data acquisition system and computer software,
- accuracy class C3 according to OIML R60,
- feasibility to develop "Plug and Measure" connection,
- adjustable sampling frequency between 0.02 Hz and 19200 Hz,
- the applications of inductive displacement transducers also provide high accuracy measuring and
- the stable operation of the software strongly depends on the version of the operation system.

3.2. Experience on the Controls measuring equipment

The measuring system from Controls consists of a Sercomp 7 automatic control console, an Advantest 9 servo-hydraulic unit and a PC cabinet with the connected 4 different hydraulic frames. In case of the Controls system, the whole measurement process can be controlled by a PC software. The manufacturer developed the measuring system for concrete and cement testing in the first approach; therefore we should take it into consideration during the adjustment. In nut shell, we experienced the followings in connection with the HBM system:

- simple connection between data acquisition system and computer software,
- the enclosed design of the loading frames provide safety for the users, but it makes the tests with inductive displacement transducers uneasy, in some cases irresolvable,
- after several file management actions there is no chance to withdrawing which could lead to data loss,
- pre-loading force is not adjustable; the extent of the pre-loading force gradually decreases with the heating of the hydraulic oil *(Figure1.)* and
- sampling frequency is not adjustable.

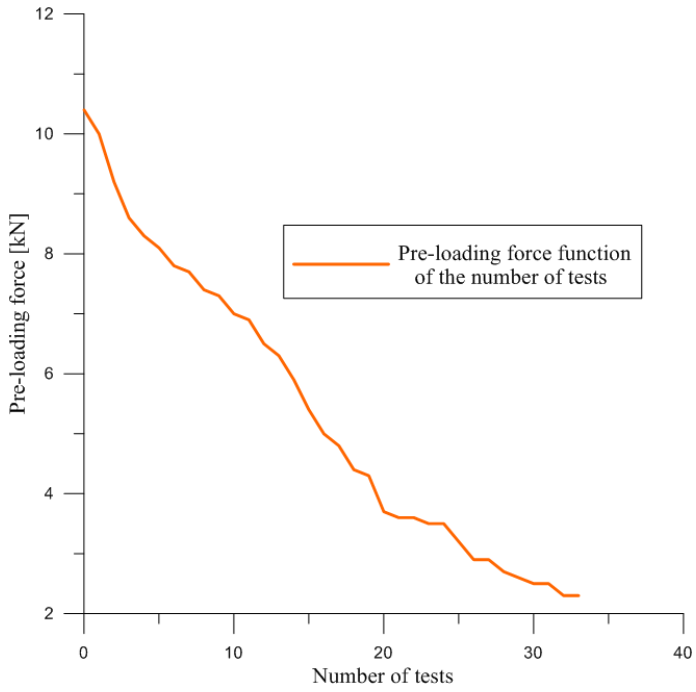

Figure 1: The decreasing of pre-loading force during the tests

4. Conclusions

To sum up, it can be concluded that using the new measuring systems increase the accuracy and reliability of the measurements. Additionally it simplify and accelerate the evaluation of the measuring data. The strain measurements carried out verified that not only the application of strain gauges, but also the inductive displacement transducers provide 10^{-6} m accurate measurements. When we measure using inductive displacement transducers, we measure the deformation of the whole sample. In case of highly inhomogeneous samples the former method can represent the deformation of the rocks better than the deformation measured using strain gauges. Several samples are not appropriate for the strain gauge measuring through the discontinuous mantle of the sample, which does not allow the sticking on the strain gauge. In this case, in our opinion the high precision measurements could be carried out using the inductive displacement transducer.

"Acknowledgement: This work was carried out as part of the TÁMOP-4.2.1.B-10/2/KONV-2010-0001 project in the framework of the New Hungarian Development Plan. The realization of this project is supported by the European Union co-financed by the European Social Fund."

REFERENCES

[1] Debreczeni, Á.: *The rock mechanics laboratory "then and now" (in Hungarian).* A Publication of the University of Miskolc Series A. Mining, Volume 76, Miskolc University Press 2009, 129–156.

[2] Bieniawski, Z. T.–Franklin, J. A. et al.: *Suggested Methods for Determining the Uniaxial Compressive Strength and Deformation of Rock Materials.* International Journal of Rock Mechanics and Mining Sciences & Geomechanics Abstracts, Vol. 16, No. 2, 1979, 135–140.

[3] Bieniawski, Z. T.–Hawkes, I.: *Suggested Methods for Determining Tensile Srength of Rock Materials.* International Journal of Rock Mechanics and Mining Sciences & Geomechanics Abstracts, Vol. 15, No. 3, 1978, 99–103.

Geosciences and Engineering, Vol. 1, No. 1 (2012), pp. 93–101.

THE EFFECTS OF BLACK, BROWN AND GREEN REVITALIZING INVESTMENTS ON THE LABOUR MARKET AND ECONOMY

ZSUZSANNA DABASI-HALÁSZ–ÁGNES HEGYI-KÉRI[1]
University of Miskolc, Institute of World- and Regional Economics
3515 Miskolc-Egyetemváros
alkduf@uni-miskolc.hu, hkagi@uni-miskolc.hu

Abstract
In this paper first of all we are going to present the method of revitalization, the main characteristics of brown field investment and its way going to "greening areas", with its economic-environmental-sociological model. One of the most important tools in the rehabilitation, revitalization of contaminated areas is brown field investment. In the Central-Eastern European territory of economic transition, the forced industrialization of former socialism, and its questionable concept of the planned area development, today created a situation that requires large-scale changes. Nowadays we think differently about the development or the quality of the various environmental factors. In our opinion the revitalization concept needs to be interpreted broadly, and extended to social processes as well. In our immediate environment in the labour market surroundings of the abandoned industrial sites the process of social erosion begins.

Taking into consideration the social conditions, ethical values of people living in the surrounding areas of the industrial sites or the so-called "slums" the answer is searched to what extent the revitalization of the area would or could affect the participation in the labour market of people living there. First of all, the economic and environmental sociological model of investments in the brown fields and the methods of revitalization are examined. A city is never totally identical with its immediate state. Buildings outlive people and street network outlives buildings. State investment sources were used to build the socialist big industries and housing estates, but the old buildings in the city centers were refused to be rebuilt and renewed. The need to revitalize the industrial sites with the spillover effects on residential environments still have huge impact on social and economic/financial considerations. A change in population started in "the slums" resulting in the decadence in terms of human potentials. In this way embarking on a new path became impossible. According to our hypothesis, the revitalization of an area induces the re-flow of population, and thus, that of labour force in a good sense. The theory of circular migration states that those coming back have more knowledge, experience and capital, as well. Our opinion is that the economic policy of the area is to be in connection with the environmental, economic and social effects of the investments in the brown field.

1. Introduction

Polluted Areas, Sustainable Development in the View of Human Resources

Intervention in the natural processes increased during the past one or two hundred years as well as in the Central-Eastern European countries. Inhabitants live in flats which are not only older than they actually these housings are the spatial footprints of extinct ages as well. Besides extensions, cities have, time related cross sections too. The actual inhabitants

[1] Whom research was supported by „Közösen a Jövő Munkahelyeiért Alapítvány" (Together for Workplace of the Future Foundation)

of a city live in buildings, streets, spaces that have traces of different ages, different structures of society, power-relations, mentality, faith, symbolism (Erő, 2009).

At the same time, the inhabitants not only demolish, ruin and rebuild their cities but also live in them, in other sense using, redefining the spaces of a city according to their social relations, connections, mentalities, styles. The measure, style and character of intervention reflect and refer back to different ages. The emphasis on what was aesthetic, economically effective was different in the 1920s, 1970s and at the turn of the 21st century. Today people think in another way about development and the quality of environmental elements.

The policy that considered the socialist era housing estates of superior status, neglected those estates and flats which were of lower status, defined the concept as "progressive space approach".

The city policy of socialism meant that "estate economy" searched only a breakout point both for flats and "districts". It was not different after the regime change either; the physical and social decline of the old housing estates and industrial zones became stronger, leading to the formation of slums.

In addition the socialist housing estates turned up with a population with lost living space and eroding every days[2]. Selective privatization increased the concentration of socially disadvantaged population. In this sense several people tried to get rid of their flats that they had just privatized. Instead of the previous population another one of lower social status came from the bottom of the social ladder. Because of their disadvantageous ages, lack of qualifications or ethnicity, these families were in a strongly excluded position in the labour market.[3] The role of industrial belts decreased during the 1990s when several factories and plants were shut down. Re-utilization of the abandoned buildings of factories and storehouses has reutilized only partly. The functional change of the "rust belts" was hindered by their environmental state and low prestige, thus entrepreneur and foreign capital avoided them.

In Hungary it is especially true for the North Eastern and South Western counties which were subjected to forced industrialization during the socialist era. The lack of revitalization has generated migration and the population change in Miskolc, Ózd, Salgótarján, Bátonyterenye, Pécs, Komló, Mohács and again Northern Borsod[4].

All these processes lead to the impoverishment of territories. In this work the English *slum* term is used in order to define the rundown suburbs of big cities where the poor live. We avoid the usage of *ghetto* since it may sound more negative and pejorative than the neutral *slum*. First the researchers of the Chicago school dealt with the phenomena of slumming in the beginning of the 20th century. Referring to the definition of Wirth (1929) slum becomes a part of an ascending spiral. In this way slumming becomes a self-generated

[2] An example to this is the housing estate of Avas where drug, alcohol problems become more regular. As well as debts resulting from unemployment and gloominess following "debt-trap"

[3] Today's example is the popluation of the housing estate of Avas who arrived there due to "the nestling project".

[4] The surveys of Károly Fazekas (2000) proved that the growth in the regional differences between unemployment and employment were affected by the expansion of foreign companiesduring the past years. The appearance of structural unemployment in North Hungary increased concerning other regions. Ont he top of that, growth in employment occured mainly in the more developed regions with high employment rates only among companies with foreign ownership.

feedback and as a result bringing out a rundown, overcrowded territory where socially hindered groups are living on the periphery in overcrowded homes. As a consequence people living there move further down the *poverty spiral* losing their motivation regarding work, becoming hopeless and unemployed. The socializing process of children is hindered by the material and ethical backgrounds of the parents who are unemployed. We would like to extend the definition of revitalization to the economic dimensions of a certain territory, in this case the abandoned and polluted brownfields where slums emerge. Since the 1970s and 1980s a lot of public money has been spent on the rebuilding and revitalization of the slums in many cities of Western Europe and the USA. The UK surveys of Doick et.al. (2009) point out the main characteristics of investments in the brownfields and the logical model introduced to help measure the success of revitalization.

Revitalization and Investments in the brownfields

One of the main important instruments regarding rehabilitation and revitalization of the polluted territories are the investments in the brownfields. Brownfields are those territories that were previously used for industrial or military purposes, and even rail-way and at the present are abandoned or underutilized struggling with real or supposed problems of pollution. They can be found mainly in city centers and there is a huge need for intervention to achieve effective reutilization (Barta, 2003). Underutilization in this sense means that a territory is used with less efficiency than its environment would enable. Environmental pollution (either real or supposed) hinders economic expansion or the reutilization of real estates (Alvarez, 2001). Subsequently the territory loses its population retention capacity since destruction of workplaces is continuous. Barta (2003) suggests that the biggest disadvantages of these territories, besides soil pollution, are the disorder of ownerships, the general speculations with building sites and real estates and the low prices in the real estate market. Those who did not escape in the right time are unable to sell their buildings and, due to decreasing number of workplaces, cannot maintain their environment. By selling buildings under their real values social strata appear that represent worse market positions.[5] In addition, it is not the person responsible for the environmental pollution is who caused it but the new owner is to compensate after having discovered it. In many cases the new owner is the local government that cannot cope with these problems. Territories were sold under their current price to "venture businesses" which deepened the crisis during the past years hindering the process of revitalization with disordered ownership.[6] We wish to emphasize that our survey mainly focuses on the weak human resources due to missing environmental revitalization and aims to put an end to the problem of slums. In the area of the brownfields the neglected population with eroded and weak labour market position is attractive neither to the higher social stratus nor to home industries and foreign capital.

[5] The lower social status, lack of qualifications, worse health and the tendency to crime are meant.

[6] The rehabilitation of the brownfields: according to surveys in 2006, 58% of the brownfields are in private hands and 26% belongs to the local authorities in the North Hungarian region.

2. Findings

Model Planning: Evaluating Economic, Environmental and Sociological Viewpoints

By the concept of rehabilitation Czifra and Kukely (2003) mean mainly the recycling of environmental factors while others connect it with the concept of sustainable development.

Our opinion is that the definition should be interpreted in a wider spectrum and should be used for social processes as well. It is characteristic to our immediate environment that social erosion starts in those areas which are not involved in industrial production. All these result in the migration of population causing enormous economic and social problems. The task of the economic policy is ensuring productive and competitive human resources based on the migration strategy of attraction, support and protection (Dabasi-Halász, 2009) through revitalization[7].

Environmental recultivation after the changing of the political system has stopped due to the economic crisis of the 21st century, the number of territories having been withdrawn from industrial production has risen and investments in the brownfields have come to a standstill. In parallel with the decline in industrial production environmental pollution caused by the factories (now closed) of the brownfields ceased or reduced. Environmental problems were not generated by the new production, functions that appeared on a certain territory. The inherited environmental damages are more tragic, especially soil pollution concerning environmental protection and city planning. Bad reputation remains even after eliminating environmental damages unless appropriate recycling facilities are ensured during the rehabilitation of territories. Revitalization is defined as "revival" or "recalling" and it is extended to social and environmental viewpoints regarding the recycling of a certain industrial area. It is meant as a complex definition namely as the restoration of environment, finding new economic functions and increasing the presence of human resources in the labour market. In our first model those factors are highlighted that can affect the necessity and success of the revitalization of a certain territory. Concerning productivity concrete factors can support the success of projects. For example, the migration of qualified workforce (its migration potential) among young people with higher education qualifications can be high if they are unable to find adequate jobs at certain fields. The costs of education are passed on to local governments and migration in this sense means a loss. Besides population decline maintaining the present school structures in long term can increase the expenses of local authorities. The process of migration can lead to a fall in demography, consumption and to the transformation of consumption structure. The first step of building a more attractive business environment is the elimination of environmental damages afterwards the territory is to enter the economic life more effectively. While surveying the characteristics of "the rust belts" in Budapest Hakszer et al. (2003) examined the sizes of companies. Adequate business environment is possible to erode easily so appropriate volume can influence the economic success of revitalization. The necessity and success of revitalization are affected by employment. Unemployment, the number of those receiving allowances and low employment rate are the causes and

[7] On the other hand, it is circular or the task of the strategy is to establish circular migration. Implementing facilities that support people involved in education or work abroad to return home. All these mean aiding research and carrier trips that aim to highlight returning (Dabasi, 2009).

consequences of the missing revitalization. It becomes urgent to start the process of revitalization since low employment and high unemployment rates pass enormous costs onto the society, local governments and the state.

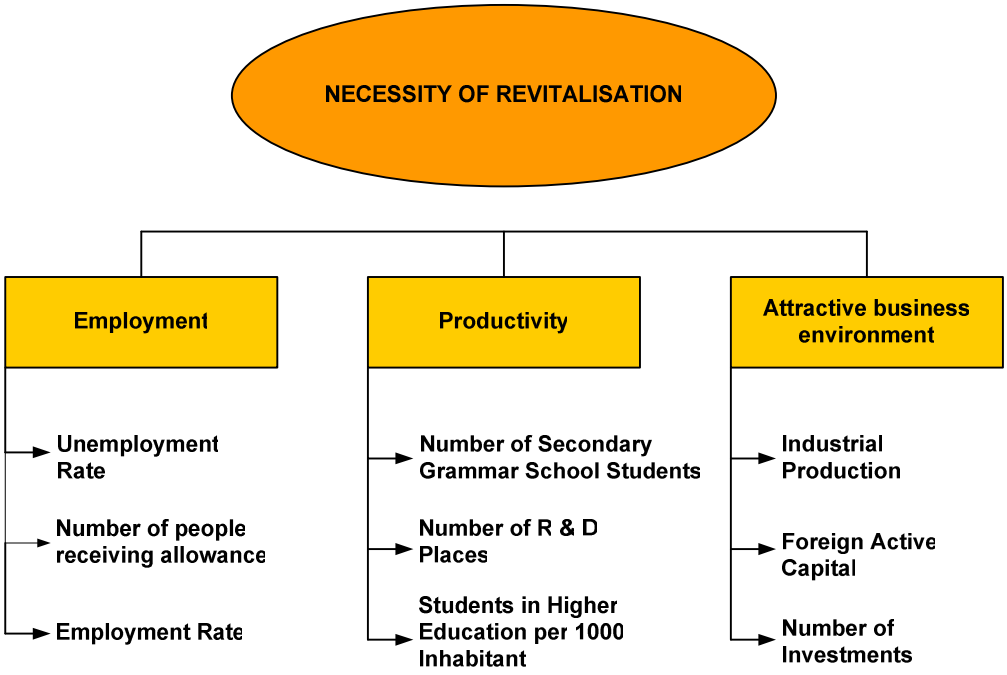

Figure 1: The indicators of complex revitalization
Source: Own compilation

The theory of "broken windows" by Wilson and Kelling (1982) deals with the connection between the destruction of built environment and the relation to the social order of those living there. According to their theory the accumulation of graffities and waste materials and crumbling buildings that need to be rebuilt make people feel sensitive and refuse participation in the preservation of social order. With the absence of recultivation the process of an ascending spiral leads to further migration, increasing unemployment and non-conform, deviant behavior. Revitalization becomes more difficult without the involvement of people living there; the process can easily be unsuccessful. It is vital to plan a cost and profit analysis[8] during social transitions placing participation in the foreground. Bielcka–Król–Korczak (2010) emphasizes the involvement and support of local population during revitalization. Factors were analyzed in five groups about the revitalization of "rust belts" during their static surveys. According to their viewpoint, the percent of social integration and the closeness of buildings are in relation with the space of territories having been separated from social factors. Environmental factors were separated from hydro geological or technical factors. In their analysis, concrete economic factors were not

[8] The amount of allowance in Borsod County in 2008 (14,1 billion HUF) was almost identical with similar costs of the whole Transdanubian region (14,8 billion HUF).

defined. The rate of unemployment, number of businesses and the presence of traditional industrial activities characteristic of the area were counted as social factors. Revitalization is to be supported by position, embeddedness into city structures and accessibility. The aims of changes are that the investors and decision makers should agree with each other in the long term concerning utilization interests. The emergence of a more attractive and ordered environment, the decreasing rate of unemployment or increasing productivity are those factors that can start the revival and revitalization of a territory. Doick et al. (2009) also emphasize in their model of revitalization the importance of economic, social and environmental factors. In the spotlight of the model of revitalization are not the factors of economic utilization but the sustainable criteria of areas regarding cityscape. Before having published their model they examined the "greening" of six UK industrial sites in more detail. As an outcome of the "greening" projects they identified those social changes that referred to areas used for social unitization. Furthermore, the growth in volunteering and the appearance of social occasions, events on the revitalized areas were also surveyed. The authors concerned the final results of the process according to economic, social and environmental guidelines as the following table shows:

Table 1

The result of "the greening" of urban areas

Social	Environmental	Economic
Decreasing number of crimes	Natural environment	Spillover effects on the neighboring areas
Society with sense of belonging	Increasing biodiversity	Increase in the utilization of flats
Social relations	Useful plants	Growth in the prices of real estates
Positive attitude		Growth in tax-paying citizens
Aesthetic values		
Reintegrated area		

Source: Own work with reference to K. J. Doick et al. (2009) work

Due to the absence of revitalization while surveying the labour market position of an area one receives a rather negative picture. Even for this reason it is important that cities have strategies of rehabilitation relating to the current "rust belts" in order to avoid the emergence of "slums" in certain territories. At the University of Miskolc, Department of Human Resources a model was planned in 2010 on social erosion, the factors of revitalization as a consequence of decline in economic environment and the indicators of the new growth path.

Decrease in economic activity come from the supplier system and lower consumption. Economic researches prove that people's satisfaction with their relationships, social integration, and the subjective sense of happiness became important economic pulling factors. That is the reason why social capital is highlighted in our model. In those fields where high percentage of participants of the labour market was characterized by unem-

ployment trust in the society decreased. Mental and financial factors of unemployment were projected to the economy having questioned a person's memberships to communities and long-term plans for the future (Skrabski–Kopp).

Table 2

The economic and social model of revitalization

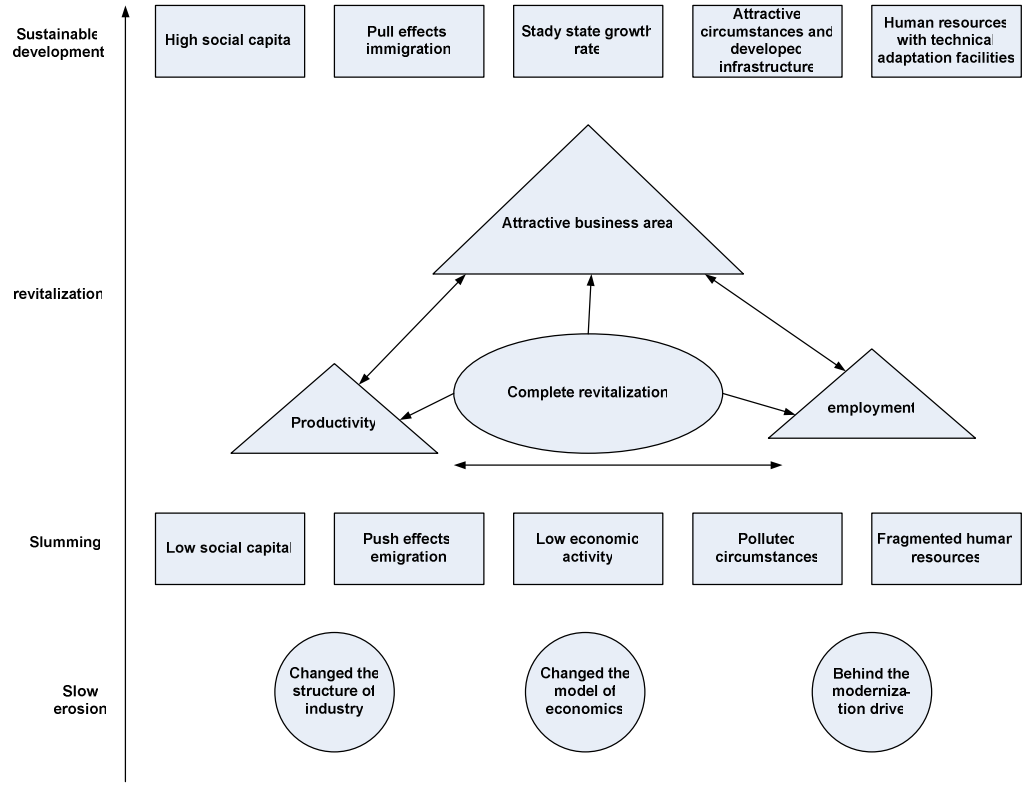

Source: Tóth, Dabasi-Halász and Hegyi-Kéri, 2010.

Special controlling instruments of economic policy and environmental protection have not been realized in the areas of "rust belts". Subsequently the problem of revitalization remained unsolved. Due to the absence of these processes part of the population belonging to the primary labour market choose migration. As a result of decline in economic activity, the labour market potential and economic structure of a settlement changes. In the course of time, the owners of flats change ("filtration") and poorer strata move to certain areas, the components of a given labour market change, the secondary segment becomes dominant. Consequently a special circular migration emerges in the brownfields meaning human resources with lower and lower qualifications. After the migration of the qualified strata intervention for the economic policy becomes more expensive and pressure increases on the

labour market of the territory. At the same time the social situation of those remaining there becomes worse, human potential decreases as a consequence and foreign investment tends to avoid these areas. In the above mentioned model, we intend to stress the revitalization of human resources. If social factors are neglected during revitalization, it can hinder the strengthening of the primary segment of labour market, the successful production of companies working in the area or can decrease the number of investments. In the model of Bielecka–Król Korczak (2010) the building and utilization of social places have leading roles. On the contrary, in our model these two factors are given since they have been present in the lives of industrial sites for several decades and helped the emergence of social cohesion, relations and social capital. These factors were reluctant to change (were partly destroyed) but are still present in the examined fields. Remedy and rehabilitation are to be extended not only to the territories but also to the revitalization of people living there.

3. Conclusions

In spite of the fact that the literature emphasizes the importance of revitalization investments in the brownfields, Miskolc invested only 5 million euro in developing an appropriate industrial infrastructure of a "green field" (0, 36 km^2/36 ha). On the other hand, the revitalization and rehabilitation of an industrial site with 2, 45 km^2 (245 ha) in the brownfield have not yet started. The former industrial site is characterized by a decreasing economic and social infrastructure worsening the situation of "slumming" territories. In the city there is population decline and migration seems to be incontrollable. The University of Miskolc, as one of the largest rural campuses, appears to fight against migration and "brain drain" without success. Medical centers in the city meet a gap, shortfall in doctors and specialist. The secondary segment of the labour market of the city strengthens. In primary schools teachers' dismissal have begun. In our opinion revitalization and its human factors should receive more roles in the region.

"Acknowledgement:This work was carried out as part of the TÁMOP−4.2.1.B−10/2/KONV−2010−0001 project in the framework of the New Hungarian Development Plan. The realization of this project is supported by the European Union, co‐financed by the European Social Fund."

REFERENCES

[1] Alvarez, K.: *A barnamezők és rozsdaövezetek gazdasági újjáélesztési programja az Egyesült Államokban.* In: Éri Vilma (szerk.) *Terjeszkedés vagy ésszerű városfejlődés?* Budapest, Környezettudományi Központ, 2001, 75–79.

[2] Barta, Gy.–Lőcsei, H.: *Vállalatok Budapest barnaövezetében*. Területi Statisztika, 2003.

[3] Barta, Gy. (szerk.): *Gazdasági átalakulás Budapest barnaövezetében. Tanulmány a Fővárosi Önkormányzat megbízásából*. Budapest, MTA RKK, 2002b.

[4] Barta, Gy.: *Rehabilitációs megoldások az európai nagyvárosok rozsdaövezetében*. MTA RKK KÉTI BO Tanulmány (Survey). December, 2003.

[5] Barta, Gy.: *A magyar ipar területi folyamatai 1945–2000.* Budapest–Pécs: Dialóg, Campus Press, 2002.

[6] Czira, T.–Kukely, Gy.: *Az átalakuló iparú térségek környezeti konfliktusainak fenntarthatósági értékelése Északkelet-Magyarországon.* Környezetállapot értékelés Program Pályázati tanulmányok, 2003–2004.

[7] De Sousa, C.: *Brownfields Redevelopment and the Quest for Sustainability.* London: Elsevier Science/Emerald Group Publishing, Current Issues in Urban and Regional Studies Series, Volume 3. 2008.
[8] Dobák, J.: *Miskolc ipari társadalmának kialakulása a befogadó települések tükrében.* 2007.
[9] Erő, Z.: *A városmegújítás lehetőségei*. http://bfl.archivportal.hu/id-364-ero_zoltan_varosmegujitas_lehetosegei.html 2009.
[10] Fazekas, K.: *A külföldi működő tőke-beáramlás hatása a munkaerőpiac regionális különbségeire Magyarországon.* Budapesti Munkagazdaságtani Füzetek, 2000/5.
[11] *Integrált Városfejlesztési Stratégia Miskolc Antiszegregációs Terv* – www.miskolc.hu (12/03/2010)
[12] Doick, K. J.–Sellers, G.–Castan-Broto, V.–Silverthorne, T.: *Understanding Success in the Context of Brownfield "Greening" Projects: The Requirement for Outcome Evaluation in Urban Green Space Success Assessment*. 2009.
[13] Lévesque, C.–Murray, G.: *Understanding Union Power: Resources and Capabilities for Renewing Union Capacity.* European Review of Labour and Research, 2010, 16, 333.
[14] Marzena, B.–Król-Korczakb, J.: *Hybrid Expert Ssystem Aiding Design of Post-Mining Region Restoration*. Ecological Engineering, 2010, 1232–1241.
[15] Papp, Gy.–Kőrösi, V.–Gyöngyössy, Sz.–Búzásné, J. V.–Dernei, B.: *Barnamezős területek rehabilitációja Észak-Magyarországon.* REVITAE, Bay Zoltán Alkalmazott Kutatási Közalapítvány, 2006.
[16] R. Nagy, J.: „*Nekünk má' semmise a gyár…*" *Identitásbeli azonosságok és különbségek a rudabányai és a diósgyőr-vasgyári munkások esetében*. 2000.
[17] Skabski, Á.–Kopp, M.: *A bizalom, mint a társadalmi tőke központi jellemzője*. 2007.
[18] Tóthné Szita, K.–Dabasi Halász, Zs.–Hegyi-Kéri, Á.: *Воздействие на рынок труда ревитализации деятельности, регенерации старых промышленных зон (brownfield) „Caffé-lette" The Effects of the Brown Field Investment to the Labour Market*. VESZTNYIK, Harkiv. (To be published)
[19] Wirth, L.: *The Ghetto*. New Brunswick, NJ, 1928.

Geosciences and Engineering, Vol. 1, No. 1 (2012), pp. 103–111.

ANALYSIS OF PRECIPITATION GROUPS AND RELATED WATER LEVEL PEAK TIMES IN THE BÜKK MOUNTAINS

ENIKŐ DARABOS
Department of Hydrogeology and Engineering Geology, University of Miskolc
3515 Miskolc-Egyetemváros, Hungary
daraboseniko@gmail.com

Abstract
Within the frame of Bükk Mountains Karst Water Monitoring System currently 34 different monitoring wells and springs are metered continuously with DATAQUA type metering and data collecting appliances. The analysis of data is currently an ongoing task. Earlier definition of effective precipitation groups had to be rephrased: the total of separate daily precipitations that can be treated as one with regards to their effect, and which reverse the decreasing water level with 5 to 10%, depending of measurement location. The effective precipitation groups between 1993 and 2006 occurring at the measurement sites I studied and their average values calculated by above definition.

The peak periods, meaning the time period passing between the water level decrease reversing with 5 to 10% and reaching local water level maximum was determined for each measurement sites as well. It also can be stated that water levels at all measurement sites react to precipitation within 1 day, but the length of time until the peak level differs for each.

The relationship between the measurement sites was also determined. These are important because by using the correlation of the data series, missing data can be calculated. There is a high correlation between the water level recording sites, in certain cases as high as 0.8 to 0.9, but there are some sites where the correlation is below 0.4. But the lower values of correlation characterize measuring points which are in significant distance from each other.

1. Introduction

The examination of data recorded with the Bükk Karst Water Monitoring System has been going on for a long time. The first karst water monitoring devices were installed in 1992. Today continuous monitoring is taking place at 34 locations in wells monitoring wells, and boreholes, using electric DATAQUA measuring and recording devices. Recordings are taken at 15 to 30 minutes intervals in water production facilities and springs, and at 15 to 60 minutes in monitoring boreholes [3]. In the course of my examinations I worked with daily precipitation data and karst water level data.

For precipitation data, I mostly used recordings of the precipitation measuring weather station at Jávorkút, situated 690 m above Baltic sea level (from now on: aBS). For my purposes also Felsőhámor (257 aBS), Ómassa (495 aBS). In the course of my work I used daily precipitation and karst water level data. ÉKÖVIZIG allowed me to have their data recorded at Bánkút (855 aBS), Rejtek (545) and Bélapátfalva (318 aBS).

2. Materials and Methods

2.1. Effective precipitation groups

During my analysis I found that at some measurement sites the water level does not respond to each precipitation event. The water levels recorded in Nv-17 are shown together with the Jávorkút precipitation data in *Figure 1*. It is clearly apparent that there are occasions when the water level does not react to precipitation, either when its value is very small, or it falls in a certain period (for example in the time of a strong decrease). There are also precipitation events that fall right next to each other so that their effect is additive. These grouped events should be treated as one precipitation.

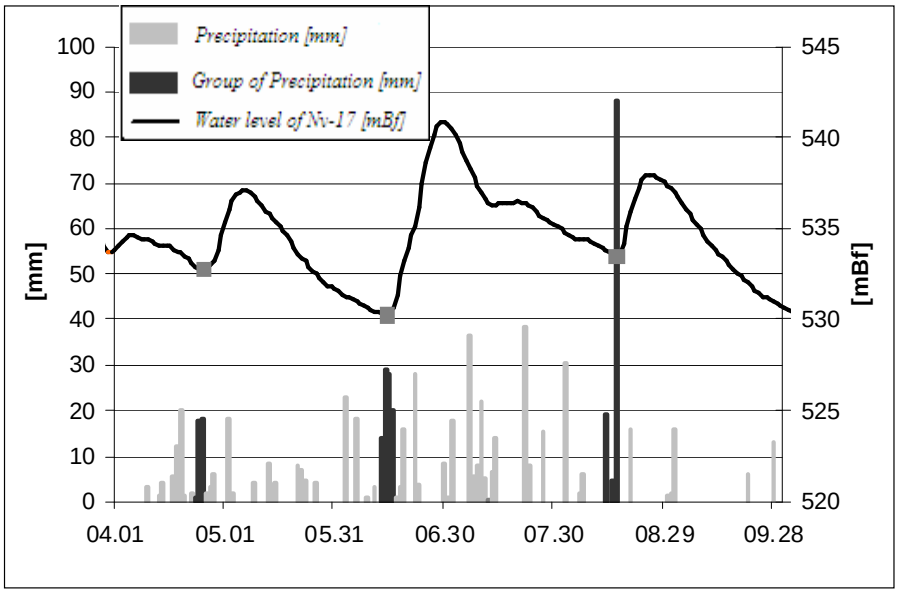

Figure 1: Nv-17 water level and Jávorkút precipitation data in the hydrological summer season of 1999

As a result of these, two new definitions must be added to the analysis:

1. 'Precipitation group': the total amount of precipitation falling in multiple events in one day that can be treated as one with regards to its effect on water levels at the monitoring stations.
2. 'Effective precipitation, or precipitation group': volumes of precipitation that are large enough to effect the water level; reversing water level decline (recession) with at least 5 to 10% of the amount of the difference between the highest and lowest water level recorded in the examined interval. In the course of my work I have determined this amount for each measuring site.

2.2. Time of peak periods

At the different measurement sites the number of precipitation events included in one group depends upon the number of days elapsed between the time of the precipitation and the steepest increase in water level.

2.2.1. Nv-17 water level monitoring well.

First I examined what is the amount of precipitation that can reverse a declining water level here. This value depends on many factors, for example how long has it been decreasing, and how great is the decrease. *Table 2* shows occasions between 1996 and 1998 in the case of Nv-17 when the water clearly began increasing after a recession period. At Nv-17 the reverse means that the water level increases with at least 10% of the greatest fluctuation of the considered period. The columns of the table cite the date of the measurement, the amount of precipitation for each member of the precipitation group that caused the reversing effect, the summary of these values (the size of the precipitation group), and the trend. The trend gives us the average value of the water level decline in $^{m}/_{day}$ for a six day period. Basically it means how steeply the curve is decreasing:

$$Tendency = \frac{\frac{s_1 + s_2 + s_3}{3} - \frac{s_4 + s_5 + s_6}{3}}{3} \quad (1)$$

s_1: first day of precipitation, s_2: second day of precipitation etc. [1].

The reason for selecting the six-day period is the length of time it took the water level to change; change follows (lags) the precipitation by a certain amount of time. It is suggested by the timing of the peak water level, which will be evaluated later in detail, that this interval can be as much as 16 days in length.

For the Nv-17 measurement site it appears that the greater is the precipitation group, the longer is the time lag to the peak. In the period between 1996 and 2006 it never exceeded 13 days in case of precipitation groups under 100 mm. Above 100 mm it was maximum 16 days.

The average precipitation input (single event or group) in the data set is 67.8 mm. There are also a few very low and very high values – below 12 and above 190 mm. These outliers can skew statistical results, so it is better to apply cut-off α averages, meaning we will not take the top and bottom 10% into consideration [6]. The average amount we end up with is 65.1 mm. Thus we can conclude that, in the case of Nv-17, an average of 65 mm precipitation is necessary to reverse the water level from a decrease to an increase). The duration of grouped precipitation events ranged from 1 to 4 days, but sometimes there were more individual events within the group.

The peak period arrives between 3 and 16 days after the precipitation, (10 days on average), but if we exclude precipitation exceeding 70 mm, it is 8 days. On average we can state that there is a longer time lag until the peak if either the precipitation is greater, or the starting water level is higher. This is due to the conclusion reached in an earlier paper stating that there is a maximum infiltration speed, and maximum water level increase speed. This is 1.67 $^{m}/_{day}$ in the case of the Nv-17 [1].

Figure 2 plots the time lag to peak period against and size (volume) of the precipitation groups; a logarithmic trend curve is displayed. The data become denser in the interval between 70 and 120 mm precipitation, and 10 and 12 days time lag.

2.2.2. Total of 5 measurement sites shown together.

Above, we determined the effective precipitation groups. Displaying these values together in Table 1 yields interesting results: descending towards Baltic Sea level with the locations of the measurement sites, the total volumes of precipitation necessary to form effective precipitation groups becomes less, and the average water levels decrease except in the Garadna spring. The time lag to the peak periods is plotted for all measurement sites in *Figure 3.*

2.3. The relationships between the water levels measured at the sites.

The relationship between the measurement sites is important because, based on the correlation of the data series, missing data can be complemented by the use of cross regression [5].

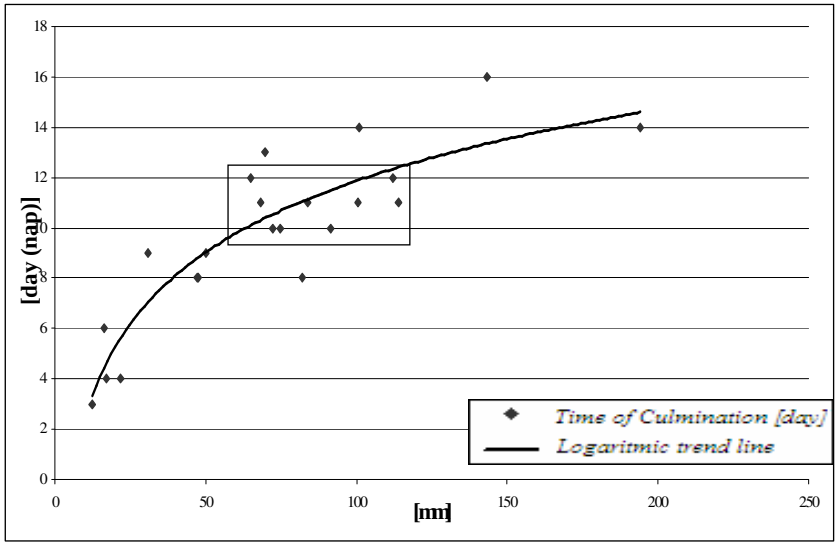

Figure 2: The precipitation groups and the peak period of Nv-17 station marked with points where there was at least 10% reverse of water level, with the logarithmic trend curve for 1993–2006 fitted

In order to show the relationships between the measurement sites I calculated the correlations. During this process all measurement sites were compared with each other between 2001 and 2006. Correlation coefficient values of water levels at measurement sites are shown in *Table 3.* After comparing the curves it can be shown that not only are there significant relationship but it seems that all of the measurement sites react to precipitation

within one day, regardless of the timelag to the peak period which differs for each site. As an example let us compare site Nv-17 with the Garadna spring. In Figure 4 the water level values are shown in percentage. Water level increase starts immediately at both locations but it differs in how long it lasts. Peak values are reached on average after10 days in the case of Nv-17, but only 2 days in the case of Garadna Spring.

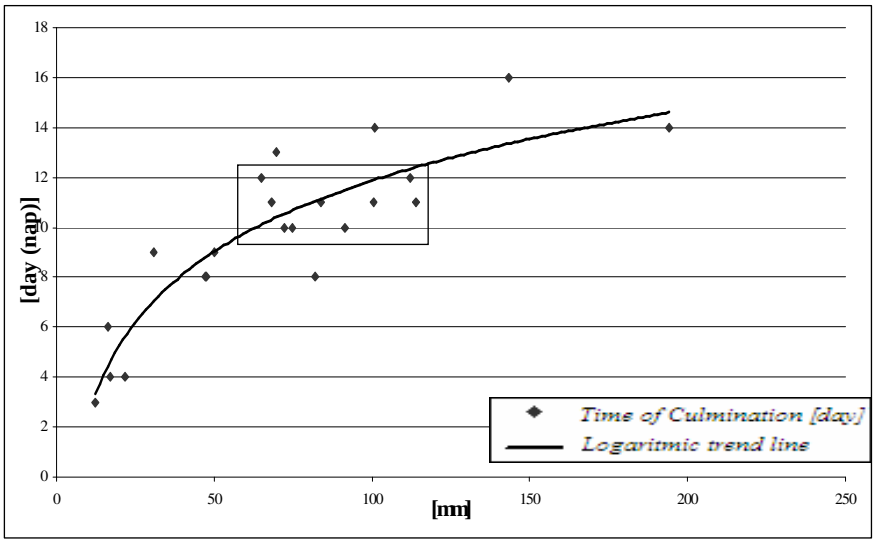

Figure 2: The precipitation groups and the peak period of Nv-17 station marked with points where there was at least 10% reverse of water level, with the logarithmic trend curve for 1993–2006 fitted

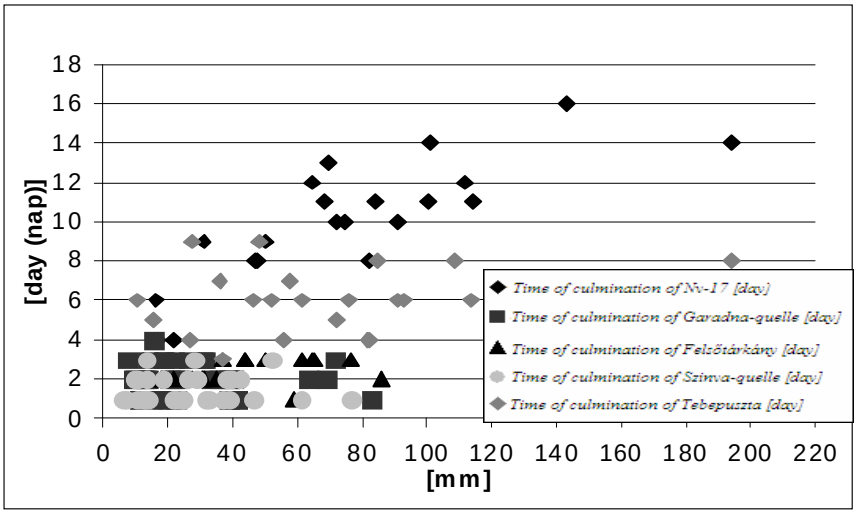

Figure 3: The peak periods determined for the measurement sites evaluated

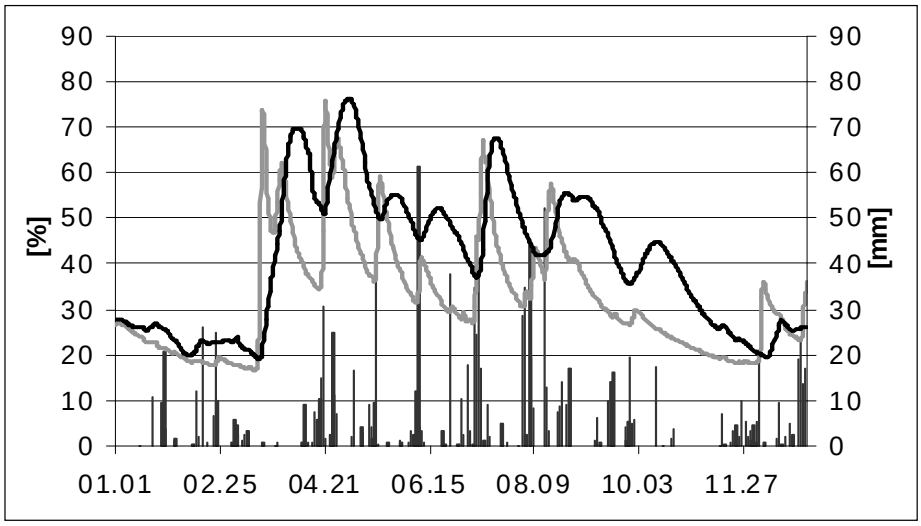

Figure 4: Water level fluctuation in percentage
(Minimum and maximum of available data considered as 0% and 100%)
at the Garadna spring and Nv-17 measurement sites (2005)

3. Results

My aim was to determine the precipitation groups of the examined interval and to define the effective precipitation group. Earlier the definition of effective precipitation group was the following: "Effective precipitation groups are the totals of daily precipitation that is falling for days, sometimes with 1 or 2 days of interruption, significantly effect the karst water level, and the total value is close to, or exceeds 50 mm" [2]. This definition had to be rephrased. The new, more exact definition is: effective precipitation groups are the total of separate daily precipitations that can be treated as one with regards to their effect, and which reverse the decreasing water level with 5 to 10%, depending of measurement location. The size and the average size of effective precipitation groups of examined measurement sites between 1993 and 2006 were determined. For the Nv-17 measurement site the average of the precipitation totals is 67.8 mm. There are also a few very low and very high values, below 12 and above 190 mm. These can deform our results, so it is better to form cut-off α averages, meaning we will not take the top and bottom 10% into consideration. The average amount we end up with is 65.1 mm. So we can conclude that in the case of the Nv-17, an average of 65 mm precipitation is necessary to achieve the reverse effect (changing the water level from decrease to increase). The precipitation groups consist of precipitation falling within the period of 1 to 4 days, but sometimes there are more members to the group.

For further measuring sites the cut-off α averages are:

Garadna Spring	36,95 mm
Szinva Spring	36,99 mm
Tebepuszta	54,6 mm
Felsőtárkány	24 mm

Showing these values together in Table 1 brings interesting results: moving downward above Baltic Sea level with the locations of the measurement sites, the precipitation total necessary to form effective precipitation groups becomes less. I have not yet found an accurate explanation of this connection.

The peak periods, meaning the time period passing between the water level decrease reversing with 5 to 10% and reaching local water level maximum was determined for each measurement sites as well. The peak periods of the given measurement sites are shown in one diagram. *Figure 3* shows that values of a measurement site are forming groups on a specific precipitation size and peak time interval. The longest peak periods and greatest precipitations represent Nv-17. The data of the Tebepuszta measurement site is smaller than the Nv-17 data, but it is still in the range of greater peak periods and greater precipitations. The Garadna Spring and Felsőtárkány data are all falling into the range of precipitation less than 90 mm, and 4 day peak periods. The data of the Szinva spring represent less than 80 mm precipitation and 3 day peak time. The relationship between the measurement sites was also determined. These are important because, by using the correlation of the data series, missing data can be calculated. There is a high correlation between the water level recording sites, in certain cases as high as 0.8 to 0.9, but there are some sites where the correlation is below 0.4. These are usually in quite a distance from each other.

In order to show the relationship of the water level of different measurement sites I calculated correlation. During this process all measurement sites were compared with each other between 2001 and 2006. Correlation values of the measurement sites are shown in *Table 3*. These are important because by using the correlation of the data series, missing data can be calculated [4].

After comparing the curves it can be shown that not only are there significant relationships but it seems that all of the measurement sites react to precipitation within one day, regardless of the time lag to the peak period which differs for each site.

Table 1

Effective precipitation groups in the case of measurement sites studied

Measurement site	**Average [mm]**	**α cut-off average [mm]**	**Average depth of water level [m]**
Nv-17 (779.90 aBS)	68	65	249,66
Tebepuszta (498,97 aBS)	60	55	163,38
Garadna Spring (497 aBS)	39	37	0,98
Szinva Spring (346,2 aBS)	39	37	5,72
Felsőtárkány (241aBS)	28	24	4,77

Table 2

Precipitation groups detected in the case of Nv-17 (1996–1998)

Date	Precipitation [mm]	Precipitation total [mm]	Water level [aBS]	Tendency	Peak period [days]
1996.05.07	13,5		532,49		
1996.05.08	1,5	15	532,44	–0,1019	4
1996.08.19	3,4		527,64		
1996.08.20	9,1	12,5	527,74	–0,0088	3
1997.06.05	6,5		529,06		
1997.06.06	15		529,01		
1997.06.07	48	69,5	528,98	–0,0752	13
1997.07.18	9,5		530,42		
1997.07.19	5,8	15,3	530,49	–0,0359	6
1998.04.14	17		527,95		
1998.04.15			527,83		
1998.04.16		17	527,75	–0,0702	4
1998.05.16	1,6		532,60		
1998.05.17	15,6		532,59		
1998.05.18	46,5		532,53		
1998.05.19	36,8	100,5	532,56	0,0218	11
1998.07.24	1,6		528,47		
1998.07.25	16		528,41		
1998.07.26	27,4		528,38		
1998.07.27	13	58	528,35	–0,0506	8

Table 3

Correlation coefficient values of the water levels of measurement site pairs

Measurement site 1	Measurement site 2	Value of correlation
Garadna Spring	Nv-17	0,85
Garadna Spring	Szinva Spring	0,81
Garadna Spring	Tebepuszta	0,36
Garadna Spring	Felsőtárkány	0,42
Nv-17	Felsőtárkány	0,45
Nv-17	Tebepuszta	0,68
Szinva Spring	Tebepuszta	0,37
Szinva Spring	Nv-17	0,67
Szinva Spring	Felsőtárkány	0,34
Tebepuszta	Felsőtárkány	0,91

4. Summary

The most important quantitative monitoring system is the Bükk Karst Water Level Observing System which is run by Institute of Hydrogeology and Engineering Geology of University of Miskolc. Installation of the first detectors was in 1992, which was initiated by the karst water using water companies. The goal of this endeavour was to know the quantitative parameters of karst water and to help the planning of water-supply in Miskolc and in the region of Miskolc. Reason of this enterprise was the extreme drought and rainfall because they caused problems in service in the previous years (between 1945 and 1992).

Determination of amount of effective precipitation groups is important because the lower precipitation groups from aspect of water-supply are irrelevant. For investigations the five most relevant monitoring well were chosen from region of Bükk Mountains. In this paper the peak period, the conception and volume of effective precipitation groups and correlation of water level in observing points were determined.

"Acknowledgement: This work was carried out as part of the TÁMOP−4.2.1.B−10/2/KONV−2010−0001 project in the framework of the New Hungarian Development Plan. The realization of this project is supported by the European Union, co‐financed by the European Social Fund."

REFERENCES

[1] Darabos, E.–Lénárt, L.: *Csapadék és karsztvízszintek összefüggéseinek vizsgálata a 2006. évi bükki karsztárvíz elemzése során*. XIII. Karsztfejlődés, Szombathely, 2008.

[2] Lénárt, L.: *Some aspects of the „3E's" (Economics-Environment Ethics) model for sustainable water usage int he transboundary Slovak and Aggtelek karst region based on some examples from the Bükk Mountains*. (PhD Thesis Work), Kassa, 2005.

[3] Lénárt, L.: *A karsztvízszint csökkenésének jellemzői a Bükki Karsztvízszint Észlelő Rendszer 1992–2005 közötti adatai alapján.* Táj, környezet és társadalom. Ünnepi tanulmányok Keveiné Bárány Ilona professzor asszony tiszteletére. Szeged, 2006, 425–434.

[4] Lénárt, L.: *Karsztvízszint előrejelzés a Bükk hegységben*. MicroCAD, B szekció, Vízgazdálkodás és környezetvédelem, március 22–23. Miskolc, 2007, 65–70.

[5] Németh, Á.: *A Bükki Karsztvízszint Észlelő Rendszer hiányzó mérési adatainak pótlása, a pontosított adatsorok alapján előrejelzések kidolgozása*. Miskolci Egyetem, Műszaki Földtudományi Kar, Környezetgazdálkodási Intézet, Hidrogeológiai-Mérnökgeológiai Intézeti Tanszék, Diplomamunka, 2008.

[6] Szűcs, P.–Madarász, T.: *Adatfeldolgozás, adatértékelés* (Miskolci Egyetem. Hidrogeológiai-Mérnökgeológiai Intézeti Tanszék, http://www.hidrotanszek.hu/hallgato/Adatfeldolgozas.pdf 2005.

Geosciences and Engineering, Vol. 1, No. 1 (2012), pp. 113–119.

SOME REMARKS ON THE FAILURE CURVES OF ROCKS

ÁKOS DEBRECZENI
Institute of Mining and Geotechnical Engineering, University of Miskolc
3515 Miskolc-Egyetemváros, Hungary
bgtda@uni-miskolc.hu

Abstract
Hyperbolic failure curves of rocks applied and developed by the Institute of Mining and Geotechnical Engineering, University of Miskolc (Hungary) are presented in the paper. By using these curves and a so-called 'ME-method' developed in the Institute [5], good estimation can be obtained for the strength parameters of fractured rocks. One of the most important advantages of this method is that all of its elements are based on measured characteristics therefore it can be considered a good alternative to the widely used Hoek–Brown method.

1. Introduction

Some mechanical properties of rocks are similar to the ones of metals, others are quite different. Their mechanical behavior depends on the stress state and the magnitude of the load. Mechanical properties of the rocks can be studied only using sophisticated tests.

Significantly different mechanical properties can be observed for solid materials depending on the load if it is high enough and if it is close to the failure. Usual models of behavior of materials describe not only properties but mechanical condition of the material as well.

Idealized models of materials should be selected and adjusted to the characteristics of the rock and its properties must be determined by measurements to obtain accurate results. Mathematical and computational methods can provide acceptable results if the properties used for the model describe the behavior of the rock mass properly.

In situ characteristics of the rock must be taken into consideration consequently measurements should be always done on the site if possible. As in situ results are available to a limited extent, usually laboratory tests of rock samples are required. These are obtained in labs and are converted into the characteristics of the rock mass itself according to experiences and theoretical considerations as well and using conversion factors based on the comparison of in situ and laboratory test results.

In the beginning, the failure states of rocks were described according to the criteria applied for metals such as the Mohr, Murrel, Huber–Mises or Huber–Mises–Hencky criteria. Practice has testified that the Mohr limiting condition can well be applied to rocks. It is a disadvantage of the Mohr condition that it leaves the impact of the middle principal stress out of consideration but approximation occurs in favour of greater safety.

The Mohr limiting condition may be investigated with the application of several failure curves such as the Mohr-Coulomb yield line as well as parabolic and hyperbolic curves. The Hoek–Brown curve, now widely used to describe fractured rock bodies, is also based on the Mohr condition.

There also exist more generally formulated criteria like the Mogi, Drucker–Prager, Wiebols–Cook and Lade criteria. These more complex criteria are successfully applied in certain special fields. (For example, the Lade criterion is applied in the stability studies of boreholes.) In other cases however, despite their complexity, they are not more useful that the Mohr–Coulomb linear limiting condition. (For example, the Drucker–Prager criterion

overestimates the role of middle principal stress, which may lead to an approximation at the expense of safety.)

In this paper, hyperbolic failure curves applied in the Institute of Mining and Geotechnical Engineering at the University of Miskolc is presented. On the basis of these curves and the method (ME method) developed in the institute, the strength properties of cracked rock bodies can be estimated. (Abbreviation 'ME' comes from the initials of the Hungarian name of University of Miskolc.) The advantage of the method is that every element of the process is based on measurement results, and thus it is a realistic alternative to the Hoek–Brown method, widely applied nowadays.

2. General remarks on failure limiting conditions

Limiting conditions can mostly be expressed as a function of the invariants of the stress tensor or of the deviator tensor calculated from it. The reason for this is that while stress tensor elements depend on the position of the coordinate system, limiting conditions should be true independently from the chosen directions. The so called octahedral stresses, which are perpendicular (σ_{oct}) and parallel stresses (τ_{oct}) formed on the faces of an octahedral of a specific position (body diagonals are in the directions of the three principal stresses). On every face of the octahedral the absolute value of stress components is identical *(Figure 1).*

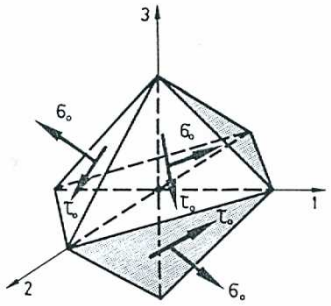

Figure 1: Octahedral stresses

Octahedral normal stress is:

$$\sigma_{oct} = \frac{1}{3} \cdot I_1 = \frac{\sigma_1 + \sigma_2 + \sigma_3}{3} \quad \text{and}$$

octahedral tangential stress is:

$$\tau_{oct} = \sqrt{\frac{2}{3} J_2} = \frac{1}{3} \sqrt{(\sigma_1 - \sigma_3)^2 + (\sigma_2 - \sigma_3)^2 + (\sigma_3 - \sigma_1)^2} \ ,$$

where:

I_1 – first invariant of stress tensor

$I_1 = \sigma_1 + \sigma_2 + \sigma_3$

J_2 – second invariant of deviator tensor

$$J_2 = \frac{1}{6}[(\sigma_1 - \sigma_2)^2 + (\sigma_2 - \sigma_3)^2 + (\sigma_3 - \sigma_1)^2]$$

σ_1 ; σ_2 ; σ_3 – principal stresses ($\sigma_1 \geq \sigma_2 \geq \sigma_3$)

Detailed discussion of limiting conditions and failure curves and surfaces based on them is not expedient in this paper, consequently the most important concepts are highlighted. The following figure *(Figure 2)* shows the measurement results for unconfined compression ($\sigma_1 > 0$; $\sigma_2 = \sigma_3 = 0$), biaxial ($\sigma_1 > 0$; $\sigma_2 > 0$; $\sigma_3 = 0$), conventional triaxial ($\sigma_1 > \sigma_2 = \sigma_3 > 0$) and polyaxial ($\sigma_1 \geq \sigma_2 \geq \sigma_3$) experiments.

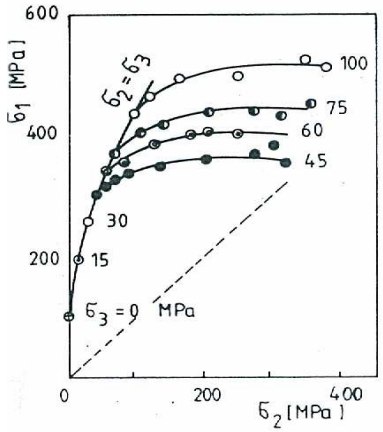

Figure 2: Measurement results for dolomite sample bodies [4]

The figure shows, that failure is not independent from middle principal stress (σ_2). Failure criteria based on the Mohr theory (leaving the impact of σ_2 out of consideration) is applicable only to a limited extent under general stress conditions.

In some cases a sufficiently accurate calculation of failure stresses requires the application of relatively complicated correlations. For example the modified Lade criterion is preferred in the description of the stress conditions formed around boreholes [1]:

$$\frac{[(\sigma_1 + S) + (\sigma_2 + S) + (\sigma_3 + S)]^3}{(\sigma_1 + S) \cdot (\sigma_2 + S) \cdot (\sigma_3 + S)} = 27 + \frac{4 \cdot (\mathrm{tg}^2\varphi) \cdot (9 - 7 \cdot \sin\varphi)}{1 - \sin\varphi},$$

where:

$$S = \frac{c}{\mathrm{tg}\varphi}$$

Obviously in the case of deep boreholes, both the support of borehole wall and the determination of the pressure necessary for rock fracturing requires enhanced circumspection and precise calculations. In such a case, it is not possible to counterbalance the inaccuracy of calculations by choosing high safety parameters.

However in the overwhelming majority of rock mechanics problems, it is unsuitable to use a complex criterion similar to the modified Lade criterion. The most important reason for this is that laboratory tests are performed on intact pieces of rock, the stress parameters of which are significantly better than those of the fractured rock body. Influence of the measure of the fracturing of the rock body and parameters of the cracks on the strength of the rock mass is several orders of magnitude larger than of the middle principal stress. Accordingly in practice it is most typical to use criteria based on the Mohr failure condition. (Let me remark here that due to the ignorance of the impact of σ_2, rock strength is underestimated, which works in the direction of higher safety in the case of cave stability studies.) Such criteria based on the Mohr failure condition are the Mohr–Coulomb yield line, parabolic and hyperbolic curves and the Hoek–Brown curve as well.

Hoek–Brown curves are widely used nowadays for the determination of characteristics of fractured rock masses. The curve in question was modified several times and was adjusted to evaluate in situ observations can be described as follows:

$$\sigma_1 = \sigma_3 + \sigma_c \cdot \sqrt{m \cdot \frac{\sigma_3}{\sigma_c} + s}$$

where *m* and *s* are functions of rock quality and rock structure GSI (Geological Strength Index).

For laboratory tests

$$\sigma_1 = \sigma_3 + \sigma_c \cdot \sqrt{m_i \cdot \frac{\sigma_3}{\sigma_c} + 1}$$

where m_i is a value between 5 and 35 describing intact rock mass.

In addition to its simplicity, such a widespread application of the Hoek–Brown limiting condition is due to the fact that the authors processed a large number of empirical data. However, when it is applied to a new site, the question always arises: to what extent a fundamentally empirical formula based on data from another site may be adopted for a site with different rock parameters.

As an alternative process, the method developed in the Institute of Mining and Geotechnical Engineering of the University of Miskolc (Hungary) is suitable to solve this problem. This method, the so called 'ME Method' was evaluated with professor Somosvári's leadership [5]. The basic idea of this method is the determination of a reduction coefficient based on the test results enabling the determination of the strength of the rock mass using laboratory test results.

3. A hyperbolic curve based on laboratory measurements and the 'ME Method'

It is a well-known fact that no linear curves may be applied in the whole range of stresses (compressive and tensile stresses). In the range of tensile stresses and small compressive stresses, failure may well be described with parabolic curves but such curves

yield no good approximation in the case of large compressive stresses. In this range the correlation between normal and shear stresses is much more linear. All this led to the idea that it is suitable to apply a hyperbolic failure curve across the whole range of stresses.

The main advantage of the process proposed in this paper is, that every element is supported by measurement results. Uniaxial tensile and compressive strength, furthermore conventional triaxial compressive strength at different confining pressures should be measured to obtain accurate results (no less than three or even more times each if possible). The average values of the measurement results obtained in this way are plotted on the σ–τ plane (Mohr plane). Then, according to the usual principles of function approximation, the hyperbolic failure curve, best accommodated to measurement results, is determined *(Figure 3).*

A failure curve based on more measurement results is more accurate. Each parameter of the rock is determined using several test results. Reliability can be increased by increasing the number of tests, although dispersion of the results basically depends on the inhomogeneous character of the rock and not on the accuracy of the measurements. Usual error of recent measuring devices is significantly (10–100 times) lower than the expectable standard deviation of the rock parameters. Consequently the rock itself can be characterized by the dispersion of the laboratory test results, if enough (more than 5) results are available.

It should not be forgotten however, that in laboratories probes formed from intact pieces of rock are examined. Therefore the hyperbolic curve thus constructed characterizes intact rock blocks instead of fractured rock bodies. The 'ME method' offers an opportunity to convert the strength parameters obtained in laboratory into parameters of fractured rock bodies.

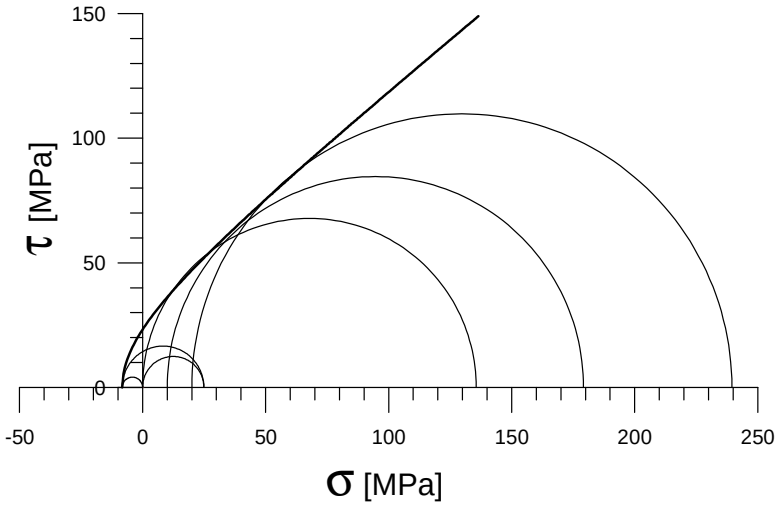

Figure 3: Hyperbolic curve best fitted to laboratory measurement results

If the ME Method is used, static rock parameters are determined by laboratory tests of the samples. *In situ* characteristics are estimated using a conversion factor from laboratory test results. The conversion coefficient in question (*R*) is the ratio of *in situ* dynamic elastic

modulus (E_s) determined by seismic method and of dynamic elastic modulus measured in lab (E_d)

$$R = \frac{E_s}{E_d}$$

Seismic elastic modulus can be determined by geophysical methods in boreholes and dynamic elastic modulus in laboratories by acoustic measurements. Using this reduction coefficient curve of failure based on laboratory tests can be converted to a one which can be used for fractured rock masses. An advantage of this method is that all of its elements are based on results obtained from measurements.

4. Conclusions

A method of determining the main strength characteristics of a rock mass, clearly based on results of tests was described in the paper. Hyperbolic type of failure curves of best fit were determined for numerous groups of rock samples in domestic rock mechanics research (e.g. low and medium activity nuclear waste disposal facility near Bátaapáti etc.), furthermore the so-called ME method was used as well. It was proved by results that the suggested method can complete other generally used methods, mostly application of Hoek–Brown failure curves.

"Acknowledgment: This work was carried out as part of the TÁMOP-4.2.1.B-10/2/KONV-2010-0001 project in the framework of the New Hungarian Development Plan. The realization of this project is supported by the European Union, co-financed by the European Social Fund."

List of Symbols

σ_1; σ_2; σ_3	principal stresses [MPa]
c	cohesion [MPa]
ϕ	internal friction angel [°]
σ_c	uniaxial compressive strength [MPa]
σ	normal stress [MPa]
τ	tangential (shear) stress [MPa]
σ_{oct}	octahedral normal stress [MPa]
τ_{oct}	octahedral tangential stress [MPa]
I_1	first invariant of stress tensor [MPa]
J_2	second invariant of deviator tensor [MPa^2]
R	conversion coefficient [–]
E_s	in situ dynamic elastic modulus [GPa]
E_d	dynamic elastic modulus measured in lab [GPa]
m , s , m_i	are functions of rock quality and rock structure [–]

REFERENCES

[1] Ewy, R. T.: *Wellbore-Stability Predictions by Use of a Modified Lade Criterion*. SPE Drill. & Completion, Vol. 14, No. 2, 1999.
[2] Hoek, E.–Brown, E. T.: *Practical Estimates of Rock Mass Modulus*. Int. J. Rock Mech Min. Sci, No. 43. 1997.
[3] Jaeger, J. C.–Cokk, N. G. W.: *Fundamentals of Rock Mechanics*. Blackwell Publishing Ltd., 2007.
[4] Somosvári, Zs.: *Geomechanika I.* Tankönyvkiadó, Budapest, 1987.
[5] Somosvári, Zs.–Debreczeni, Á.: *A repedezett kőzettest szilárdsági paramétereinek meghatározása és repedezett kőzetkörnyezetben nyitott vágatok utólagos megerősítésére irányuló kutatások a Miskolci Egyetem Bányászati és Geotechnikai Tanszékén*. Mérnökgeológia Kőzetmechanika 2006, Műegyetemi Kiadó, Budapest, 2006.

Geosciences and Engineering, V. 1, No. 1 (2012), pp. 121–127.

EVALUATION OF SEPARATION PROCESSES AND ITS PRACTICAL SIGNIFICANCE

IMRE GOMBKÖTŐ*–SÁNDOR NAGY**
Institute of Raw Material Preparationand Environmental Processing
H-3515 Miskolc-Egyetemváros, Hungary
*ejtimreg@uni-miskolc.hu
**ejtnagys@uni-miskolc.hu

Abstract
In Hungarian practice of waste processing, a relatively slight attention is paid to classic performance curves and to the recovery curves usually applied in mineral processing. The application of the related processing basic tests can cause a significant savings in choosing optimal size of equipment and a lower costs of those, furthermore in certain cases, the products with a higher added value may be produced, and the profit can be increased, besides the environmental utility. It helps significantly the sustainable development of the industry. These methods and the use of the application of those are presented in our study.

1. Conditions of effective separation

The separation processes are the principal processes in primary and secondary (wastes) raw material processing. During separation we utilize most simply one of the different physical, physical-chemical or chemical characteristics of the components to be separated. The physical (mechanical) processes are based mainly on the difference in physical properties, which are applied for coarse disperse mass flows, such as metal containing consumer wastes, demolition wastes, slag, municipal solid wastes, biomass.

Basically two conditions should be fulfilled in order to separate effectively each components of the raw material to be processed. One of the conditions is that the single component should stand apart from each other, i.e. should be liberated. In the intergrown state their separation is not possible by physical methods, hence the coalesced particles in the equipments, as a result of the forces effecting on them, get either into one or the other product, but always move together.

Liberation of components (getting liberated of each other) is carried out by physical application, comminution, which is a particle-size reducing physical procedure. For this reason the material is crushed or grinded to the size of the smallest component. The majority of the particles in the resulting crushed or grinded material will be composed of only one component (a chemically homogeneous material, some sort of mineral, iron, plastic etc.). To define in which range of particle-size the desired degree of liberation can be reached is determinative basically from planning and economic points of view.

Crushing and grinding of the particles to an unnecessary small size means significant and redundant costs and for this reason it is recommended to be avoided.

It is also a very important condition for separation processes, that there should be at least one property of the particles that sufficient difference can be measured. If there is such condition separation can be carried out using this particular property. In mechanical process engineering, density optical properties, magnetic and electrostatic properties, surface properties or geometrical mechanical properties are exploited for separation. If there is no such condition or there are very small differences between physical properties, mechanical separation cannot be done.

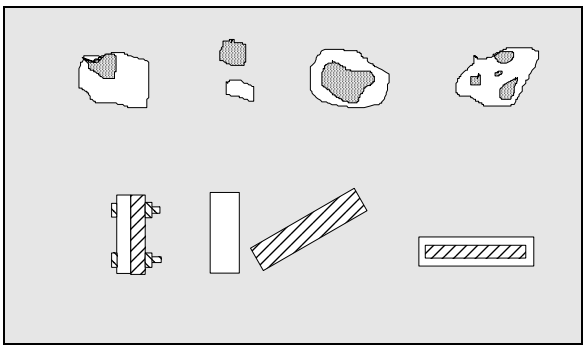

Figure 1: Examples for intergrown and liberated state in case of mineral and waste particles

The quality of separation at many types of equipment is also the function of the grain size range of feed (e.g.: air separator, eddy current separator etc.). Systematic examinations are necessary to determinate the particle size range which can be feed simultaneously on the given separator. During the experiments the behaviour of particles with different size and physical properties are determined at varying separator parameters.

2. Determination of quality of separation

During separation processes, our goal is to separate a mixture of A and B type components into A and B products, as pure as it is possible or as it is demanded. If A and B components is separated from each other at 100%, we are dealing with perfect separation. The possibility of such perfect separation is very low, though, because based on the working principle or construction method of the separation instrument, there are always A components in the B product and vice versa (for example: the air velocity in an air stream separator is technically zero among the wall). The case however even worse, because due to economic reasons A and B type components never reach 100% liberation, therefore A and B components are together in many particles at a distribution which deriving fault in separation. It is a question of consideration than, that liberation grade is what we want to increase at very high costs, or at optimum liberation level, only one component, A or B can be go tat pure form. In this case not only recovery rate, but yield of the component also has to be consider.

Determining the efficiency of a separation process, performance curve is generally used of which yield of fault particles in each product can be determined. For density separations, the performance curve can be determined by carrying out density analysis of the heavy and light products. In the case where mixture contains only two different type of components (“A” and “B” makes the determination of the performance curve impractical because performances “curves” become two spot which is hard to evaluate. Instead of the performance curves, the component recovery functions can be used to analyse the efficiency of the separation.

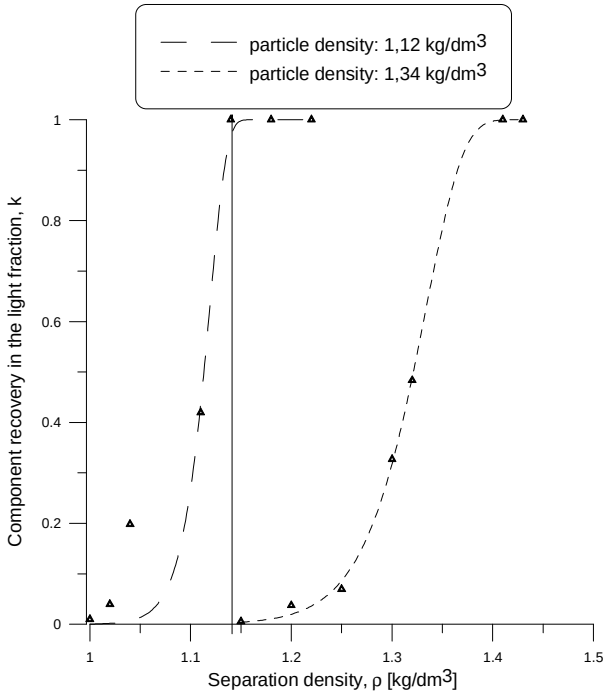

Figure 2: Example for recovery curve in case of A and B particles where good separation can be reach

3. Practical example of using recovery curves

Applicability of component recovery curves are going to be demonstrated by the authors using a laboratory vortex tube separator, but these type of curves can also used at many other waste separation equipment (e.g.: eddy current separator for shredder residues, air separator for demolition wastes, ...). Vortex tube separator is a cylindrical device where separation media feed into the instrument on the inner surface of the cylinder tangentially. At sufficient velocity of the media, it is flowing from one end of the cylinder to the other end while forming spire along the inner surface of the cylinder. There are circular gaps at both end of the cylinder at along the central line which through the processed solids are fed and a portion of a separation media is released out from the system. The other portion of the separation media is released in a tangential gap at the inner surface of the cylinder *(Figure 3.).* Operation principle of the vortex tube is simple. Solid particles of which has higher density than the separation media are forced to settle toward the cylinder due to high centrifugal force effecting. Light particles however are not able to settle down, therefore remaining at the air core along the central line. Particles are moving together with the media, therefore heavy particles are moving to the gap at the inner surface of the cylinder, while light particles are moving with the centre line gap of the tube.

Measures (H x W x D)[mm]:

1800 x 500 x 1100

Volume: 40 Litre
Maximum Flow Rate: 2 m^3/hours
Particle size: 1–10 mm
Maximum angle: +/–45°

Figure 3: Vortex tube at the laboratory

A vortex-tube separator was built using literature data by Tarján [1]. The whirlpool tube was made of transparent PVC, with 400 mm or 300 mm long tubes (See *Figure 1*). The inner diameter of the tube was 50 mm. The end sections, where central feeder vortex finder and tangential medium in and out flows could be found, were made of bonamide, which is easy to manufacture. The feed and the vortex finder were made of stainless steel and attached to the tube through the central hole of the bonamide section using "O" – ring sealing. The feeder had 19 mm, the vortex finder 25 mm inner diameters with conical openings to reduce the missed particles because of the thickness of the vortex finder itself. The length of the vortex finder could be adjusted freely from 240 mm to 0 mm (in case of 400 mm tube length) to examine the effect of separation length in the separator. The separation media was stored in a 30 litre stainless steel tank beneath the separator, from where a centrifugal pump pumped the medium through the separator. The outlet of the separator flowed back to the tank, while the separated boxes with semi-permeable bottom cached the particles. The pump drive was a 400 W three-phase electric engine, which supplied electricity through a frequency converter. By this solution the flow rate could be adjusted for the separator at a given separator geometry and setup. The flow velocity was kept at the optimal value, so that a centred and stable air core was formed inside the vortex-tube separator. The pressure loss of the separator could be measured by a Digibar pressure meter, while the flow rate by a built in flow meter. A vortex-tube separator installation set up in the experimental was appropriate for the measuring the effect of the separation media density, the feed pressure, geometric parameters of the separator, as well as the feed rate and solid concentration. Measurements were carried out first on the model plastics.

As it can be seen from the Figure the composition of the light product can be estimated. It is highly evident that the separation is the perfect one in case if the only light particles are in the light product. The proportion of the heavy particles misplaced into the light product will determine the efficiency of the separation. From the other hand, the width of the

interval of the recovery curve, does determine the minimal particle density difference at which the separation will cause the minimal contamination of the products. In our case, this density range was found as follows: $\Delta\rho$ = 0.1–0.2 kg/dm^3, where the separation can be carried out effectively for the both products in one-stage. If the density difference is lower, a good separation can be carried out only for one of the products, it will be accompanied by lower recovery rate.

It can be proved that the component recovery curves can be well described by Rosin – Rammler distribution. It has a significant importance from the point of view of design of separation steps and the determination of the cut density of separation. Based on data obtained by a small installation and small scale, the component rates in the products can be estimated by calculations. Furthermore, the separation densities of a multi-component mixture can be determined as an optimal cut points, depending upon the needs of the market.

As it was mentioned earlier, the separation efficiency can be measured by the rate of the components in the products.

Figure 4 shows how the recovery of the light plastic, and the rate of both plastics change as a function of their rate in the feed. If the proportion of the light particles in the feed is around 10%, its rate in the product reduces dramatically using the cut point just slightly higher, than its particle density. If the feed contains a larger proportion of the light particles, the change is not so dramatic. It means, that if one of the components has higher proportion in the feed, the density control of the separation medium could be easier, because even the higher shifts in medium density has no dramatic effect on the separation efficiency. This is relevant if the density difference between the two components is big enough in comparison with the medium density shifting. The recovery curves can be used for the modelling as well. To determine the effect of the density differences between two components, the recovery curves can be shifted. Using the recovery curve to scan along the axis of separation density, the effect of the density differences between two components and their effect on the rate of the particles in the products can be determined. *Figure 5* illustrates the case of the original 1.12 kg/m^3 poly-olefin recovery curve which was shifted towards to the recovery curves of PA6 plastic. At each step the particle density was increased by 0.05 kg/dm^3 and the recovery rate was calculated using the estimated distribution of the original recovery curve. The separation took place at the cut density of the mean density of the particle (ρ light + ρ heavy/2) and the concentration of the components was 50/50% in the feed.

It can be determined that the high rate of the light particles can be reached if there is a significant difference in density between the particles, and if the density difference drops to the very low value, the rate of the light component remains as high as 100%.

If the separation density is lower than the density of the light particles, the recovery would be very low in this case, therefore it is not rational to use the one-stage operation.

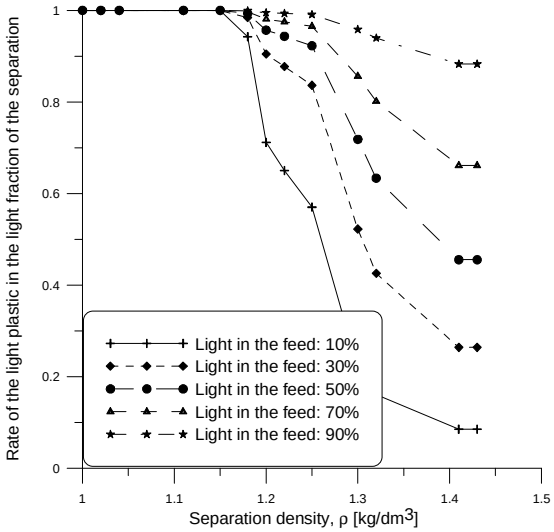

Figure 4: Light plastic ratio in the light product as a function of its rate in the feed, at given separation density

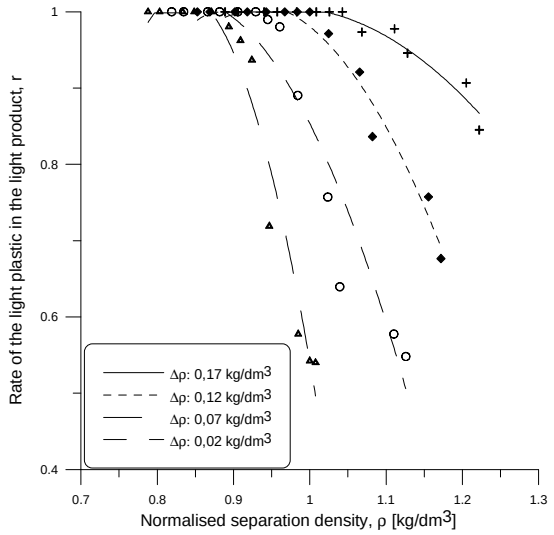

Figure 5: Light plastic rate in the light product as a function of the density difference between the two particles being separated

4. Conclusion

At separation processes, it is economically reasonable to determine the separation efficiency before it is actually takes place. It can be seen clearly that using component recovery curves, and determining the yield of each product point out that particular separation process is easy to carry out or more separation stage is required. It is also fact that economic parameters of the whole process are revealed as well. Based on these data required liberation grade and particle size parameters are also possible to calculate.

"Acknowledgement. This work was carried out as part of the TÁMOP−4.2.1.B−10/2/KONV−2010−0001 project in the framework of the New Hungarian Development Plan. The realization of this project is supported by the European Union, co‐financed by the European Social Fund."

REFERENCES

[1] Tarján, G.: *Mineral Processing*. Vol. 2., Akadémiai Kiadó, Budapest, 1981, 119–142.
[2] Bokányi, L.–Pethő, Sz.–Tompos, E.–Bőhm, J.: *Estimation of Three-Product Separation by Tromp-Functions.* Proceedings of the 11th International Coal Preparation Congress. 22–25. October, 1990, Tokyo, 97–100.

Geosciences and Engineering, Vol. 1, No. 1 (2012), pp. 129–138.

POTENTIAL OF CO_2 GEOLOGICAL STORAGE IN POROUS SEDIMENTARY FORMATIONS IN NORTH HUNGARY

ÉVA HARTAI
Institute of Mineralogy and Geology, University of Miskolc
3515 Miskolc-Egyetemváros, Hungary
foldshe@uni-miskolc.hu

Abstract
Storage of anthropogenic CO_2 in geological formations (CCS technology) is one of the options to reduce climate change. The author examines the sedimentary formations in North Hungary, which can have the potential for CO_2 storage. In the studied area, there are Oligocene, Miocene and Pannonian porous sedimentary rocks, which can be storage sites if further examinations prove their suitability.

1. Introduction

In the scientific literature, there is a strong consensus that global surface temperatures have increased in recent decades and that the trend is caused mainly by human-induced emissions of greenhouse gases [1]. No scientific body of national or international standing disagrees with this view. Conventional predictions of future temperature rises depend on estimates of future GHG emissions and the climate sensitivity. Models referenced by the Intergovernmental Panel on Climate Change (IPCC) predict that global temperatures are likely to increase by 1.1 to 6.4 °C between 1990 and 2100 [10]. Others opinions state that temperature increases may be higher than IPCC estimates.

In 1997 in the Kyoto Protocol 37 countries committed themselves to a reduction of CO_2 (and other greenhouse gases) below the 1990 level. By September 2011, 191 states signed and ratified the protocol (USA hasn't ratified).

One of the options to reduce carbon emission is the application of CCS (Carbon Capture and Storage), in other terms CO_2 sequestration technology. CCS involves capturing CO_2 at coal- or gas-fired power stations and industrial facilities (steel mills, cement plants, refineries etc.), transporting it by pipeline or ship to a storage location, and injecting it via a well into a suitable geological formation for long-term storage. Industrial-scale research projects on CCS have been conducted in Europe, the United States, Canada, Australia and Japan since the 1990's.

There are four major possibilities for the geological storage of CO_2: (1) injection into saline aquifers, (2) injection into depleted gas fields, (3) injection into oil fields with enhanced oil recovery (EOR), (4) injection into unmineable coal seams, possibly with enhanced coalbed methane recovery (ECBM) [4].

In Hungary all the four options are potentially available. In the frame of the recent study we review the sedimentary formations in the North Hungarian area, which can potentially be taken into account for CO_2 sequestration

2. Storage of carbon-dioxide in saline aquifers

A saline aquifer can refer to a porous and permeable sedimentary rock body saturated with non-potable water, from which the water can be drawn, and into which fluids can be injected to be stored for a longer period of time. The water of saline aquifers has usually

high dissolved material content (a few percent to tens of percent). Saline aquifers are believed to have the greatest potential to store CO_2.

The size of a saline aquifer for CO_2 storage is 0.05–50 km^3.The porosity of a potential CO_2 reservoir is typically 5–30%, with pore diameters of nm-mm. Suitable aquifers should have a cap rock of low permeability to minimize CO_2 leakage. Injection of CO_2 into deep saline reservoirs would use techniques similar to those for oil and gas fields. The world's CO_2 storage capacity in saline aquifers is estimated 400–10 000 Gt, while the annual CO_2 emission is 27 Gt [8]. In the light of these numbers this storage option seems to provide unlimited opportunities but as our knowledge about the deep-seated layers is very limited we have to take a lot of uncertainty into account.

The behaviour and transport of any fluids in rocks are influenced by the density, viscosity, solvability and miscibility of the fluid. All these parameters for the CO_2 are desired to be high in order to get the optimal storage conditions. This will help prevent it from escaping upwards since a dense fluid tense to descend. The efficiency of CO_2 storage in geological media, defined as the amount of CO_2 stored per unit volume increases with increasing CO_2 density. The high viscosity of the injection fluid makes injection more difficult, but on the other hand it prevents CO_2 to escape from the reservoir. Both solvability and miscibility also have to be high because when CO_2 is coupled with the in situ fluid already present in a reservoir rapid escape from the reservoir is prevented [9].

In order to get the optimal fluid conditions, CO_2 should be in supercritical stage. For this reason, the sequestration can be applied to rock bodies at a depth of about 800 m. Taking the world-wide average geothermal gradient, this depth corresponds the pressure and temperature values for the critical point of CO_2 (31,1 ºC temperature, 7,3 MPa pressure). At these values the density of CO_2 is 50–80% of that of the water. The CO_2 is partly dissolved in the formation water, partly fills the open pore spaces and due to the buoyancy effect it is enriched in the upward arching structures. In some formations it would slowly react with cations to form carbonates, which would lock up the CO_2 essentially permanently [4].

Based on these conditions a saline aquifer, which is a potential CO_2 reservoir, should complete the following requirements:

- large horizontal and vertical extent for the storage capacity,
- high porosity and permeability,
- impermeable caprock above the storing unit,
- the geological structure restrains CO_2 from escape,
- tectonically stable (no joints, faults, folds as potential paths for escape),
- isolation from fresh water bodies.

These requirements are usually fulfilled by porous sandstone formations. A potential problem that might occur is that if the pressure increases to a high level it can potentially fracture the seal above the aquifer and push salt water from the aquifer into shallower, possibly fresh water layers. With large-scale injection being considered, this pressure build-up issue needs to be examined closely.

The most significant sequestration project related to saline aquifers is the Sleipner project in Norway. The project started in 1996 and annually 1 million tone of CO_2 have been injected into the Utsira Formation at a depth of 800–1000 m. The total injected amount is planned to be 20 million tone. The reservoir rock is sandstone, covered by thick, impermeable shale.

3. Geology and CCS potential of the examined area

The examined area embraces the southern foreland areas of the Cserhát, Mátra and Bükk Mountains and the northern margin of the Hungarian Plane. Basically, the karstified carbonate rocks with large fresh water reserves of the Bükk Mountains and the thick volcanic formations of the Mátra and Cserhát Mountains have to be excluded.

In the followings we describe the rock types of the examined area in a chronological order, with a special emphasis on the CCS potential.

3.1. Mesozoic formations

Although Paleozoic rocks outcrop in the northern part of the Bükk Mountains, it is built up mostly by Mesozoic carbonate rocks and slightly metamorphosed shale *(Figure 1)*. The Triassic carbonate formations are of several kilometers in thickness containing valuable karstwater. The Jurassic clayey shale in the South Bükk have low porosity and permeability, that is why cannot be considered as potential CO_2 reservoirs.

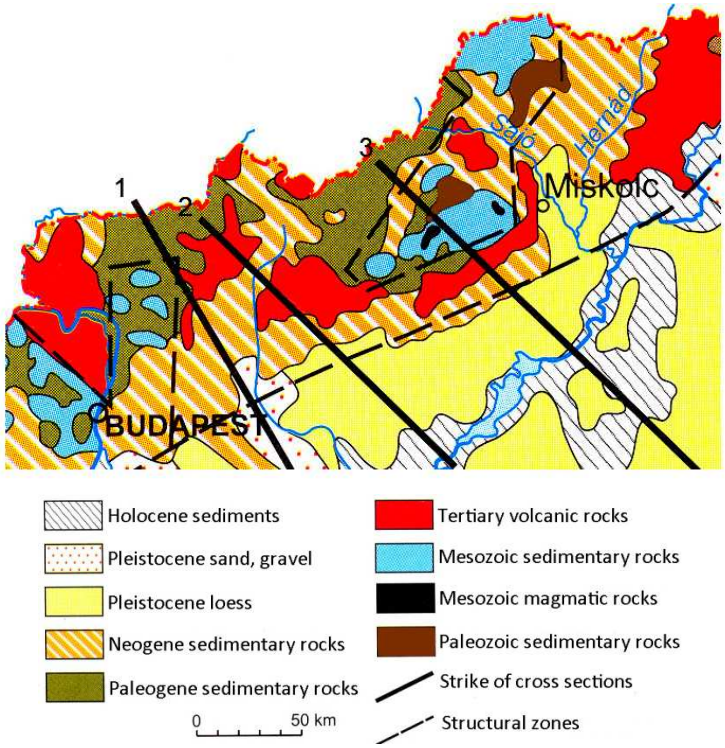

Figure 1: Geological sketch of the examined area. Black lines marked with numbers show the directions of the geological sections in Figure 2, 3 and 4 (After Haas et al., 2001)

3.2. Paleogene-Neogene basins

The Paleogene-Neogene basins are built up by variable sedimentary rocks, with a thickness of maximum 5 km. In the Carpathian Basin this area represents the largest vertical and horizontal extent of the Eocene–Oligocene–Miocene sequence. The deepest part of the basin is situated below and in the southern forefront of the Cserhát Mountains. From south, the basin is margined by the Bugyi–Tura–Hatvan–Mezőkövesd blocks, from the west by the Pilis Structural Zone and from the east by the Tokaj Mountains [6].

3.3. Tertiary formations

In the western part of the basin the basement of the Tertiary sequence is built up by Veporian crystalline metamorphites. In the eastern part the basement is formed by the Bükk-type Triassic carbonates, shales and a fragment of the Darnó Ophiolite Complex [2].

3.3.1. Eocene formations

The marine transgression in the area started in the Late Eocene and resulted the formation of light grey limestone and limy marl ("Szépvölgy Limestone", "Buda Marl"). The "Szépvölgy Limestone" contains abundant fossils. The thickness of the Eocene formations is 30–40 m [2]. Because of the low porosity, the low thickness and the limited extend the Eocene formations are generally not suitable for CO_2 storage, although in the Mezőkeresztes–Demjén–Fedémes–Bükkszék oil fields the exploitation takes place partly from Triassic and Eocene fractured carbonate rocks [3].

3.3.2. Oligocene formations

During the Oligocene the transgression became more extended in the North-Hungarian area. The marine area was separated from the opened ocean and reductive environment, euxinic facies became characteristic. This sedimentary environment favoured the formation of the dark grey, bituminous "Tard Clay" in the Early Oligocene (Kiscellian Age). This formation is considered as the source rock of the oil fields at Bükkszék. Its thickness varies from 30 to 100 meters.

Following the formation of the "Tard Clay", there was an uplift and the area became a dry land for a short time. Then, as a result of the new transgression, the "Kiscell Clay" was formed in the open marine areas while in the marginal parts the Hárshegy Sandstone was deposited. The latter one is found outside the examined area, In the Buda Mountains and the Esztergom Basin. The "Kiscell Clay" is similarly bituminous to the "Tard Clay". It is thought to be the source rock of the hydrocarbon fields of the Hungarian Plain. In the central parts of the basin, its thickness exceeds 1000 meters [2].

In the Late Oligocene regression started in the basin area, which resulted the deposition of shallow marine sediments. In the western part of the basin the "Törökbálint Sandstone" was deposited, which is a slightly consolidated rock with pelitic matrix. Its thickness is about 250 meters.

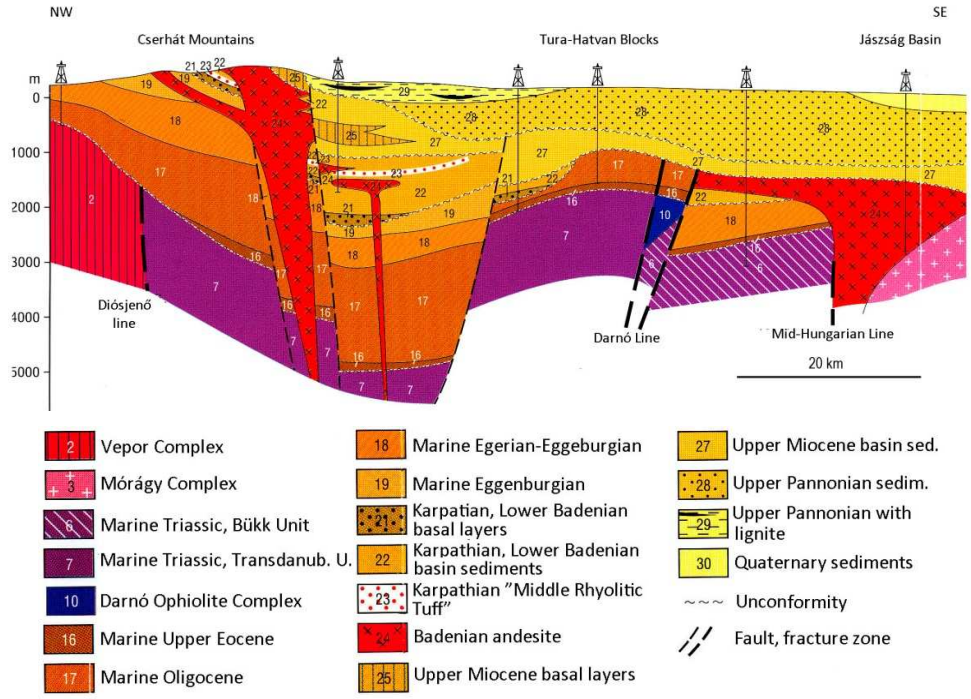

Figure 2: Geological cross section along line 1 in Figure 1 (After Haas et al., 2001)

In the eastern margin of the basin the Eger Formation was formed, which represents a continuous regressive sequence. The lower unit is represented by glauconitic sandstone in a thickness of 3–40 m, it is covered by molluscan clay of 40–50 m, then shallow marine sandstone in similar thickness. In the Nógrád–Cserhát–Ózd–Rimaszombat area the "Szécsény Schlier" was deposited in a thickness about 800 m. In the marginal parts shallow marine glauconitic sandstone (Pétervására Formation) was formed. At the end of the Oligocene the Paleogene the sedimentary sequence filled up the Paleogene Basin the area was lifted and became a dry land [2], [5], [6].

As for the CCS potential of the Oligocene sequence the followings can be summarized:

- The reservoir rocks of the Mezőkeresztes–Demjén–Fedémes–Bükkszék oil fields are Eocene and Triassic fractured limestone, Oligocene sandstone and Miocene pyroclasts. Because of the low porosity and permeability of these rocks the exploitation is problematic, which is even increased by the high density of oil. The depleted parts of the reservoir can be taken into account as CO_2 storage sites.
- The Lower Oligocene "Tard Clay" and "Kiscell Clay" are not suitable for CCS *(Figure 2, 17; Figure 3, 23; Figure 4, 17).*
- In the Late Oligocene sedimentary sequence there are certain formations, which have CCS potential as they are deep-seated, porous and permeable. These are the marine Egerian-Eggenburgian sandstones between the Tura-Hatvan Blocks and the Cserhát Mountains *(Figure 2, 18).* The problem can be that their position is too deep (2000–3000 m), which would significantly increase the injection costs.

– In the area between the Cserhát and Mátra Mountains these sandstones seem to be more applicable *(Figure 3, 24),* although their lateral extent is probably not large enough.
– The depth of this formation is also convenient in the Vatta-Maklár Trench *(Figure 4, 18).*

It can be decided after detailed examination (drillholes, formation water quality, impermeability of the caprock, lateral migration connections, e.t.c.) if these formations is suitable for CCS.

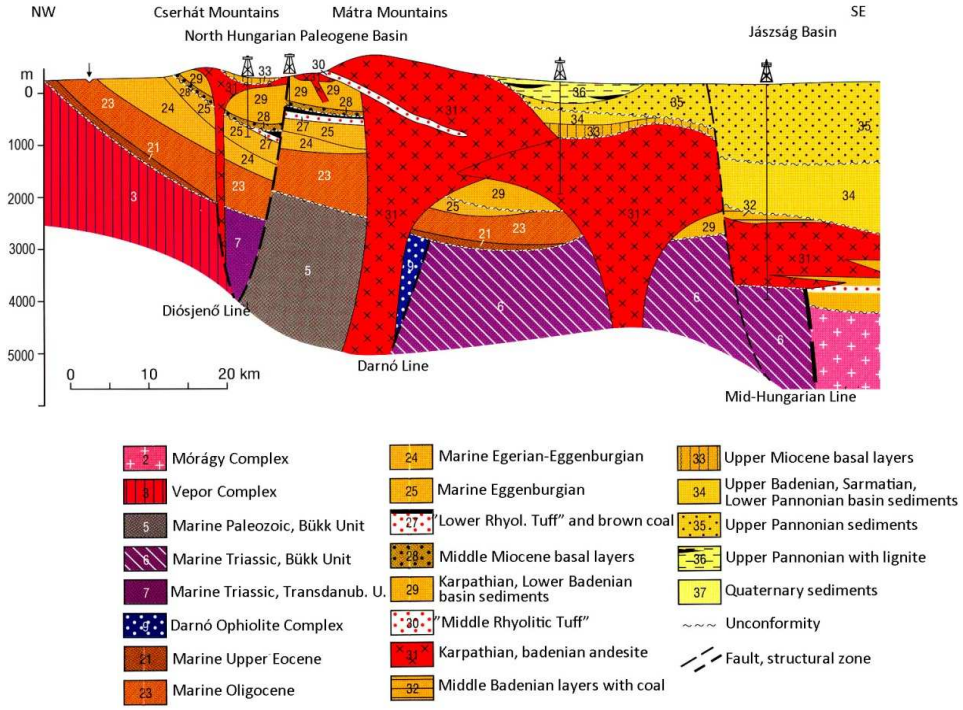

Figure 3: Geological cross section along line 2 in Figure 1 (After Haas et al., 2001)

3.3.3. Miocene formations

The structural units of the ALCAPA and Tisza–Dacia plate blocks, which form the Palaeozoic–Mesozoic basement of Hungary arrived at their recent place in the Early Miocene. With the setting of the plate blocks, the sinking of the Carpathian Basin started.

During the Early Miocene the Eggenburgian transgression came from southeast. Due to the continuous uplift of the Carpathians rivers from north started to build the ancient deltas, indicating the early filling up of the Carpathian Basin. Along the marginal fractures of the lifting blocks, the Gyulakeszi Rhyolitic Tuff came to surface by explosive eruptions (earlier called "Lower Rhyolitic Tuff"). In the swampy marginal parts of the Ottnangian sea brown coal deposits were formed in the Nógrád and Borsod area. At the same time, in the shallow marine areas sandstone and molluscan limestone were deposited [7].

In the Middle Miocene Karpatian Age the rhyolitic explosive activity restarted (Tar Dacitic Tuff, earlier "Middle Rhyolitic Tuff). This introduced the widespread andesitic

volcanism, which occurred in the whole Inner Carpathian Belt. In the North Hungarian basin areas sandstone was deposited. In the Badenian, the fossil-rich, shallow marine limestone (Rákos Formation, earlier "Lajta Limestone") is widespread, but in the Nógrád area fine-grained sandstone, sandy clay, marl and silt also occur [5], [7].

In the Late Miocene the Pannonian Basin was formed. The central part of the basin started to sink intensely and the southern part of the region became a part of the Hungarian Plane. The Late Miocene is characterized by a large sedimentary cycle, with an Upper Badenian, Sarmatian and Pannonian transgressive sequence followed by regression from the end of the Pannonian. During the Sarmatian Age, the explosive rhyolitic volcanism started for the third time (Galgavölgy Rhyolitic Tuff, earlier "Upper Rhyolitic Tuff". In the southern margins of the lifting mountains, shallow marine, porous limestone was deposited. The swampy areas started to form along the northern sea margins in the Pannonian Basin. The sedimentation was continuous until the end of the Pannonian Age [2], [7].

The Miocene sandstones can be the subject of further examinations to reveal their CCS potential. Those sandstone bodies can be taken into account, which have relatively large horizontal and vertical extent, have impermeable caprock and are situated below 800 m depth. These sandstone bodies are as follows:

- Marine Egerian-Eggenburgian sediments in the Ózd Trough *(Figure 4, 27);*
- Karpatian– Lower Badenian basin sediments *(Figure 2, 22)* and Late Miocene basin sediments *(Figure 4, 19)* in the area between the Cserhát Mountains and the Tura–Hatvan Blocks;
- Upper Badenian, Sarmatian and Lower Pannonian basin sediments in the Vatta–Maklár Trough *(Figure 4, 27)*

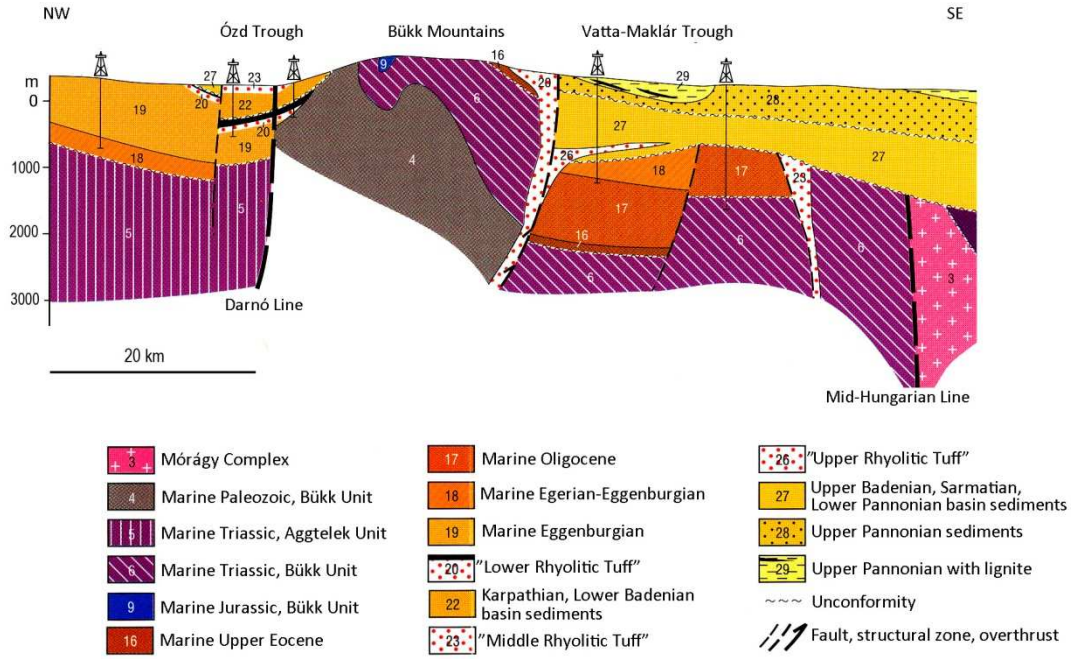

Figure 4: Geological cross section along line 3 in Figure 1 (After Haas et al., 2001)

3.3.4. Pannonian formations

In the Pannonian Age, which comprises the latest Miocene and the whole Pliocene (Pannonian s.l.), the Pannonian Inland Sea covered most of the Carpathian Basin. Rivers from the surrounding mountains built huge delta systems. The submerging basin was continually filled by clastic sediments, which are finally as thick as 4000–5000 m. In the Pannonian Age clastic sediments are dominant [2].

The examined area was situated in the northern margin of the basin. In the Nógrád area and the foreground of the Cserhát, Mátra and Bükk, fluvial, limnic and delta sediments were deposited, mostly sand and gravel (Borsod Gravel Formation, Edelény Formation) [5], [7].

In the Late Pannonian the inland sea margin became a limnic-swampy area, and grey-bluish gray clayey sediments were formed with interlayering lignite of maximum 15 m in thickness (Bükkalja Lignite Formation). By the end of the Pannonian the basin became completely filled up [5], [6].

As for the CCS potential, the Pannonian sandstones have good parameters. As we have to find layers deeper than 800 m, only those blocks can be considered, which were faulted down along the multiply fault systems at the mountain margins. Taking this into account we can find potential formations for CO_2 storage in the following areas:

- The Upper Miocen basin sediments between the Cserhát Mountains and the Tura–Hatvan Blocks *(Figure 2, 27)*. The Upper Pannonian sandy layers *(Figure 2, 28)* cannot be considered because of their high position.
- In the southern foreland of the Mátra Mountains the Badenian, Sarmatian and Lower Pannonian basin sediments *(Figure 3, 34)* have good potential. The Upper Pannonian sediments *(Figure 3, 35)* can be also suitable.
- In the Vatta–Maklár Trough, the Upper Badenian, Sarmatian and Lower Pannonian basin sediments *(Figure 4, 27)* can be applicable if they have the impermeable sealing layers.

3.4. Quaternary formations

During the Quaternary intense vertical movements were characteristic in the Carpathian Basin. In the last 2.4 million years the mountains have emerged to 200–300 m, while the lowland areas have submerged to 150–700 m. The blocking structure is shown in *Figure 3* and *4*. In the Pleistocene the recent river systems were already formed, and the mountains and hills were exposed to denudation. The ancient river beds are marked by cobble horizons, and in the floodplain areas fine-grained sediments were deposited. In the southerd foreland of the North Hungarian Mountains loess was accumulated [6].

Because of their high position, the Pleistocene sediments cannot be considered as CO_2 storage sites.

4. Conclusions: CCS potential of the examined area

Summarizing the characteristics of rock types and their position in depth, as potential formations for CO_2 storage the following units can be considered – if they have the suitable physical parameters and do not contain fresh water reserves:

- Reservoir rocks of the Mezőkeresztes–Demjén–Fedémes–Bükkszék oil fields: Triassic and Eocene fractured limestone, Oligocene sandstones and Miocene pyroclasts and sedimentary rocks,
- Marine Egerian–Eggenburgian sedimentary rocks in the Vatta–Maklár Trough (depth: 500–1000 m, thickness: 300 m),
- Miocene sandstones and sandy sedimentary rocks (depending on the depth, isolation and sealing) in the following areas:
    - The range between the Cserhát Mountains and the Tura–Hatvan blocks: The Karpathian-Lower Badenian basin sediments are at a depth of 1500-2000 m, their thickness is maximum 500 m; the Upper Miocene basin sediments are positioned between 0–1600 m depths, their thickness varies from 200 to 800 m.
    - The Vatta–Maklár Trough: Upper Badenian, Sarmatian and Lower Pannonian basin sediments positioned between 0 and 1600 m depth, their thickness varies from 500 to 1000 m.
- Pannonian sandstones (if they have impermeable caprock) in the following areas:
    - The southern foreland of the Mátra Mountains: Lower Pannonian basin sediments at a depth between 1000–2500 m, in a thickness of 800–1500 m
    - The Vatta–Maklár Trough: Lower Pannonian basin sediments at a depth between 0–1600 m, in a thickness of 200–800 m.

Further examinations are needed on these formations in order to decide about their CCS potential. These examinations are:

- Structural geological and stratigraphic interpretation of the former geophysical data,
- Interpretation of the former drillhole documentations in the area,
- Mineralogical, petrological, geochemical and sedimentological analysis of the drillcores,
- Interpretation of the formation water quality data.

These examinations are necessary to determine the position and extent of the given formation, the physical parameters of rocks (grain size, sorting, porosity, permeability, adsorption capacity) as well as the quality of the pore fluid (excluding the fresh water reservoirs).

It is also important to clarify if there is a proper sealing by impermeable clayey rocks above the storage formation and if the formation fluid is isolated from fresh water reservoirs. To make these conditions clear several drillholes have to be carried out in the potential area.

"Acknowledgement: This study was carried out as part of the TÁMOP-4.2.1.B-10/2/KONV-2010-0001 project in the framework of the New Hungarian Development Plan. The realization of this project is supported by the European Union, co-financed by the European Social Fund."

REFERENCES

[1] AMERICAN NATIONAL RESEARCH COUNCIL (ANRC): *Advancing the Science of Climate Change*. The National Academies Press, Washington, 2010.

[2] Bérczi, I.–Jámbor, Á. (ed.): *Stratigraphy of the geological formations of Hungary (in Hungarian).* MOL–MÁFI, Budapest, 1998.

[3] Csíky, G.: *The result of the new hydrocarbon exploration and prospects int he Northern Paleogene Basin (in Hungarian).* Földtani Közlöny, 98, 1968, 14–40.

[4] Davidson, J.–Freund, P–Smith, A.: *Putting carbon back into the ground*. In: IEA Report, Greenhouse Gas R&D Programme, Cheltenham, 2001.

[5] Gyalog, L.: *Codes for the geological maps and the short descriptions of the stratigraphic units of Hungary (in Hungarian).* MÁFI, Budapest, 1966.

[6] Haas, J.–Hámor, G.–Jámbor, Á.–Kovács, S.–Nagymarosi, A.–Szederkényi, T.: *Geology of Hungary*. Eötvös Egyetemi Kiadó, Budapest, 2001.

[7] Hámor, G.: *Explanatory notes to the Miocene palaeogeographic maps of the Carpathian Basin.* MÁFI, Budapest, 2001.

[8] IEA ENERGY TECHNOLOGY ANALYSIS: *Prospects for CO2 capture and storage.* www.iea.org/textbase/nppdf/free/2004/prospects.pdf

[9] Sasaki, Kenta–Fujii, Takashi–Niibori Yuichi–Ho, Takatoshi–Hashida, Toshiyuki: *Numerical simulation of supercritical CO2 injection into subsurface rock masses*. Energy Conversion & Management 49, Elsevier, 54–61. www.sciencedirect.com

[10] Solomon, S.–Qin, D.–Manning, M.–Chen, Z.–Marquis, M.–Averyt, K. B.–Tignor, M.–Miller, H. L. (ed.): *Contribution of Working Group I to the Fourth Assessment Report of the Intergovernmental Panel on Climate Change*. Cambridge University press, Cambridge–New York, 2007.

Geosciences and Engineering, Vol. 1, No. 1 (2012), pp. 139–145.

APPLICATION OF GMT (GENERIC MAPPING TOOLS) SOFTWARE FOR VOLUME COMPUTATION IN MINING INDUSTRY

I. HAVASI–M. FERENC
Department of Geodesy and Mine Surveying, Institute of Geophysics and GIS,
University of Miskolc
3515 Miskolc-Egyetemváros, Hungary
gbmhi@uni-miskolc.hu; gbmfm@uni-miskolc.hu

Abstract
In a brief introductory part of this study both our former research in this theme and decree regulation of mining volume computation are overviewed. After that problems of determination of volume in home practice are discussed, and then GMT programme is introduced compactly. Finally, doing comparison analysis, application of GMT software to the task given in the title is tested in case of concrete mining depots of irregular shapes.

1. Introduction

In our former study [1] we dealt with problems of volume computation connected to mineral deposits and introduction of suitable programmes, and comparison of their results. In that article, considering carefully the setting possibilities of each software and different use among them, we performed volume calculation tests using generated point sets modelling mathematical bodies with known parameters and measured ones of real mining depots (of regular and irregular shape). After analysing the results we stated that the volume computation programmes used in home mining practice, the suitable methods and settings run with the required accuracy approaching to the real value well which is, actually, one of the key points of quality connected to measuring a depot.

Theoretically numerous points would be needed when a depot is measured so that we could obtain the volume suitable to reality, however, it is unfeasible in most cases or rather it is not justified. Moreover, it is also unsure – considering the extra work – that the large number of the measured points improves the later results at all; consequently, it is necessary to get to a compromise in the interest of the required accuracy.

Mine surveying tasks including the questions of volume computation are regulated by a separate governmental decree. As far as the registration of waste rock and mineral raw material are concerned the later is of greater significance. A mining entrepreneur, however, is obliged to survey the excavated mineral raw material, since it is the basis of determining the mining annuity which must be paid for the state. The *Government Decree No. 54/2008. (III. 20)* about mineral raw materials and the specific value of geothermic energy [2] deals with the declaration of mining annuity, determination of the volume of mineral raw material and the role of a chartered mine surveyor in this process. The Section 2 of this Decree regulates the payment of mining annuity with reference to solid raw materials as follows:

"Section 2, subsection 2. The licensee exploiting the mineral raw material and having an authorization is obliged to determine the quantity of the excavated mineral raw material by means of mine surveying /geodetic/ methods or other suitable ways. Documentation must be made about the applied method and its result.

The licensee is obliged to determine the quantity change of the mineral raw material by geodetic computation (volume computation) within 60 days after finishing the production of the mineral raw material in question."

"Section 2, subsection 3. *A mining entrepreneur is obliged to determine the quantity of the exploited mineral raw material by mine surveying (geodetic) methods*. In case of underground mining it can be performed by mass surveying. The change must be displayed on the exploitation map. *The quantity change of mineral material related to the actual year must be determined by computation on the basis of geodetic surveying (volume computation)*. The result of measurement and computation must be recorded in a document."

In surface mining practice naturally determination of waste rock mass is essential for many respects. This however is mainly important for an entrepreneur because he is not obliged to pay any annuity for the exploited waste rock.

2. Determining the quantity of mineral raw material and waste rock in home practice

The quantity of exploited waste rock and the excavated useful mineral can be determined either in an *operative way* or with a *mine surveying method* [3].

The *operative registration* results in only a preliminary estimation, it is not accepted officially and therefore here we do not intend to deal with it in details.

The *mine surveying registration* includes a comparison of monthly updated mining maps and volume computation. Examining the afore-discussed two methods mine surveying (geodetic) is more accurate and it is required from the mining authority as it was mentioned earlier.

If a depot volume is determined in a surface mine with a mine surveying method, then *graphic* and *numerical procedures* come into consideration. The *graphic method* is based on the comparison between the previously measured mine positions fixed on the map. When a numeric technique is used 3D surface models are established on the basis of coordinate sets related to each measured position by means of programmes known in home practice (*Surfer*, *DigiTerra*, *AutoCAD Civil 3D* etc.), then cutting them correctly we compute the difference between them.

3. Surface-fitting in practice

As it was already mentioned the application of some software known in home practice was tested in our former study [1]. In it we executed computations using artificial and measured coordinate sets modelling known mathematical bodies on the one hand and true regular and irregular mining depots on the other hand. In that case Kriging and *Triangulation* with linear interpolation algorithm produced the results which could be near the true value (that was proved on the basis of our comparison analysis of the modelled point sets as well). Considering the afore-mentioned two procedures the results of the latter one demonstrated the most consistent picture on the basis of both modelled and real measured point sets.

4. Surface-fitting and the TIN model

We consider the TIN model important because the surface of an examined body is formed as a result of linear triangulation and – considering the afore-mentioned study – the most promising results were produced on the basis of this principle when we tested point sets describing known bodies.

The TIN is an acronym which includes the initials of the English words: Triangulated Irregular Network. It means a regular triangle grid, that is to say the surface is covered by a grid (triangles) consisting of irregular grid points. In case of an irregular point set on a plane, it is possible to construct a polygon around each point the inner points of which are closer to the point in question than to all the other ones. Consequently the polygon sides are perpendicular to the lines connecting the point in question and the other points and even halve them. The parts of this polygon will consist of only those lines from whose intersections a closed convex polygon is developed. At the same time these polygon lines determine the neighbouring points considered from each point, since the formation of a polygon is influenced by only those points which bisect perpendicular lines of radius directed towards them as parts of this polygon. If we connect all the points according to the afore-mentioned conditions, in plane case we obtain an unambiguous and optimal division of triangles (from a certain point of view). This division is called *Delaunay-triangulation* and the polygons are termed *Voronoy*-ones [*Figure 1*].

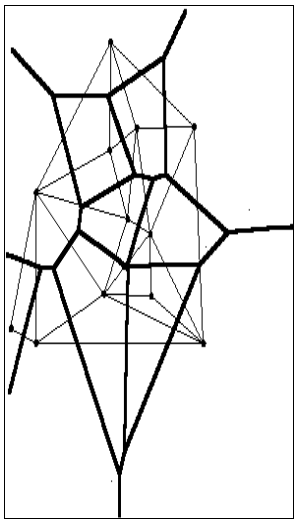

Figure 1: Delaunay triangulation,
Voronoy-polygons

In a spatial case connecting the determined points as neighbouring ones it results in an unambiguous and optimal tetrahedron division [4, 5].

5. The GMT (Generic Mapping Tools) software

In fact it is a mapping and viewing system which contains nearly 65 smaller programmes. It was originally written for Linux operation system and issued under GNU general public licence. It is not really wide-spread in practice. The GMT programme package has been developed and maintained in an updated form by now with the help of *Paul Wessel*, *Walter H. F. Smith* and many voluntary and enthusiastic specialists from all over the world. On the official website (http://gmt.soest.hawaii.edu/) 30 examples are used for introducing the possibilities of GMT software, and we can read its install; moreover the use and capability of each programme [6]. It has also become clear for the users visiting the afore-mentioned website that today this software runs in Windows or Macintosh OS X operation systems as well.

Basically there are two reasons why we are dealing with this programme package, the first one is that it is *free*, the second one is that it is also *appropriate excellently for volume computation* competing with other available software for this special purpose on the market. The grid system that we selected serves as a basis of volume determination and is computed by means of a *Shewchuk-algorithm*.

6. Point sets deriving from real depot surveys

The main point of our article is the following: we performed volume computation tests for four concrete mineral depots by means of Surfer and GMT (Generic Mapping Tools) software. Their results are illustrated in the following Figures 2–5. In these Figures surfaces fitted to the measured point sets of each depot and the obtained volumes with the help of GMT (upper picture) and Surfer (lower one) programmes can be seen.

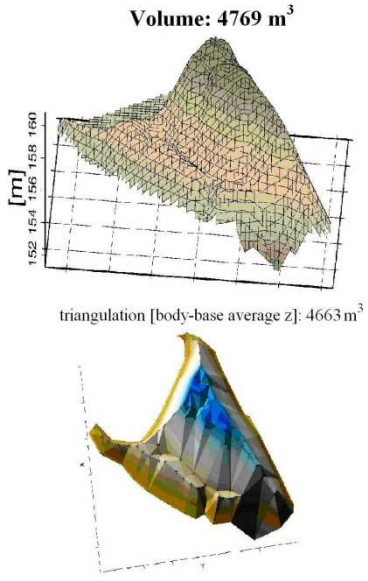

Figure 2, Depot 1

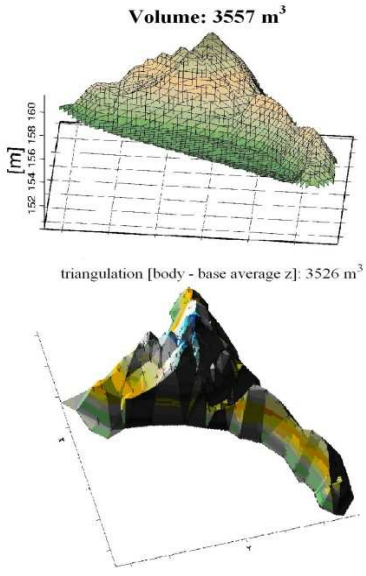

Figure 3, Depot 2

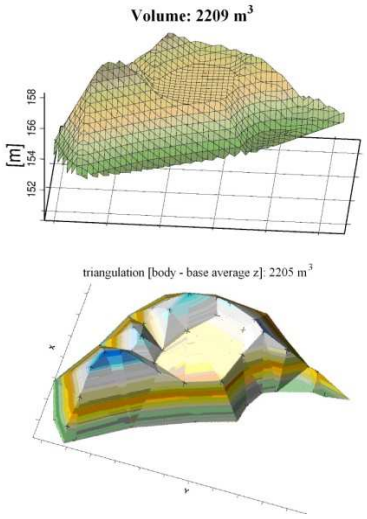

Figure 4, Depot 3

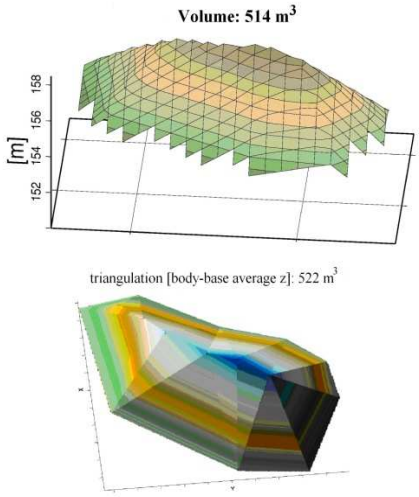

Figure 5, Depot 4

It can also be seen in each Figure that the terrain point sets available are derived from *depots of irregular shape*. It is evident from the following table that the results of *triangulation solution of Surfer programme* were considered to be relevant values [*100%*], and in connection with each depot we applied them as reference values to which the results of Kriging and GMT triangulation were compared. Here it is also important to mention that in our former studies [1], [7] where we performed similar tests using point sets modelling known mathematical bodies and deriving from terrain surveys, all the compared programmes (DigiTerra, AutoCAD 3D and Surfer) showed good results, consequently we could have considered any of them listed before as a reference one. So the *triangulation with linear interpolation* in Surfer was selected to be reference procedure. As the results show well in *Table 1* the free GMT can also be taken into account among the recommended programme lists previously mentioned since it is a potential alternative which can be used easily and well in practice and is capable of computing mining volumes.

Table 1

Comparing the results of volume computation connected to Surfer and GMT software

	Surfer		*GMT*
	Triangulation [m^3] (reference data)	*Kriging* [m^3] [difference]	*Triangulation* [m^3] [difference
Depot 1	4663	4937 [+5.9%]	4769 [+2.3%]
Depot 2	3526	3637 [+3.2%]	3557 [+0.9%]
Depot 3	2205	2425 [+10%]	2209 [+0.2%]
Depot 4	522	627 [+20%]	514 [–1.5%]

At the four depots the differences from each reference value were less than *3%* in all cases (*reference data of Surfer* and *GMT ones*), that is to say they fulfilled the expected requirements connected to volume computation in practice in general.

7. Conclusions

In our study we performed surface-fitting and volume computation tests with the help of two programmes (Surfer and GMT). The Surfer – as it is known – is a grid-based, 3D surface mapping and viewing software. This programme uses a grid in all cases. To produce this grid it uses survey points with X, Y and Z coordinates located in a random way and fixed in data sets measured by a mine surveyor. The software applies various mathematical procedures to develop the afore-mentioned grid to each grid file using each coordinate set. The volume is computed on the basis of a grid. The grid with regular spacing produced in this way has the same Y grid points in certain rows and the same X coordinates in certain columns, and the programme computes their Z values by means of the mentioned mathematical methods [4].

The other software, GMT is however such a complex programme package which provides map viewing of global data, capable of treating and editing terrain models.
In the circle of specialists it is known that the quality of surface fitted to a set of points is decisively influenced by the followings [7]:

- the experience in geodetic survey /identification and surveying of the most characteristic field points and lines;
- the number of survey points (it is advisable to measure as many detail points as possible, of course, in a rational manner;
- the selected and applied interpolation procedure in the programme.

We have to mention that it is advantageous if the specialist who performs data processing knows the survey site, that is to say, he could see it earlier thereby he is able to form an opinion of the surface forms after each interpolation technique.

Our present investigations however proved that the user has to consider many viewpoints when applying each programme to determine the correct volume. Among these we can mention the followings [7]:

- the geodetic survey should be detailed properly and describe the depot geometry correctly;
- it is essential what kind of software we have and the geodetic data capture must be fitted to it;
- correct selection of the necessary settings in the available programme /e.g. method, grid size/.

We would like to call the attention to the fact that volume calculation – similarly to other geodetic/mine surveying tasks – requires *checking computation* as well. It naturally can be performed *traditionally* or by means of *other professional software*.

Finally we can state that the favourable results of our test computations with GMT software confirmed us that we can strongly recommend this free programme to kind attention of Hungarian mining specialists/mine surveyors.

"Acknowledgement: This work was carried out as part of the TÁMOP-4.2.1.B-10/2/KONV-2010-0001 project in the framework of the New Hungarian Development Plan. The realization of this project is supported by the European Union, co-financed by the European Social Fund."

REFERENCES

[1] Ferenc, M.–Havasi, I.–EKE, Z.: *Studying surface-fitting and volume computation methods.* XLVIII. Conference on Mine Surveying, Conference Proceeding, Szolnok–Szajol, Alcsi Holt-Tisza Leisure Centre, 2009, 27–40.
[2] *Government Decree 54/2008. (III. 20).*
[3] HOVÁNYI, L.–KOLOZSVÁRI, G.: *Geodesy and Mine Surveying (Mine Surveying I.).* University notes, Budapest, 1985.
[4] Elek, I.: *Introduction to Geo-informatics*. Book, 2006.
[5] Elek, I.: *Practices in GIS*. Book, 2007.
[6] Wessel, P.: *GMT–Generic Mapping Tools* documentation and website. http://gmt.soest.hawaii.edu/
[7] Havasi, I.–Ferenc, M.: *Numerical volume calculation in Hungarian mining practice.* XIV International Congress of ISM (International Society of Mine Surveying) Proceeding Book, Session 1–2, Sun City, South Africa, 2010, 13–19.

Geosciences and Engineering, Vol. 1, No. 1 (2012), pp. 147–157.

ADAPTATION AND ESTENSION OF SULFONAMIDE AND OTHER ANTIBIOTICS DETERMINATION BY SOLID-PHASE EXTRACTION FOLLOWED BY LIQUID CHROMATOGRAPHY AND MASS SPECTROMETRY

LAJOS KADENCZKI[*]–HENRIETTA STEFÁNNÉ SZOPKÓ[**]
*Department of Chemistry, University of Miskolc
**SGS Hungária Kft Nyíregyháza
3515 Miskolc-Egyetemváros, Hungary
green.park@chello.hu, henrietta.szopko@sgs.com

Abstract
The present study is an adaption, extention, validation and a practical application of an analytical method based on solid-phase extraction and liquid chromatography-tandem mass spectrometry (SPE-LC-MS/MS) for the simultaneous determination of 21 sulfonamides and three other antibiotics in different water matrices. MS/MS detection was carried out in a quadrupole-linear ion trap mass analyzer. Target compounds were identified in the selected reaction monitoring (SRM) mode, recording two transitions between precursor ions and the two most abundant product ions. The method developed was applied to evaluate the occurrence of the target antibiotics in different water samples.

1. Introduction

1.1. History of Sulfonamides. Sulfonamide drugs were the first antimicrobial drugs, and paved the way for the antibiotic revolution in medicine. The first sulfonamide, trade-named Prontosil was a prodrug [1]. Experiments with Prontosil began in 1932 in the laboratories of Bayer AG, at that time a component of the huge German chemical trust IG Farben. The Bayer team believed that coal-tar dyes able to preferentially bind to bacteria and parasites might be used to target harmful organisms in the body. After years of fruitless trial-and-error work on hundreds of dyes, a team led by physician/researcher Gerhard Domagk (working under the general direction of Farben executive Heinrich Hoerlein) finally found one that worked: a red dye synthesized by Bayer chemist Josef Klarer that had remarkable effects on stopping some bacterial infections in mice. The first official communication about the breakthrough discovery was not published until 1935, more than two years after the drug was patented by Klarer and his research partner Fritz Mietzsch. Prontosil, as Bayer named the new drug was the first medicine ever discovered that could effectively treat a range of bacterial infections inside the body. It had a strong protective action against infections caused by streptococci, including blood infections, childbed fever, and erysipelas, and a lesser effect on infections caused by other cocci. However it had no effect at all in the test tube, exerting its antibacterial action only in live animals. Later it was accidentally discovered by a French research team, led by Ernest Fourneau, at the Pasteur Institute, that the drug was metabolized into two pieces inside the body, releasing from the inactive dye portion a smaller, colorless, active compound called sulfanilamide. The discovery helped establish the concept of “bioactivation” and dashed the German corporation's dreams of enormous profit; the active molecule sulfanilamide (or sulfa) had first been synthesized in 1906 and was widely used in the dye-making industry; its patent had since expired and the drug was available to anyone.

The result was a sulfa craze. For several years in the late 1930s, hundreds of manufacturers produced tens of thousands of tons of myriad forms of sulfa. This and nonexistent testing requirements led to the elixir sulfanilamide [2] disaster in the fall of 1937, during which at least 100 people were poisoned with diethylene glycol. This led to the passage of the Federal Food, Drug and Cosmetic Act in 1938. As the first and only effective antibiotic available in the years before penicillin, sulfa drugs continued to thrive through the early years of World War II [3]. They are credited with saving the lives of tens of thousands of patients, including Franklin Delano Roosevelt, Jr. (son of President Franklin Delano Roosevelt) (in 1936) and Winston Churchill. Sulfa had a central role in preventing wound infections during the war. American soldiers were issued a first-aid kit containing sulfa pills and powder, and were told to sprinkle it on any open wound. During the years 1942 to 1943, Nazi doctors conducted sulfanilamide experiments on prisoners in concentration camps [4, 5].The sulfanilamide compound is more active in the protonated form, which in case of the acid works better in a basic environment. The solubility of the drug is very low and sometimes can crystallize in the kidneys, due to its first pK_a of around 10. This is a very painful experience, so patients are told to take the medication with copious amounts of water. Newer compounds have a pK_a of around 5–6, so the problem is avoided [6]. Many thousands of molecules containing the sulfanilamide structure have been created since its discovery (by one account over 5400 permutations by 1945), yielding improved formulations with greater effectiveness and less toxicity. Sulfa drugs are still widely used for onditions such as acne and urinary tract infections, and are receiving renewed interest for the treatment of infections caused by bacteria resistant to other antibiotics.

1.2. Using of Sulfonamides nowadays. The sulfonamide antibiotics most frequently used in the veterinary field. It is estimated that more than 50 million kg-s of antibiotics are produced each year in the Word. With approximately 40% used in animal production to treat diseases (therapeutic use) [7, 8, 9] and increase animal weight gain (growth promoting use). System, approximately 25% of small feedlot cattle operations and 70% of large feedlot operations used antibiotics in the feed (USDA/APHIS/Veterinary Services, 1999). A significant portion of the administered antibiotics in animals is excreted in an un-metabolized formand could result in the contamination of soil and waterthrough cropland application of animal wastes.

2. Materials and methods

2.1. Definitions

2.1.1. Laboratory Reagent Blank (LRB). An aliquot of reagent water or other blank matrix that is treated exactly as a sample including exposure to all glassware, equipment, solvents, reagents, internal standards, and surrogates that are used with other samples. The LRB is used to determine if method analytes or otherinterferences are present in the laboratory environment, the reagents, or the apparatus.

2.1.2. Laboratory Fortified Blank (LFB). An aliquot of reagent water or other blank matrix to which known quantities of the method analytes are added in the laboratory. The LFB is analyzed exactly like a sample, and its purpose is to determine whether the methodology is

in control, and whether the laboratory is capable of making accurate and precise measurements.

2.1.3. Stock Standard Solution. A concentrated solution containing one or more method analytes prepared in the laboratory using assayed reference materials or purchased from a reputable commercial source.

2.1.4. Primary Dilution Standard Solution (PDS). A solution of several analytes prepared in the laboratory from stock standard solutions and diluted as needed to prepare calibration solutions and other needed analyte solutions.

2.1.5. Quality Control Sample (QCS). A solution of method analytes of known concentrations which is used to fortify an aliquot of LRB or sample matrix. The QCS is obtained from a source external to the laboratory and different from the source of calibration standards. It is used to check laboratory performance with externally prepared test materials.

2.1.6. Calibration Standard (CAL). A solution prepared from the primary dilution standard solution or stock standard solutions and the internal standards and surrogate analytes. The CAL solutions are used to calibrate the instrument response with respect to analyte concentration.

2.1.7. Procedural Standard Calibration. A calibration method where aqueous calibration standards are prepared and processed (e.g., purged, extracted and/or derivatised) in exactly the same manner as a sample. All steps in the process from addition of sampling preservatives through instrumental analyses are included in the calibration. Using procedural standard calibration compensates for any inefficiencies in the processing procedure.

2.2. Interferences

2.2.1. Analyses of laboratory reagent blanks provide information about the presence of contaminants. When potential interfering peaks are noted in laboratory reagent blanks, the analyst should search for the source, including instrument, glassware, reagents, or solvents. Subtracting blank values from sample results is not permitted.

2.2.2. Interfering contamination may occur when a sample containing low concentrations of method analytes is analyzed immediately after a sample containing relatively high concentrations of method analytes. A preventive technique is analyzing blank samples between environmental samples.

2.2.3. Waste water samples have to be diluted prior to analysis in order to avoid any interference during pre-concentration and analysis.

2.3. Instrumentation

2.3.1. HPLC system: Pflexar 100 PercinElmer
2.3.2. Mass spectrometer: AB Sciex 3200 Q TRAP MS/MS System
2.3.3. Visiprep Vacuum Manifold with Disposable Liner
2.3.4. Equipment and supplies:
2.3.4.1. Separation column: Kinetex 2,6 µ XB-C18 100A 50x2.1 mm
2.3.4.2. Brown glass bottles, nominal volume 1000 mL
2.3.4.3. Glass bottles with screw cap, volume: 500 mL
2.3.4.4. Vials: 1 mL and 10 mL from Supelco
2.3.4.5. Micro vial inserts from WGA, volume: 100 µL
2.3.4.6. Graduated cylinders, nominal volume: 100 mL, 250 mL, 500 mL, 1000 mL
2.3.4.7. Volumetric flasks, nominal volume: 10 mL, 25 mL
2.3.4.8. Syringes (5 µL, 10 µL, 25 µL, 50 µL, 100 µL, 500 µL) from Hamilton or Agilent Technologies
2.3.4.9. Analytical balance from Sartorius
2.3.4.10. pH Meter from Schott instruments
2.3.4.11. Drying oven

2.4. Chemicals

2.4.1. Solvents. All solvents have to be of p.a. purity and shall be stored at room temperature.
2.4.1.1. Acetonitrile
2.4.1.2. Methanol
2.4.2. Reagents. All reagents have to be of p.a. purity and shall be stored at room temperature.
2.4.2.1. Ammonium acetate
2.4.2.2. Triethylamine
2.4.2.3. 1 M Sodium hydroxid
2.4.2.4. Hydrochloric acid, 32%
2.4.2.5. Acetic acid, conc.
2.4.2.6. Demineralised and decoct water
2.4.2.7. Ethylenediaminetetraacetic acid (EDTA disodium salt)
2.4.2.8. Sodium azide
2.4.3. SPE Material
2.4.3.1. Isolute ENV+ from Separtis
2.4.4. Method analytes
2.4.5. Stock standard solutions

All analytes must be purchased from SIGMA ALDRICH as standard quality. The reference materials have to be stored according to the recommendations from the manufacturer.

For each of the target compounds a separate stock solution in methanol is prepared. Their concentrations depend on the solubility of the target compounds in methanol. For the preparation of each of the stock solutions, between 1 and 10 mg of the pharmaceutical compound are added on an analytical balance to a 10 mL volumetric flask. The volumetric flask is filled up to volume with methanol. From the exact weight of the antibiotic and the

volume of methanol, the exact concentration of the stock solution is calculated taking into account the purity of the target compounds. The stock solutions have to be stored in the freezer and are stable for 1 year.

2.4.6. Primary Dilution Standard (PDS) of the target compounds. Few mL of methanol are added to a 25 mL volumetric flask. Then a defined volume of each stock solution of the method analytes is added with a syringe to achieve a concentration of 1 ng/µL. The volumetric flask is filled up to volume with methanol. The PDS of the target compounds has to be stored in the freezer and is stable for 3 months.

2.4.7. Standard mixture for Quality Control Sample. The standard mixture for the QCS contains the following antibiotics: chloroamphenicol, roxithromycin, clarithromycin. For preparation of the standard mixture for the QA/QC sample, few mL of methanol are added to a 25 mL volumetric flask. A defined volume of each stock solution of the target compounds is added with a syringe to achieve a final concentration of 1 ng/µL. Then the volumetric flask is filled up to volume with methanol.The QA/QC sample of the target compounds has to be stored in the freezer and is stable for 6 months.

2.4.8. Solvent mixture for reconstitution of the dry residue. In a 100 mL graduated cylinder a mixture of 5 parts per volume acetonitrile and 95 parts per volume of an aqueous solution of 20 mM ammonium acetate is prepared. This solution can be stored in the refrigerator for a maximum of 1 week.

2.4.9. Calibration samples of target compounds. Eight glass bottles (V = 1000 mL) are filled with 500 mL tap water with a graduated cylinder. Then different volumes of the standard mixture of the target compounds (see Section 2.4.6.) are added with a syringe. The added volumes as well as the resulting concentration levels are given in Table 7-1 in the Annex.

2.4.10. Eluent A: Aqueous 20 mM ammonium acetate solution. An aqueous 20 mM ammonium acetate solution is prepared in a 500 mL glass bottle with screw cap. This solution can not be stored and has to be prepared freshly for each day of analysis.

2.4.11. Eluent B: 2:1 (v:v) mixture of acetonitrile and methanol. In a 500 mL glass bottle with screw cap, two parts per volume acetonitrile are mixed with one part per volume of methanol by using a graduated cylinder. Then a defined amount of ammonium acetate is added to achieve a final concentration of 20 mM. This solution can be stored at room temperature for a maximum of 1 week.

2.4.12. Elution solvent. In a 100 mL graduated cylinder a mixture of 90 parts per volume acetonitrile, 10 parts per volume of demineralised and decoct water and 0.5 parts per volume of triethylamine is prepared. This solution can not be stored and has to be prepared a new each day of analysis.

2.5. Sample collection, preservation and storage

2.5.1. Sample Collection and Dechlorination. Sampling is done in 1000 mL brown glass bottles. If samples, such as finished drinking waters, are suspected to contain residual chlorine, 100 mg of sodium thiosulfate should be added for each 1000 mL of water sample.

2.5.2. Sample Storage. Storage of samples is done in the cold storage room at 4 °C and must not exceed a time period of 3 weeks. Extracts must be stored in the freezer and are stable for at least 2 weeks.

2.5.3. Sample preservation. For preservation of surface water, groundwater and drinking water samples 100 mg/L sodium azide are added immediately after sampling.

2.6. Procedure

2.6.1. Extraction. First 1.3 g of ethylendiaminetetraacetic acid are added to 500 mL of water sample. Then the sample is adjusted to pH 5 by addition of 32% hydrochloric acid or 1 M NaOH. PH is checked with a pH meter. Conditioning of 100 mg Isolute ENV+material is done automatically (Autotrace system) with 5 mL acetonitrile and subsequently with 5 mL demineralised and decoct water. For pre-concentration of the target analytes, the pH adjusted water sample is automatically pumped through the conditioned SPE material. Flow rate is 7.0 mL/min. After pre-concentration the SPE material is dried for 30 min. with nitrogen gas. Elution of the target analytes is done automatically with 5 mL acetonitrile and 5 mL of elution solvent (see Section 2.4.12.). After passing through the SPE material the elution solvent is collected in a 10 mL vial. The solvent is completely evaporated in a stream of nitrogen. The dry residue is reconstituted with 100 µL of the solvent mixture (see Section 2.4.8.). Then, the sample is ready for HPLC/MS-MS analysis.

2.6.2. HPLC/MS-MS analysis.
AB Sciex 3200 Q TRAP MS/MS System Interface:
Electrospray
Spray position: z = 4.0 y = 3.5
Heater temperature: 200 °C (300 °C for analysis of chloroamphenicol)
Nebuliser Gas (GS1): 45 units
Heater Gas (GS2): 45 units
Ionisation mode: positive (negative for analysis of chloroamphenicol)
Ionisation voltage: +5500 V (–4200 V for analysis of chloroamphenicol)
Curtain gas: 20 units
CAD: 3.00
All other parameters depend on the compounds and are documented in the laboratory.

2.6.2.1. Operation of the HPLC/MS-MS system. Operation of the HPLC/MS-MS system is done as described in the manufacturer's manual. Prior to analysis of environmental samples, a blank run is started to check the pressure conditions and to flush the column with solvent. For checking the MS detector, a standard solution is analysed. 25 µL of the standard mixture of the target compounds are evaporated to dryness in a stream of nitrogen and reconstituted with 100 µL of the solvent mixture (see Section 2.4.8.). Subsequently,

12.5. µL are injected into the HPLC/MS-MS system. Criteria for checking the performance of the system are signal height, retention time and peak performance.

2.6.2.2. Calibration. Calibration is done for the overall procedure. Calibration samples are prepared as described in Section 2.4.9. and analysed. A new calibration is prepared for each batch of samples or whenever the QA/QC sample gives striking results.

2.7. Data analysis and calculations

2.7.1. Complete chromatographic resolution is not necessary for accurate and precise measurements of analyte concentrations if unique ions with adequate intensities are available for quantitation. If the response for any analyte exceeds the linear range of the calibration established in Section 2.6.2.2., obtain and dilute a duplicate sample. Do not extrapolate beyond the calibration range.

2.7.2. Evaluation of the chromatograms, i.e. correlation of retention times and mass spectra to target compounds and determination of the peak areas is done by the software tool Analyst 1.2. If necessary, manual integration is done.

2.7.3. Linear calibration functions are established by plotting the peak area of the respective target analyte against the concentration of the target analyte in the respective calibration solution.

2.7.4. The recovery for the overall procedure is determined by a comparison of peak areas of pre-concentrated samples and direct injections according to the following equation: with Ypre-concentrated = peak area of a compound after pre-concentration Ydirect = peak area of a compound after direct injection. The recovery is determined each time that the batch of SPE material or elution solvent is changed.

2.8. Quality control

2.8.1. QC requirements. Quality control (QC) requirements are the initial demonstration of laboratory capability followed by regular analyses of laboratory reagent blanks, field reagent blanks, and laboratory fortified blanks. A MDL for each analyte must also be determined. Each laboratory must maintain records to document the quality of the data generated. Additional quality control practices are recommended.

2.8.2. Laboratory Blanks. With each batch of samples processed as a group within a work shift, analyze a LRB to determine the background system contamination.

2.8.3. Calibration Check. In order to check the calibration, a LFB is processed with each batch of samples. For each of the method analytes the result of the LFB must be within 30% of the spiked concentration. If the deviation between spiked and measured concentration exceeds this range, appropriate measures must be taken to improve the quality of analysis before analysis of environmental samples can be continued.

2.8.4. QC control chart. For QA/QC purposes control charts are used. A QA/QC sample is analysed each day of analysis.

2.8.4.1. The QA/QC samples are prepared by adjusting 500 mL of tap water to a pH of 5 by addition of 32% hydrochloric acid or 1 M NaOH. Then 100 μL of the standard mixture for the QA/QC sample are added. The QA/QC sample is treated as any environmental sample according to the procedure described in Section 2.6.0. The results of these QA/QC measurements for sulfamethoxazole, trimethoprim and ronidazole are evaluated and documented in control charts by the SQS software from Perkin Elmer.

2.9. Pollution prevention

No solvents are utilized in this method except the extremely small volumes of methanol and acetonitrile needed to prepare calibration standards and elution solvents. The only other chemicals used in this method are the neat materials in preparing standards and sample preservatives. All are used in extremely small amounts and pose no threat to the environment.

2.10. Waste management

SPE cartridges are only used once and are disposed with the domestic waste. Solutions containing solvents are collected in glass bottles. Full glass bottles are shipped to a special unit for proper waste disposal.

3. Results

Prof. H.-J. Brauch and Dr. F. Sacher and coworkers [10] worked out a very good procedure for analyzing sulfonamides and some other antibiotics in surface, ground and drinking waters. The method originaly was developed the following seven compounds:

Table 1

The compounds that the method was originaly developed

Sulfonamides	Q1	Q2	Q3	RT (min)
1 Sulfadiazine	251	92	156	1,29
2 Sulfadimidine	279	108	186	3,4
3 Sulfamerazine	265	65	108	2,1
4 Sulfamethoxazole	271	254	156	6,71
5 Trimethoprim	291	230	123	1,91
6 Metronidazole	172	128	82	8,6
7 Ronidazole	201	140	55	0,53

We successfully adapted and extended this method additional seventeen sulfonamid antibiotics. During our experiment we checked and determined the LOQ of all analytes and summarised the recovery results two different levels. *(Table 2)*

Table 2

Sulfonamid antibiotics that the method was adapted and extended

Sulfonamides	Q1	Q2	Q3	RT (min)
1 Sulfabenzamide	277	108	156	10,04
2 Sulfacetamide	215	108	156	1,01
3 Sulfaquinoxaline	301	108	156	11,41
4 Sulfadoxine	311	108	156	8,6
5 Sulfaguanidine	215	108	156	0,53
6 Sulfameter	281	108	156	3,46
7 Sulfamethizole	271	108	156	3,58
8 Sulfamethoxypyridazine	281	108	156	4,03
9 Sulfamoxole	268	108	156	3,3
10 Sulfanilamide	173	108	156	0,57
11 Sulfapyridine	250	108	156	1,77
12 Sulfadimethoxine	311	108	156	11,22
13 Sulfamonomethoxine	281	108	156	5,69
14 Sulfathiazole	256	108	156	1,63
15 Sulfisomidine	279	108	124	1,05
16 Sulfisoxazole	268	108	156	9,35
17 Sulfachloropyridazine	285	108	156	5,47

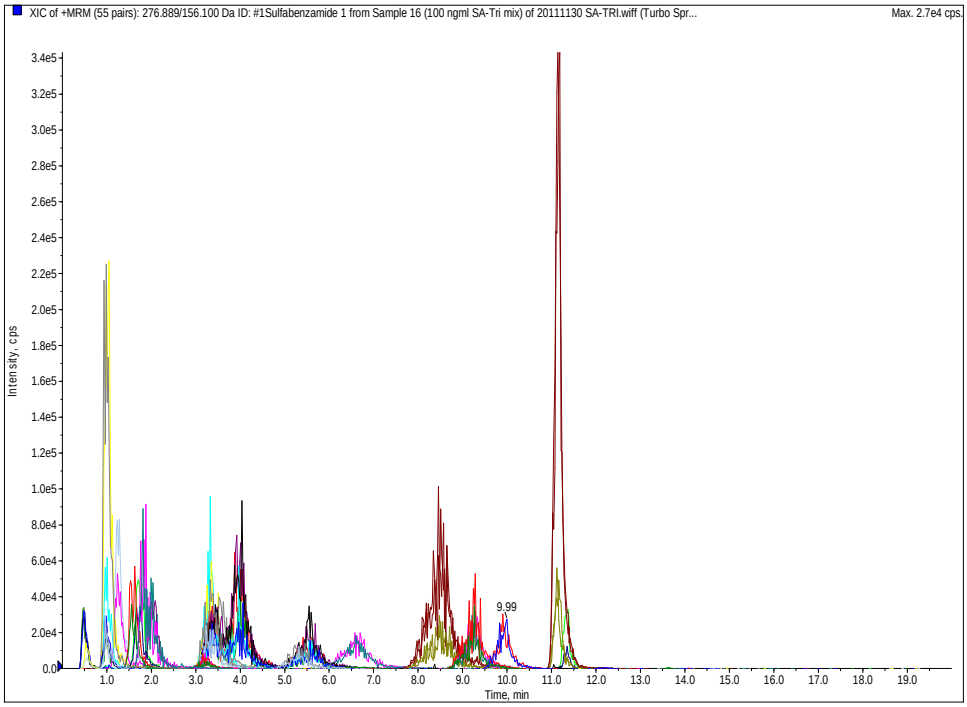

Figure 1: Total ion chromatogram of 24 antibiotics

After pH adjustment the target compounds are pre-concentrated by solid-phase extraction onto a hydroxylated styrene-divinylbenzene polymer. Elution of the target compounds is done by a mixture of acetonitrile, water and triethylamine. After evaporation of the solvent and reconstitution of the dry residue, an aliquot is injected into the HPLC/MS system. Method detection limits (MDLs) depend on the compound and on the matrix. For surface, ground and drinking waters the MDLs for all method analytes are in the range of 10 ng/L. The application range is approximately 10–500 ng/L. Samples with higher concentrations have to be diluted before extraction.

Table 3

Recovery results for the determined sulfonamid antibiotics

Sulfonamides	**LOQ (ng/l)**	**R% 10ng/l**	**n**	**RSD**	**R% 100ng/l**	**n**	**RSD**
Sulfadiazine	1	81,3	5	6,8	93,1	5	7,1
Sulfadimidine	1	86,2	5	7,5	87,1	5	7,6
Sulfamerazine	1	79,6	5	10,1	80,3	5	9,3
Sulfamethoxazole	1	87,9	5	11,2	85,3	5	10,3
Trimethoprim	1	92,1	5	9,3	89,6	5	10,1
Metronidazole	1	88,6	5	9,8	87,1	5	8,9
Ronidazole	1	89,4	5	6,7	85,6	5	7,6
Sulfabenzamide	2	81,9	5	8,2	82,1	5	11,2
Sulfacetamide	1	96,1	5	5,8	94,3	5	5,6
Sulfaquinoxaline	2	83,6	5	8,9	84,2	5	9,7
Sulfadoxine	1	89,3	5	7,2	90,1	5	8,4
Sulfaguanidine	1	79,9	5	11,3	82,1	5	12,3
Sulfameter	1	85,2	5	7,3	88,4	5	8,9
Sulfamethizole	1	85,0	5	7,9	86,1	5	8,8
Sulfamethoxypyridazine	1	82,1	5	8,5	83,1	5	13,1
Sulfamoxole	2	80,9	5	9,6	81,2	5	9,8
Sulfanilamide	5	92,3	5	5,9	92,1	5	8,2
Sulfapyridine	1	91,6	5	6,4	93,1	5	7,9
Sulfadimethoxine	1	92,1	5	6,9	92,6	5	8,1
Sulfamonomethoxine	1	87,2	5	7,1	88,4	5	7,9
Sulfathiazole	1	83,3	5	10,2	84,1	5	13,1
Sulfisomidine	1	88,1	5	8,4	89,1	5	9,5
Sulfisoxazole	1	83,1	5	9,2	84,3	5	10,8
Sulfachloropyridazine	3	91,6	5	6,8	92,1	5	8,1

4. Conclusion

The extended multi residue method is useable to determine a lot sulfonamide and others antibiotics in surface, ground and drinking waters. Under optimal conditions, the method detection limits achieved were in the range 1–5 ng/L for surface water samples. The instrumental repeatability, expressed as RSD, was usually below 15% for the different water matrices. The recovery results were betveen 70–110% at levels of 10–100 ng/l.

List of symbols

SPE	solid phase extraction
LC	liquid chromatography
MS	mass spectrometry
MS/MS	tandem mass spectrometry
SRM	selected reaction monitoring
RSD	relative standard deviation
LOQ	limit of quantification
RT	retention time
Q	Qualifier ion
pK_a	acid dissociation constant
MDL	method detection limit
LRB	laboratory reagent blank
LFB	laboratory fortified blank
PDS	primary dilution standard
QCS	qualitycontrol sample
CAL	calibration standard
QA/QC	quality assurance/quality control

"Acknowledgement. The described work was carried out as part of the TÁMOP-4.2.1.B-10/2/KONV-2010-0001 project in the framework of the New Hungarian Development Plan. The realization of this project is supported by the European Union, co-financed by the European Social Fund."

REFERENCES

[1] http://www.britannica.com/EBchecked/topic/37246medicine/35670/Sulfonamide-drugs
[2] http://blogofbad.wordpress.com/2009/02/09/bad-health-elixir-sulfanilamide/
[3] http://home.att.net/~steinert/wwii.htm#The%20Use%20of%20Sulfanilamide%20in%20World%20War%20II
[4] http://books.google.com/?id=5kkEAAAAMBAJ&lpg=PA81&dq=sulfa%20ravensbruck&pg=PA81#v=onepage&q=sulfa%20ravensbruck&f=false.
[5] http://www.adl.org/education/dimensions_19/section3/experiments.asp
[6] http://www.onsettx.com/docs/clarifoam/Clarifoam%20EF%20Prescribing%20Information_PN%202603-pf_Rev%202.pdf
[7] SA Tilles: *Practical issues in the management of hypersensitivity reactions: sulfonamides.* Southern Medical Journal 94 (8): 817–24., 2001.
[8] CG Slatore–Tilles, S: *Sulfonamide hypersensitivity.* Immunology and Allergy Clinics of North America 24 (3): 477–90.,VII., 2004.
[9] Brackett, C. C.–Singh, H.–Block, J. H.: *Likelihood and mechanisms of cross-allergenicity between sulfonamide antibiotics and other drugs containing a sulfonamide functional group.* Pharmacotherapy 24 (7): 856–70., 2004.
[10] Sacher, F.–Lange, F. T.–Brauch, H.-J.–Blankenhorn, I.: *Pharmaceuticals in groundwaters-Analytical methods and results of a monitoring program in Baden-Württemberg, Germany.* J. Chromatogr. A 938:199–210., 2001.

Geosciences and Engineering, Vol. 1, No. 1 (2012), pp. 159–165.

DETERMINATION OF NATURAL GROUNDWATER RECHARGE WITH THE HELP OF GROUNDWATER MODELING AND TRITIUM FIELD MEASUREMENTS

[1]LÁSZLÓ KOMPÁR–[2]PÉTER SZŰCS–[3]LÁSZLÓ PALCSU–[4]JÓZSEF DEÁK
[1]PhD student, [2]Head of Department, Professor, [3]Head of Department, [4]Managing director
[1, 2]Department of Hydrogeology and Engineering Geology, University of Miskolc
[3]Institute of Nuclear Research of the Hungarian Academy of Sciences
[4]GWIS Ltd.
[1, 2]3515 Miskolc-Egyetemváros, Hungary, [3]18./C Bem tér 4026 Debrecen, Hungary
[4]45. Alkotmány u. 2120 Dunakeszi, Hungary
[1] hgkompar@uni-miskolc.hu, [2] hgszucs@uni-miskolc.hu, [3] palcsu@atomki.hu, [4] deak47jozsef@gmail.com

Abstract
The Duna–Tisza region is one of the largest recharge area in Europe. There is an international project, which is coordinated by the IAEA to investigate the natural groundwater recharge at some test places in Europe. In Hungary a special research group carries out this special research program at a sampling site named Méntelek. The aim of this research is to build a flow and transport model for the sample site, which is based and calibrated on tritium isotope measurements. After the field investigations we could estimate the annual groundwater recharge and we could understand the underground hydraulic situation of this area.

1. Introduction

A quantification of natural groundwater recharge was performed using environmental tracer techniques, mainly based on use of bomb peak tritium and the $^3H/^3He$ technique at suitable locations using multilevel wells in Hungary [1]. A special transport model based on the MODFLOW and MT3DMS packages was built, which was calibrated by the measured tritium contents under the surface at different depths.

2. Materials and methods to estimate groundwater natural recharge

The ^3H is the radioactive isotope of the hydrogen. The only difference is the number of the neutrons. The tritium is formed in the upper atmosphere during $-\beta$ decay. It has a half time, during the tritium decays to ^3He, which is 12,4 years in this case. The content of the tritium is usually measured in Tritium Units, where 1 TU is defined as the ratio of 1 tritium atom to 10^{18} hydrogen atoms. Near natural conditions this content is 2–10 TU. From the 1950s the high-altitude nuclear tests introduced large amounts of tritium into the atmosphere. Because the short half-time of the tritium we can get some information from the last 50 years happening.

Tritium isotopic measurements were applied at the lysimeter site in Méntelek, which is 12 km far from Kecskemét. The test area is located on the Great Hungarian Plain between the Danube and Tisza rivers. The aim of the field measurements was get more information from the well-nest, which was built in 1998. This well-nest contains 4 smaller diameter wells. Each well filters different layers in different depth.

Figure 1: Groundwater level measurement in the well-nest

This area is a typical recharge area with nearly vertical groundwater flow [2, 3]. This is the reason why this place was selected as a test area in Hungary. Tritium contents profile was measured here in 1998 at 11 different levels under the surface [4]. A numerical transient transport model was created covering the 60-year-long time period between 1951 and 2010. The tritium content of the Hungarian precipitation was estimated for this period using measured data of Hungarian precipitation since 1972 [4], wine samples of 1960 to 1977 [5] and GNIP data of Vienna and Ottawa.

The research site in Méntelek developed in the early 1950s. Some hydrological parameter became measurable, like: groundwater level, groundwater temperature, soil temperature, precipitation, evaporation, interception, solar radiation and wind velocity. Some lysimeter stations were also developed for monitor the groundwater recharge in 1955.

For the investigation of the general geological characterization of the site, a trench was deepened. The sampling showed that the main rock in this region is the sand, and the gravel-sand. At the lower parts the clayey sand and clay are the dominant components. The change of the moisture content was established on the soil profile. The horizontal hydraulic conductivity was estimated about $5*10^{-5}$ m/s, the vertical component is lower with 2 orders of magnitude with the depths.

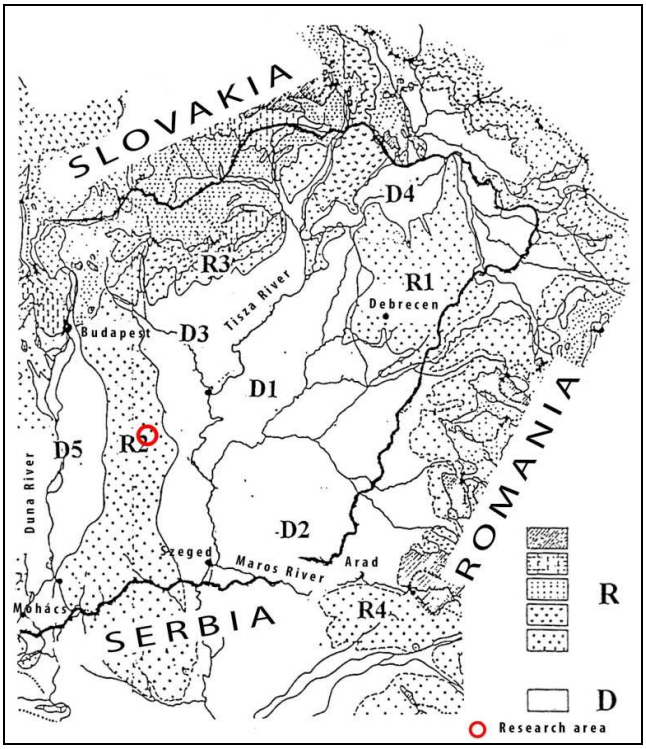

Figure 2: The Duna–Tisza region is the main recharge area in Hungary

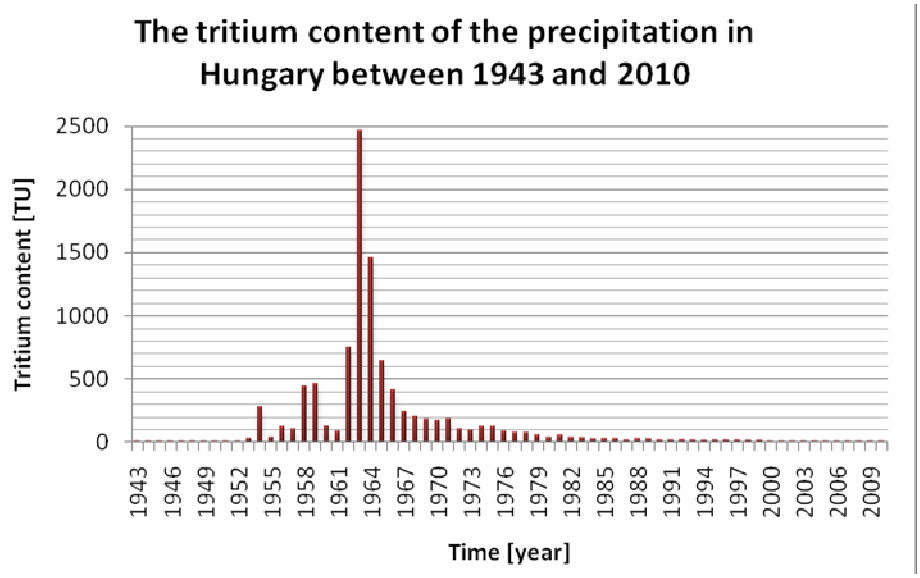

Figure 3: The tritium content of the precipitation in Hungary

Based on these data and information the transient tritium transport model was calibrated with the field data from 1998. Nearly perfect match was achieved between the measured and simulated tritium data. The calibration result confirmed the reliability of the transport model [6]. As a result, the average groundwater recharge and the dispersion behavior of the investigated subsurface layers were determined. The derived average groundwater recharge is 53 mm/year and the vertical dispersivity is 0.3 m.

The new tritium profile at four different depths was also measured in Méntelek in 2010. Based on these results a new calibration will be carried out to determine how the average recharge changed between 1998 and 2010. This would be a significant result, because this new value can reflect whether there is a change in groundwater recharge due to climate change. This new transport model calibration will be carried out in March 2012.

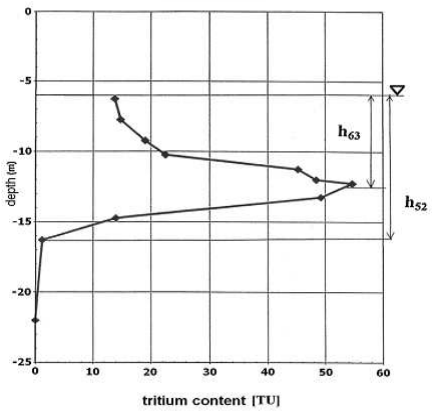

Figure 4:
The tritium profile from 1998

Table 1

The measured tritium contents

Méntelek, 1998.12.05	
depth [m-m]	tritium [TU]
6–6,5	13,8
7,5–8,0	14,8
9–9,5	19,1
10–10,5	22,5
11–11,5	45,3
11,5–12,5	48,5
12–12,5	54,7
13–13,5	49,3
14,5–15	14,0
15,8–16,9	1,2
21,1–23,1	0,0

Groundwater flow and transport modeling and simulations based on the all available information can help the decision makers to find the most effective and environment friendly solutions. In our case the Processing MODFLOW for Windows 7.0 (PMWIN Pro) software [7] was used for natural groundwater recharge estimation. The finite-difference MODFLOW 2000 module [8] is an industrial standard used to create accurate and reliable 3-dimensional groundwater flow models. The PMWIN Pro can handle contamination transport processes using its well-known MT3DMS program. In most cases transient-state simulations are required to follow up the consequences of the time dependent processes.

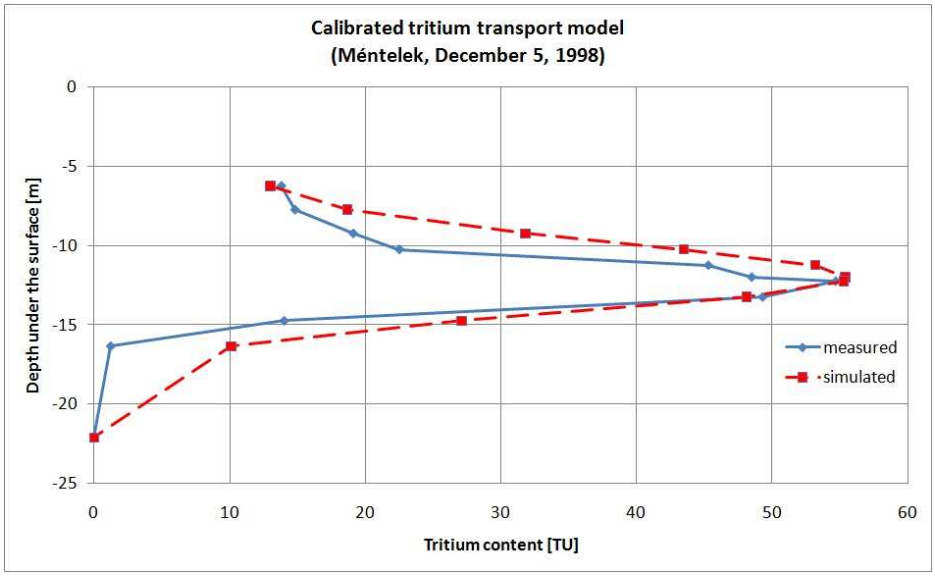

Figure 5: The measured and calculated tritium profile under the surface based the calibrated tritium transport model

MODFLOW is a U.S. Geological Survey modular finite-difference flow model. This computer code can solve the groundwater flow equation. The governing partial differential equation solved numerically in MODFLOW is given in the following form:

$$\frac{\partial}{\partial x}\left(K_{xx}\frac{\partial h}{\partial x}\right)+\frac{\partial}{\partial y}\left(K_{yy}\frac{\partial h}{\partial y}\right)+\frac{\partial}{\partial z}\left(K_{zz}\frac{\partial h}{\partial z}\right)+W=S_S\frac{\partial h}{\partial t} \qquad (1)$$

Where K_{xx} $K_{yy,}$ and K_{zz} are the values of the hydraulic conductivity along the x, y and z coordinate axes (L/T), h is the hydraulic head (L), W is the volumetric flux per unit volume representing the sources and sinks of groundwater, for which the negative values denote extractions while the positive values denote injections (T^{-1}), S_S is the specific storage of the investigated aquifer (L^{-1}) and t is time (T). This program is widely used throughout the world by hydrogeologists to simulate the flow of groundwater through aquifers. The code is free software, written in the FORTRAN language and can be compiled and run on the DOS, Windows or UNIX operating systems. Since its original development in the early 1980s [9], the USGS have released four major versions of this code, and is now considered to be the de facto standard industrial code among the groundwater specialists for aquifer simulation. Currently, there are many actively developed commercial and non-commercial graphical user interfaces for MODFLOW.

The MODFLOW-2000 version was released on July 20, 2000. Many new packages and enhancements were also released, including new solvers and stream and saturated flow packages. The following packages of MODFLOW-2000 were used to describe the different source and sink terms during the above-mentioned simulation activity of the present

studies: General-Head Boundary, Drain, Evapotranspiration, Reservoir, Lake and Well and Recharge.

There are several graphical interfaces to MODFLOW, which often include the compiled MODFLOW code. These programs provide convenient means of supplying the input data for creating MODFLOW models. Commercial MODFLOW programs are typically used by governments and consultants for practical applications of MODFLOW to real-world groundwater problems. The applied PMWIN-Pro may be considered as a professional commercial version of MODFLOW. A three-dimensional flow model considering forty-four-layers was implemented with the help of the MODFLOW-2000 module in the current project work. This model was used to characterize the nearly vertical groundwater flow of the investigated area in Méntelek, which a main recharge region on the Hungarian Great Plain [10]. The input data required for the flow model were readily available from an earlier geological and hydrogeological prospecting activity. The flow model was first calibrated to the measured groundwater level data prior to the simulation of the natural groundwater recharge phenomena [11]. The calibrated flow model describes the real groundwater flow system quite accurately. Therefore the calibrated well-working flow model could be used to simulate successfully the different recharge scenarios. Besides the flow model, a transport model was also built to investigate tritium concentration distribution under the surface due to the groundwater recharge from precipitation. The tritium transport movement investigations were carried out in the field-study by the help of the MT3DMS model [12], where MT3D stands for the Modular 3-dimensional transport model and MS denotes the multi-species structure for accommodating add-on reaction packages. MT3DMS has a comprehensive set of options and capabilities for simulating the advection, dispersion, diffusion, radioactive decay and chemical reactions of contaminants in groundwater flow systems under the general hydrogeologic conditions. The MT3DMS was developed for use with any finite-difference flow model such as MODFLOW, and is based on the assumption that changes in the concentration field will not affect the flow field appreciably.

The partial differential equation describing the fate and transport of chemical components or contaminants of the species *k* in a three-dimensional space in transient groundwater flow systems can be written as follows:

$$\frac{\partial\left(\phi C^{k}\right)}{\partial t}=\frac{\partial}{\partial x_{i}}\left(\phi D_{ij}\frac{\partial C^{k}}{\partial x_{j}}\right)-\frac{\partial}{\partial x_{i}}\left(\phi v_{i}C^{k}\right)+q_{s}C_{s}^{k}+\sum R_{n} \tag{2}$$

Where ϕ denotes porosity of the aquifer, dimensionless, (fraction), C^k is the dissolved concentration of species k, (M/L^3), t is time (T), $x_{i,j}$ is distance along the respective Cartesian coordinate axis (L), $D_{i,j}$ is the hydrodynamic dispersion coefficient tensor (L^2/T), v_i is the seepage or linear pore water velocity based on the Darcy equation L/T), q_s is the volumetric flow rate per unit volume of aquifer representing fluid sources and sinks(1/T), C_s^k is the concentration of the source or sink flux for species *k* (M/L^3) and $\sum R_n$ is the chemical reaction term ($M/L^3/T$).

3. Conclusion

Nowadays the isotope hydrology is the most accurate tool for the determination of relative groundwater age. A hydrodinamic and transport model can be a useful and practical solution for the reliable estimation of natural groundwater recharge conditions. These special calculations are based on the dating of the groundwater. In this case the appropiate isotope tool was the tritium technique. With the measured and appropiate data the transport model became calibrated, so the model run realistic. The obtained results give new information to understand the groundwater flow behavior of the Hungarian Great Plain.

"Acknowledgement: This work was carried out as part of the TÁMOP-4.2.1.B-10/2/KONV-2010-0001 project in the framework of the New Hungarian Development Plan. The realization of this project is supported by the European Union, co-financed by the European Social Fund."

REFERENCES

[1] Juhász, J.: *Hydrogeology* (in Hungarian). Academy Publisher, Budapest, 2002, 1–1176.
[2] Erdélyi, M.: *Outlines of the Hydrodynamics and Hydrochemistry of the Pannonian Basin.* Acta Geologica Academiae Scientiarum Hungaricae, Tomus 20, (3–4) 287–309. 1976.
[3] Deák, J.: *Comparison of groundwater flow modelling and environmental isotope results on the Great Hungarian Plain, in Use of Isotopes for Analyses of Flow and Transport Dynamics in Groundwater Systems*. IAEA Vienna, Results of a co-ordinated research project 1996–1999. 2002.
[4] Deák, J.: *Isotope hydrological study of the groundwater flow regime of Danube–Tisza interfluvial area* (in Hungarian with English abstract). PhD Thesis, Eötvös L. University of Budapest, 2006, 1–101.
[5] Kozák, K.: *Reconstruction of environmental tritium content for 1960 to 1977 by analyzes of bottled wine samples of known ages* (in Hungarian with English abstract). PhD Thesis, Eötvös L. University of Budapest, 1980, 1–63.
[6] Szűcs, P.–Civan, F.–Virág, M.: *Applicability of the most frequent value method in groundwater modeling.* Hydrogeology Journal, 2006, 14: 31–43.
[7] Chiang, W.H.–Kinzelbach, W.: *3D-Groundwater modeling with PMWIN. A simulation system for modeling groundwater flow and pollution.* Springer-Verlag, 346. 2001.
[8] Harbaugh, A.W.–Banta, E. R.–Hill, M.C.–McDonald, M. G.: *MODFLOW-2000. The U.S. Geological Survey Modular Ground-Water Model – User guide to modularization concepts and the ground water flow process.* U.S. Geological Survey, Open-File Report 00–92. 2000.
[9] McDonald, M. G.–Harbaugh, A.W.: *The History of MODFLOW.* Ground Water, 41 (2), 280–283. 2003.
[10] Tóth, J.: *Hydraulic continuity in large sedimentary basins.* Hydrogeology Journal (3), no. 4, 4–16., 1995.
[11] Szűcs, P.–Ritter, Gy.: *Improved interpretation of pumping test results using simulated annealing optimization.* ModelCARE 2002, Proceedings of the 4th International Conference on Calibration and Reliability in Groundwater Modeling. Prague, 17–20 June 2002. ACTA UNIVERSITAS CAROLINAE – GEOLOGICA 2002, 46 (2/3), 238–241., 2002.
[12] Zheng, C.–Wang, P.: *MT3DMS: Modular Three-Dimensional Multispecies Transport Model for Simulation of Advection, Dispersion and Chemical Reactions of Contaminants in Groundwater Systems.* Documentation and User's Guide. U.S. Army Corps of Engineers, Contract Report SERDP-99-1, 1–169., 1999.

Geosciences and Engineering, Vol. 1, No. 1 (2012), pp. 167–176.

HUNGARIAN GEOTHERMAL ENERGY IN THE COMMON VISION OF THE EUROPEAN RENEWABLE ENERGY

ATTILA KUJBUS
University of Miskolc, Faculty of Earth Science and Engineering
3515 Miskolc-Egyetemváros
akujbus2010@gmail.com

Abstract
The increasing significance of the renewable energy resources and also the geothermal energy as an admirable development opportunity of the Hungarian energy sector are well known in Europe. During the last year the Hungarian National Renewable Energy Action Plan and the Energy Strategy till 2030 were issued. The two documents show the direction for the domestic geothermal energy. It is important to review the opportunities and constraints of the Hungarian geothermal energy sector in connection with the development of European renewable energy resources and European geothermal energy.

1. Common Vision of the Renewable Energy Heating and Cooling Technology Platform

The vision of the European renewable energy (RE) sector depends on the economy politics of the European Union, because RE needs financial supports and subsidies in order to improve their competitiveness. As a product every renewable energy source is in the early phase of its lifecycle in spite of the century long traditions of some RE resources. Only wind energy provided a kind of boom but it is also little compared to the real technical opportunities.

A few years ago Renewable Energy Heating-Cooling Technology Platform (RHC-TP) has been established and aimed to support the development of RE sources [1]. In May 2011 in Budapest, in the 2nd Annual Conference RHC-TP presented its Common Vision for the Renewable Heating and Cooling sector in Europe. This vision assists to estimate the opportunities of the Hungarian geothermal energy in medium and long term.

1.1. Renewable energy potential of Europe

1.1.1. Geothermal energy

Geothermal energy does not have geographical restriction, it exits wherever on the Earth. Ground source heat pumps (GSHP) and enhanced geothermal system (EGS) technologies can be employed in areas with low geothermal potential and without thermal water reservoir as well.

The world record development speed of the Scandinavian peninsula with extreme low geothermal potential *(Figure 1)* is an excellent evidence. Sweden and Norway have started to produce significant geothermal resources and also they are already in the top ten of the World [9].

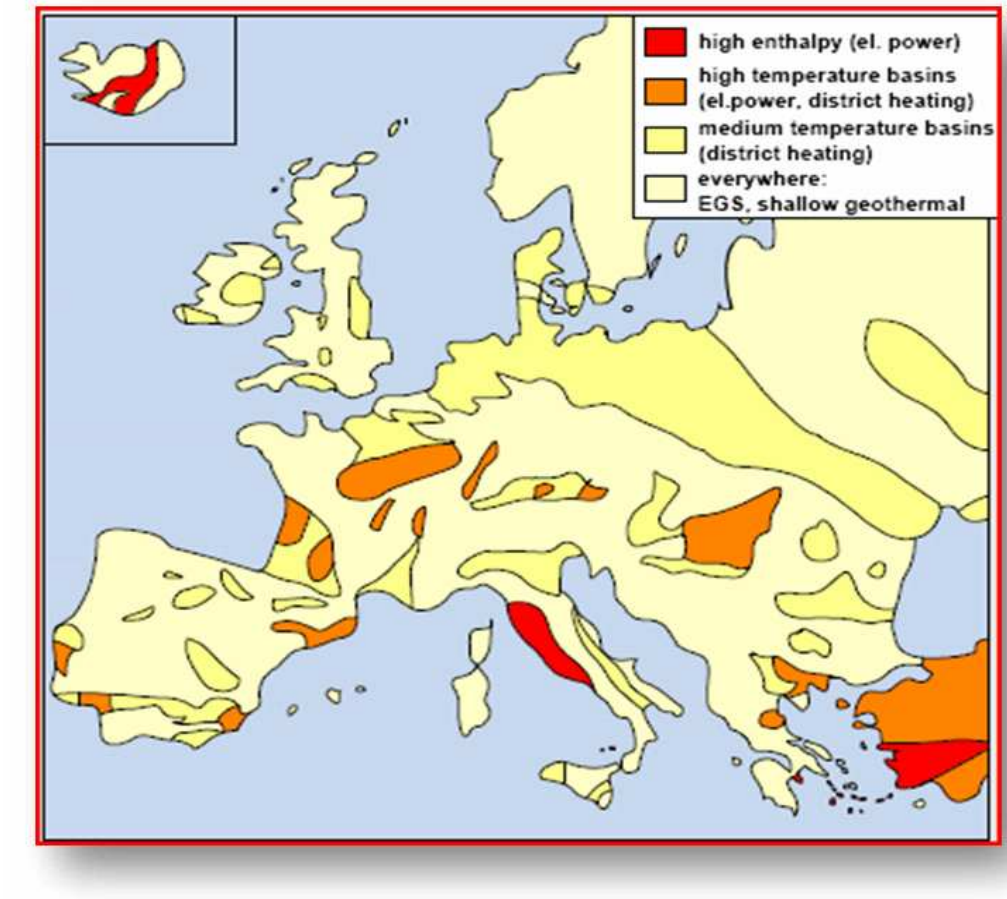

Figure 1: Geothermal potential of Europe (Source: EGEC 2009) [3]

It is no time limitation in the operation of geothermal systems. The operation of geothermal energy production is continuous except for maintenance time and trouble-shooting. Generally 8000 hours operation per year can be planned. In case of solar or wind technology, the operating time is 1700–2100 hours per year.

The different temperature ranges open the door to utilize the heat in different ways. Over 120 ^{o}C temperature range electricity production is to be evaluated. The temperature range between 60 ^{o}C–120 ^{o}C is appropriate for communal heat supply for heating and cooling, district heating and domestic hot water heating.

Where the porosity and permeability were not appropriate for natural formation of hydrothermal systems, GSHP and EGS long term utilization is to be evaluated.

According to the scenario that includes the technology development the EU-27 geothermal heating and cooling production will be 160 TWH by 2020. This value would be increased 1750 TWh by 2050 [4].

1.1.2. Solar energy

Solar thermal technology is suitable for heating water (40–80 ^{o}C) both for domestic and communal supply. There are many units in developed countries (Germany, Sweden, Denmark and Austria) for supply low temperature warm water and manufacturing capacity is also created. The development of combined heating – hot water systems are over the demonstration projects. 100% solar-heated buildings are already constructed in Central-European climate [7].

According to the scenario that includes the technology development the EU-27 solar thermal heating and cooling production will be 190 TWh by 2020. This value is estimated 1552 TWh in 2050 [2]. Solar power production will be increased as well, its result depends on the development of technology and economy.

1.1.3. Biomass

Biomass has already had significant achievements, more than half of the RE heating comes from this energy source in Europe. It surely will be dominant in the future as well. Chiefly wooden and agriculture waste can be the energy source in long term for biomass energy production.

According to the scenario the biomass based heating and cooling energy production will be 1447 TWh in 2020 and 2696 TWh in 2050. The biomass based electricity and biofuel production will also be significant, its size can be similar to the heating and cooling rate.

1.1.4. Hybrid and complex technologies

An important way of the abovementioned future development is the maturation of hybrid and complex technologies. Presently hybrid systems are rare, because even separately, renewable energies are being developed. However, due to research and development new systems will emerge that are at design stage at this moment.

There are already examples of district heating systems as well as heat pumps supplied by two different energy sources. Complex geothermal and biomass power plants, as well as thermal water production wells with solar power and an electricity supplying system can be emerged in the near future.

The development of the three RE source is presented in *Table 1.*

Table 1

Expected growth of the heating and cooling energy production of the three RE resources [RHC]

Energy source	**2007 (TWh)**	**2020 (TWh)**	**2050 (TWh)**
Geotermal	8,4	160	1750
Solar	10	190	1552
Biomass	722	1447	2696
Altogether	743	1797	5998

The presented Vision was formed by RHC-TP experts, based on EUROSTAT method. Presently geothermal and solar energy production has a low rate. They need to develop significantly, in accordance with domestic and European action plans, development strategies.

1.2. Heating and cooling demand of Europe

The existence of heat market fundamentally influences the future of geothermal energy sector. The database of Geothermal World Congress 2010 shows a significant development difference between Northern and Southern Europe. Italy and Turkey have excellent geothermal potential. It is no large heat demand in Italy and Turkey, therefore they develop mainly geothermal based electricity production. However in Northern countries heat demand is strong and heat pumps develop well.

48% of the energy consumption of EU-27 was heating in 2007. 43% of this share supplied households [4]. There are two scenarios to estimate the future.

One estimates no significant changes in heat supply technology or in consumption. The population of Europe doesn't change notably and there will be a lot of energy saving programs. Therefore heating demand of EU-27 decreases by 5% until 2020, the decrease achieves 10% till 2030 and 20% till 2050. The second scenario includes a strong research and development program and the heat demand falls 10% by 2020, 20% by 2030 then 30% by 2050 [4]. Estimations show 470 Mtoe heat demand in 2020.

However cooling demand will increase significantly. According to the RHC-TP in 2020 the cooling demand will be four times higher than in 2010. The increase of the cooling demand is almost as high as the decrease of the heating demand. According to the estimations the increase of the cooling demand is not so significant after 2020.

Due to decreasing of heat demand and increase of renewable energy production, the RE could cover the whole heat demand in EU-27 in the decade of 2030 [4]. It would have three main advantages: decreasing import energy dependence, environment protecting energy supply and energy price reduction because of the technology development and market competition.

2. Technical and Economic Directions of the Development of Geothermal Energy Production

The abovementioned estimations remain only statistics if they don't have technical and economic basis. Experts of RHC-TP declared that the three RE resource possesses the necessary nature potential. The European Union needs a clear vision of the technical and economic development.

2.1. Technical – technological development

The technological development was evaluated in special panels by the experts of RHC-TP. *Table 2* summarizes the main technological directions of the geothermal energy production.

Table 2

Main development lines of the geothermal energy production

Development professional area	**Description of the development**	**Timing, term**	**Advantages**
Reduction of drilling and well completion costs	Optimizing of rig operations and technologies, utilization cheaper tools, instruments and operations	Short (urgent) and long term	Improves the competitiveness of geothermal projects
Reduction of environmental footprint	Emission reduction during construction and operation	Short term	Strengthen the positions of geothermal among RE sources
Surface geophysical acquisitions	Creating models, involving widespread geological and geophysical exploration methods	Middle term	Reducing the geological risk
Binary power plant systems	Better thermodynamic circle and efficiency by changing working fluids and optimizing the cooling system	Short term	Increasing the produced electricity and the competitiveness of the project
Development of raw materials	Materials that resistant to high temperature, pressure, corrosion and erosion	Short term	Widening the utilization both by geography and depth
Production pumps	More stabile units with better regulation and suitable for higher temperature	Middle term	Reducing the parasitic energy and breakdowns
Geological evaluation	Longer range geological concepts with wider approach	Middle term	Significant reduction of geological risk
Modular concepts	Project and technological unit types in every segment of geothermal business	Middle term	Enabling large number of projects and their external financial support
Reinjection 100% of the produced thermal water	Full amount reinjection into the original layers, if no water recharge	Long term	Making the geothermal production sustainable and reduces the emissions
High temperature and pressure instruments	Manufacturing high temperature and pressure instruments	Middle term	Enabling wider range of projects
EGS systems	Comprehensive concepts and models, demonstration projects	Short and middle term	Widening the utilization both by geography and depth
Hybrid systems	Complex technologies with other renewables and traditional energy sources	Long term	Improving competitiveness of geothermal projects
Supercritic systems	Utilization the enthalpy of thermal water over 300 ^{o}C	Long term	Enable projects with large power

2.2. Financial and investment opportunities

The competitiveness of renewable energies to fossil energy resources is limited. One of the main causes of this fact is the undeveloped infrastructure. Investors and political leaders haven't got technical and financial solutions that are appropriate to launch large numbers of projects. There is no stabile manufacturing and servicing background available. Only little number and short experience accumulated concerning the sustainable technologies so far. There are only few well educated, experienced professionals. More demonstration projects and programs need to go forward from this situation. Further supports from the European Union national and regional institutions are needed as financial tools to develop the RE infrastructure.

Financial support of projects
This is the simplest and most popular supporting form in Hungary, it is not so popular in other countries [10]. Formerly KIOP, presently KEOP abbreviated operative program supported and supports a lot of projects in Hungary. This is the main driving force of the domestic geothermal sector, but it isn't enough to achieve the aims of European Vision and the national objectives. It is not appropriate to support technological research and development programs.

Obligatory and subsidized electricity takeover
In Hungary the feed-in tariff system is under reconstruction now. In the countries, where the development of geothermal based electricity is strongly subsidized (Germany, France etc.), the takeover price is over 20 eurocents and further bonuses can be received for combined heat and power and EGS technologies. In order to achieve Hungary's ambitious strategic aims we should join these countries.

Tax allowances
It is common in Europe, in Hungary this subsidy doesn't exist. It is a practical solution in countries, which have tight cash flow, because during the support process the state doesn't need to pay cash [10].

Risk insurance
This support is not a financing tool, because it doesn't improve the profitability of the project. However it is one of the most important, because it handles the two most significant problems of a geothermal project; the geological risk and that this risk emerges at the early phase of the project. Traditional insurances can't offer solutions for the geological/exploration risk.

This insurance ensures the majority (70–90%) of the invested amount of the geothermal exploration if the cause of the failure comes from geological situation that can't be foreseen before. The investor pays insurance fee and cost allowances (5–20%).

This kind of insurance only exists in Germany, France and Switzerland among the European countries. The Geothermal Energy Development Fund (GeoFund) operates this insurance tool in international processes. Hungary is not yet a targeted country because of the size of the Gross Domestic Product, therefore only market based or state subsidized fund can be established in Hungary.

2.3. Changes in heat and electricity market

The reduction of the import dependency is a key question in the domestic energy policy; therefore the interest in the geothermal energy is strongly increasing. The reputation of the technology is still not enough to make always a professional decision in regional and local energy investment alternatives.

Geothermal energy can't be a dominant source in the electricity production, but it can support the decentralization that is an important energy political objective [5].

We have to recognize the significance of the European Vision and the adaptability for Hungary that by the 2030s REs will be able to cover the whole heating-cooling demand. We should take this Vision into consideration in long term planning of residential, communal and district heating demand of heat markets as well as heat demand of agricultural, agro-industrial and industrial areas.

3. Middle and Long Term Role of the Geothermal Energy in Europe

The significant increase of geothermal energy can be achieved if all segments provide strong development.

3.1. Geothermal energy production till 2020

Ground source heat pumps (GSHPs) showed exponential development even in the decade of 2000–2010 from the main segments of geothermal energy production. The development was remarkable mainly in those countries which were able to provide the financial basis of the background infrastructure. Their driving forces were the undeveloped gas network and the large heat demand because of the cold climate. With regards to the fact that the ground source heat pump market hasn't developed well yet, a lot of counties including Hungary, set up ambitious increase in the number and power of GSHPs. Heat pumps will be dominant in the geothermal energy development [6].

Direct heat service development will be mainly in those countries that have high geothermal potential, as it is shown in *Figure 1*. The rising of the price of fossil energy resources and cost reduction from technology development increases the competitiveness of geothermal projects and enables the growth.

The doubling of geothermal based electricity production by 2020 is estimated. Several countries, including Hungary will establish the first geothermal power plants. The geothermal based electricity production will rise in the continental areas of Europe. EGS system demonstration projects will be finished.

3.2. Geothermal energy production between 2020 and 2030

The cooling demand of southern countries ensures market for growing of GSHP segment. The European market won't be fully covered by 2020, so further significant rise can be estimated. The development of direct heat supply will be based on the solutions of the key technological questions from the 2010s.

Further growth of geothermal electricity production will be based on the EGS technology. Hybrid technologies will be emerged both with fossil energy resources and with other renewable energies. Heat storage will increase the profitability of the existing geothermal systems.

3.3. Geothermal energy production till 2050

In GSHP development new generation of pumps can ensure the further development. The market size will be the main constraint of the direct heat supply segment. In case of new geothermal power plant units the EGS will become dominant. Widespread utilization of hybrid and heat storage technologies will contribute in growth of geothermal energy production.

4. Potential of Domestic Geothermal Energy Production

4.1. Tasks and opportunities in short, middle and long term

There are a lot of tasks and opportunities emerged related to the domestic geothermal energy sector.

- Operation of the old and anachronistic technologies. With regards to the age of the domestic operating system, large cost and expertise is necessary for the maintenance. It is not regular in the domestic practice. Raising level of the maintenance technologies is needed for Hungary to remain among the top ten of the world in direct heat supply.
- In spite of the financial crisis the geothermal energy production has to be installed on a development spiral. It is not only an economic question. The development needs educational and scientific activity as well.
- The geothermal energy has to be placed on its reasonable rank in all energy strategies and plans. All decision making level has to know that Hungary is very rich in geothermal energy, one of the richest of the World except for active volcanic areas.

In the middle term the National Renewable Energy Action Plan [2] shows the direction. The Action Plan is qualified ambitious both in international [9] and in domestic [1, 8] evaluations. However, based on the excellent geothermal potential, the Plan can be regarded as a technologically realistic estimation.

Table 3

Growth of the three main segments of the domestic geothermal energy production [8]

	2010	**2020**	**Growth**	**(2020/2010)**
Heat pumps, heat service/year	0,250 PJ	5,99 PJ	5,740 PJ	23,96
Ground source heat pumps, heat service/year	0,208 PJ	4,48 PJ	4,272 PJ	21,54
Direct heat supply with thermal water production. Heat service/year.	4,23 PJ	16,43 PJ	12,2 PJ	3,88
Geothermal based electricity production, power	0 MW	57 MW	57 MW	–
Geothermal based electricity production, electric energy	0 GWh	410 GWh	410 GWh	–

The long term development will be chiefly determined by the new technologies of the 2010s.

4.2. Proposed middle and long term development directions

The Hungarian economy is an integral part of the European economy; therefore the geothermal energy production sector has to move in the mainstream of the abovementioned European directions. However the traditions and geological specialties of Hungary must be taken into consideration.

- The traditions of the up-to-date international geothermal projects include a geological exploration phase before the preparation of the pre-feasibility study. In Hungary the geothermal energy sector emerged from water supplying, spa and also from hydrocarbon exploration and production sectors. Therefore the geothermal energy – that is a heat mining sector – is often regarded as water management question or branch of the hydrocarbon exploration and production sector. In the middle term geothermal energy project establishment and operation has to be based on professional regional and local geothermal exploration data.

- In the middle term the reliable reinjection technology into sandstone reservoirs must be created, as well as in the long term must be employed. In the long term geothermal technologies will not be acceptable in Europe without reinjection. European Union based supports cannot be received for anachronistic technologies as well as the more and more rigorous environmental regulations. They also force the projects into the direction of sustainable technologies.The long term domestic geothermal vision can't be based on unsustainable technologies. Therefore reinjection has to be a key question in domestic technical and financing concepts. In the international co-operation Hungary has to develop connections with countries where the reinjection into sandstone reservoir is also a key question (the neighbors, Germany and France).

- Geothermal energy projects cannot finance exploration well or wells. Therefore during the exploration phase it is necessary to collect the most information that supports the right technical and financing decisions. A part of the supporting resources of the State is needed to spend for regional data collection and creation up-to-date technologies.

- After minimizing of geological risks the competitiveness of geothermal projects shows significant improvement. We can achieve more social value if a part of state support would be spent for domestic risk insurance fund instead of single project support.

5. Summary

The domestic geothermal potential is significant among the European Union member states. Geothermal energy as a product is at the early phase of its lifecycle. The indices show high social values [8] of the geothermal energy, therefore widespread utilization exists in the European Renewable Energy Common Vision.

It is necessary to develop all the three geothermal segments both on European and national level. However the excellent potential can be exploited if the reliable reinjection

technology is developed into sandstone reservoirs in the 2010s. In the middle term the solution of reinjection is the most important question of the Hungarian geothermal energy sector. A state supported decade-long professional program is needed in order to solve this key technological issue.

"Acknowledgement: This work was carried out as part of the TÁMOP-4.2.1.B-10/2/KONV-2010-0001 project in the framework of the New Hungarian Development Plan. The realization of this project is supported by the European Union, co-financed by the European Social Fund."

REFERENCES

[1] Kujbus, A.: *How to Achieve the Geothermal Objectives of the National Renewable Energy Action Plan of Hungary?* International Geothermal Energy Workshop, Budapest, May 2011.
[2] MINISTRY OF NATIONAL DEVELOPMENT: *National Renewable Energy Action Plan*, December 2010.
[3] European Geothermal Energy Council 2011
[4] EUROPEAN TECHNOLOGY PLATFORM ON RENEWABLE HEATING AND COOLING: *Common Vision for the Renewable Heating & ooling sector in Europe*, Publication Office of the European Union, Luxembourg, 2011.
[5] INTERNATIONAL ENERGY AGENCY: *Geothermal Heat and Power Technology Roadmap, Paris,* 2011.
[6] EUROPEAN RENEWABLE ENERGY COUNCIL, BRUSSELS: Mapping Renewable Energy Pathways Towards 2020, 2011.
[7] EUROPEAN RENEWABLE ENERGY COUNCIL: *Renewable Energy in Europe*, Brussels, 2010.
[8] Kujbus, A.–Halász, Gy.-né: *Domestic Geothermal Energy Production and Environment Awareness*, Study Book of 2nd Environment and Energy Conference, October 2011.
[9] EUROPEAN GEOTHERMAL ENERGY COUNCIL: *EGEC Evaluation on NREAPs*. February 2011.
[10] GEOFAR IEE PROJECT: *Financial Tools for Supporting Geothermal Projects*, 2010.

Geosciences and Engineering, Vol. 1, No. 1 (2012), pp. 177–186.

BUCKET AND CUTTING TOOTH DEVELOPMENTS FOR THE BUCKET WHEEL EXCAVATORS OF MÁTRA POWER STATION LLC

GÁBOR LADÁNYI–ISTVÁN SÜMEGI
Department of Geotechnical Equipments, University of Miskolc
3515 Miskolc-Egyetemváros, Hungary
gtblaga@gold.uni-miskolc.hu

Abstract
The paper deals with the presentation of the concept, design and results obtained by testing, of new bucket and cutting tooth for the Bucket Wheel Excavators used in open pit lignite mines of RWE Mátra Power Station LLC. The results of this approach led to serious improvements in energy consuption, reliability, productivity and other parameters which are documented and illustrated in the paper.

1. Introduction

Bucket wheel excavators are used for removing surface refuse at the open-pit lignite mines of RWE Mátra Power Station LLC. The occurrence of useful minerals does not enable production to be performed at one single mine. The two mines – situated at about 60 km distance from each other – are located near to the settlements of Visonta and Bükkábrány. In spite of the considerable distance most of the refuse covering the lignite consists of sand and sandy clay, respectively, and gravel at both mines. In spite of this similarity, however, the two refuse layers show significant differences, as well. While the greatest difficulty at Bükkábrány is caused by the high abrasiveness of the stripped material – at Visonta hard sandstone ribs are encountered frequently. The locations of these cannot be foreseen in most cases. If the excavator is operated with the usual mining parameters when reaching such sandstone ribs, then rupture failures can be avoided only with cutting structures are capable of withstanding the higher stresses acting on these occasions.

Because of the long-standing problems of mining technique – high cutting tooth wear, frequent failure of buckets, high specific power demand – RWE specialists requested in year 2000 the collective of the Geotechnical Equipment Department of Miskolc University to compile a research and development program. We had opportunities for presenting the steps of this development process ongoing for the past eight years as well as the partial results achieved also during this series of conferences. The tangible results, however, could not be presented as yet. We present therefore in this article of ours only the major steps of the development process and then its results experienced at the mines during operation.

The objective was to elaborate a testing and planning methodology ensuring the verification of the new components (buckets, cutting teeth) developed following the review of the excavators' cutting structures used until then having more advantageous features than those of the earlier ones. The most important features among these are listed below.

The new cutting structures ensure:

- Breaking with a lower specific power demand than the previous one;
- Longer service life for the cutting tools;
- Simpler fabrication & renewal and easier cutting teeth replacement;
- The drives of both the bucket wheel and the upper turntable to be operated without overload with the use of the recommended optimal technology.

Building on the experiences obtained in the course of our earlier works, we had elaborated a series of development steps – as described below – employed also in this case:

- Review of the excavator in respect of geometry, technology, dynamics and energetics
- Formulation of the optimal technology
- Bucket and cutting tooth improvement based on information obtained in the above two steps
- Preparation of fabrication documents for the new designs
- Implementation of modifications required eventually on the basis of the initial operating experiences

2. Main steps of bucket and cutting tooth development

1. Review of the geometry of cutting edges and cutting teeth on the basis of the three-dimensional (3D) model of old buckets *(Figure 1)* and the cinematic diagram of movements. Determination of the cutting angles, relief angles and angular adjustment errors suitable for the optimal technological parameters.
2. Drawing of the chipping patterns *(Figure 2)* obtained by mining with the old buckets and then the analysis of same. The investigation of mining conditions, cutting edge design, the positioning along it and the combined performance of cutting teeth at the same time.

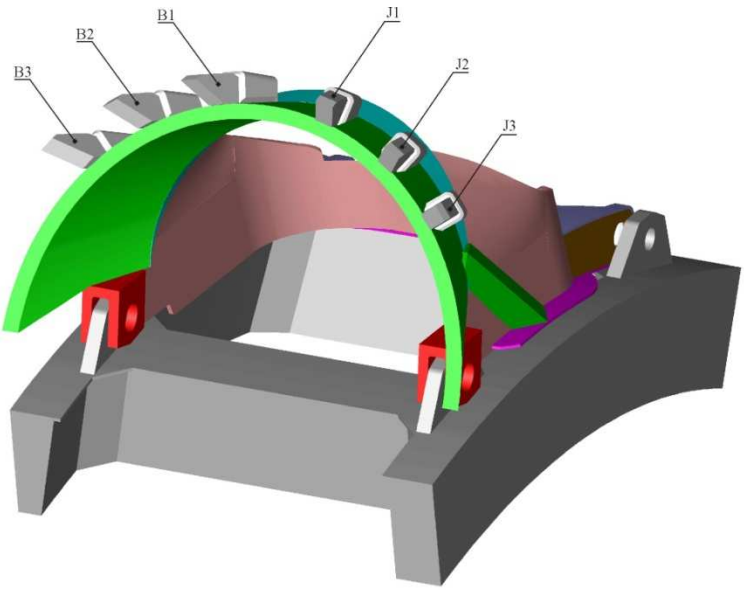

Figure 1

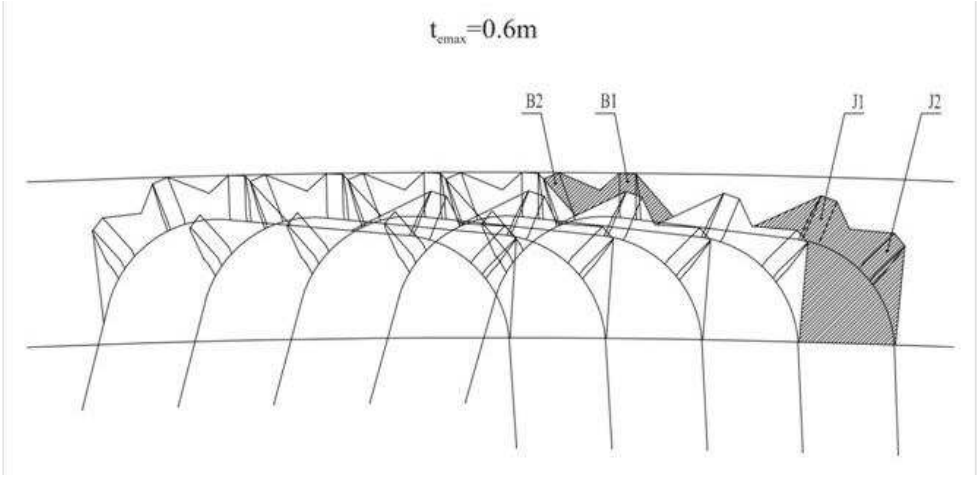

Figure 2

The analyses completed according to the above two points facilitates the development of the new design. Our most significant finding related to the buckets of the excavators operated at Visonta and Bükkábrány is that symmetrical cutting under the same conditions with the cutting wheel positioned asymmetrically on the boom can be ensured in both swinging directions only with asymmetric bucket and cutting edge designs, respectively.

3. Strength review of old buckets with finite elements method. Determination of rated and dynamic peak loads acting on the buckets on the basis of the information obtained from rock cutting tests and machine specifications. Identification of the weak points of design – in necessity of strengthening – on the basis of test & analysis results *(Figure 3).*

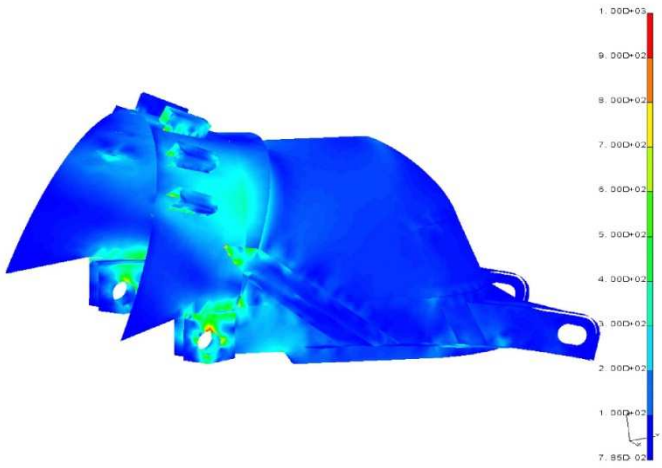

Figure 3

3. The results of the development project described in this article can be summarised in the following six points

1. New cutting teeth were designed in order to eliminate the deficiencies experienced with the cutting teeth in use previously. The results of rock machining performed in laboratory were taken into account to the greatest extent in the course of design engineering. Two cutting teeth – built on the same principle but differing in size – were designed for the five machine types (cutting tooth No.1 & 2).

The design of the cutting teeth employed originally has left several desirable features unrealised.

Only the most significant ones of the changes related to these and their effects are listed below:

- The width of the cutting edge was increased by choosing a negative side angle for the cutter tip.
- The cutting teeth were installed also on top of the cutting edge. This is not only more advantageous in respect of force transmission but offers a more precise solution also for the adjustment of the cutting teeth than the previous one.
- The collar portion of the cutting tooth protects the cutting tooth holder against wear.
- Cutting teeth do not jam because of being seated on top, they are easier to replace.
- The mode of the attachment of cutting teeth was redesigned in order to enable their easier replacement.

The design drawing and model view of cutting tooth No. 1 are shown in *Figure 4.*

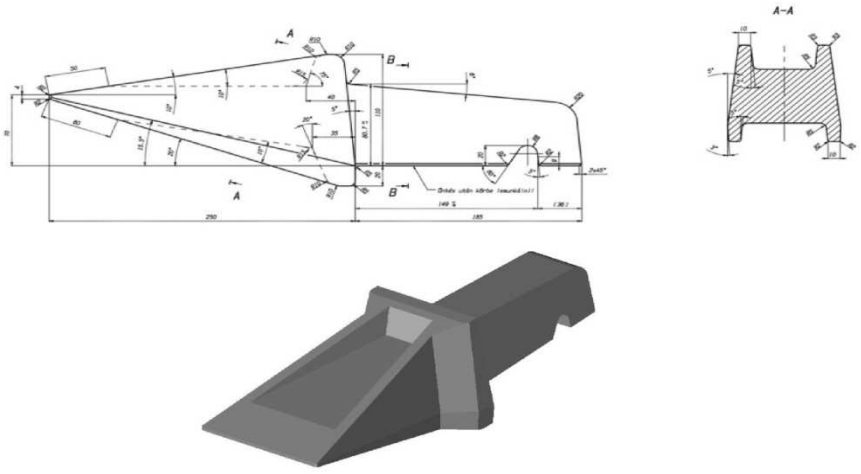

Figure 4

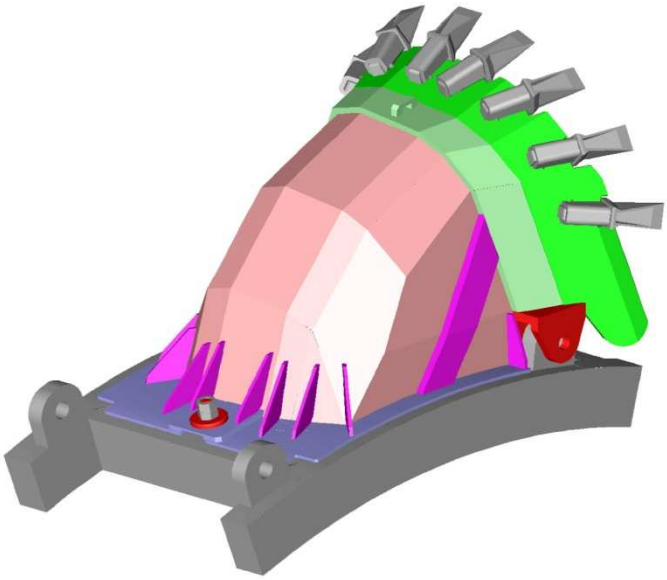

Figure 5

2. We were forced frequently to design new cutting edge geometrics in the course of the engineering process. Cutting edges consisting of flat plates were designed instead of the earlier curved cutting edges. Asymmetric cutting edges consisting of five and seven flat plates, respectively, were obtained in this way for the new designs comprising six and eight cutting teeth *(Figure 5).* Fabricating accuracy has been improved considerably thereby. The completed buckets are of the same size within close tolerance limits enabling their easier installation and interchangeability.
   The cutting teeth and edges have been set for the optimal technological processes so that the operating edge geometry would be favourable around 0° angular adjustment error, enabling the cutting tooth wear patterns to become symmetrical.
   The operating experiences have supported the correctness of the theory that the cutting teeth have to be set in the direction of the mean resultant vector determined for the optimal technological parameters.
3. A multiangular bucket backing is being designed for the multiangular, asymmetric cutting edge with the filling and dumping conditions also taken into consideration. Lining the backing built up in this way with adhesion reducing inserts can be done easily due to the flat plates.
4. The surroundings of the seating surface have been ribbed for supporting the cutting edge. A design more resistant to cyclical fatigue stresses than earlier solutions could be achieved thereby. A new back attachment method has been chosen also in order to mitigate the harmful effects of cyclical stresses. This was initially a wedged then a bolted joint.
5. The stressing review of the newly designed buckets indicated values approaching the limit stress causing failure at some places, mainly when dynamic loads were added. Increasing material thickness would have caused surplus weight and fabricating difficulties in some cases. For this reason we endeavoured preferably to resolve this

problem by the improvement of material qualities and selecting high-strength, fine-grained structural materials for critical components (cutting edges, fixing lugs, support skirts).

6. An accepted solution is to close the back by chains in the case of open buckets. In the case of the buckets designed by us the closing elements are made of rubber bands. This multiplies the service life compared to chains according to operating experiences.

The assembly drawings and detail drawings of the buckets for fabrication are prepared on the basis of the finalised 3D spatial model. The complete development design engineering and commissioning period encompassed more than seven years. Eleven new buckets and two new cutting teeth have been designed during this period for five different types of bucket wheel excavators. These are shown in *Table 1*.

Table 1

Machine Model	Item No.	Mining Plant	Type of fabricated bucket & cutting tooth
SRs 1200	MT4 MT5	Visonta	Closed, open and loosening (cutting tooth No. 1)
SRs (H) 401	MT10, MT11 MT12	Bükkábrány	Closed & open (cutting tooth No. 2)
SRs 1400	MT6	Visonta	Closed, open and loosening (cutting tooth No. 1)
SRs 2000	MT7	Visonta	Closed & open (cutting tooth No. 1)
VABE 1300	MT9	Visonta	Closed (cutting tooth No. 1)

The results achieved speak for themselves and – as expected – their direct effects were demonstrated in two fundamental areas: in the extended service life of the buckets and the reduced number of cutting teeth consumed. The extended service life of the buckets is clearly shown by the numbers in *Table 2,* indicating the average service life extension achieved in the two mines instead of the increases obtained separately for each excavator. The 4,2 times and 3 times extensions of the life cycles exceeded our initial expectations.

Table 2

	Bucket cycle time [days]		Ratio
	Old	New	
Visonta Mine	90	380	4,2
Bükkábrány Mine	180	540	3,0

The effect of the extended service life is well illustrated by the diagram shown in *Figure 6*. At Visonta Mine the specific costs per one million m^3 inert material (refuse) because of the expenses of fabrication started in 2004. The fabrication process executed over several years in a scheduled manner was completed in 2007 and the beneficial effect of the new buckets became sensible already in 2008.

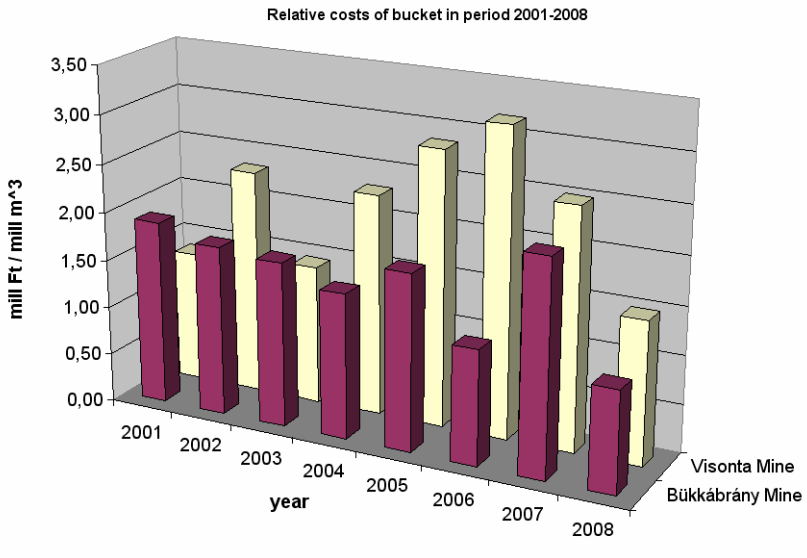

Figure 6

The development project at Bükkábrány Mine was completed by 2005 and the first set of buckets was installed. The positive effect of this appeared already in 2006. Based on the good experiences another set was fabricated in 2007. Because of the extended service life of these no additional set needed to be fabricated in 2008 and thus expenses of this type were reduced. The extended service life of the buckets is only one of the beneficial effects. The adjustment of the cutters as required for the particular process reduces also the power demand of mining.

This is true for the power consumption of both the motor driving the bucket wheel and the motor swinging the boom. Taking only averages into account again, it can be stated that the current consumption of the bucket wheel motor decreased nearly by 30%, while that of the boom swinging motor dropped even more, by about 40%. These statements can be verified in *Figures 7* and *8*, showing the current consumption of the bucket wheel motor (bottom red curve) during a three-hours production period operating with the old *(Figure 7)* and the new *(Figure 8)* buckets, respectively.

No additional explanation is necessary with regard to the reduction achieved in the power demand of mining operation. The operation of the drive motors at lower load levels has, however, also an additional benefit which entails material savings indirectly. Namely the overloading of both drive trains was a frequent occurrence previously. Overload protection intervened in most cases but failures involving breakage and causing more severe damages had occurred even in spite of this.

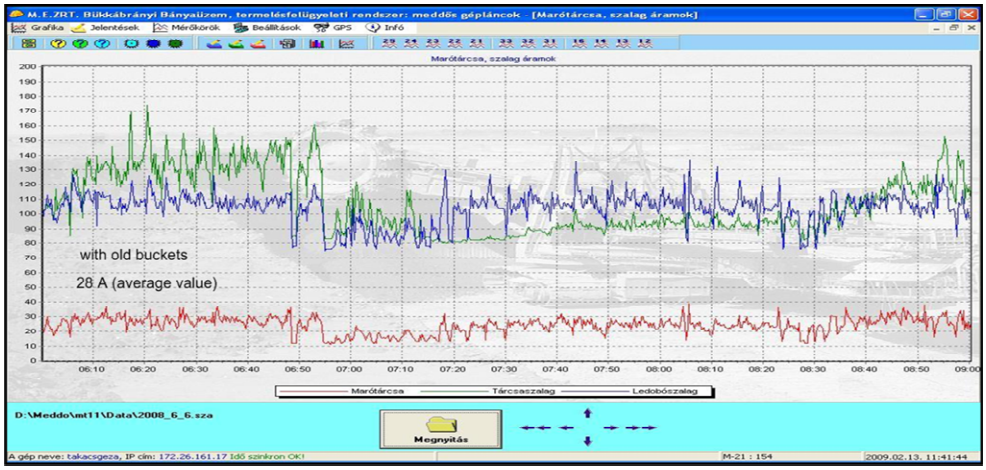

Figure 7

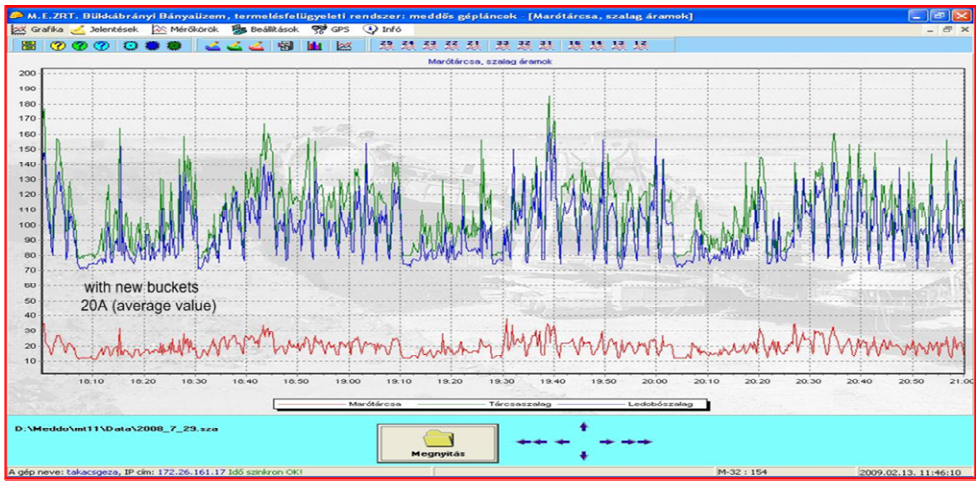

Figure 8

The durations of machine outages due to unexpected failures entailing long periods of time for repairs and restoration were not negligible either. Following the installation of the new buckets machine outages due to shutdown because of overloading dropped back to the level acceptable as normal if the machine was operated with optimal technology. The number of cutting teeth consumed had decreased dramatically.

This is verified unequivocally by the comparison of the respective data recorded in years 2007 and 2008, respectively.This reduction can be seen in Figure 9 showing the numbers of cutting teeth consumed during the stripping of one million m^3 refuse at the Bükkábrány Mine compared to the 2007 January quantity as the baseline. The variation of associated costs is shown in Figure 10. As detectable this is somewhat less than the rate of reduction seen in respect of quantities.

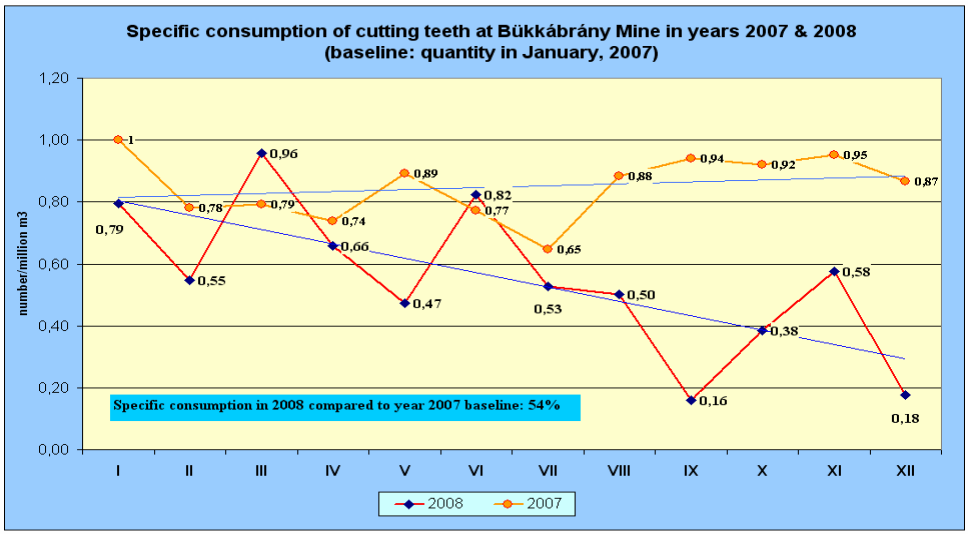

Figure 9

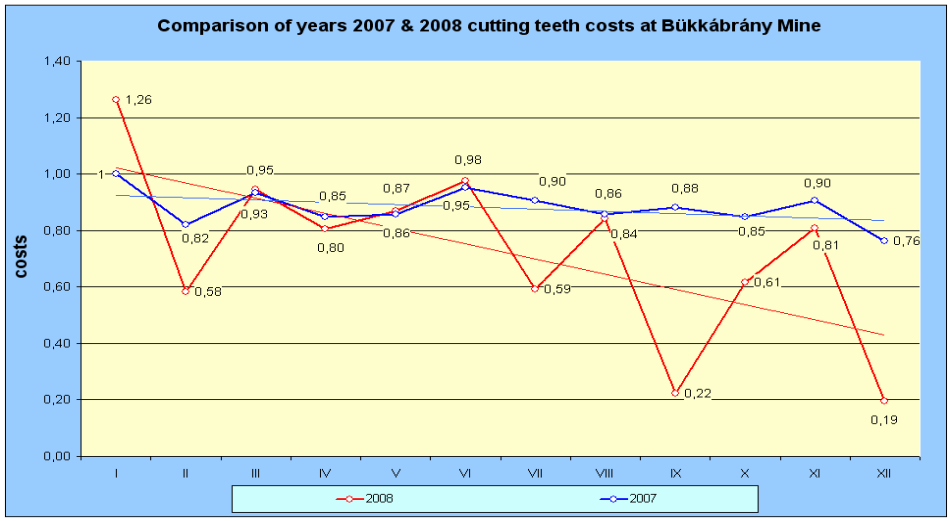

Figure 10

The new buckets, the new cutting tooth shape and the cutting tooth setting matched to the technological process comprise only one reason for the quantitative reduction. Another contributor is the process whereby the cutting edges of worn teeth are renewed by deposit welding with the use of a wear-resistant material as filler metal. The cost of renewal is less than the price of a new cutting tooth but – naturally – influences the variation of costs and therefore lower reduction can be seen in respect of costs on the average than that seen in the number of teeth consumed.

In regard of this topic presentations were held at several international conferences [2, 3, 4, 5, 6], technical article published [7] and a PhD paper [1] prepared about the research works.

4. Conclusions

The main conclusion of the paper can be summed up as follows.
The adjustment of the cutters as it is required by the technology has three benefits:

- Reduces the power demand of cutting
- The number of cutting teeth consumed decrease dramatically
- The operational costs decrease too.

"Acknowledgement: This work was carried out as part of the TÁMOP-4.2.1.B-10/2/KONV-2010-0001 project in the framework of the New Hungarian Development Plan. The realization of this project is supported by the European Union, co-financed by the European Social Fund."

REFERENCES

[1] Sümegi, I.: *Theoretical examination and developing of cutting mechanism of opencast bucketwheel excavators*. PhD. theses. University of Miskolc, 2002.
[2] Ladányi, G.–Sümegi, I.: *Cutting edge development for opencast bucketwheel excavator based on examination of winning process*. In. Mining Tecniques 2003, International Conference, 2003. szeptember 16–19., Krakow–Krynica, Proceeding of the conference, 139–150.
[3] Ladányi, G.–Sümegi, I.: *Some issues of the technological design of bucketwheel excavators*. In. Mining Tecniques 2005, International Conference, 2005. szeptember 21–23. Krakow-Krynica, Proceeding of the conference, 47–56.
[4] Ladányi, G.–Sümegi, I.: *Some issues of the technological design of bucketwheel excavators*. In. Proceeding of University of Miskolc, Mining 2006, Vol. 70. 101–112.
[5] Ladányi, G.–Sümegi, I.: *Optimisation of buckets of bucket-wheel excavators based on operating experience*. In. Mining Tecniques 2007, International Conference, 2007. szeptember 18–21. Krakow-Krynica, Proc. of the confer. 103–110.
[6] Ladányi, G.–Sümegi,I.–Virág, Z.: *Laboratory Rock Cutting Tests on Rock Samples from Visonta South Mine*. In. International conference of Elektromechanics. Petrosani, România. Proceeding of the conference, Vol. 1, 209–218.

Geosciences and Engineering, Vol. 1, No. 1 (2012), pp. 187–204.

RESERVOIR CONFORMANCE ENHANCEMENT IN GAS FIELDS USING MICROEMULSIONS

ISTVÁN LAKATOS[1]–JULIANNA LAKATOS-SZABÓ[1]–TIBOR BÓDI[1]–
ÁRPÁD VÁGÓ[2]–GABRIELLA SZENTES[1]
[1]Reserach Institute of Applied Earth Sciences, UM, 3515 Miskolc-Egyetemváros
lakatos@akki.hu
[2]Hungarian Oil and Gas Plc. (MOL), E&P Division, Kiskunhalas
Hungary

Abstract
The primary aim of the research project was to develop such chemical systems, which triggered by mixing with water will form the blocking phase. As a novelty water sensitive homogeneous solutions and water external microemulsions were developed, which are stable until they are diluted with water forming thus stable macroemulsions. Transformation of different metastable systems to stable ones in reservoir space having high water saturation may radically restrict the water flow through their high viscosity and entrapment of the dispersed particles by the pores. As dispersed phases organic silicon compounds, tensides and natural crude oil fractions were tested. The transformation and structure of phases and size of particles were analyzed by photon correlation spectrometry, rheometry, while the flow properties were studied in natural sandstone systems.

The core studies confirmed that all metastable systems reduce the flow of water by 80–90% in water-saturated sandstone. Using chemical-free postflush the flow resistance remains substantial against water in case of silicones; meanwhile the permeability deterioration against oil or gas is negligible. The metastable systems are effective and single step disproportional permeability modifying fluids.

The metastable systems may offer an excellent opportunity for water shutoff in matured oil and gas fields and gas storage facilities. The unique properties of the techniques are that flow resistance may occur only in water saturated reservoir space and in case of technical failure; the flow barrier can be eliminated by oil and gas injection.

1. Introduction and background of R&D activity

Identification, prediction and understanding of conformance problems are fundamental in optimal design of production technology in both oil and gas fields. Appropriate application of reservoir conformance control, particularly in depleted fields, can significantly lead to improved and enhanced oil and gas recovery (IOR/EOR), and hence the profitability of operations. The term “conformance” in its original form is defined as the measure of the volumetric sweep efficiency during the recovery and the forced intervention into the reservoir [1]. The term also refers to a measure of and the treatment of excess water (rarely gas) production. Excess water production usually imparts indirectly a negative influence on volumetric sweep efficiency and as a result deteriorates the profitability of production operations [2]

The idea of water shut-off treatments has arisen already in 1922 when injection of silicate solutions into oil producing wells with the aim at in-situ gelation to form a blocking phase was patented. However as far as the hydrocarbon industry is concerned, a real necessity to control flow profile around wells became known only in the middle of the sixties. Since that time a great variety of *polymer methods* using polymer solutions, rigid and weak gels as diverting/blocking agents and disproportional permeability modifiers have been developed. The most frequently reported methods form three main groups: *injection of*

polymer solution, *in-situ cross-linking of chain like polymers* and *in-situ polymerization of monomers*. Their general feature is that they are based on application of macromolecular materials. Such a common denominator cannot be found as far the blocking mechanism is concerned. Since the philosophy of profile correction methods is that deliberate formation damage or a drastic mobility reducing effect must be developed in a right reservoir space and in a proper stage of production, the different known techniques, in a wider sense, can be classified as follows:

Mobility control by modification of rheological properties
- – Injection of polymer solutions;
- – In-situ cross-linking of linear polymer;
- – In-situ polymerization of monomers;
- – Combined, multifunctional methods;
- – Precipitation of gel-like inorganic compounds;
- – Precipitation of crystalline inorganic compounds.

Mobility control by modification of pore structure

Theoretically the reservoir engineering concept of the profile correction or in-situ barrier formation is invariant to the factors whether the viscosity of fluids, pore structure the reservoir or simultaneously both of them are modified in the target area. Positive and negative arguments may aptly be listed beside all solutions. Despite the fact that "chemical safety of gelation" under laboratory condition is close to 100% though, the field results often fall short of expectation. Reason of unsuccessful treatments might be that the flow resistance against water flow often develops not in the right time and reservoir space. Analyzing the reasons of unsuccessful well treatments, we may conclude that placement of gel-forming liquids and timing of gelation is controlled by great variety of techniques but the presence of water is rarely considered directly as factor triggering the build-up flow resistance against of water.

Surprisingly polymers were used in majority of routine well treatment jobs; meanwhile other materials, e.g. inorganic compounds were almost completely neglected as barrier-forming agents. Therefore the focus of the Hungarian research projects in the past, comprising more than two decades, was to analyze the silicate, silicate/polymer, alcoholic polymer solutions, metal hydroxides, silicone microemulsions and alcoholic polysiloxane solutions as alternatives and to evaluate the potential of such methods under field conditions [3–11]. Study of the mechanism of the last two methods [10, 11] it was recognized that the flow resistance developed against the water flow could be traced back to transformation of the microemulsion and the ideal polysiloxane solution to high viscosity macroemulsion when mixing with water. Therefore the primary aim of the recent research projects was to develop similar chemical systems, which will form the blocking phase contacting with water.

2. Thermodynamic consideration and concept of methods

Any thermodynamic system is in equilibrium (state of rest) when none of its properties change in time. However many systems have apparently stable states that show no change with time, and thus can be regarded for practical purposes as equilibrium state, even though they are not representing minimum internal energy. Such condition is called metastable state. Transition from metastable state to real stable state needs excess energy to overcome the threshold potential. That excess energy can be provided or introduce into the systems with different ways. When this surplus energy gets into the system, different processes are induced and taking place: chemical reactions, phase transition, etc. and these processes may radically change the physical and chemical properties of systems.

Surveying the most frequently applied well treatment techniques we have to point out that transition of metastable to stable state is in the background of barrier-forming processes. For instance, mixing of stable polymer and cross-linking solution in the mixing zone triggers in-situ bulk phase gelation of polymer/Cr^{+} systems at elevated temperature. However it is clear that contact between the formation water and the treating fluid is not an active triggering factor in the mentioned cases, and hence, we cannot be certain that the selective flow resistance develops exactly in the highly water saturated reservoir space what we want to isolate. These weak points of the routine well treatment technologies encourages us to study and develop such chemical systems, which may work exactly on transition mechanism of metastable state to stable one initiated by in-situ mixing of homogeneous and microheterogeneous treating fluids with formation water.

3. Experimental conditions, materials, and procedures

The laboratory studies comprised complex colloid chemical, rheological and hydrodynamic studies using untreated and the treated reservoir cores. Primary aim of the measurements was to determine the changes of all parameters, which may influence the selective flow of water and gas, respectively. Details of the laboratory studies are summarized in the following subchapters.

Fluids. The fluids used for saturation of cores and flow measurements were selected according to the target field conditions where the method was expected to be tested.

Gas phase:	natural gas with 95% CH_4 content, nitrogen
Formation water:	2.6 g/l $NaHCO_3$
	2.6 g/l Na-acetate
	0.5 g/l NaCl
Crude oil:	light paraffinic (Algyő field, Hungary)
	light hydrocarbon cut (petroleum)
Treating solutions:	silicone ME with 33.0% polysiloxane content
	silicone solution in methyl alcohol with 33.0% amino functional polysiloxane
	gemini tenside No.1 in IPA containing solution with 10 g/l active content
	gemini tenside No.2 in IPA containing solution with 10 g/l active content

gemini tenside No.3 in IPA containing solution with 10 g/l active content
petroleum (light and medium) external microemulsion
lubricant oil external microemulsion
alcohol/keton external microemulsion

Abbreviations: The Wacker-Chemie GmbH, Germany provided the silicone oligomers in form of micro- and macroemulsion and pure chemical compounds. The microemulsions were stabilized by two (anionic and ionic) surfactants in aqueous carrier phase. The Gemini tensides were ethoxylated and alkoxylated diols manufactures by the Air Products Chemicals BV (USA) in form of pure compounds (No. 1 and No. 3) and mixtures of two components (No. 2). These materials are characterized by limited solubility in water and hence, their ideal, homogeneous solution could only be made by addition of different amount of IPA to aqueous phase. Because their flow properties in porous media were unfavorable, and their application for conformance improvement was out of question, data of laboratory studies are not included hereafter. The petroleum external microemulsions contained less than 15% fatty acid/ester and 15% water.

Core material. Both synthetic and natural cores were used for flow measurements. The former ones served for serial measurements, while the later ones were used to control the results and predict the real effects under field conditions. The cores were characterized by He- and Hg-porosimetry, and determination of the absolute, effective and relative permeability, capillary pressure and wettability. The following data are relevant to the synthetic and formation cores:

Synthetic cores:

Special laboratory technique developed by the institute was use for preparation of the synthetic porous cores. Those cores were prepared from formation rocks using the whole crushed material and adding less 5% thermoplastic resins. Setting the size fractions appropriately cores with 180–210 mD permeability were prepared. The artificial consolidation was carried out by thermal treatment of the pressurized cores. The core porosity and pore size distribution were close to each other within 10 rel. percentage. The wettability however was shifted from the water wet character toward the intermedier range because of partial coverage of the rock surface by the melted and then solidified resins.

Formation cores

The formation rocks derived from different sources. Most of the cores represented the Algyő field, Hungary. In majority of cases the natural Fontainebleau sandstone cores were used. Its properties measured by high pressure Hg-porosimetry (Thermo Finnigen Pascal 440) are listed in Table 1. The natural formation rocks were cut in horizontal direction from the original drilled cores. Since their properties were remarkably different, those pieces were selected for lab studies that had similar physical and hydrodynamic characteristics. Average data of cores were as follows

Diameter: 2.48 cm
Length: 7.00 cm
He-porosity: 12.12–16.23%
Gas permeability (abs.): 144.56–155.11 mD

Table 1

Characteristic data of the Fontainebleau sandstone cores

Average pore radius	19.45 μm
Most frequent pore radius	17.72 μm
Total porosity	12.43%
Bulk density	2.32 g/cm^3
Apparent density	2.64 g/cm^3
Specific surface area	0.26 m^2/g
Gas permeability	400–600 mD
Water permeability	250–400 mD

Procedures. The rheological measurements were carried out with Contraves Low Shear 30 rheometer in range of 10^{-3}–10^2 1/s shear rate range at ambient temperature. The structure of microheterogeneous systems and determination of particle (droplet) size were studied by photon correlation spectrometry using transmission and back scattering laser techniques (Malvern Zeta and NanoSizer). Standard linear flow tests were used to demonstrate the effect of different barrier forming media. For correct comparison of the experimental results, those data will be presented here that were obtained for Fontainebleau sandstone cores. The tests were performed with identical injection protocol. First 10 PV formation water was injected into the core with aim at determining the basic data (water permeability and mobility). The water preflush was followed by injection of 10 PV treating agent. In the final phase of the flow tests, injection of 10 PV formation water served to drive the treating fluids out from the cores. In certain cases organic phase, light hydrocarbons (petroleum) was injected after the water postflush to study the permeability reconstruction. The fluids were injected at constant flow rate and measuring the differential pressure the mobility was calculated. Because of numerous data were obtained, only those diagrams will be shown here, which are representative for change of the mobility through the flow tests.

4. Characterization of treating fluids

General feature of all tested treating fluids is that contacting or mixing with water their structure fundamentally changes. The radical change of fluid character can be often visualized by naked eye in case of light, medium and heavy hydrocarbon external microemulsions shown in *Figures 1–3*. The appropriate microemulsions were diluted by formation water in different ratios and it is clearly seen that phase inversion and microemulsion⇨macroemulsion type transformation is immediately taking place in the system when relatively small amount of water (less than 20%) is added to the microheterogeneous colloids. Unfortunately similar change could not be observed in case of alcohol/keton external microemulsion because of its poor stability *(Figure 4.).*

As a consequence of the mentioned changes, the viscosity of emulsions as a function of water content steeply increases in range of 5–20% water content, and then it drops down above 50–60% *(Figure. 5).*

Figure 1: Effect of water content on phase behaviour of petroleum (medium) external microemulsion (c_w = 0⇒95%)

Figure 2: Effect of water content on phase behaviour of petroleum (light) external microemulsion (c_w = 0⇒95%)

Figure 3: Effect of water content on phase behaviour of lubricant oil external microemulsion ($c_w = 0 \Rightarrow 95\%$)

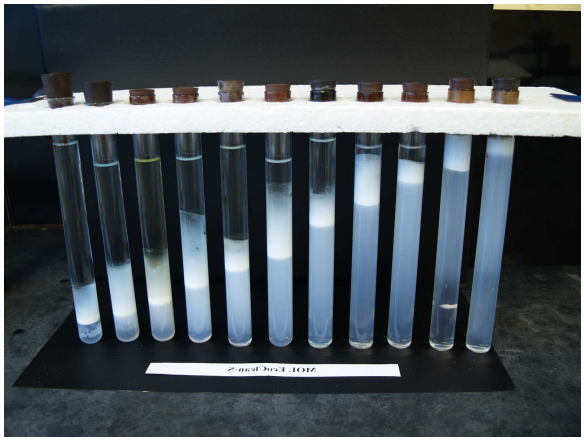

Figure 4: Effect of water content on phase behaviour of alcohol/keton external microemulsion ($c_w = 95 \Rightarrow 5\%$)

The region shown in *Figure 5* as discontinuity of the curves representing extremely high viscosity can be interpreted as phase inversion, viz, at the left-hand side curve represents the microemulsion; meanwhile the right-hand side belongs to macroemulsion phase. Between these two limits, depending on the type of systems, the viscosity can be higher than 10,000 mPa s and these materials are cream like in nature and not mobile even at high deformation forces *(Figure 6).* Practical importance of that fact is, that such systems form immobile barrier against flow in any porous or fractured systems when the microemulsion penetrates high water-saturated zones and layers. Not surprisingly the water containing macroemulsions show strong Non-Newtonian flow behaviour and the dependence of the viscosity on shear rate becomes more pronounced as the water content approaches the range of 20–40% *(Figur. 7).*

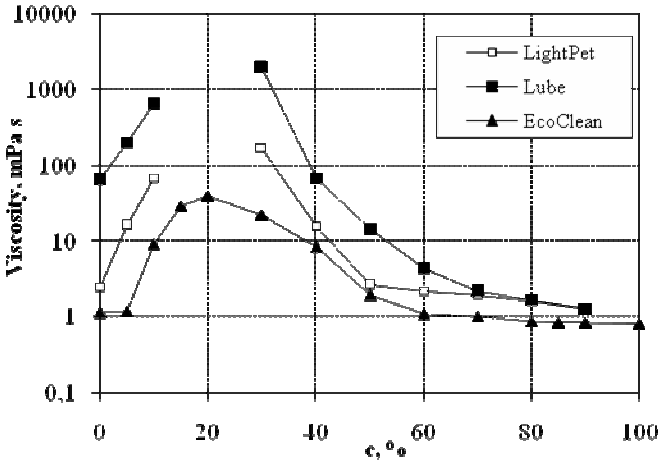

Figure 5: Effect of water on viscosity of different microemulsions

Figure 6: Consistency of water-containing microemulsion at phase inversion

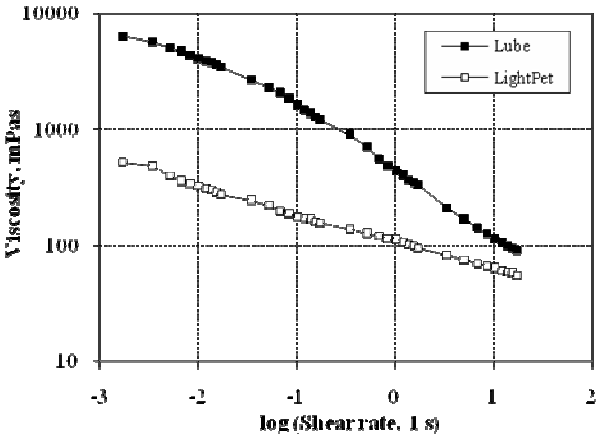

Figure 7: Non-Newtonian viscosity of water-containing microemulsion

It is needless to say that structural modification of the original treating fluids is in the background of the rheological changes. Determination of the particle (droplet) size of the dispersed phase definitely proved that the fine microstructure of the original materials transformed to a coarse macroheterogeneous colloids. According to the shape of the curves shown in *Figures 8* and *9*, the trend of the Z average droplet diameter is in full convergence with the viscosity changes illustrated in *Figure 2*. In addition, it deserves attention that the single-peak like size distribution curve became composite in character indicating thus a strong aggregation of the dispersed microdomains in the macroemulsions *(Figure10).*

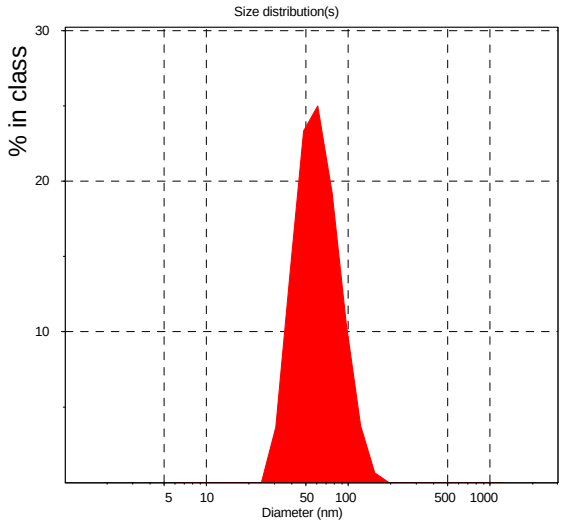

Figure 8: Size distribution of undiluted silicon microemulsion (c_w = 0%)

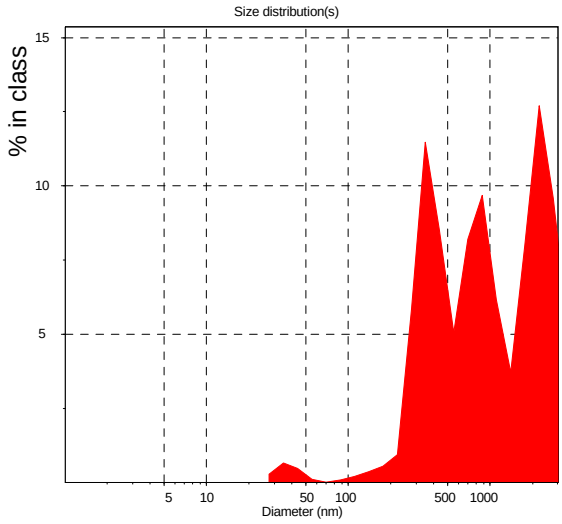

Figure 9: Size distribution of diluted silicon microemulsion (c_w = 30%)

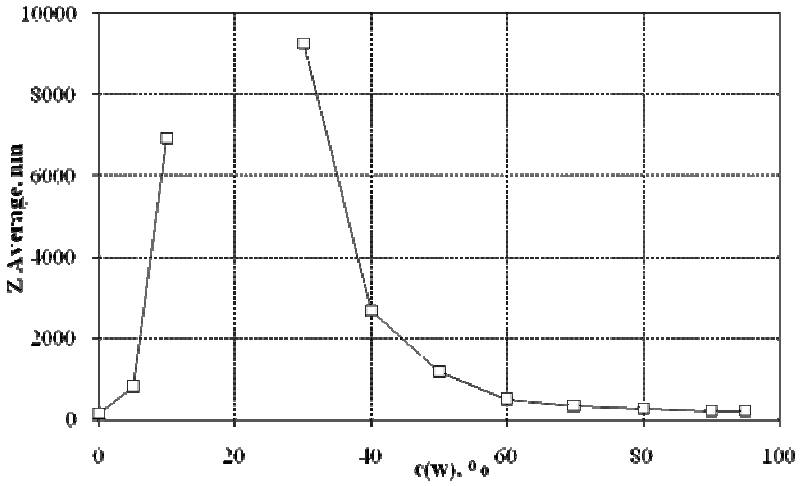

Figure 10: Effect of water content on average droplet size of silicon emulsion

It is worth mentioning, however, that using water external macroemulsions as treating fluid as suggested by Sobanova et al. [12], Romero at al. [13] and Stavland et al. [14] such unique phenomena cannot be observed. Dilution of any macroemulsions with water is followed by gradual decrease in viscosity and usually constant droplet size until a critical phase ratio of the induced coalescence. In contrast the silicone microemulsions suggested first for treatment of gas wells by Pusch et al. [15] and studied earlier in detail [10] proved to be an excellent model to demonstrate the general features of metastable, water sensitive chemical systems.

Based on the results of the laboratory experiments we may notify in advance that substantial flow resistance will develop in those zones, layers or even capillaries and pores where the water saturation is high and the water contact and mixing induce a structural modification in the potential treating fluids. The phenomena are selective and nothing may happen if water is absent, and the fluids remain unchanged until they get into water containing reservoir space. From chemical point of view the metastable ideal solutions or microheterogeneous systems transform to a more stable (lower internal energy) state and that change initiated just by the presence of water. From reservoir and production engineering point of view the important consequence is that the flow resistance ensues only against water and only in highly water-saturated reservoir space. Now the answer for such questions is that both the high viscosity of water containing emulsions and the large droplet aggregates and network of domains formed in-situ jointly result in a stable impediment against the propagation and flow of water in water-saturated porous systems; meanwhile in oil- and gas-saturated flow path no flow resistance build-up.

5. Study of flow phenomena in porous media

As mentioned earlier, numerous flow tests have been carried out in the frame of the project. Although the results of the laboratory studies were convergent, the extents of changes were different depending on the core materials used as porous media. Extensive study of silicone microemulsions and stabilized ideal silicon solutions were reported in two

SPE preprints [10, 11]. Despite that fact the results of their flow tests is repeated here to compare and evaluate the new chemical options. Identical experimental conditions and similar porous cores were used and only the treating fluid was different. In Figures 11–16, the effect of potential treating fluids on mobility is shown as a function of injected pore volume. Basically 100–100 cm^3 preflush water, chemical system and postflush water were continuously injected into the cores. In case of the last two tests the experiment was finished by injecting 100 cm^3 petroleum to study the barrier breaking effect.

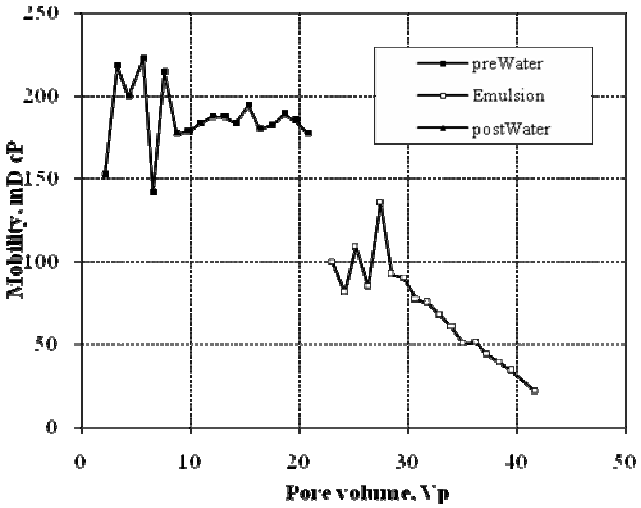

Figure 11: Effect of diluted silicon microemulsion on mobility in porous media

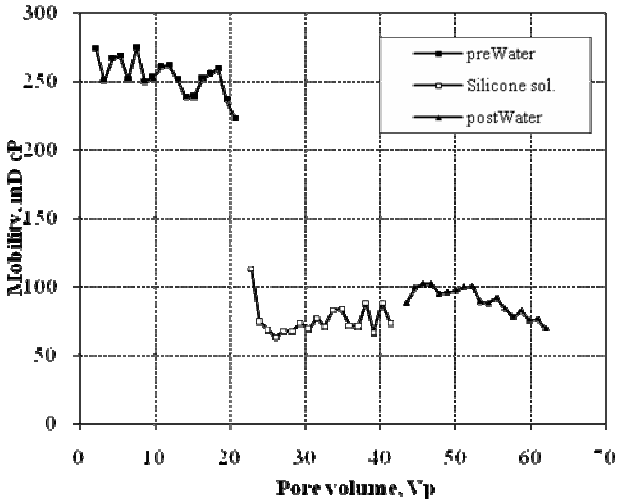

Figure 12: Effect of diluted silicon solution on mobility in porous media

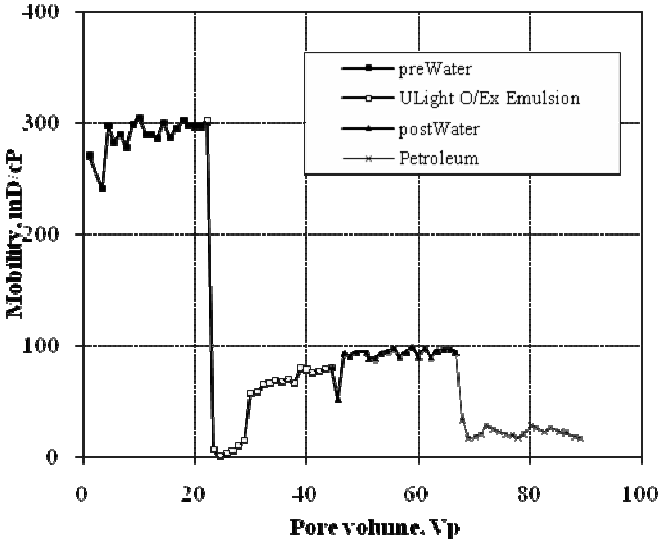

Figure 13: Effect of diluted light petroleum microemulsion on mobility in porous media

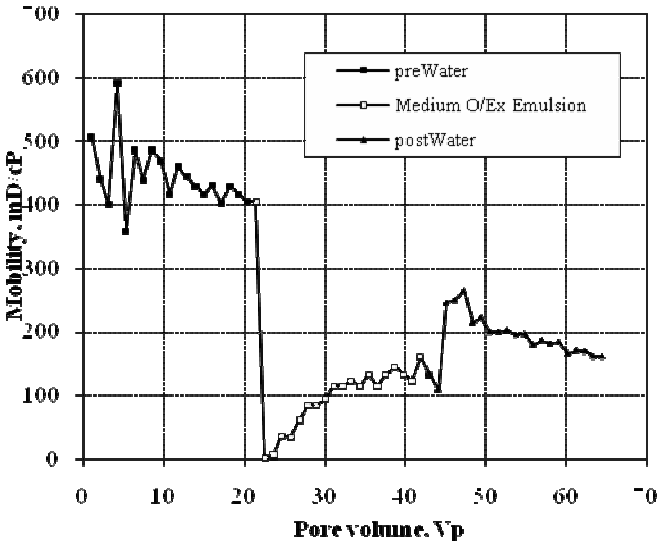

Figure 14: Effect of diluted medium petroleum microemulsion on mobility in porous media

The results of the flow tests can be summarized as follows.

1. Both silicone fluids (microemulsion and IPA solution) resulted in a significant mobility modification in cores.
2. The mobility reduction is extreme and permanent in case of diluted, water-containing silicon systems. Sweeping out the silicone fluids from the cores the mobility increased slightly, however it stabilized at level about 50% of the original. It is characteristic also for both treating systems that the residual mobility reduction remained constant through 20 PV water injection.

3. Stunning and peculiar phenomena are that injecting highly diluted silicone fluids, independently of whether the silicone is present as a dispersed phase in water or dissolved in i-propanol.

4. Comparing the efficiencies of the mobility reducing effects, the silicone microemulsion is obviously more effective. Using this treating system the mobility gradually decreases not only through the slug injections, but also in the water post-injection phase.

5. The hydrocarbon external microemulsions are also very effective mobility controlling and reducing agents. Except a few cases the mobility was practically reduced to zero during their injection of these fluids.

6. The experiments however took an unexpected turn when the microemulsions prepared with ultra light, medium and high viscosity carrier or external phases were tested. Contrary to all expectation the least effective mobility reduction during the postflush was obtained with the microemulsion having the highest viscosity *(Figure 15);* meanwhile the best results were observed when the ultra light microemulsion was injected.

7. Surprisingly, the application of the ultra light microemulsion had residual "memory" effect, but that favorable effect was completely absent in case of heavy oil external microemulsion (Figures 13–15).

8. The post-injected petroleum decreased the partially reconstructed mobility in all cases *(Figure 16).* These phenomena are attributed to secondary emulsification promoted by the stabilizer (fatty acids and esters) retarded (adsorbed and entrapped) by rock surface and pores. It is characteristic however that this effect was also more pronounced in case of the ultra light microemulsions than of heavy hydrocarbon emulsion.

The results of the flow tests clearly proved that microemulsions, whatever they are might be considered as selective and effective barrier forming agents. Injection of these water sensitive and metastable fluids may develop substantial resistance against the flow of water and that beneficial effect may build-up only in those reservoir spaces and zones where the mobile content or the residual water saturation is high. Since the possibility of a secondary in-situ emulsification cannot be completely excluded when oil starts to flow through the treated porous media, and there is a little chance for similar phenomena in gas/water systems, the microemulsions as treating agents are primarily recommended for water shutoff in gas producing wells.

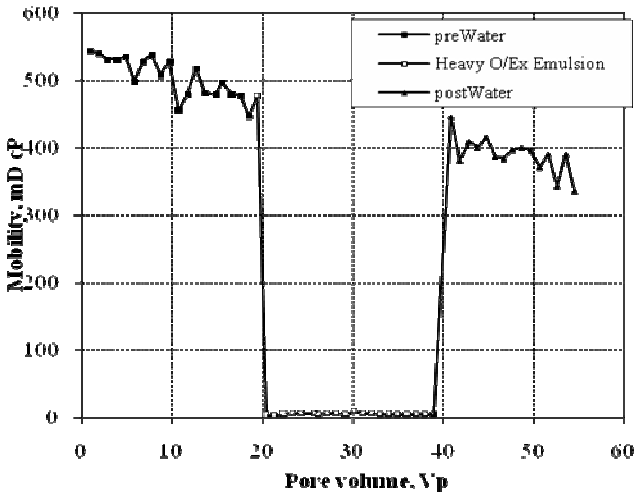

Figure 15: Effect of diluted lube (heavy) microemulsion on mobility in porous media

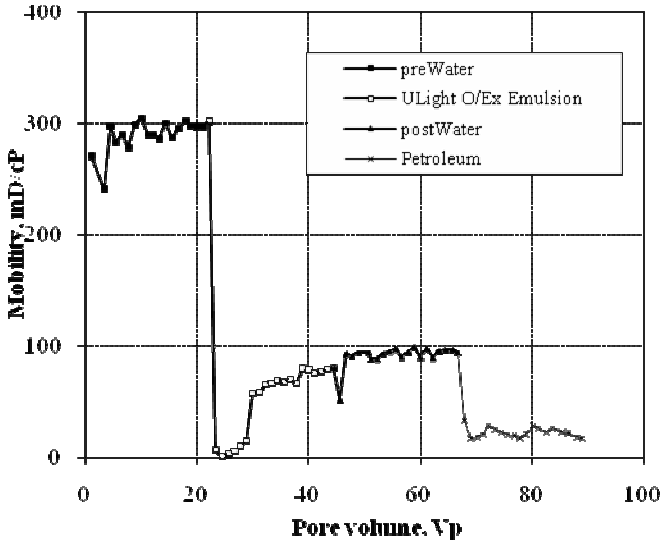

Figure 16: Effect of petroleum post-injection on mobility modification in porous media using light petroleum microemulsion

6. Field application of microemulsions

The pilot test was performed in the Algyő field, Hungary. The target area was the Szőreg-2 layer in the stacked field. The depth of the layer (perforation) is between 1803 and 1807 m. Prior to treatments the production characteristics of the well were unfavorable: the gas production was less than 8,000 m^3/d accompanied by a stable 120–130 m^3/d water production. After appropriate preliminary actions (bottomhole clean-up, analysis of log data and production history) 225 m^3 diluted microemulsion containing 0.2 g/l siloxane and 5 g/l KCl was injected, which was followed by injection of 5,000 Nm^3 nitrogen to disperse the silicon fluid and to reach deep penetration in the reservoir. The microemulsion injection was carried out at zero well-head pressure. Technical problems or failures have not arisen during the treating period. Opening the well, observation production data lasted 10 months and the gas production is illustrated on *Figure 17*. The main field experiences make possible the following conclusions to draw:

1. The gas production gradually increased right after the treatment and reached 25,000 m^3/d on average through more than a half year. Thus the job tripled the gas output and the operation could not be suspended during this period.

2. The gas/water ratio changed according to the enhanced gas production.

3. The cumulative surplus gas production is estimated to be 2.5–2.9 M m^3. Taking this result into account the job was close to the profitability.

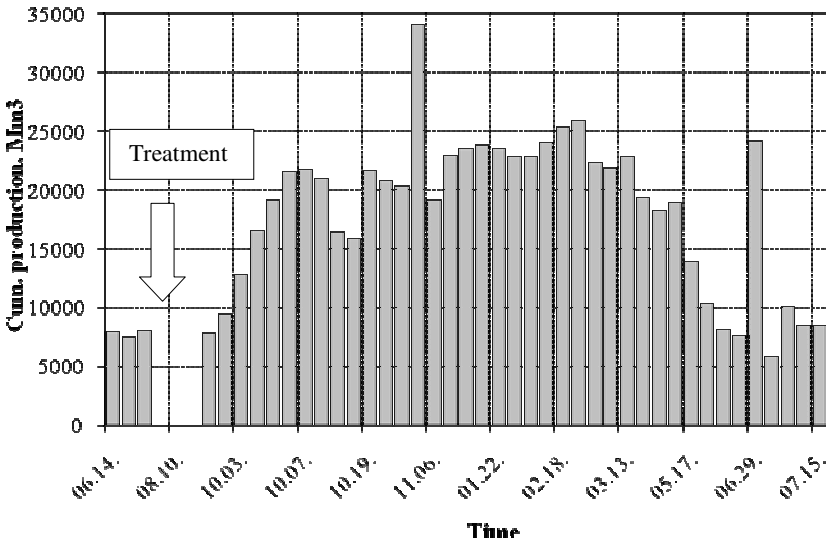

Figure 17: Gas production prior and after microemulsion treatment of Alg. 529 well

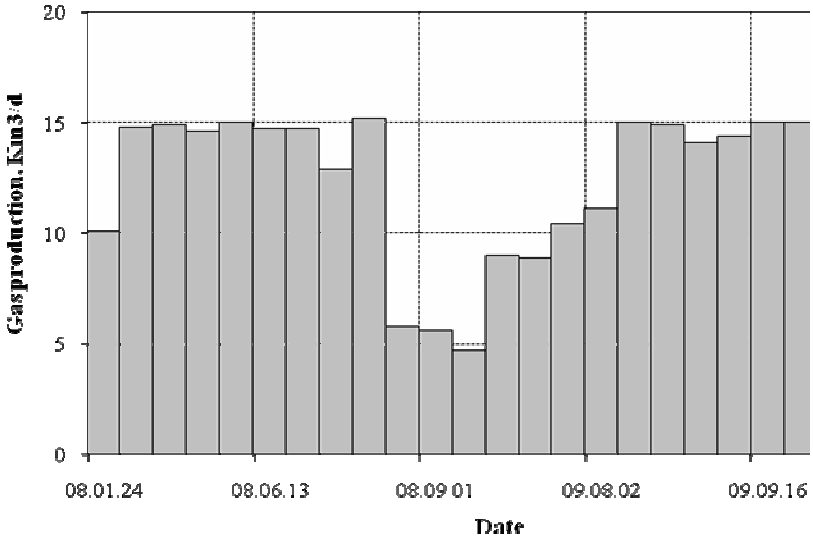

Figure 18: Gas production of Psz-20 well

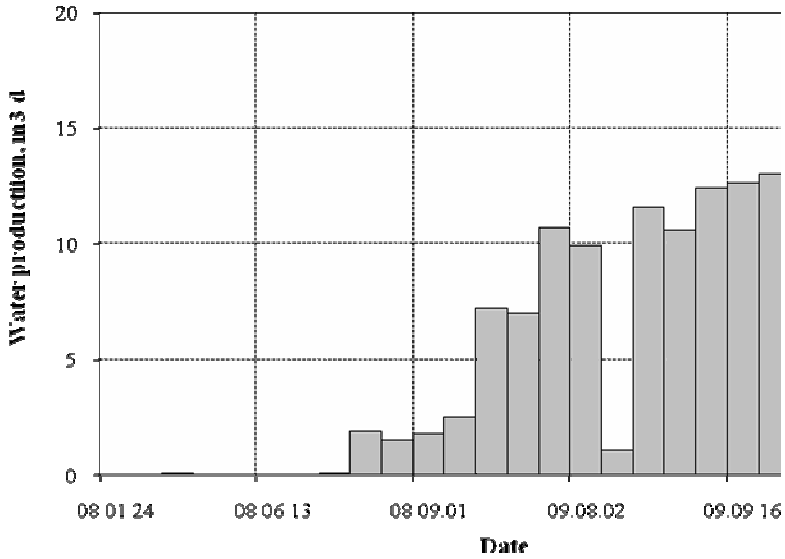

Figure 19: Water production of Psz-20 well

Since restriction of water production in gas wells is vital for the operator – just tens of wells might be a target in Hungary – and the field experiment was encouraging for the Hungarian experts, the R&D activity continued in search for more efficient, long lasting in positive response and more profitable treating techniques utilizing different microemulsions. Recently the main efforts were focused on development of cheap, but efficient microemulsions, which may replace the expensive silicon fluids. The successful R&D activity entitled us to recommend appropriate technology to enhance production efficiency at gas fields. The preliminary overview of well candidates has shown that several wells definitely have poor performance, which can be traced back to high water encroachment and production. The well candidates for the field campaign are listed in *Table 2.*

Table 2

Well candidates for water shutoff by microemulsion injection

Well	Perforation, m	Form. pressure, bar	Temperature, °C
Pf-1	1682–1688	152.4	124
Psz-20	943–946	89.6	78
Alg.-97	1794–1798	103.6	92
Hpi-D-6	1872–1884	187.6	107

As an example the gas and water production in Psz-20 well are illustrated *in Figures 18* and *12*. Although the gas production is relatively constant in the monitored period, the water production after breakthrough steeply increased and 18 m^3/d. That value is not really high; however its liquidation at the well site was impossible. Therefore the operator decided to shut-in the well loosing 14 Km^3/d gas production. Using similar well selection concept, at the end of 2011 two gas producing wells were assigned for pilot test in the Algyő-2 and the Szeged-3 formation. The Alg.-1007 well has 6–7 Km^3/d gas rate with 40–60 m^3/d water production; meanwhile the Alg,-588 has relative high, but declining gas rate (40–60 Km^3/d), but the accompanying water production is 60–80 m^3/d jeopardizing the stable and profitable gas production. Based on the evaluation of the production history, the well were selected as good candidates for water shutoff treatments to be carried out in 2012 using the petroleum external microemulsions.

7. Conclusions

1. Different metastable water sensitive chemical systems were developed, which may be used as water shutoff agents in gas producing wells.
2. Their mechanism is based on transformation of a microheterogeneous system to a more stable macroheterogeneous barrier-forming phase and that process is exclusively induced by contacting and mixing with water.
3. The most effective treating fluids are the water external silicone and the hydrocarbon external fatty acid containing microemulsions.
4. Designing the composition of microemulsions (through concentration of tenside stabilizers and water content), the microemulsions can be easily tailored to specific field and well conditions.
5. The metastable and water sensitive chemical systems having unique barrier-forming mechanism may open new vistas in water control and shutoff at matured oil and gas fields.

"Acknowledgements: This work was carried out as part of the TÁMOP-4.2.1.B-10/2/KONV-2010-0001 project in the framework of the New Hungarian Development Plan. The realization of this project is supported by the European Union, co-financed by the European Social Fund. The authors wish to express their appreciation to the Hungarian Oil and Gas Plc."

REFERENCES

[1] Sydansk, R. D.–Romero-Zenom, L.: *Reservoir Conformance Improvement*. Society of Petroleum Engineers (SPE), Richardson, USA, 2011.

[2] Sydansk, R. D.: *Polymers, Gels, Foams and Resins*. In. LAKE, L. W. (ed.) Petroleum Engineering Handbook. Vol. V(B), 13:1149–1260, SPE, Richardson, USA, 2007.

[3] Lakatos, I.–Lakatos-Szabó, J.–Tóth, J.–Munkácsi, I.–Trömböczky, S.: *New Possibility*. In. EOR: A Combined Well Treatment Technique", Proc. pp. 827, 4th European Symposium on Enhanced Oil Recovery, Hamburg, 1987.

[4] Lakatos, I.–Kretzschmar, H.-J.–Czolbe, P.–Bittkow, P.–Wassermann, I.: *Polimerinjektionen zur Stimulierung oder Abdichtung von Öl-, Gas- oder Wasserbohrungen*. Erdöl-Erdgas-Kohle, (1988) 104(1) 19–24.

[5] Lakatos, I.–Munkácsi, I.–Trömböczky, S.–Lakatos-Szabó, J.: *Potential of Repeated Polymer/Silicate Well Treatments.* SPE Techn. Paper 20996 (1990), SPE production and Facilities, 4:269–275., 1993.

[6] Lakatos, I.–Lakatos-Szabó, J.–Tiszai, Gy.–Kosztin, B.–Palásthy, Gy.–Trömböczky, S.–Boldola, M.–Pattermann-Farkas, GY.: *Application of Silicate-Based Well Treatment Techniques at the Hungarian Oil Fields.* SPE Techn. Paper 56739 (1999)

[7] Lakatos, I.–Lakatos-Szabó, J.–Kristóf, M.–Kosztin, B.: *A Novel Well Treatment Method Based on In-Situ Hydrolysis and Flocculation of Inorganic Compounds*. SPE Techn. Paper 35380 (1996)

[8] Lakatos, I.–Lakatos-Szabó, J.–Kosztin, B.–Palasthy, Gy.–Kristóf, P.: *Application of Iron-Hydroxide Based Well Treatment Techniques at the Hungarian Oil Fields*. SPE Techn. Paper 59321 (2000)

[9] Lakatos, I.–Lakatos-Szabó, J.–Kosztin, B.–Palásthy, Gy.: *Disproportional Permeability Modification by Alcohol-Containing Polymer Solutions: Laboratory Studies and Field Experiences.* SPE Techn. Paper 75185 (2002)

[10] Lakatos, I.–Tóth, J.–Lakatos-Szabó, J.–Kosztin, B.–Palásthy, Gy.–Wöltje, H.: *Application of Silicone Microemulsion for Restriction of Water Production in Gas Wells.* SPE Techn. Paper 78307 (2002)

[11] Lakatos, I.–Tóth, J.–Bauer, K.–Lakatos-Szabó, J.–Kosztin, B.–Palásthy, Gy.–Wöltje, H.: *Comparative Study of Different Silicone Compounds as Candidates for Restriction of Water Production in Gas Wells*. SPE Techn. Paper 80204 (2003)

[12] Sobanova, O. B.–Fridman, G. B.–Arefyev, Y. N.: *Laboratory and Oil Field Testing for Application of Compositions Including Hydrocarbons and Surfactants for Restricting Water Influx into Producing Wells.* 7th European Symposium on IOR, Moscow (1993)

[13] Romero, L.–Ziritt, J. L.–Marin, A.–Rijas, F.–Mogollón, J. L.–Manrique, E.–Paz, F.: *Plugging of High Permeability Fractured Zones Using Emulsions*. SPE Techn. Paper 35461 (1996)

[14] Stavland, A.–Lohne A.–Olsen, A.: *Improved Oil Productivity by Selective Water Control*. In. Lakatos I. (Ed.) Progress Mining and Oilfield Chemistry, Vol. 3. 101, Akadémiai Kiadó, Budapest, 2001.

[15] Pusch, G.–Meyn, R.–Burger, W.–Geck, M.: *Method for Stabilizing the Gas Flow in Water-Bearing Natural Gas Deposits or Reservoirs.* US Patent 6,206,102 B1 (2001)

Geosciences and Engineering, Vol. 1, No. 1 (2012), pp. 205–216.

EXAMINATION OF UTILIZATON OF GYÖNGYÖSOROSZI FLOTATION TAILING MATERIAL AS AGGREGATE FOR CONCRETE

VIKTOR MÁDAI
University of Miskolc, Institute of Mineralogy and Geology,
Department of Mineralogy and Petrology
3515 Miskolc-Egyetemváros, Hungary
askcesar@uni-miskolc.hu

Abstract
Utilization of mining wastes as secondary raw materials is of great importance. Utilization of ore processing wastes, often presented in a great volume, containing pyrite and other heavy metal sulphides in environmentally hazardous concentrations, could mitigate the environmental problems by decreasing the stored volume of the waste, hereby decreasing the dissolved heavy metal content. Such utilization can be the application of tailings as concrete aggregate.

Considering the fact, that the oxidation process of sulphides could continue in the solidified concrete, the study of its influence on the components of the concrete is crucial. The intermediate and by-products of the bacterially catalyzed electrochemical oxidation of the pyrite are secondary minerals (e.g. ferri-oxides, ferri-oxihydroxides and gypsum). The pyrite-rich grain in consequence of the electrochemical alterations will enlarge its volume, by doing so internal stresses will be generated in the concrete. The oxidation process generates acidic fluids which begin to dissolve the other components of the concrete (Ca-hydroxides, C-S-H-gel). Close to the surface of the solidified concrete body the products of the oxidation will cause the appearance of conspicuous tail-like brown patches. The above mentioned phenomena cause the strength decreasing of the concrete and confinement of the application on fully visible surfaces.

The aim of the present study, using mineralogical methods, is establishing whether the approximate 2.5 million m^3 Gyöngyösoroszi flotation tailings, deposited in the northern border of the village, is suitable for utilization as concrete aggregate.

On the material of the ZT4 shallow drill, X-ray diffraction and scanning electron microscopic measurements were carried out to investigate the mineralogical composition, with especial regard to pyrite content. Based on the examination of the oxidation process, taking place in the solidified concrete and considering the mineralogical constituents of the waste, it can be concluded that, the limitation of the possibility of applications of the solidified concrete is necessary. If the solid concrete is isolated from moisture and oxygen of the air or the bacterial catalyses of the pyrite weathering is confined, the concrete is capable of everyday usage.

1. Introduction

In this study a possible utilisation of the Gyöngyösoroszi flotation waste material as aggregate was examined.

Gyöngyösoroszi is situated in the northern-eastern part of Hungary in the Mátra Mountains. This little village is settled in the valley of Toka stream. The southern part of the valley is already the outer part of the town of Gyöngyös. All the flood area is used for agriculture. Between the main road and Gyöngyösoroszi an agricultural reservoir can be found.

The Száraz- and the Toka streams flow into this lake. Between the two valleys of these streams the flotation waste dump was established *(Figure 1).*

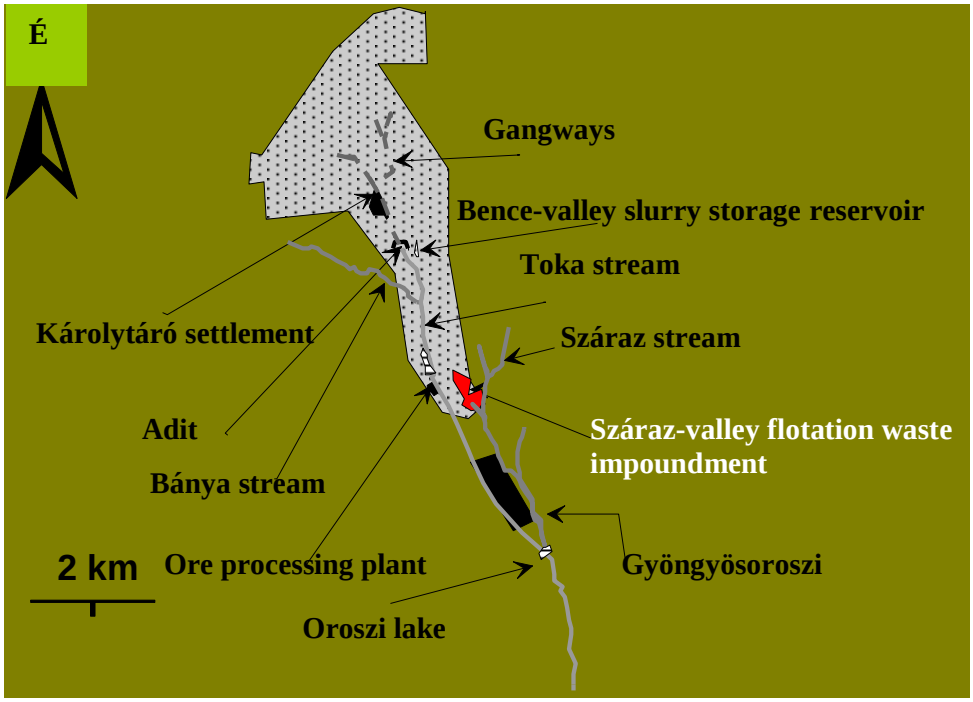

Figure 1: Localisation of the Száraz-valley flotation waste impoundment

The run-of-mine ore was pre-concentrated using heavy medium separation, then by flotation process. At the end of the process, the products were Zn-concentrate (sphalerite, zinc-sulfide) and Pb-concentrate (galena, lead-sulfide), Pb-Cu by-product (galena with chalcopyrite, lead-sulfide with copper-sulfide), and pyrite (ferro-sulfide) powder. During the concentration processes in the heavy suspension phase the aqueous suspension of ferrosilicon (74–78% Fe with 10–20% silicon) was used as a heavy medium. Its remaining, very fine powder was discarded to the flotation waste dump. At the end of the 1970-s the operation of the mine became unprofitable, the mine was closed. At the end of the working period of the mine about 2.5 million m^3 waste was deposited. This still deposited flotation waste is an environmentally hazardous material in accordance with the new legal criteria.
The weathering of rocks and mining wastes is a natural process affecting a large variety of artificial materials and minerals. Most rock types are subjected to the transformation of some of their original components into new phases. For instance a common mineral, such as orthoclase, is progressively transformed into kaolinite ($Al_2Si_2O_5(OH)_4$) [1]. In the natural environment these alteration processes are very slow and should be considered at the geological time scale. However the incorporation of rock as aggregate into concrete may lead to a drastic acceleration of the rock deterioration. Concrete represents quite an aggressive environment for the minerals compared to the natural conditions the rock had previously been exposed. The concrete pore liquor is mainly composed of alkaline and hydroxide ions, and the pH is generally higher than 13.0 [2].

A harmful reaction affecting rocks is the oxidation of pyrite (FeS_2) and pyrrhotite ($Fe_{1-x}S_x$), which are common minerals, disseminated in various rock types. These minerals are unstable in the presence of water. Their oxidation leads to a series of chemical reactions and to the formation of products of a higher volume than the initial volume of materials. At first there is oxidation of the iron sulphides in the presence of water and oxygen, followed by the formation of iron hydroxide (goethite, FeOOH) and sulphuric acid:

$$FeS_2 + 15/4\ O_2 + 5/2\ H_2O \rightarrow FeOOH + 4\ H_2SO_4 \quad (1)$$

Sulfuric acid could react with calcite ($CaCO_3$) to form expansive gypsum ($CaSO_4 * 2\ H_2O$):

$$H_2SO_4 + CaCO_3 + 2\ H_2O \rightarrow CaSO_4 * 2\ H_2O + CO_2 \quad (2)$$

This reaction is the source of several problems in the world, causing a large range of damage to building foundations and concrete slabs [3]. If reaction (1) occurs in an already hardened concrete, the sulphuric acid reacts with the portlandite ($Ca(OH)_2$), which is one of the hydration products of Portland cement and gypsum is formed according to the following reaction:

$$Ca(OH)_2 + H_2SO_4 \rightarrow CaSO_4 * 2\ H_2O. \quad (3)$$

The gypsum then reacts with aluminates in the cement (with its anhydrous or hydrated components as well), leading to the formation of potentially expansive secondary ettringite ($Ca_6Al_2(SO_4)_3(OH)_{12}\cdot 26H_2O$ or in concrete chemistry $(CaO)_3(Al_2O_3)(CaSO_4)_3\cdot 32H_2O$)

$$3\ CaO*Al_2O_3 + 3\ CaSO_4 * 2\ H_2O + 26\ H_2O \rightarrow (Ca_6Al_2(SO_4)_3(OH)_{12}\cdot 26H_2O \quad (4)$$

This secondary ettringite must be strictly differentiated from the primary ettringite normally formed in the first days of cement hydration by the gypsum and the aluminate phase of the cement (the tricalcium aluminate, $3\ CaO*Al_2O_3$). Thereafter the primary ettringite turns into a more stable form of sulfoaluminate, which is monosulfoaluminate ($3CaO * Al_2O_3 * CaSO_4 * 12\ H_2O$) and finally, into hydrogarnet (C_4AH_{13}). The remaining sulfate ions are trapped in the C-S-H gel. Secondary ettringite might be expansive; if the germination degree is higher than the crystalline growth degree the product formed will be more or less crystallized, having a molar volume three to eight times larger than that of the initial solid. If there is sufficient space for the ettringite to crystallize, needle-shaped crystals will be formed [4].

The pyrite oxidation reaction is greatly exothermic, producing about 1410 kJ of heat by a mole of oxidized pyrite, which contributes to a local increase of the temperature and accelerate the oxidation reactions of pyrite [5]. In concrete the main factor increasing the oxidation degree of pyrite, found either in framboidal or massive form, is a high pH, related to the amount of OH-ions in the pore liquor. In concrete both forms of pyrite have the same behaviour in a high-pH solution; the higher the alkalinity of the solution, the faster the reaction is [6].

The porosity and the pore connectivity of the aggregate and concrete also represent important parameters regarding aggregate weathering, as well as concrete deterioration.

Certain aggregates are more subject to weathering and deterioration, owing to their petrographic nature. For instance schist and shale rocks have a laminar structure, which increases the permeability and porosity of the rock. Moreover shale rocks contain a certain amount of clay minerals that absorb water and oxygen. If a significant proportion of aggregate particles are cracked before their incorporation into concrete, due to tectonics or to quarrying operations, such as drilling, blasting and crushing the pyrite disseminated in the aggregate particle would then be more accessible for water and oxygen and may react faster [7].

2. Materials and methods

2.1. Field and laboratory samples

The whole area of the flotation tailing impoundment was sampled, gathering materials from the heavily oxidized upper layer of the already dried tailing pond. In the middle section of the finely ground waste heap the ZT4 drill hole is situated. Undisturbed core samples were taken from the drilled material. Each sample was at least about 200 g, and after extracting from the drilled material, the samples were closed to plastic bags to prevent undesired secondary oxidation caused by oxygen and moisture rich air.

2.2. Analytical methods

A qualitative characterization of the mining and flotation waste material as aggregate samples was performed using X-ray diffraction (XRD) analysis. XRD analysis enables the identification of the crystalline phases. Every crystalline species will give a characteristic set of diffraction peaks, whose position and intensity correspond to a specific crystalline structure. Prior to the X-ray analysis, samples were manually ground to fineness lower than 45 μm, put and compacted on the rough surface of a glass blade to be randomly disorientated. A Bruker D8 Discovery model was used to perform the XRD analysis. The X-ray beam was produced by a tube, that consists of a cathode and an anode made of copper using 40 kV accelerating voltage and 40 mA heating current. The samples prepared from the cores were also observed under a scanning electron microscope (SEM). For the SEM analysis, fresh and oxidized surfaces of bulk samples were used. The originally finely ground flotation waste material was sprinkled onto a sticky surface of a plastic tape. To increase the conductivity of the surface, a thin layer of gold of 100–200 Å in thickness was applied on the face of samples. The elementary analysis of crystals detected on the surface was conducted by the energy dispersive X-ray spectrometer (EDXS). The SEM used for this study was a Jeol JXA 8600 superprobe, coupled with an X-energy analysis system. The chemical analysis using EDS was done with a Tracor EDS system (model 5500) Li/Si crystal detector and an accelerating voltage of 15 kV.

3. Results and discussion

3.1. Petrography of the aggregates

From the point of view of petrology, the material of the flotation tailing impoundment is fine-grained sand [8, 9]. If the light or dark gray quartz rich material oxidized fully or partly, the result is a yellow discoloration. The cause of the intense change in color the precipitation of jarosite and ferro-oxihydroxides mixed with gypsum. The material of the waste is more or less homogeneous. The upper heavily oxidized cover mixed with soil

contains more sulphates and ferro-oxides as well as oxy-hydroxides. The quartz content, because of the chemical stability of the so-called perfect tectosilicate structure, is constant. However the chemically stabile silicon-dioxide was under stress, together with the pore fluid of the concrete it will react to form alkali silica gel structure cracking the aggregate particles and the concrete. The pyrite content is about 5%. This mineral is the main source, by its atmospheric oxidation, the further forming sulphates and ferro oxihidroxides in the concrete. Carbonates in case they are present in any form (about 5%) might cause other problems in the concrete. The subsequent carbonation in cold wet environments can seriously crack the already solidified concrete. The generalized mineralogical composition of the fresh gray and oxidized yellow waste material using X-ray diffractometry can be seen in *Table 1*.

Table 1

Mineralogical composition of the Gyöngyösoroszi flotation tailing material. Mineral quantities are in mass percentages [8, 10]

Minerals/Sample numbers	**Gray material**	**Yellow, oxidized material**
Montmorillonite	2	2
Illite	6	0
Kaolinite	1	1
Chlorite	3	2
Quartz	61	54
Feldspar	5	6
Plagioclase	2	4
Pyrite	4	6
Siderite	2	5
Dolomite	2	1
Jarosite	3	7
Gypsum	Traces	4
Augite	0	5
x-ray amorphous	3	3

3.2. Sulfide minerals and secondary oxidation products under the surface of the tailing impoundment

Materials from ZT4 drill hole situated in the middle section of the tailing impoundment are illustrative of the whole tailing body. The undisturbed drill hole material was examined by optical stereomicroscope and scanning electron microscope *(Figure 2).*

Figure 2: Tailing material under stereomicroscope. Larger grains have about max. 50 μm diameter

Because of the intense crushing and grinding operations in the ore processing plant, a high amount of the tailing material is mineralogically homogenous, e.g. only pyrite- (*Figure 3* and *4*) and Ca-containing feldspar (*Figure 5* and *6*). The surfaces of these mineral grains are exceptionally well exposed to the weathering processes e.g. hydrolysis and other solvent reactions.

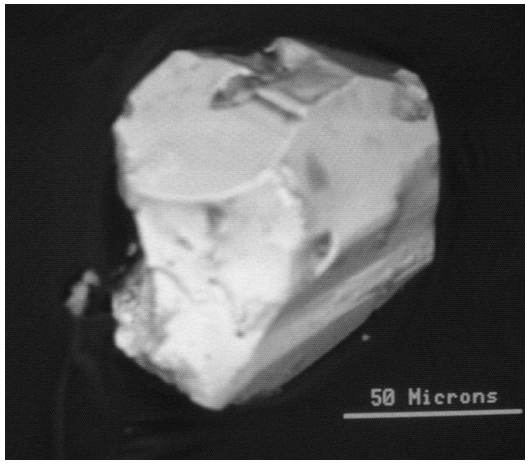

Figure 3: SEM image about a fresh pyrite grain

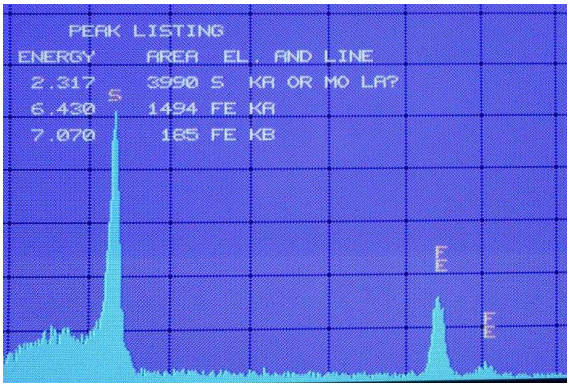

Figure 4: EDS spectrum of the pyrite grain

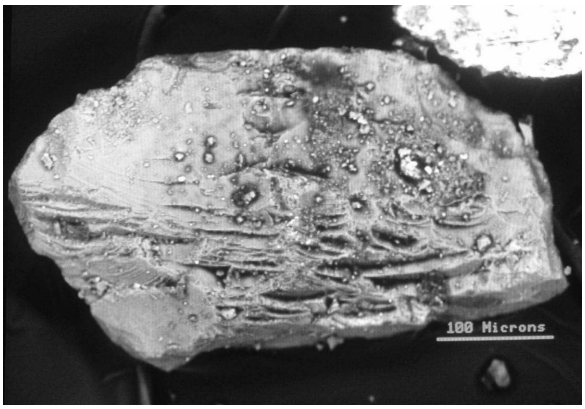

Figure 5: SEM image of a Ca containing feldspar (orthoclase)

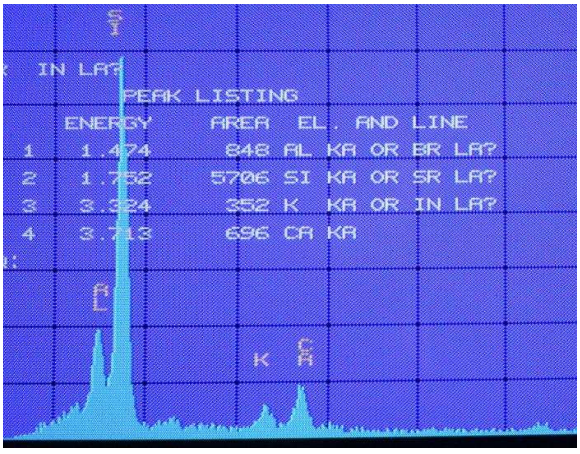

Figure 6: EDS spectrum of the orthoclase grain

However, other parts of the tailing material consist of heavily oxidized grains. Generally the surfaces of these particles are covered with secondary minerals, mainly with sulphates (*Figures 7–8.* and *9.*)

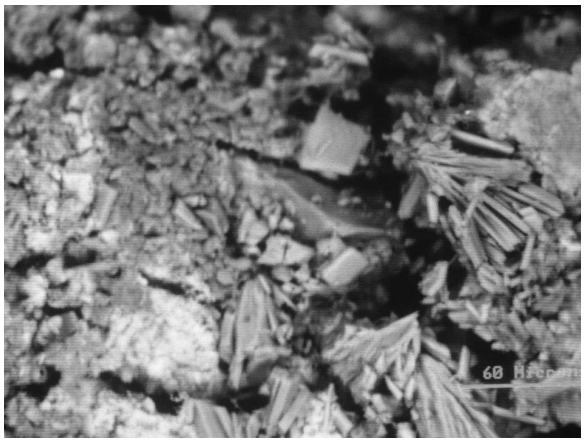

Figure 7: Secondary minerals (mainly lamellar gypsum crystals) on the surface of a Mn containing calcite grain

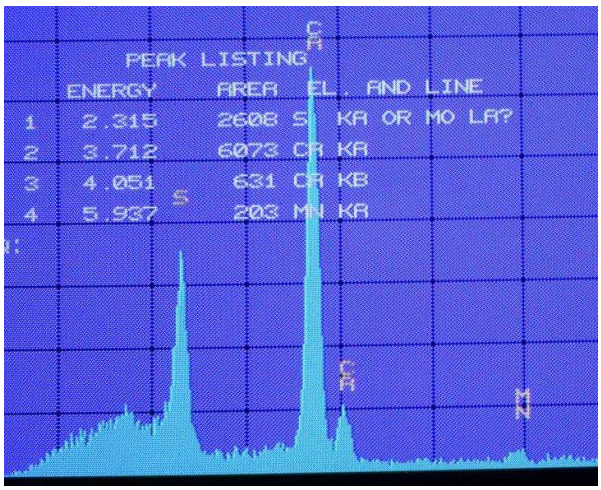

Figure 8: EDS spectrum of a gypsum crystal from the surface of the above mentioned Mn containing calcite grain

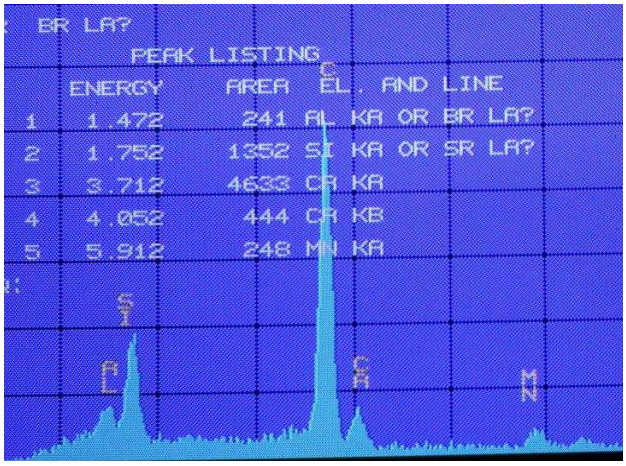

Figure 9: EDS spectra of the Mn-containing calcite grain

3.3. Possible manifestation of damage in the concrete microstructure

Having known the mineralogical properties of the flotation waste we have the possibility to predict the chemical reactions and weathering processes in a completed concrete structure.

3.3.1. Aggregate reaction

The iron sulphide containing concrete may show significant cracking of the aggregates. Generally most of the cracks originate from iron-sulfide containing regions within the aggregates and then extend into the cement paste. It appears that the degradation can be directly linked to the reaction of iron sulphides, which leads to an increase in volume within the aggregates that in turn crack and expand the concrete [11]. However some minor cracks in the aggregates caused by the iron sulfides particles might have been present in the aggregates before the concrete might be made originating from natural weathering. The investigated aggregates show ASR reactivity because of its high quartz content. The degree of reaction of the iron sulfides seems to be related to the position of the particles within the aggregates. Particles close to the surface of the aggregates show a higher degree of reaction than those near the center. It also looks like that some cracking of the aggregates along grain boundaries contributes to higher degrees of reaction, possibly by facilitating the ingress of oxygen. However, generally the extent of this reaction does not appear to be related to the position in the structure. For example in a dam concrete material particles in aggregates near to the surface of the dam did not appear to be more reacted than those far from the surface (even 3 to 4 m) inside [12].

Generally the specific volume increase of the degrading iron sulfides can be calculated and theoretically increase up to 1.3, respectively, 1.7 times. When it is assumed that the entire amount of iron sulfides degrades to half goethite (FeO(OH)) and half iron hydroxide [$Fe(OH)_3$], the maximum expansion of the aggregates can be calculated to be 0.07%. These critical expansion values might be larger than the intrinsic strain limits of the aggregates,

which are between 0.016% and 0.018% [13]. Beyond these critical values, the expansion starts to develop stress, which leads to cracks within the aggregates and finally cracks propagate into the cement paste. Thereby already small iron sulfide particles can provide enough stress to crack the aggregate in the concrete matrix. Iron sulfide degradation may be the main factor leading to the expansion in the concrete, but the possible secondary ettringite formation may contribute in a minor way to the degradation process. In general the expansion of the concrete is not homogeneous. The expansion of small inclusions inside aggregates may actually magnify the volume increase of the inclusions.

3.3.2. Secondary ettringite

Appearance of secondary ettringite crystals attributable to the release of sulfate from the iron sulfides inclusions might mainly form close to residual aluminate sources. These secondary ettringite deposits in the cement paste are typical for sulfate attack [14].

The ettringite formed in the microstructure, either from normal hydration or from the additional sulfate released from the iron sulfides, can be clearly identified in porous regions of the microstructure, mainly inside the shells left by hydrating grains. There is no evidence of distress around such deposits, however, even in systems where expansion due to internal sulfate attack is known to occur [4], these large deposits of ettringite are not believed to be the origin of expansion. Instead expansion is believed to arise from the reaction of submicroscopic crystals of calcium alumina monosulfate (monosulfate), within the C–S–H to form ettringite. The signature of expansion related to such internal sulfate attack is the formation of gaps around the aggregates as the expanding paste expands away from the nonexpanding aggregates. First the expansions are very low, so the predicted gaps would hardly be visible and secondly, it is likely that the aggregate is expanding. Due to these factors it is difficult to conclude about the contribution of ettringite formation from release of sulfates to the expansion of the concretes [12].

3.3.3. Thaumasite caused problems (TSA)

The thaumasite form of sulfate attack (often abbreviated to TSA) requires some kind of source of sulfate and also of carbonate. Thaumasite can occur rarely as a natural mineral as an alteration product of limestones. Thaumasite can form in concrete and in mortar. The cement hydration products normally present, mainly calcium silicate hydrate and calcium hydroxide are decomposed as a result of both sulfate attack and of carbonation. Since it is the calcium silicate hydrate in concrete that provides most of the strength, thaumasite formation results in severe weakening. Thaumasite has the chemical formula: $[Ca_3Si(OH)_6.12H_2O](SO_4)(CO_3)$ or $CaSiO_3.CaCO_3.CaSO_4.15H_2O$. Thaumasite crystals tend to form at low temperatures, typically about 4 ^{0}C–10 ^{0}C. As it forms the concrete or mortar converts to a friable material. Concrete severely affected by thaumasite formation can easily be broken with the fingers and the coarse aggregate lifted out. A source of additional water is also required for thaumasite formation. Damp cementitious render over brickwork, especially where the render is cracked, and concrete and masonry in cool, damp cellars are typical examples of where thaumasite may occur. Normal sulfate attack usually results in the formation of ettringite. This uses aluminium provided by the cement and clearly this is limited in quantity in normal concrete. However thaumasite formation does not involve aluminium; given an adequate supply of sulfate and carbonate, thaumasite can continue to form until the calcium silicate hydrate is completely decomposed. Consequently

while the use of sulfate-resisting Portland cement provides some defence against normal sulfate attack, it does not give any particular protection against thaumasite formation. Sulfate in that case can be supplied from the sulfate content of the heavily oxidized parts of the tailing material. Carbonate can be supplied from the calcite and Ca-containing silicates present in the flotated tailing material. Serious damage to concrete or masonry due to thaumasite formation is not a common occurrence, even in cool, damp climates [15].

4. Conclusions

The Gyöngyösoroszi flotation tailing pond material contains quartz, pyrite, chalcopyrite, galena, sphalerite, calcite, and gypsum. The material of the waste is partly oxidized. From the point of view of concrete industry the material contains some problematic components. Firstly its high quartz content, because the material is able to cause alkali silica reaction. Secondly the oxidation of the pyrite grains would cause staining on the surface of the concrete, and every region of the concrete, where oxygen and moisture diffusion is high enough to support the oxidation process. The resulting secondary minerals, e.g. sulphates and ferri-oxi-hydroxides because of their larger volume would cause undesirable internal stresses. And in addition to these phenomena, the high sulphate content would cause secondary ettringite production. If the concrete would be placed in a cold and dump environment, the thaumasite formation could cause cracking and strength decreasing. It might be concluded that every kind of environment, where oxygen or water diffusion is confined seriously, e.g. dry internal parts of buildings or completely waterlogged underwater structures are proper application possibilities.

"Acknowledgement: This work was carried out as part of the TÁMOP-4.2.1.B-10/2/KONV-2010-0001 project in the framework of the New Hungarian Development Plan. The realization of this project is supported by the European Union. co-financed by the European Social Fund."

REFERENCES

[1] http://faculty.unlv.edu/lachniet/geomorphology_files/Lecture_02%20–%20Weathering.pdf
[2] Andersson, K.–Allard, B.–Bengtsson, M.–Magnusson, B.: *Chemical composition of cement pore solutions.* Cement and Concrete Research, Vol. 19, Issue 3, May 1989, 327–332.
[3] Bing Tian*–Menashi, D. Cohen: *Does gypsum formation during sulfate attack on concrete lead to expansion?* Cement and Concrete Research 30 (2000) 117–123.
[4] Collepardi, M.: *A State-of-the-Art Review on Delayed Ettringite Attack on Concrete.* Cement and Concrete Composites, Vol. 25, Issues 4–5, May–July 2003, 401–407.
[5] Chandra, A. P.–Gerson, A. R.: *The mechanisms of pyrite oxidation and leaching: A fundamental perspective*. Surface Science Reports, Vol. 65, Issue 9, September 2010, 293–315.
[6] Caldeira,C. L.–Ciminelli, V. S. T.–Dias, A.–Osseo-Asare, K.: *Pyrite oxidation in alkaline solutions: nature of the product layer.* International Journal of Mineral Processing Vol. 72, Issues 1–4, 29 September 2003, 373–386.
[7] Rivard, P.–Fournier, B.–Ballivy, G.: *The damage rating index method for ASR affected concrete – a critical review of petrographic features of deterioration and evaluation criteria.* Cem. Concr. Aggreg., 24, (2) (2002) 80–90.
[8] http://www.mafi.hu/static/microsites/geokem/oroszi/SZINT1.html

[9] Ódor, L.–Wanty, R. B.–Horváth, I.–Fügedi, U.: *Mobilization and attenuation of metals downstream from a base-metal mining site in the Mátra Mountains, north-eastern Hungary*. Journal of Geochemical Exploration 65: 47–60., 1997.
[10] Madai, V.: *Environmental mineralogical investigation of the Gyöngyösoroszi flotation waste material*. (In Hungarian). PhD thesis, 2007.
[11] Casanova, I.– L. Agull, L.–Aguado, A.: *Aggregate expansivity due to sulfide oxidation – I. Reaction system and rate model.* Cement and Concrete Research, Vol. 26, No. 7, 993–998., 1996.
[12] Schmidt, T.–Leemann, A.–Gallucci, E.–Scrivener, K.: *Physical and microstructural aspects of iron sulfide degradation in concrete.* Cement and Concrete Research, 41 (2011) 263–269.
[13] Haha, M. B.–Gallucci, E.–Guidoum, A.–Scrivener, K. L.: *Relation of expansion to alkali silica reaction to the degree of reaction measured by SEM image analysis.* Cem. Concr. Res., 37 (2007) 1206–1214.
[14] Neville, A.: *The confused world of sulfate attack on concrete*. Cement and Concrete Research, 34 (2004) 1275–1296.
[15] http://www.understanding-cement.com/sulfate.html

Geosciences and Engineering, Vol. 1, No. 1 (2012), pp. 217–222.

EXPECTED CEMENT CORROSION PROBLEMS IN UNDERGROUND CARBON-DIOXIDE DISPOSAL

JÓZSEF MOLNÁR
Institute of Mining and Geotechnical Engineering, University of Miskolc (Hungary)
H-3515 Miskolc-Egyetemváros (Hungary)
bgtmj@uni-miskolc.hu

Abstract
Operation of high-capacity heating and power generating equipment results in great amount of carbon-dioxide emission. Numerous administrative regulations were introduced in the last years to reduce the severity of this problem. Producers of electrical energy and heat intend to avoid the high costs resulting from carbon-dioxide emission by underground disposal of the gas in question. Long-term plugging of the storage layers may lead to corrosion of the cement used as a binding agent of the plugging material. The paper discusses cement corrosion problems in plugged storage layers based on general experiences of the construction industry.

1. Introduction

If flue gas as a result of combustion in power plants containing high quantity of carbon-dioxide is disposed in abandoned hydrocarbon reservoirs, finally an efficient plugging is required to keep the gas in the layer. If technical parameters of the plugging material are to be determined the following requirements must be taken into consideration:

1. The plugging material in question must be able to solidify underground sometimes at high temperature in the presence of water and always without air.
2. It must be a gas-sealing substance i.e. it should prevent escaping of the gas from the reservoir.
3. It must preserve its sealing capability for a theoretically endless time.

Obviously portland cements are the only known binding materials that fulfill the majority of the listed requirements. Unfortunately the vast majority of inorganic non-hydraulic binding materials cannot solidify underground, bitumen may soften in higher temperatures, and polymers are extremely young inventions so it is practically impossible to estimate their lifetime.

2. Main components of the flue gas to be disposed

Composition of the flue gas produced in power plants depends on both the composition of the fuel and on the technical parameters of combustion. It can be useful as a first approach to consider the theoretical composition of the flue gas obtained by stoichiometric calculations. Some results of such an estimation based on the chemical composition of different fuel samples from Hungary [11] are shown in *Table 1.* Steam content of flue gas of natural gas combustion is obviously 1.8–3.2 times higher than of any other kind of fuel forming sulphuric acid. Furthermore it must be stressed that the vast majority of 1–2% (sometimes 5%) sulphur-oxide content of the flue gas is usually being removed by FGD (flue-gas desulphurizing) blocks in Hungarian coal-fired power plants of the Mátra and the Vértes Power Plant companies.

Table 1

Theoretical composition of the gaseous phase of incineration products of different fuels from Hungary obtained by stoichiometric calculations

Fuel	Carbon-dioxide content (mass%)	Steam content (mass%)	Sulphur-oxide content (mass%)
lignite (Bükkábrány)	79	19	2
brown coal (Márkushegy)	79	16	5
raw hard coal (Komló)	85	14	1
methane	55	45	0
fuel oil	74	25	1
oak	78	22	0
wheat straw	75	25	1

3. Some basic concepts concerning the utilization portlalnd cements as binding component of plugging materials

Although some structures were built using puzzolanas some hundreds or 1–2 thousands of years ago, artificial portland cement is a relatively young invention. Roman cement sintered from calcium carbonate rocks containing clay in their cracks was patented in 1796 by James Parker in England. This kind of cement was used even in Hungary by the beginning of the 20th century. Modern portland cement was used first in France in 1814 and it was patented in 1824. The first cement plant producing real portland cement began its operation in 1852 in Stettin (Szczecin). Sulphate-resistant (S-54) cement was used first time in 1940 in Hungary [3, 8].

Consequently modern cement as patented invention is not old enough to ensure designers to have an infinite lifetime. Usual lifetime of recently designed structures is 50 years according to recent Hungarian regulations, unless different value is prescribed by the designers.

Since portland cement clinker is usually sintered from 75–80 mass% limestone and 20–25% clay at 1,450 °C temperature, clinker itself consist of oxides *(Table 2)* forming different crystalline phases *(Table 3)* which are artificial mineral phases not occurring in nature. These artificial minerals are not quite stable as only intensive cooling can ensure quality of the portland cement for a 3-months period. Properties of cements basically are determined by the mineral composition in question and specific surface area of the ground material [1, 4, 7, 13, 16].

Table 2

Main mineral phases of portland cements [3, 6, 12, 16]

Chemical constituent	**Abbreviation according to cement chemists notation (CCN)**	**Usual quantity in portland cement clinkers (mass%)**	**Remark**
CaO	C	60–67	
SiO_2	S	19–24	
Al_2O_3	A	2–8	
Fe_2O_3	F	2–6	
MgO	M	1–5	Free magnesium-oxide content of the clinker is limited at 5 mass%.
free CaO (not forming calcium-silicates or calcium-aluminates)			Free calcium-oxide content of the clinker is limited at 5 mass%.
SO_3			Sulphur-trioxide content of the clinker is limited at 3.5 mass% and 4.5 mass% in high-strength and blast furnace slags to avoid sulphate corrosion.
Na_2O, K_2O	N, K		Potassium and sodium oxide is limited to avoid alkaline corrosion

4. Hydration of portland cements

Solidification of portland cements is the result of rather complex series of reactions [2]. Two typical chemical reactions are demonstrated as examples to highlight some basic characteristics of these processes. These equations describe suspected hydrations reactions of tricalcium silicate and (β)dicalcium silicate according to Balázs [3]

$$2\ C_3S+6\ H \rightarrow C_3S_2H_3+3\ CH$$

and

$$2\ (\beta)C_2S + 4\ H \rightarrow C_3S_2H_3+3\ CH,$$

signs of water and calcium-hydroxide are H and CH in cement chemists notation (CCN).

Some important consequences of the known and suspected chemical reactions can be summarized as follows:

Table 3

Main crystalline phases of portland cements [3, 6, 12, 16]

Crystalline phases	**Abbreviation according to cement chemists notation (CCN)**	**Chemical formula**	**Remark**
tricalcium silicate	C_3S	3 $CaO \cdot SiO_2$	C_3S content of the cement is 37–60 mass%, hydration heat 0.5 $MJ \cdot kg^{-1}$. High initial strength.
(β)dicalcium silicate	(β)C_2S	2 $CaO \cdot SiO_2$	(β)C_2S content of the cement is 15–37 mass%, hydration heat 0.25 $MJ \cdot kg^{-1}$. Low initial strength but provides higher compressive strength.
tricalcium aluminate	C_3A	3 $CaO \cdot Al_2O_3$	Very high hydration heat (1.34 $MJ \cdot kg^{-1}$) and fast setting reaction. Not sulphate resistant.
tetracalcium alumina ferrite	C_4AF	4 $CaO \cdot Al_2O_3 \cdot Fe_2O_3$	Hydration heat 0.42 $MJ \cdot kg^{-1}$. Low compressive strength, slow hydration reaction. Sulphate resistant.

1. Calcium-silicate hydrates (CSH compounds) are formed as results of the reactions in question providing the strength of the cement. Their crystals are chemically stable in alkaline environment.
2. Mass of calcium-hydroxide formed as a result of hydration amounts 15–20 % of the cement, providing definite alkaline character of the concrete.
3. Water of hydration content of solidified cement amounts 15–20 mass% of the cement at its age of 28 days.
4. Temperature of the solidifying cement can be increased to a hazardous extent by reaction heat.

5. Corrosion of portland cements in reservoirs containing flue gas

Although regular use of portland cements began after 1850, basic concepts of cement corrosion was described relatively soon in the beginning of the 20th century. Most deductions based on these observations are still valid highlighting that failure of concrete structures as a result of corrosion can start soon after construction.

Möller [12] described corrosion induced by hydrochloric, sulphuric and even carbonic acid back in 1929. These adverse effects are listed in recent Hungarian and European standards too [10], which must be taken into account by designers.

The main problem of corrosion is that calcium-oxide or calcium-hydroxide content is transformed as a result of certain chemical reactions with reagents contained in flue gas to be disposed in underground reservoirs.

- Some inorganic acids furthermore soft water containing aggressive carbon-dioxide can remove CaO or $Ca(OH)_2$ from the concrete by leaching, thus producing acid environment:

$$Ca(OH)_2+CO_2 \rightarrow CaCO_3 + H_2O$$

and

$$CaCO_3+CO_2 \rightarrow Ca(HCO_3)_2$$

This carbonation reaction can be intensified if carbon-dioxide under pressure penetrates into the plug from the reservoir especially if the concrete is porous or cracked [14].

- Magnesium ions, sulphur-oxides and sulphates can destroy the concrete by swelling.

$$Ca(OH)_2+H_2O+½O_2+SO_2 \rightarrow CaSO_4 \cdot 2H_2O\downarrow$$

Gypsum formed in the reaction can destroy the concrete by swelling thus decreasing its strength and sealing capability.

Better sealing properties of plugging and injection materials can be obtained by using ultra fine cement instead of conventional ones, as permeability of such materials is significantly lower [9]. Reduced permeability can increase corrosion resistance too, thus avoiding leakage of the disposed flue gas for a certain period. Economic aspects must be considered as price of these special ultra-fine cements is no less than 15 times higher of the conventional ones, according to the oral communication of the authors of the paper in question [14].

6. Conclusions

As a result of the factors described in the discussion chapters an obvious cement corrosion hazard should be taken into account if carbon-dioxide content of flue gas from power plants is disposed in exhausted hydrocarbon reservoirs. Furthermore if sulphur-oxides are contained in the gas, an intensified corrosion process can be expected. Unfortunately monitoring of the corrosion process has not been solved yet.

Corrosion hazard can be reduced to a certain degree if ultra-fine cements or certain other kinds of binding materials are used for plugging. But the question of chronic failure arises for every material, as reliability must be guaranteed not only for years or decades, but for significantly longer periods.

"Acknowledgement: This work was carried out as part of the TÁMOP-4.2.1.B-10/2/KONV-2010-0001 project in the framework of the New Hungarian Development Plan. The realization of this project is supported by the European Union, co-financed by the European Social Fund."

REFERENCES

[1] Balázs, Gy.: *Beton és Vasbeton I. Alapismeretek története*. Akadémiai Kiadó, Budapest, 1994.
[2] Balázs, Gy.: *Energiatakarékos betonszilárdítás*. Műszaki Könyvkiadó, Budapest, 1987.
[3] Balázs, Gy.: *Építőanyagok és kémia*. Műegyetemi Kiadó, Budapest, 1994.
[4] Balázs, Gy.(szerk.): *Építőanyag praktikum*. Műszaki Könyvkiadó, Budapest, 1983.
[5] Biczók, I.: *Betonkorrózió, betonvédelem*. Műszaki Könyvkiadó, Budapest, 1956.
[6] Cement chemist notation. From Wikipedia, the free enciclopedia, http://en.wikipedia.org/wiki/Cement_chemists_notation. Loaded on 16th January, 2012.
[7] Chen, W. F. (Editor-in-Chief): *The Civil Engineering Handbook*. CRC Press, Boca Raton–New York–London–Tokyo, 1995.
[8] Déry, A.: *Történeti anyagtan. Régi építőanyagok, összetételeik, technológiájuk...* TERC Kft., Budapest, 2000.
[9] Ergin, H.–Eskikaya, S.: *The properties of an Innovative Ultra-Fine Cement Produced in Turkey.* 22nd World Mining Congress&Expo, 11–16. September, 2011, İstanbul (Turkey). *In:* Sinasi Eskikaya (editor): Proceedeings of 22nd World Mining Congress. Turkish National Committee. Vol. III, 121–128. (Takim), (3. Cilt)
[10] Kovács, J. (szerk.): *Cement-beton zsebkönyv 2006*. Duna–Dráva Cement Kft., Vác, 2006.
[11] Molnár, J.–Debreczeni, Á.: *Comparison of Emission Rates of Power Generation Using Coal or Biomass as Fuel.* 22nd World Mining Congress&Expo, 11–16 September, 2011, İstanbul (Turkey). *In:* Sinasi Eskikaya (ed.): Proceedeings of 22nd World Mining Congress. Turkish National Committee. Volume III, 103–109. (Takim), (3. Cilt)
[12] Molnár, J.: *Építőanyagok, 6. rész: Cementek*. Oktatási segédlet. Miskolci Egyetem, Bányászati és Geotechnikai Intézet. Miskolc, 2009.
[13] Möller, K.: *Építőanyagok I. Az építőanyagok gyakorlati kézikönyve*. Dunántúl Egyetemi Nomdája, Pécs, 1929.
[14] Mörbe, K.–Morenz, W.–Pohlmann, H. W.–Werner, H.: *Korrózióvédelem az épületgépészeti gyakorlatban*. Műszaki Könyvkiadó, Budapest, 1986.
[15] Palotás, L.–Kilián, J.–Balázs, Gy.: *Betonszilárdítás*. Műszaki Könyvkiadó, Budapest, 1968.
[16] Palotás, L.: *Mérnöki szerkezetek anyagtana II. Fa, kő, fém, kötőanyagok.* Műszaki Könyvkiadó, Budapest, 1979.

Geosciences and Engineering, Vol. 1, No. 1 (2012), pp. 223–236.

POWER PLANT FLY ASH AS A VALUABLE RAW MATERIAL

GÁBOR MUCSI–BARNABÁS CSŐKE
Institute of Raw Materials Preparation and Environmental Processing
3515 Miskolc-Egyetemváros, Hungary
ejtmucsi@uni-miskolc.hu, ejtcsoba@uni-miskolc.hu

Abstract
Fly ash is a pozzolanic powdery residue collected in electric or mechanical dust collectors following combustion of coal in coal fired power plants. A relatively new method of utilizing fly ash might be the direct application of mechanically activated (ground) fly ash as an individual hydraulic binder. There are many possible applications of this cheap binder, among others, the road construction industry can use it in large quantities, reducing the costs and solving environmental problems as well. According to the experimental results carried out at the Institute of Raw Material Preparation and Environmental Process Engineering at the University of Miskolc the pozzolanic activity of fly ash can be readily controlled by fine grinding in order to produce a hydraulic binder. Another prosperous application of power station fly ash is the manufacture of geopolymer products. The utilization of this by-product as a geopolymer raw material can effectively solve the environmental risk due to its good mechanical behavior and immobilization capacity. Based on laboratory experimental results it can be concluded that mechanical activation of the raw fly ash has a positive effect on geopolymerisation. The present paper deals with a general overview of fly ash and with special regard to the above mentioned two prosperous fly ash utilization possibilities: 1) hydraulic binder and 2) geopolymer through laboratory experimental results.

1. Introduction

Given the EU regulations it is crucial to develop new technologies that allow the recycling of coal fly ash into added-value products. It is generally known that the fly ash has been used as cement additive due to its pozzolanic property. For this purpose generally the "fresh" – active – fly ash coming directly from the power plant is used and the deposited material remains on the dump area without utilization. However the investigation of the deposited fly ash utilization is of great importance in order to save valuable fields as well as to reduce environmental risk and dusting. Further advantage of the fly ash based binder utilization instead of clinker is that CO_2-emission significantly can be reduced; additionally big amount of natural resources (limestone and clay raw materials) can be saved. The rational primary raw material management is of great importance.

Fly ash is one of the solid by-products – beside bottom ash, slag and gypsum – formed during the combustion of coal during electric power generation in coal-fired power plants. These by-products are called Coal Combustion By-products (CCB) or Coal Utilization By-products (CUB). Power station fly ash is the by-product of the coal firing energy production which is generated in huge amounts worldwide – for example in China and India about 300 million tons yearly. Depositing this enormous big quantity is problematic from several points of view, e.g. fly ash dumpsites reduce the valuable fields from agricultural activity and furthermore they may cause environmental risk.

Fly ash is a finely dispersed material with average particle sizes between 10 to 30 μm. Particle size distribution of the fly ash depends on minerogenetic composition of the fuel coal, the fineness of grinding and parameters of the system the fly ash was collected in. Furthermore fly ash is a heterogeneous material with various physical, chemical and mineralogical properties, depending on the mineralogical composition of the coal fired and

on the combustion technology used. The utilization of fly ashes is determined according to their properties, fineness, specific surface area, particle shape, density, hardness, resistance to frost/thaw, mineral and phase composition as well as the pozzolanic activity depending on the above properties.

The largest user of fly ash is the cement and concrete industry. Concrete is the most widely-used man-made building material in the world. It is used in sidewalks, roads, bridges, parking structures and in building structures such as foundations, floors, and walls. Concrete is a mix of gravel, sand, cement, and water. Cement is the "glue" that binds the material together to form a hardened product. It is also the most expensive component in concrete; it has to be manufactured by mining several raw materials which are burned in a kiln. In cement manufacturing, fly ash is used to replace typical raw feed materials such as limestone, sand, clay, and iron. Because fly ash is largely silica, alumina, and iron (plus calcium in some cases), it can replace a portion of these raw materials, resulting in less mining of natural resources and avoiding the associated carbon footprint of mining equipment and quarrying activities.

According to the results of the international literature it can be stated that the utilization of fly ash in the concrete industry has the following advantages:

- Better workability, due to the spherical particles the viscosity of the concrete mixture will be better.
- The strength of the concrete can be improved by filling the pores by small fly ash particles (filler effect).
- The heat of hydration is reduced.
- The waterproofing is improved.
- The fluid concrete can be pumped easier.
- Better insulation effect can be reached.
- The efflorescence generated by $Ca(OH)_2$ and salts can be diminished.

Geopolymers or also known as inorganic polymers or artificial stones are alumino-silicate materials prepared in alkali hydroxide media (NaOH, KOH) which exhibit excellent physical and chemical properties. Due to its special characteristics they can be applied in diverse range, e.g. non-structural elements, concrete, pavements and products, containment and immobilization of toxic, hazardous and radioactive wastes, advanced structural tooling and refractory ceramics, and fire resistant composites used in buildings etc. The main advantage of the technology is that there is only a minimal CO_2 generation during the production of geopolymers (about 10–20 % of the Portland cement production!).

Figure 1a) and *b)* show examples for geopolymer application in the construction industry (paving, precast panels). The projects required that the concrete met all of the technical specifications of the local authority (van Deventer et al., 2012).

Figure 1: E-Crete™ in Port Melbourne, Australia: (a) 25 MPa footpath along Westgate Freeway extension. (b) 55 MPa precast panels across Salmon Street bridge (van Deventer et al., 2012)

2. Laboratory experiments and methods

The extent to which hydraulic additions modify the properties of cement usually depends on the amount added. With these cements the heat of hydration, the initial strength and 28-day-strength are lower, the water demand and secondary hardening (at 90 days) is higher, the sulfate resistance is usually better and the freeze-thaw resistance is worse (because of the higher content of combined water) than for pure Portland cement. The suitability of hydraulic additions for use in the cement industry must be checked for a given chemical composition with the aid of a suitable test method. There are various methods for investigating and comparing the activity, i.e. the reactivity of the additions in the activated (ground) state and in the untreated state.

2.1. Hydraulic activity of fly ash

One of the above mentioned methods is the chemical way by lime absorption. The investigation of the hydraulic activity of the fly ash by lime absorption was carried out as defined in the standard CK HSZ 4706-2 “Cement additions. Natural pozzolanic materials (trass)”. In the test 1 g of the ground material obtained by grinding for different times and 100 ml lime solution were placed in a 100 ml measuring cylinder with ground glass stopper and then shaken thoroughly. The solution was then shaken daily and every second day 50 ml were removed by pipette and titrated. After each titration 50 ml saturated lime solution was added to the original solution and shaken.

2.2. Activity index

Other important characteristic number is the activity index determined through strength measurement, where the specimens are made of a mixture of one part by weight binder three parts by weight sand and had a water-cement ratio of 0.5. The binder of the mortar specimens contained 75% of reference cement (CEM I 42.5) and 25% of fly ash. In every

case 2 x 3 specimens (size of 40 mm x 40 mm x 160 mm) were used. Specimens were stored together with the moulds in an atmosphere of min. 90% relative humidity in water sealed storage vessel. After 24±2 hours specimens were removed from the moulds, and after marking were immediately placed into water filled basin. Compressive and bending strengths of specimens were measured after 28 and 90 days, respectively (MSZ EN 196-1).

2.3. Strength of concrete specimen made of fly ash-based binder

Designs of roads require specific investigation of the concrete's strength. Investigations of the compressive strength (cylinder strength) were therefore also carried out at different mixing ratios as specified in the MSZ-EN 12390-3:2002 specification without the addition of cement. Fly ash in the activation stage "Activated I" (20 minutes' grinding time) was used in all cases as binder's component; the strength values were measured after 28, 56 and 84 days.

2.4. Geopolymer investigation

It is well known that the pozzolanic activity of fly ash can be improved significantly by mechanical activation (Csőke et al., 2007). Based on this fact a comparison investigation was fulfilled on the geopolymerisation process when the grinding time was the variable parameter. The dried raw fly ash was ground in a batch ball mill with steel grinding media for 10, 20, 30, 60 and 120 minutes resident time. Then the spent liquor alkaline activator with 35 wt % solid concentration was added in a proper quantity (fly ash:activator = 2:1) to the fly ash and they were mixed carefully. The slurry obtained was poured into a cylindrical mould with a size of Ø50x50 mm, compacted by stamping and kept in 95% relative humidity for 3 hours. Then the specimens were released from the mould and than dried at ambient temperature for 16 hours followed by heat treatment at 150 ^{o}C in an electrical furnace for 4 hours and than cooled to room temperature for further tests.

During the above described process the size and the moisture content of the specimens were measured and registered. After 7 days ageing the compressive strength of the specimens was determined using a uniaxial compression testing machine. The phase composition of fly ash and geopolymer was measured by a Bruker D8 Advance XRD apparatus.

3. Experimental results and discussion

3.1. Hydraulic activity of fly ash

In this research work two different kinds of deposited fly ash were investigated, one acid and another basic one. Three different ground products with specific surface areas of about 5000, 5500 and 6000 cm^2/g were produced with the laboratory ball mill from each of the two fly ash samples under investigation.

From *Figure 2* it can be seen that:

- Mechanical activation has a very significant effect on the hydraulic activity of the fly ash sample from Tiszaújváros (acid); after 60 days the CaO absorption capacity of the ground fly ash was 125.9%.

- For the basic fly ash sample from Ajka the CaO absorption decreased by 7.56% with increasing fineness.
- A linear relationship can be observed between the specific surface area and the CaO absorption for both ground fly ash samples.

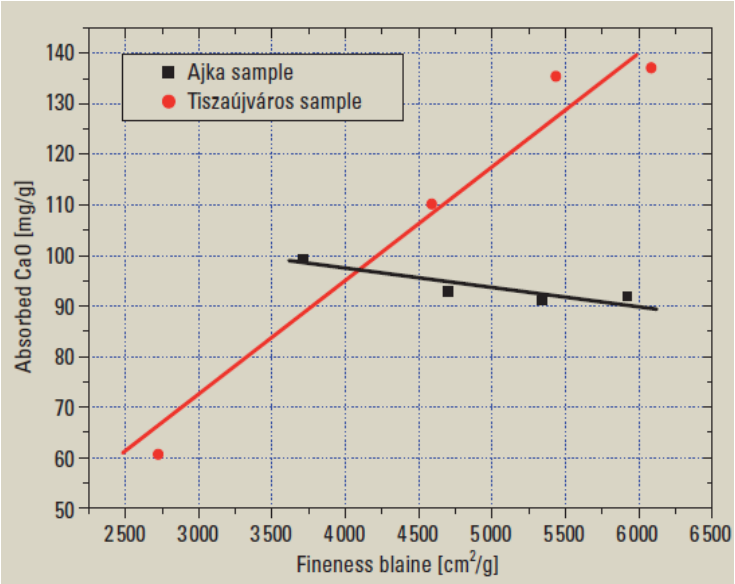

Figure 2: Cumulative value of the quantity of CaO absorbed from the saturated lime solution by 1 g of fly ash sample under investigation as a function of the specific surface area of the ground material
(Csőke et al., 2007)

3.2. Activity index of fly ash

After proving the applicability of deposited fly ash based hydraulic binder in laboratory the research was focused on the investigation of fresh fly ash. In this research work mechanical strength of specimens containing raw and ground fly ash was determined in the laboratory of H-TPA Co. in Miskolc with collaboration of the University of Miskolc. The raw fly ash from Visonta coal fired thermal power station was directly delivered to the laboratory after collecting, so it was fresh fly ash.

Compressive and bending strength measurements were carried out with differently activated fly ash to find the optimal activated state in the age of 28 and 90 days. Results can be found in *Table 1*. There were two kinds of activated state of the fly ash: activated I and activated II., the samples were ground in a laboratory ball mill for 20 and 30 minutes respectively.

The specimens were produced using the above mentioned components in accordance with the method written in the Standard No. MSZ EN 450.

From *Figure 3* the change of compressive strength of mortar specimens prepared using Visonta fly ash and cement CEM I as function of time can be seen, furthermore the effect of mechanical activation is demonstrated in the age of 28 and 90 age. Additionally the strength of reference cement is found.

Table 1

Bending and compressive strength of fly ash samples in different consolidation time

	28 days age		90 days age	
Sample	**Bending strength [N/mm^2]**	**Compressive strength [N/mm^2]**	**Bending strength [N/mm^2]**	**Compressive strength [N/mm^2]**
Raw Visonta fly ash	3.80	13.03	5.70	19.18
Visonta fly ash activated I	4.60	21.47	7.70	38.99
Visonta fly ash activated II	5.10	21.38	7.80	38.29
Reference cement	7.60	37.74	9.80	49.84

Regarding the bending strength the same parameters are plotted in *Figure 4*. Comparing the compressive and bending strength results of mortar specimens it can be stated that the mechanical activation by grinding is of great effect on the mechanical strength of fly ash based mortar.

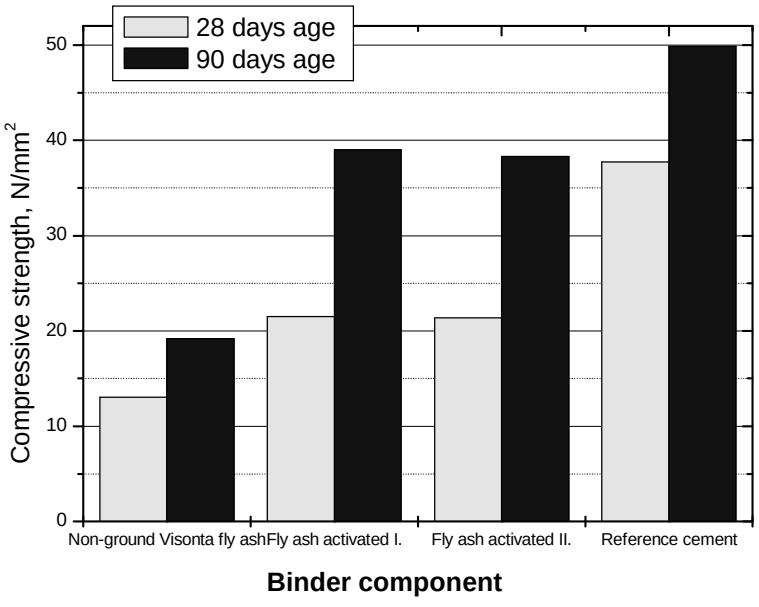

Figure 3: Compressive strength of mortar (containing fly ash in different activated state) specimens as function of consolidation time

Both strengths increased significantly due to the preparation step. However the intensity of strength increase was different in the age of 28 days as function of activation time, i.e. the compressive strength increased suddenly from 13.03 N/mm^2 (raw) up to 21.47 N/mm^2 (activated I.) showing 64.77% higher value and thereafter the strength did not continue to grow in the case of activated II (21.38 N/mm^2). Concerning the bending strength progressive hardening was observed, namely 21.05% and 10.87% strength improvement was found between the activation stages.

On the other hand both the compressive and the bending strengths stagnated after the fly ash reached the activated state I. in the age of 90 days. Furthermore similarly to the results received after 28 days more considerable solidification was found in the case of compressive strength (103.28%) than that of bending strength (35.09%) after 90 days.

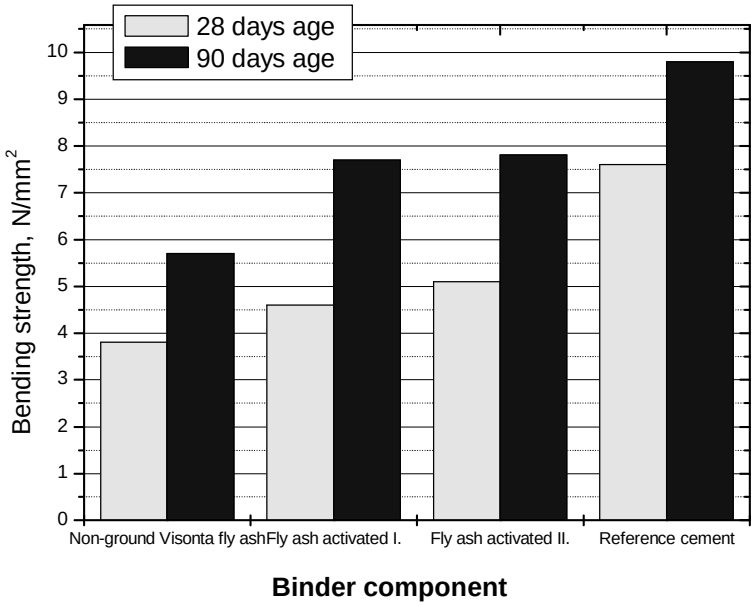

Figure 4: Bending strength of mortar (containing fly ash in different activated state) specimens as function of consolidation time

Bearing in mind the intended use of grinds in road construction the hydraulic activity of the material is characterized with an activity index (in compliance with the standard MSZ EN 450). The activity index refers to the measure of applicability of fly ash to replace cement. The activity index is interpreted as the percentage ratio of strength of a standard test piece made with 75 wt.% reference cement and 25 wt.% fly ash to the compressive strength of a standard test piece made purely with reference cement. Compressive strength measurements must be made under identical conditions. The activity index is expressed by the ratio of strength of specimen containing binder 75% reference cement/25% fly ash and the strength of 100% reference cement.

According to measurement of strength after 90 days *(Figure 5)* the activity index of the Visonta fly ash mechanically activated through 20 minutes was 0.78 compared to 0.39 measured value of raw (not ground) fly ash. Further specific surface area increase did not result further grow of activity. Experimental results suggest that pozzolanic activity of the investigated acid fly ash can be reasonably controlled by grinding.

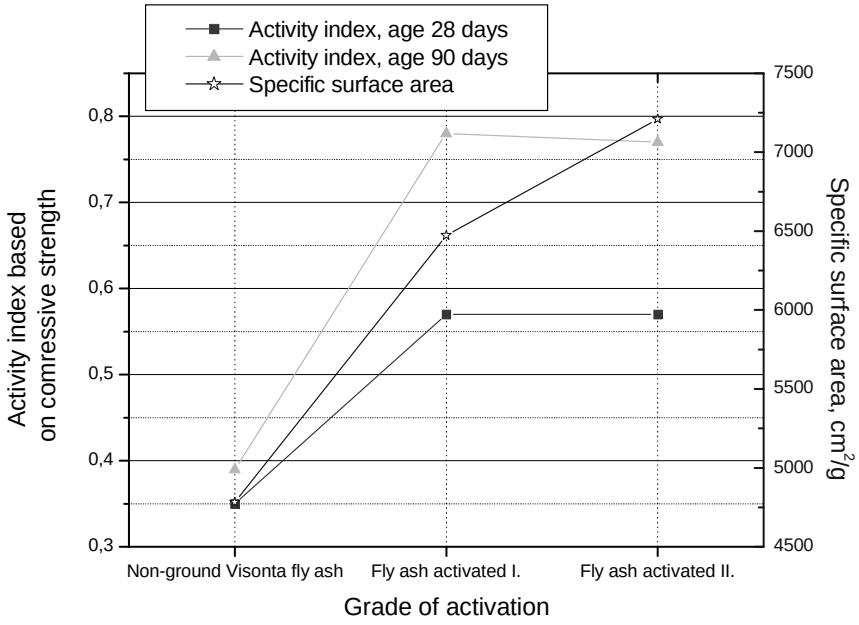

Figure 5: Activity indices (compressive strength) and specific surface area of activated and raw Visonta fly ash samples

The calculated activity indices using compressive strength results, the specific surface area and the median particle size of the initial and activated fly ash samples can be seen in *Table 2.*

Table 2

Activity indices (compressive strength), specific surface area and median size of fly ash samples

Sample	Activity index 28 days	Activity index 90 days	Specific surface area, cm^2/g	Median µm
Raw Visonta fly ash	0.35	0.39	4783.27	42.98
Fly ash activated I	0.57	0.78	6471.61	19.11
Fly ash activated II	0.57	0.77	7210.28	16.09

Contrary to the above presented characteristic curves of activity index using compressive strength, the shape of the curve of activity index using bending strength results followed the change of specific surface area as function of grinding time.

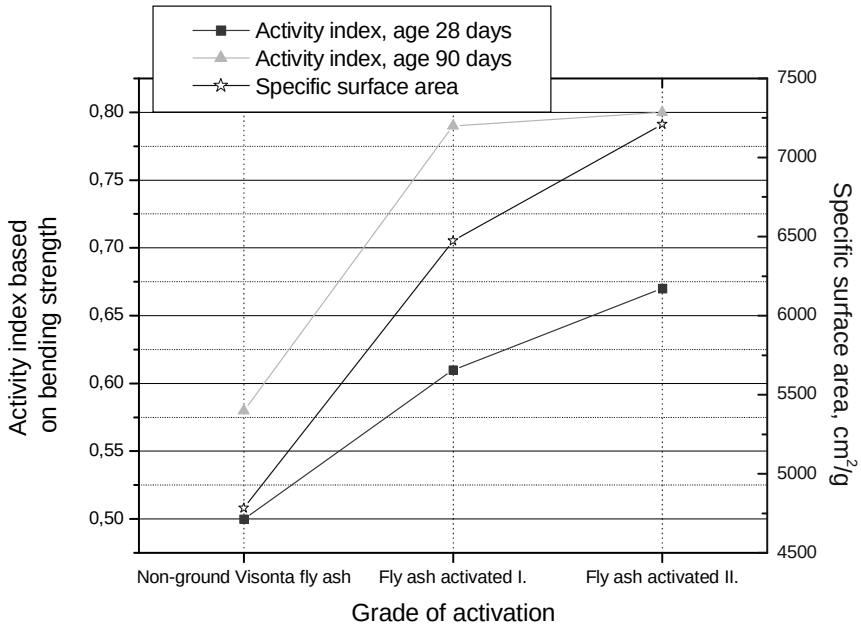

Figure 6: Activity indices (bending strength) and specific surface area of activated and raw Visonta fly ash samples

Table 3

Activity indices (bending strength), specific surface area and median size of fly ash samples

Sample	Activity index 28 days	Activity index 90 days	Specific surface area, cm^2/g	Median µm
Raw Visonta fly ash	0.5	0.58	4783.27	42.98
Fly ash activated I	0.61	0.79	6471.61	19.11
Fly ash activated II	0.67	0.80	7210.28	16.09

Based on the above activity index results it can be stated that the optimum mechanical activation time of Visonta fly ash is 20 minutes where the activity calculated from compressive strength reached maximum point from the investigated three cases (0, 20 and 30 min).

3.3. Strength investigations of the fly ash – $Ca(OH)_2$ binder

These investigations and the results of the activation tests were also used as the basis for determining the mixing ratio that is required to achieve the strength required for use in road construction. An Infratest compression testing machine was used for carrying out the strength investigations. Three mixes with binder contents of 135 kg/m^3 (Mix 1), 170 kg/m^3

(Mix 2) and 205 kg/m^3 (Mix 3) were investigated with the fresh lignite fly ash used. During the production of the concrete test specimens a fly ash with activation stage I was used in a proportion of 75%, while $Ca(OH)_2$ was used in a proportion of 25% as a binder. The slaked lime in powder form was provided by Carmeuse Hungária Co. Ltd.

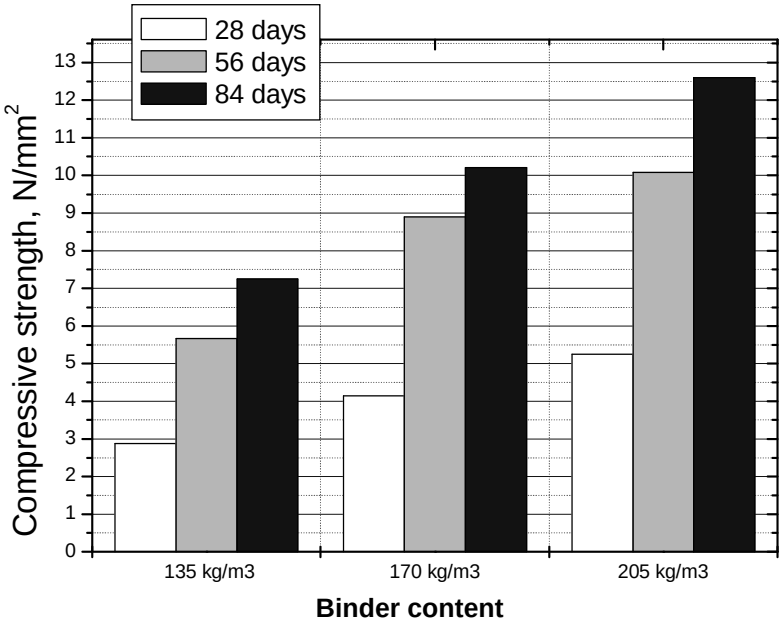

Figure 7: Compressive strength of cylindrical concrete specimens made from mechanically activated Visonta fly ash under different binder content as function of time

The changes in the strength values for the three mixes are shown in *Figure 7* as a function of time. Based on the 28-day compressive strength values determined from the sample cylinders (H/D = 1.5) and according to technical specifications for road construction (Technical Specifications-2–3. 207–2007.). Mix (1) with fly ash from Visonta should be assigned to the C1,5/2 strength class while Mixes (2) and (3) should be assigned to the C3/4 strength class. It was also established that Mix (1) can be use as a protective layer in road construction. The term "protective layer" is used as a collective term covering the frost protection, percolation, filter and similar layers in the road subbase. The protective layer which always forms the top of the subgrade, is part of the earth structure. Mixes (2) and (3) are also suitable for inclusion the road superstructure as a load-bearing layer, shown by Mucsi et al. (2009).

3.4. Geopolymer

PHYSICAL CHARACTERISTICS OF RAW- AND MECHANICALLY ACTIVATED FLY ASH AND ADDITIVES

For the investigation of geopolymer deposited brown coal fly ash was chosen. The characteristic particle sizes and the specific surface area of milled fly ash (BMFA) can be found in *Table 4.*

Table 4.

Characteristic particle sizes and specific surface area of milled fly ash

	BMFA 10	**BMFA 20**	**BMFA 30**	**BMFA 60**	**BMFA 120**
x_{10}, μm	2.92	2.64	2.21	1.55	1.09
x_{50}, μm	26.92	21.63	17.84	10.13	5.82
x_{90}, μm	85.12	83.45	79.79	43.32	26.23
Spec. surface area, cm^2/g	5540.10	6005.62	6735.17	10753.95	15444.09

COMPRESSIVE STRENGTH OF GEOPOLYMERS

The effect of mechanical activation on the specific surface area of fly ash and compressive strength of specimens can be observed in *Figure 8.* The weakest geopolymer was made of raw fly ash which has only 1.23 MPa of compressive strength. After this starting point the strength increased significantly until it reached the maximum value at 20 min (9.19 MPa), then the geopolymer strength decreased dramatically in spite of increasing specific surface area. The reason of the decreasing mechanical stability might be the generation of aggregates (see details in the monograph of Juhasz and Opoczky, 1990) from the fly ash particles (secondary particles) connected by weak bonds. The most stable structure and morphology geopolymer can be produced from particles with appropriate shape and size. Further investigation is necessary to study the behavior of geopolymers containing fly ash.

From *Figure 8* it can be stated that the relation between compressive strength and fly ash fineness is not linear. Kumar et al. (2007) investigated geopolymerisation of differently prepared fly ash (classified, untreated, vibration milled and attrition milled) and observed that higher specific surface area did not indicate higher mechanical stability of the geopolymer.

Table 5

Density of geopolymer specimens using differently prepared fly ash

	RFA	**BMFA 10**	**BMFA 20**	**BMFA 30**	**BMFA 60**	**BMFA 120**
Geopolymer density, kg/m^3	1070.11	1183.47	1213.55	1241.01	1314.26	1224.41

Table 5 shows the density of the geopolymers made of raw (unground) and ground ash. The density of the final product increased as function of milling time (fly ash fineness), the densest cylindrical specimen (1314.26 kg/m^3) was prepared from BMFA 60 starting material.

Furthermore it can be stated that a denser structure results in a geopolymer with higher compressive strength. However after 20 minutes activation when the specific surface area of fly ash reaches a certain specific surface area the compressive strength of geopolymer diminishes.

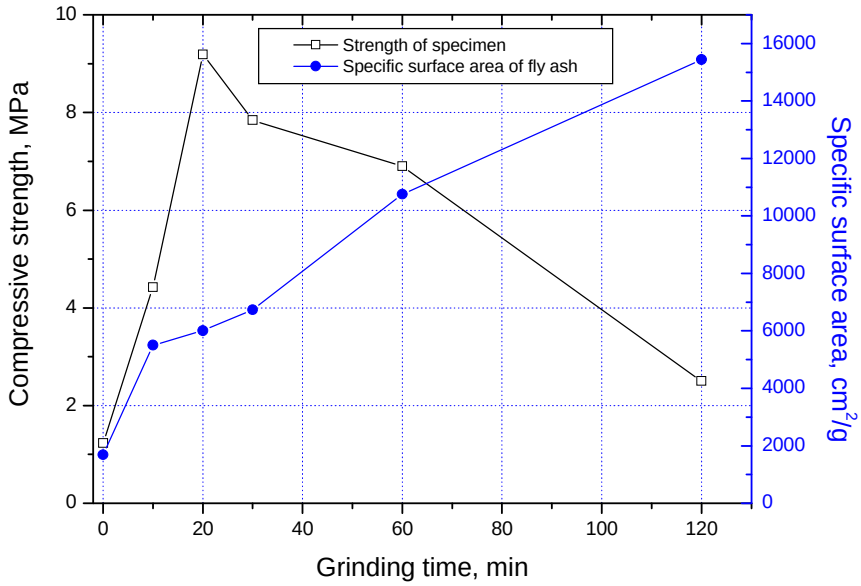

Figure 8: Compressive strength of geopolymer and specific surface area of fly ash as function of grinding time

Standard deviation was calculated for each case and values were obtained in the range of 0.25–2.65, the coefficient of standard deviation was in the interval of 9.33–28.79%.

PHASE COMPOSITION OF GEOPOLYMERS

The X-ray diffraction (XRD) measurement is of importance in the analytical technique of geopolymers even though the amount of information which can be obtained is limited due to the substantial amorphous nature of geopolymer. It provides information regarding the extent to which crystalline starting materials have reacted.

Figure 9 shows the XRD patterns of raw and mechanically activated (20 and 30 minutes) fly ash based geopolymers (without the using of any additives) and the original fly ash. It can be seen that few phases are disappeared (gypsum and christobalite) and several new phases (mostly the peak of 14 and 24 degree) are generated such like sodalites (sodium magnesium chloride silicate hydroxide: $[Na_8Mg_3Si_9O_{24}(Cl,OH)_2]$), mitridatite $[Ca_6Fe_9(PO_4)_9O_6(H_2O)_6{\cdot}3H_2O]$, wollastonite-1 A $[CaSiO_3]$, stilpnomelane $[Fe_2(Si_3O_9)]$).

The stilpnomelane probably originated from the caustic process liquor. The sodalite phase could appear due to the geopolymerisation process, it confirmed the geopolymerisation reaction.

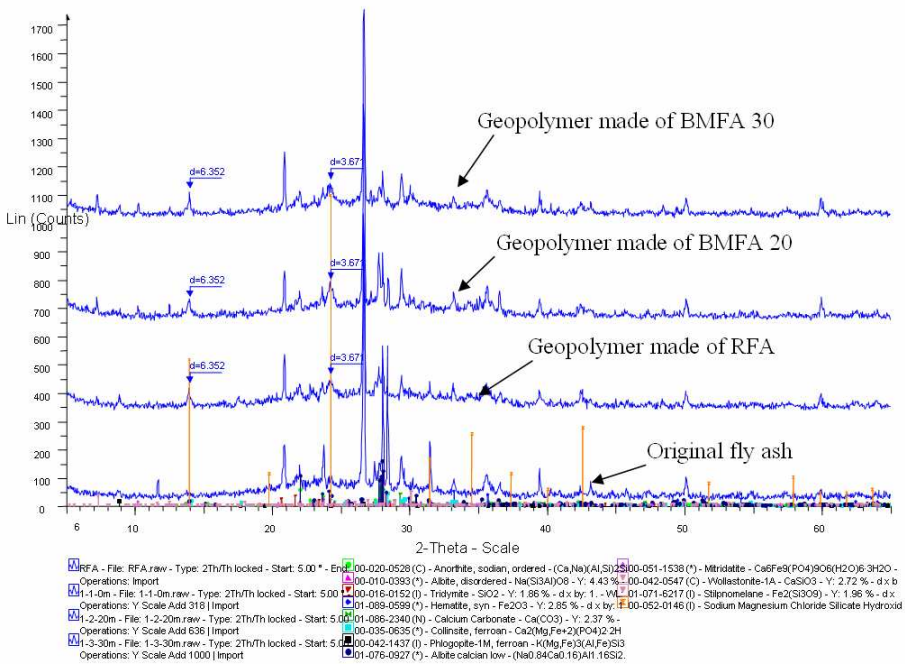

Figure 9: X-ray diffraction patterns of raw and activated Fly ash based geopolymers and the initial fly ash

4. Conclusions

Based on the experimental results it can be concluded that:

- Linear relationship was found *(Figure 2)* between CaO absorption of activated fly and fly ash fineness (specific surface area).
- Due to the fine grinding (mechanical activation) of deposited and fresh fly ash, the activity can be readily controlled in order to produce a hydraulic binder with appropriate quality (*Figures 3–4* and *7*).
- Beside the experience of fly ash based hydraulic binder the mechanical activation of the raw fly ash has a positive effect on the geopolymerisation as well, compressive strength increased significantly *(Figure 8).*

As a general conclusion it can be established that since the quality of the possible secondary raw material is very diverse, their regular physical and chemical controlling is essential in order to produce a quality guaranteed final product. From this point of view the most important material characteristics are as follows: pozzolanic activity (lime absorption), content of amorphous SiO_2, SO_3 content, loss on ignition, free lime, particle size distribution, density and morphology.

The above mentioned material characteristics can be modified by using the appropriate raw material preparation technologies and processes (grinding, classification, enrichment, mixing etc.). The final product (for example concrete) produced by this way has favorable

properties from economic and environmental aspects as well. Therefore the importance of process engineering in the secondary raw material preparation for manufacturing quality guaranteed product is outstanding since the physical and chemical properties of the initial material to be treated is very heterogeneous.

"Acknowledgements: This work was carried out as part of the TÁMOP−4.2.1.B−10/2/KONV−2010−0001 project in the framework of the New Hungarian Development Plan. The realization of this project is supported by the European Union, co‐financed by the European Social Fund. Furthermore authors greatly appreciate Dr. Viktor Mádai (University of Miskolc, Institute of Mineralogy and Geology) for XRD measurements."

REFERENCES

[1] Csőke, B.–Mucsi, G.–Opoczky, L.–Gável, V.: *Modifying the hydraulic activity of power station fly ash by grinding*. Cement International No. 6/2007. Vol. 5., 86–93.

[2] Csőke, B.–Mucsi, G.–Sík, Cs.: *Production and practical application of mechanically activated fly ash-based binding material.* VIth International Conference on Mechanochemistry and Mechanical Alloying 1–4 December 2008, Jamshedpur, India

[3] Csőke, B.–Mucsi, G.–Sík, Cs.–Gáspár, L.: *Fly ash based road construction binder.* II International Conference on Environmentally Friendly Roads, Warsaw, 15–16 October 2009. CD-ROM Proceedings, 10.

[4] Csőke, B.–Mucsi, G.–Karoliny, M.–Sík, Cs.–Gáspár, L.–Erős, Gy.: *Minőség-garantált őrölt pernye és mészhidrát-bázisú kötőanyag.* Invention: P0700644.

[5] Csőke B.–Mucsi G.–Karoliny M.–Sík Cs.–Gáspár L.–Erős Gy.–Juhász I.*: Eljárás és berendezés minőség-garantált őrölt pernye és mészhidrát-bázisú kötőanyag előállítására*. Invention: P0700645.

[6] Davidovits, J.: *Geopolymers: inorganic polymeric new materials.* J. Therm. Anal. 37, 1633–1656., 1991.

[7] Van Deventer, J. S. J.–Provis, J. L.–Duxson, P.–Lukey, G. C.: *Reaction mechanisms in the geopolymeric conversion of inorganic waste to useful products.* Journal of Hazardous Materials 2007. A139 506–513.

[8] Gáspár, L.: *Secondary raw materials in the road construction* (In Hungarian) Budapest, IHU Kht. 2005.

[9] Juhász, A. Z.–Opoczky, L.: *Mechanical activation of minerals by grinding: pulverizing and morphology of particles.* Akadémiai Kiadó, Budapest, 1990.

[10] Mucsi, G.–Csőke, B.–Gál, A.–Szabó, M.: *Mechanical activation of lignite fly ash and brown coal fly ash and their use as constituents in binders.* Cement International, No. 4/2009 Vol. 7., 76–85.

[11] Opoczky, L.: *Silicate-chemical properties of fly ash.* "For our clear environment" scientific conference. (In Hungarian) Miskolci Egyetem, A. Bányászat 55. Kötet. Környezetvédelem, eljárástechnika. 2001, 97–108.

[12] Kumar, S.–Kumar, R.–Alex, T. C.–Bandopadhyay, A.–Mehrotra, S. P.: *Influence of reactivity of fly ash on geopolymerisation*. Advances in Applied Ceramics, 2007, Vol. 106. No. 3.

[13] Van Deventer, J. S. J.–Provis, J. L.–Duxson, P.: *Technical and commercial progress in the adoption of geopolymer cement.* Minerals Engineering, 2011.

Geosciences and Engineering, Vol. 1, No. 1 (2012), pp. 237–245.

PRELIMINARY INVESTIGATION OF USING CATHODERAY-TUBE WASTE TO PRODUCE GLASSFOAM

GÁBOR MUCSI[1]–BARNABÁS CSŐKE[1]–ZSOLT ISTVÁN[2]–ERNŐ GARAMVÖLGYI[2]
[1]Institute of Raw Materials Preparation and Environmental Processing
3515 Miskolc-Egyetemváros, Hungary
ejtcsoba@uni-miskolc.hu, ejtmucsi@uni-miskolc.hu
[2]Bay-Logi Nonprofit Co. Ltd.
3519 Miskolc, Iglói u. 2.

Abstract
The paper deals with the general overview of cathode ray-tube glass waste. Furthermore it is focused on the possible utilization of this kind of hazardous waste. Physical and chemical material characteristics of CRT glass were determined as well. Optimal pelleting parameters were established for glass foam production technology using the presented raw materials. These were as follows: bentonite concentration was found to be 2.5 m/m%, plate speed was 60% of the critical speed and water content (which was the most sensitive parameter) was 20 m/m%.

1. Introduction

The corresponding law regulation which came into force in 2004 divides the electric and electronic equipment into ten categories. Those categories in which CRT is mainly applied (consumer electronics and IT) form a significant fraction (nearly 30%) of the electronic waste.

Recycling of the scrap CRT poses a special problem. There is no public demand for CRT devices any more accordingly there is no CRT recycling capacity in Europe and there are barely recycling opportunities outside of Europe. Managing this problem is critical from the viewpoint of functional WEEE treatment systems. The volume rate of the waste CRT devices based on the estimations of Bay-Logi: in the IT category is about 31% and in the consumer electronic category is about 41% of the total annual amount.

There is no demand for raw material glass with lead content because there is no CRT manufacturer in Europe. Recycling of CRTs is great problem all over Europe as the arising volume of the CRT glass waste is 400 000 tons annually and there is no practical and economic solution for recycling.

There are two kinds of cathode-ray tubes: black & white (or monochrome) and color. These two types of CRTs are made of different glass, as shown in *Figure 1* (Lee et al., 2000; Bernardo et al., 2003). The neck (~1 m/m%) and funnel (~33 m/m%) glass constitute the back part of the CRT (hidden inside the monitor or TV set). The front part usually known as the panel (~66 m/m%), is made of a barium–strontium glass that is free of lead since 1995 (Corcoran, 2001; Andreola et al., 2005), and is very homogeneous and thick. These three components are usually joined together with a solder glass called frit, which contains 85% lead.

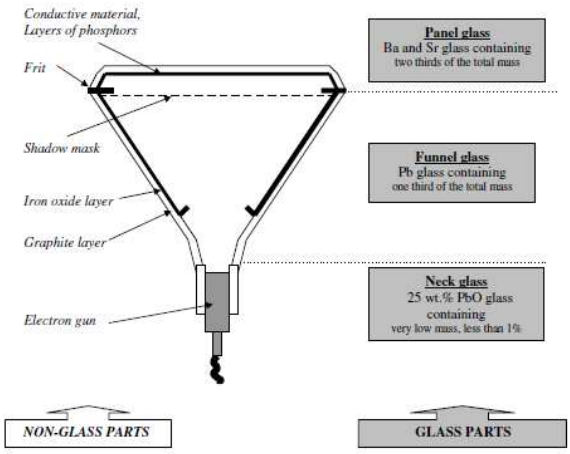

Figure 1: Parts of cathoderay-tube glass (Méar et al., 2006)

The neck glass of cathode-ray tube glass is a lead-rich silicate glass containing more than 25 m/m% PbO, which envelopes the electron gun. The lead content of funnel glass is lower than that of neck glass (~20 m/m% of PbO). The addition of lead to this glass is essential for absorbing the UV and X-ray radiation produced by the electron gun in CRTs. In the panel glass of color CRTs, however barium and strontium are used instead of lead, because this glass needs to be colorless (Méar et al., 2006).

Méar et al (2006) determined the chemical composition, densities, coefficient of thermal expansion and the glass transition temperature of waste cathode-ray tube glass originated from Asian or South-Asian manufacturers (including Japan, Taiwan and Korea). They found that color CRTs are made with two different glass formulations, one for the panel and one for the funnel, in contrast to black & white CRTs, which use only one formulation.

There are several technologies for the utilization of CRT glass in the literature. Some of them are shown below. Chen et al. (2009) investigated the recovery of metallic lead from the funnel glass and the preparation of foam glass. In the pyrovacuum process, lead in the funnel glass was firstly detached and changed to PbO, then reduced and evaporated, and was recovered in the form of pure metal with a purity of 99.3%. The maximum lead removal rate reached 98.6% when the temperature, pressure, carbon adding amount and holding time were 1000 °C, 1000 Pa, 9% and 4 h, respectively. The produced porous glass was environmentally acceptable for construction applications.

Envirocycle (a US company) developed a process (Menad, 1999) to recycle all glasses contained in CRTs; this process includes cleaning and sorting of the glass. The product obtained is used for the manufacture of new CRT glass. Some industries have used pulverized glass from CRTs in smelting processes as slagging material instead of sand or slag.

A pellet product under the name *"Geofil-Bubbles"* (Hoffmann, 1998) from industrial waste material of high glass content is manufactured by recycling technology *(Hungarian patent)*. The waste glass materials may have organic and inorganic impurities. Waste materials of high glass content are ground to appropriate particle fineness. Homogenization

is carried out with a blowing agent dosed according to the amount of impurities in the raw materials. The pelletization process is carried out by adding melting point reducer and viscosity modifying agents. The green pellet is then heat cured and coated to decrease its water absorbing capability. Sintering is carried out in a rotary furnace. The product is a lightweight artificial gravel with a diameter of 1 to 25 mm having primarily heat and sound insulating properties *(Figure 1).* This product has good bonding capability if embedded in gypsum, cement or resin matrix. This product has three main types called *Geofil A, B* and *C*. Type *A* is used for thermal insulation, type *B* is used for structural lightweight aggregate for concrete with thermal insulating property and type *C* is used for structural lightweight aggregate for concrete.

Józsa and Nemes studied different types of *"Geofil-Bubbles*" manufactured of waste glass using recycling technology which were tested at the Department of Construction Materials and Engineering Geology, Budapest University of Technology and Economics as lightweight aggregate for concrete.

Méar et al. (2006) examined the effects on foam glass microstructures by varying the elaboration parameters, reaction time, temperature and composition with scanning electron microscopy. They demonstrated that increases in the three synthesis parameters strongly affect the microstructures of the foam glasses. Increases in pore diameter lead to large reductions in mechanical resistance. Further the reduction of lead oxide content in these glasses also increases, as shown by the increase in metal lead formation in the form of droplets (bubbles) on the pore surface.

Kim et al. (2009) developed a method producing a concrete composite cross linked with minute amounts of biopolymers and a cross linking agent. Commercially available microbial biopolymers of xanthan gum and guar gum were used. This CRT– biopolymer – concrete (CBC) composite showed higher compressive strength than the standard concrete and a considerable decrease in lead leachability (good encapsulation of CRT wastes) as measured by standard USEPA methods.

2. Materials

First the received dismantled CRT waste of black & white (monochrome) and color TVs were prepared for laboratory testing. Physical material properties of the waste glass and other raw materials (bentonite, limestone, dolomite, alumina) e.g. particle size distribution, bulk and real density, moisture content and grindability were measured.

Then oxidic and phase compositions were determined. These detailed data can be found in the research report (2009). The particle size distribution was measured by dry sieving and Fritch Analysette 22 type laser size analyzer; the curves are given in *Figure 2* and *3*.

Figure 2: Sample preparation of CRT waste

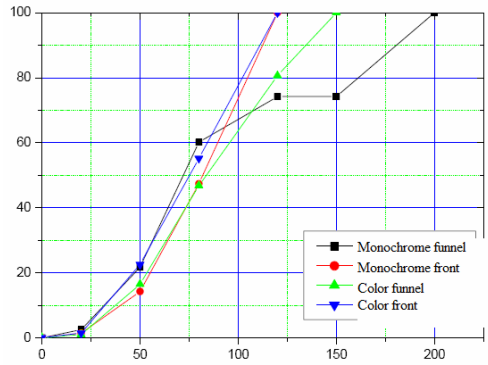

Figure 3: Particle size distribution of waste CRT (as received)

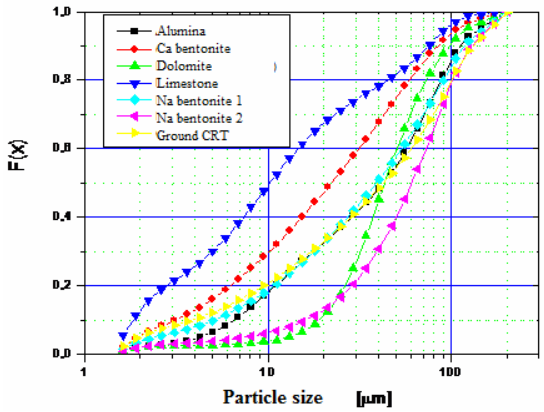

Figure 4: Particle size distribution of raw materials (treated)

The raw material properties are found in *Table 1* and *2*. From these data it can be established that moisture content was very low except of the bentonite samples. Furthermore the grindability of the front glass was a bit higher than that of the funnel glass.

Table 1

Density and moisture content of the raw materials

Sample	**Lime-stone**	**Al_2O_3**	**Dolo-mite**	**Na – bentonite 1**	**Na – bentonite 2**	**Ca - bentonite**	**Glass**
Density [kg/m^3]	2719.6	3916.2	2610.8	2192.4	2291.7	2340.5	2819.9
Moisture content, %	0.19	0.39	0.34	7.30	8.16	5.72	1.44 and 0.52

Table 2

Grindability indices of the CRT glass parts

	Monoch. front	**Monoch. funnel**	**Color front**	**Color funnel**
HGI	48.83	50.28	46.54	51.81
Bond – work index [kWh/t]	17.95	17.51	18.65	17.08

3. Experimental methods

In the research work we focused on the so called "Geofil Bubbles" product. As it was mentioned before this is a spherical shape glass foam which can be used as heat and sound insulating material due to its high porosity. One key step of the technology is the pelletization of the ground raw materials. For this purpose laboratory experiments were performed to determine the optimal conditions for producing pellets with good mechanical stability. The green pellets were manufactured with a pelleting plate in batch mode, shown in *Figure 5*.

After preparing the green pellets, they were dried in a drying cabinet at 105 ^oC for 2 hours. The mechanical strength of the dried pellets were tested with a conventional Deval drum *(Figure 6).* The resident time was 10 min (300 revolutions); then the particles were sieved to determine the mass fraction of the material finer than 1 mm. The feed of the test was the fraction of green pellets coarser than 2.5 mm.

The variable parameters for the pelleting experiments were as follows: (1) concentration of Na bentonite, (2) water content and (3) revolution of the plate.

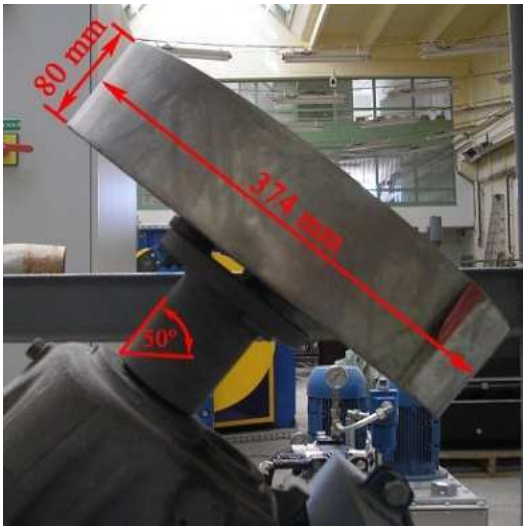

Figure 5: Pelleting plate

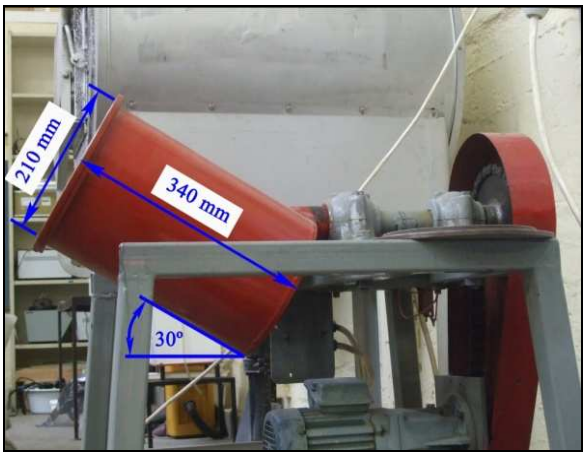

Figure 6: Deval drum

4. Results and discussion

In the first experimental series the effect of the concentration of bentonite was investigated in the dosage of 0, 2.5, 5, 7.5 and 10% for the mass of glass. The water content and the revolution of the plate were constant, 20 % and 40% of the critical speed respectively.

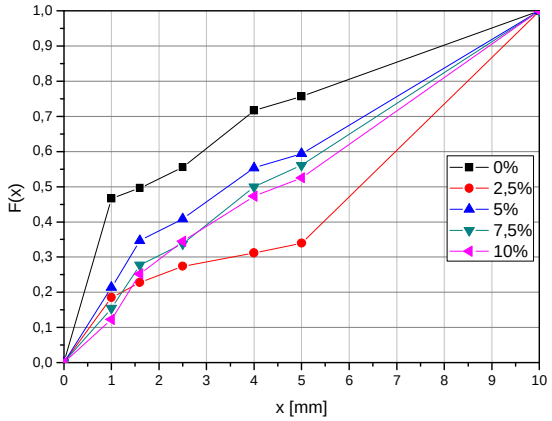

Figure 7: Particle size distribution with varying bentonite concentration

The mechanical stability of the pellets can be seen in *Figure 8.* The most significant difference (15%) was found between 0 and 2.5% bentonite content, after this point a slight increase can be seen.

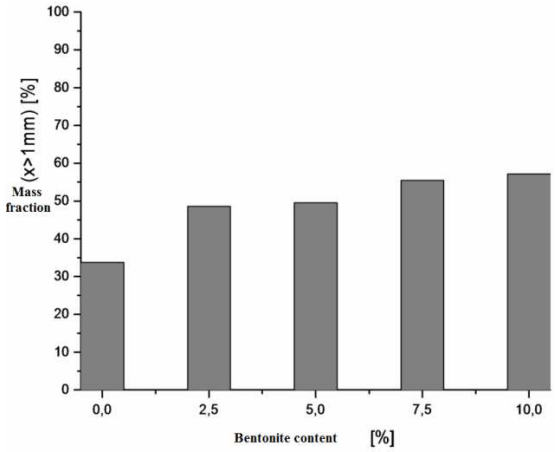

Figure 8: Mechanical stability of pellets as function of bentonite concentration

In the second step the effect of the speed of the plate was examined with 40, 50, 60 and 70% of the critical speed.

It was observed that increasing the pelleting plate's speed caused no evident changes in the mass fraction of fines *(Figure 9).* However, the shape of the particles changed significantly, i.e. more spherical shapes were achieved at higher speeds.

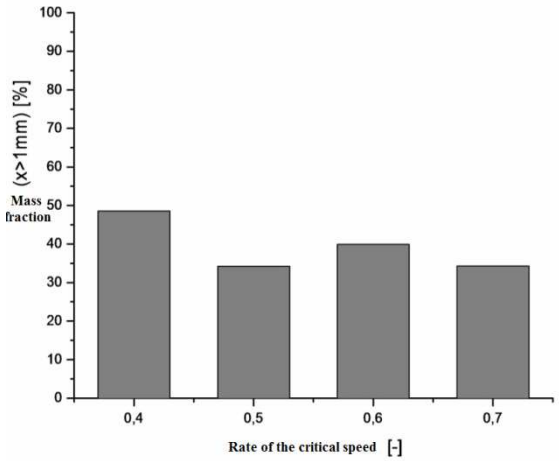

Figure 9: Mechanical stability of pellets as function of plate speed

In the third series the effect of the water content was studied with 17.5, 20 and 22.5 m/m% water dosage.

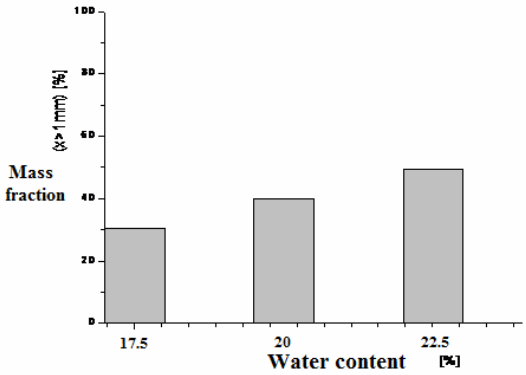

Figure 10: Mechanical stability of pellets as a function of water content

According to our results the optimal water dosage was 20 m/m%. Pellets with lower water content (17.5%) became weak due to the insufficient capillary forces. In contrast to this, the higher water content resulted better throughput (kg/h) of the valuable size fraction. At the same time the particles were generated with deformed shape and coarser diameter, furthermore the material loss increased due to the sticking of the powder to the wall of the apparatus.

5. Conclusions

Based on our study it can be concluded that using the above presented raw materials under the suitable conditions, pellets with appropriate mechanical stability can be produced. Optimal pelleting parameters were determined: bentonite concentration was found to be 2.5 m/m%, plate speed was 60% of the critical speed and water content (which was the most sensitive parameter) was 20 m/m%.

"Acknowledgement: This work was carried out as part of the TÁMOP−4.2.1.B−10/2/KONV−2010−0001 project in the framework of the New Hungarian Development Plan. The realization of this project is supported by the European Union, co‐financed by the European Social Fund."

REFERENCES

[1] Andreola, F.–Barbieri, L.–Corradi, A.–Lancellotti, I.–Falcone, R.–Hreglich, S.: *Class-ceramics obtained by the recycling of end of life cathode ray tubes glass.* Waste Manage, 2005, 25, 183–189.

[2] Bernardo, E.–Scarini, G.–Hreglich, S.: *Mechanical properties of metal-particulate lead-silicate glass matrix composites obtained by means of powder technology.* J. Eur. Ceram. Soc. 2003, 23, 1819–1827.

[3] Corcoran, Ch.: Communication in Western Electronic Product Stewardship Initiative (WEPSI) Multi-Stakeholder Meeting 3, December 12, Portland,2001, Oregon.

[4] Chen, M.–Zhang, F.–Zhu, J.: *Lead recovery and the feasibility of foam glass production from funnel glass of dismantled cathode ray tube through pyrovacuum process.* Journal of Hazardous Materials, 2009, 161, 1109–1113.

[5] Csiszár, I.: *Optimization of pelleting process during CRT waste based glass foam production.* Diploma thesis (In Hungarian), 2010.

[6] Hoffmann, L.: *Process for (especially) waste of glass materials to produce closed pore-structured silicate-foam, and product.* (Geofil-Bubbles). Patent: HU 224 808 B1.

[7] Józsa, Zs.–Nemes, R.: *Recycled glass aggregate for lightweight concrete.* Budapest.

[8] Kim, D.–Quinlan, M.–Yen, T. F.: *Encapsulation of lead from hazardous CRT glass wastes using biopolymer cross-linked concrete systems.* Waste Management, 2009, 29, 321–328.

[9] Lee, C. H.–Chang, S. L.–Wang, K. M.–Wen, L. C.: *Management of scrap computer recycling in Taiwan.* J. Hazardous Mater. A73, 2000, 209–220.

[10] Méar, F.–Yot, P.–Cambon, M.–Ribes, M.: *The characterization of waste cathode-ray tube glass.* Waste Management, 2006, 26, 1468–1476.

[11] Méar, F.–Yot, P.–Michel R.: *Effects of temperature, reaction time and reducing agent content on the synthesis of macroporous foam glasses from waste funnel glasses.* Materials Letters, 2006, 60, 929–934.

[12] Menad, N.: *Cathode ray tube recycling*. Resources, Conservation and Recycling, 1999, 26, 143–154.

[13] *Recycling of cathoderay-tube glass with lead content.* (In Hungarian) (CRTGLASS) Research report, University of Miskolc, 2009.

Geosciences and Engineering, Vol. 1, No. 1 (2012), pp. 247–254.

INVESTIGATION OF THE SOLID WASTE OF A SMALL TOWN FOR THE PRODUCTION OF RDF

[1]S. NAGY– [2]V. MÁDAINÉ ÜVEGES
Institute of Raw Material Preparation and Environmental Processing
H-3515 Miskolc-Egyetemváros, Hungary
[1]ejtnagys@uni-miskolc.hu, [2]ejtmuva@uni-miskolc.hu

[3]É. BOROS–[4]I. SZŰCS
Institute of Energy and Quality Affairs
H-3515 Miskolc-Egyetemváros, Hungary
[3]tuzeva@uni-miskolc.hu, [4]tuzsi@uni-miskolc.hu

Abstract
It is well-known that Hungary is poor in energy sources; therefore the country must rely on imports, particularly from the expensive hydrocarbons. However a considerable part of the municipal solid waste with significant chemical energy forwarded to landfills, because of the absence of incinerator capacities. From the municipal solid waste a valuable fuel can be generated with different technologies and this fuel can be suitable to provide one part of the thermal energy demand of a small town.

One aim of the research group of the University of Miskolc is to develop an energy supply model for the small and medium size towns, based on the locally available biomass and solid waste. This energy can be suitable for the substitution of the fossil fuels, especially the very expensive natural gas.

Within the framework of the research, the amount and the composition of the waste from a chosen town were measured by questionnaire, and in situ waste analysis. In this study the experimental data from the waste analysis are shown and compared with results of other towns. The possible treatment technologies for this waste are also discussed.

We give a review of the briquetting possibilities of the fuel to be produced, the main combustion technical characteristics of the pellets originated from waste – using former experimental results –, and the pellet behaviour during combustion is also mentioned.

1. Introduction

In Hungary quasi 5 million tons of municipal solid waste (MSW) is generated. About 75% of this waste deposited in landfills [5]. The treatment of the residual from the selective waste collection (the medley) is required, in order to save landfill capacities by reducing the weight and stabilizing the waste. On the other hand, energy can be obtained from the waste in form of refuse derived fuel (RDF).

At University of Miskolc during the research work, in order to substitute the fossil fuel based heating systems, a small town, Csernely was chosen for a sample town. Csernely has 830 inhabitants. The technologies able to convert municipal solid wastes (MSW) into alternative fuel were investigated. By application of the proper technology the residual waste can be divided into two parts, one fraction with high caloric value, and suitable for energetically purposes, and another fraction, a compost-like stabilate or compost like organics (CLO). The most widely used treatment method is the mechanical biological treatment (MBT).

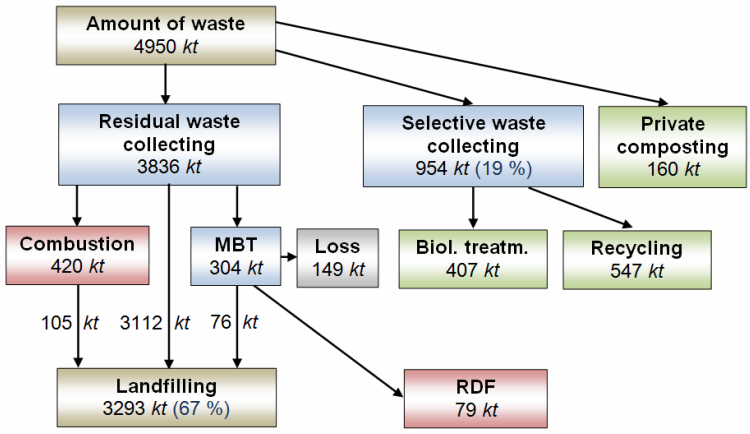

Figure 1: Municipal solid waste treatment in Hungary (2009)

One of the first steps of the research work is to determine the amount and the composition of the waste, generated at the sample town.

A comparison is given with the former results from another small town in relation to waste composition. The experimental data of a burning analysis carried out with a fuel, generated from MSW are also shown.

2. Waste processing technologies

Waste treatment

The strict rules in the field of environmental protection, prescribe the environmental friendly treatment of the MSW. The waste management of the European Union based on a hierarchical priority scheme *(Figure 2)* [8].

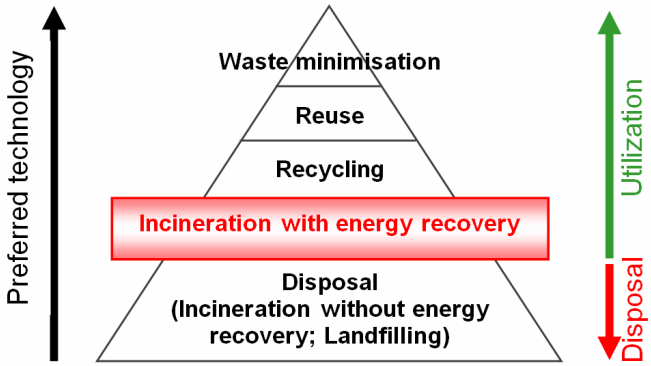

Figure 2: Principles of the waste management hierarchy

Based on the predictions the volume of the waste will increase in future [4]. One aim of the Second National Waste Management Plan – operating until 2014 – is to reduce the amount of the deposited waste below 60%. This more or less means:

- raising up the selective collection rate;
- the biologically degradable components have to be processed;
- and not least the rate of energetically utilization has to be increased.

It is important to mention that under the current legislations, the amount of the biodegradable waste at landfills is not allowed to be more than 35% by mass, correlated to the deposited amount in 1995.

Considering the international experiences, it can be only partially achieved; therefore the thermal utilization can be the complete solution.

The following methods are recommended [4]:

1. energetic utilization of the medley waste from the residual waste collection in waste incinerators;
2. after mechanical-biological pretreatment, thermal utilization of the RDF in waste incinerators or by gasification
3. after mechanical-biological pretreatment, thermal utilization of the RDF with high caloric value in cement factory or in coal-fired power plants.

MSW treatment technologies

The mechanical processes in order to produce RDF from the municipal solid wastes are known for at least 20–25 years. The biological stabilization was carried out in order to decrease the moisture content of the biodegradable part of the MSW, and for the production of a higher quality fuel. Today this complex treatment technology for the waste from the residual collection, consist of the combination of the mechanical, biological and thermal processes [3]. The general flow sheet of the mechanical biological waste treatment technology can be seen in *Figure 3*.

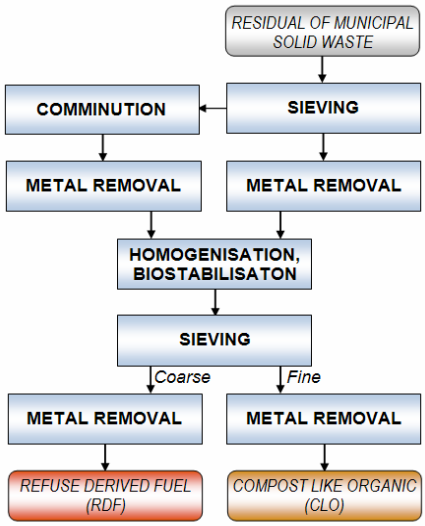

Figure 3: MBT technology in general

MBT technology in Hungary

In Hungary essentially two ways of MBT treatment are common. After comminution and metal separation, the municipal solid waste is subjected to biological treatment, and in this

case after the biological separation the coarse product of the drum screen is the useful fraction for energy purposes. In Hungary Győr–Sashegy Waste Treatment Centre and the Felső-Bácska Waste Management Ltd. are the examples for this technology [1, 2].

The other way is when after the comminution and metal separation, only the fraction below 80–100mm of the municipal solid waste is subjected to biological treatment. In this case, the energetically useful product is generated partly from the fraction larger than 80–100mm – separated in the beginning of the technology –, and on the other hand the upper fraction from the biological treatment followed by screening. The waste treatment centre of Green Bridge Region Ltd. in Kerepes, Ökörtelek Valley adopted this kind of technology [1, 2].

Refuse derived fuels generated from the MBT technology are purchased by power plants, and cement plants, but the gasifier plants and pyrolysis plants are also mean a potential market for these products [6].

3. Waste analysis of small town

From the point of view of the supply of the planed heating system it is important to know the quantity and quality of the arising MSW in Csernely.

The small specific waste amount is typical for small town (ca. 250 *kg/a/inhabitant*, against the big cities 450–550 *kg/a/inhabitant*). It can be explained with the smaller consumption (circumstance of inhabitants, private produced food), and the private composting and combustion of the waste.

The expected amount of waste can be obtained by multiplying the number of inhabitants and the specific waste amount. The weekly amount in Csernely:830 inhabitant×250 *kg/a/inhabitant*/52 week*/a* = 3990 *kg/week*.

Determination of quantity and utilisation of waste through questionnaire

The aim of the research work is to produce different fractions with high caloric value from MSW. In the given period a comprehensive public survey was made in the chosen small town (Csernely). The quantity and the fate of MSW (collecting, comminution) were determined by our questionnaire.

43. How much MSW arise in a week in your household? (*one standard bucket is 10 litre, one big dumpster is 110 litre)*

…… l/week/household

99 – don't know
0 – don't answer

44. Ratio of MSW used for heating purposes in autumn and winter:

1–0 %
2–25%
3–50%
4–75%
5–100%

9–don't know
0–don't answer

Figure 4: Questions related to the MSW

The weekly arising amount of MSW was determined by the answers for the questionnaire: 17950 *l*, it means 88 *l/household*. The mass of that is 3590 *kg* (average bulk density: 0.2 *kg/dm*^{3}) which corresponds with the calculated amount.

In situ waste analysis

We wanted to determine the amount and composition of the arising wastes with direct analysis. According standard the waste must be emptied from the collecting vehicle, and so sampled. In our case it was not possible, because the vehicle collects the waste weekly (Wednesdays) from many settlements, so the waste from different settlements is mixed. There were two possible alternatives for the composition analysis of waste according to standards MSZ 21420-28 and 29:

ALTERNATIVE 1: Collection of the sample (300–500 kg) to be analysed from randomly chosen households.

ALTERNATIVE 2: Collection of the full weekly waste amount in Csernely, and take the sample (300-500 kg) from it.

The waste analysis was carried out according to Alternative 2. The wet composition data are shown in *Table 1* and *Figure 4,* where the total combustible fraction is the sum of 2–8 fractions, the total non combustible contains 9–12 fractions.

Table 1

Results of waste analysis (Csernely and Szuha)

Small town		Csernely	Szuha	Szuha
Number of Inhabitants		830	700	700
Time		09. 2011.	05. 2009.	06. 2007.
Mass of sample [kg]		341	415	452
Material composition, categories, [% m/m]	1. Bio	34,34	39,00	27,29
	2.-3. Paper, Cardboard	7,63	4,05	11,61
	4. Composite	0,66	1,49	1,01
	5. Textile	1,55	2,76	2,59
	6. Hygienic	1,45	3,69	4,32
	7. Plastic	9,38	14,88	13,70
	8. Combustible	2,78	1,94	2,30
	9. Glass	3,96	3,63	4,83
	10. Metal	1,49	3,48	1,86
	11. Non combustible	8,42	2,01	4,52
	12. Hazardous	1,25	1,00	1,17
	< 20 mm	27,08	22,07	24,80

Date of analysis: 27 Sept 2011.
Place of analysis: Csernely
Origin of sample in the case of Csernely: from randomly chosen households

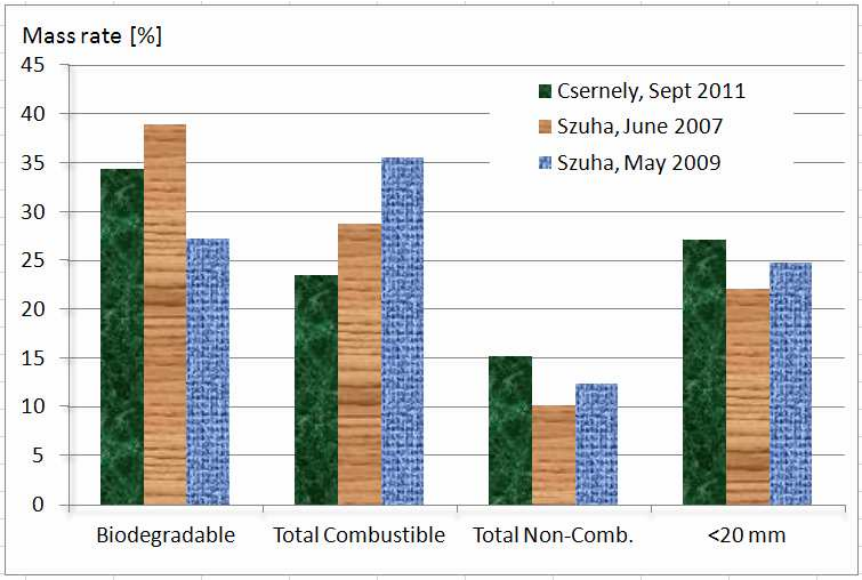

Figure 5: Main components of MSW of Csernely and the reference town

It can be seen that the waste of Csernely contains less combustible part and more fine fraction and non combustible, than the waste of Szuha. Table 1 shows that the ratio of packaging material (plastic) is significantly less than in Szuha, the non combustible (predominantly demolition waste, detritus) exceeds the values of reference small town. We should take in account this differences by the estimation of yield of high caloric values fraction.

4. Combustion technical properties

During an earlier experiment the high caloric value fraction of MBT and it's mixture with woodchips and paper were used to produce pellet (diameter: 14 *mm*) for heating by the Vertikál Zrt's flat die pelletiser [7].

Regarding to its elastic behaviour the waste had to be run over the technology twice in order to receive pellets with proper strengths. The main combustion technical properties are shown in *Table 2*.

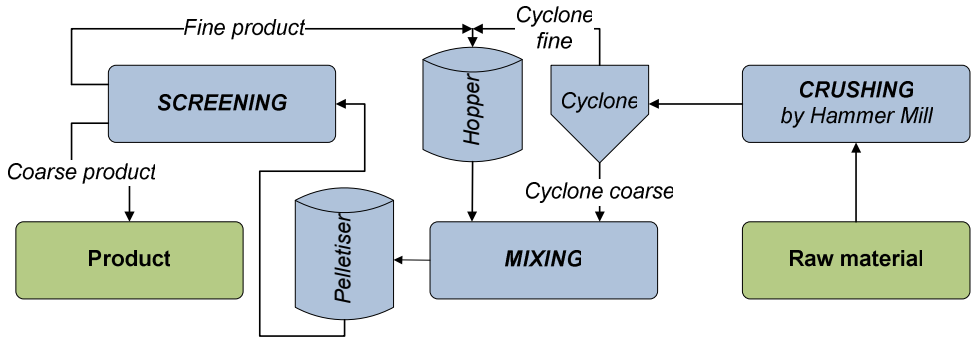

Figure 6: Pelleting plant technology in Polgárdi [6]

Table 2

Structural and chemical composition of MSW pellets [7]

Pellet composition	Water	Ash	Volatile	C	H	N
	% m/m					
Treated MSW	15,33	12,88	63,55	60,09	7,47	0,96
Treated MSW and wood	16,16	12,84	61,55	55,50	7,10	0,78
Treated MSW and paper	13,81	13,56	57,60	53,50	6,97	0,94

The measured data during combustion experiments are shown in *Table 3*. (FLEXICO HUNGARY Halmaj Kft., 40 kW heating power, regulation by frequency modulator, screw fed pellet furnace).

Table 3

Measured characteristics of pellets during burning [7]

Pellet composition	Treated MSW	Treated MSW and wood	Treated MSW and paper
T_{max} [°C]	1024	920	985
CO [ppm]	628	595	605
CO_2 [% v/v]	13,8	12,4	12,8
O_2 [% v/v]	8,8	9,6	9,2
NO_x [ppm]	680	567	590
[kJ/kg]	19 622	16 533	19 062

On the grounds of *Table 3* we can consider the CO value was significantly under the for wood heating enabled value, NO_X content was higher with an order of magnitude compared to standard pellet combustion. MSW pellet has odour after long time storage, so it is not recommended to distribute as public fuel. It can be used close to the place of production for heat energy supply of small town.

5. Summary

It can be seen that the waste of Csernely contains less combustible part and more fine fraction and non combustible as the waste of Szuha. Table 1 shows, that the ratio of packaging material (plastic) is significantly less than in Szuha, the non combustible (predominantly demolition waste, detritus) exceeds the values of reference small town. We should take in account this differences by the estimation of yield of high caloric values fraction.

It can be declared based on the measured data that it would be rewarding in the future to collect the waste possibly together with other small towns if possible. This waste can be suitable for heating purposes with a proper furnace after treatment. It would be possible to produce heat with a proper furnace after treatment. So could be new workplaces established, but the planning of this system requires further examination. By the estimation of yearly amount of high caloric value product the low combustible content of MSW compared to reference small town should be take in account. It is necessary to carry out a winter waste analysis, due to fluctuation and seasonality of composition. It is possible to produce combustible RDF from MSW. The economic safe and ecologically friendly pellet production requires further research activity.

"Acknowledgement: This work was carried out as part of the TÁMOP-4.2.1.B-10/2/KONV-2010-0001 project in the framework of the New Hungarian Development Plan. The realization of this project is supported by the European Union, co-financed by the European Social Fund."

REFERENCES

[1] Bezeczky-Bagi, B.: *A Győr–Sashegyi Hulladékkezelő Központ*. BIOhulladék 2010. október, 2–7.
[2] Bezeczky-Bagi, B.: *Példaértékű hulladékkezelés és hasznosítás a Zöld Híd Régió Kft. telepein.* BIOhulladék, 2011. január, 2–8.
[3] Csőke, B.–Alexa, L.–Olessák, D.–Ferencz, K.–Bokányi, L.: *Mechanikai biológiai hulladék-kezelés kézikönyve.* Profikomp Kft.
[4] Márton, G.: *Települési szilárd hulladékok energetikai hasznosításának elemzése*. TDK dolgozat, ME, Műszaki Anyagtudományi Kar, 2011.
[5] Nagy, Gy.: *A termékdíjas szabályozás.* Előadás anyag, Miskolci Egyetem MFK, Hulladék-gazdálkodás óra, 2011. február 12.
[6] Nagy, S.–Ferencz, K.: *Tüzelőanyag előállítása a polgárdi pelletáló üzemben*. BIOhulladék, 2010/2–3. sz.,18–22.
[7] Szűcs I.–Nagy G.–Palotás Á.–Csőke B.–Nagy S.–Boros É.: *Biomassza és szilárd települési hulladék alapú másod tüzelőanyag kifejlesztésének időszerűsége*. Anyagmérnöki Tudományok, Miskolc, 36/1 kötet, 2011.
[8] Üveg, R.: *Alternatív energiahordozók a nagy energiafelhasználású ipari létesítményekben, cementiparban*. Alternatív energiahordozók hasznosítása Magyarországon szakmai konferencia, Budapest, 2011. május 10.

Geosciences and Engineering, Vol. 1, No. 1 (2012), pp. 255–260.

SPHALERITE INDICATIONS IN THE AGGTELEK MTS

NORBEERT NÉMETH[1*]–ATTILA KASÓ[2]–JÁNOS FÖLDESSY[1]
[1]University of Miskolc, Institute of Mineralogy and Geology
3515 Miskolc-Egyetemváros
[2]Rotaqua Kft.
7673 Kővágószőlős, hrsz no.: 0222/22
*corresponding author: foldnn@uni-miskolc.hu
[10th February 2012]

Abstract
The results of the base metal exploration at Rudabánya indicate a stratiform zinc-lead mineralization in the Lower Triassic siliciclastic rocks. This observation induced the assumption of a mineralized horizon in the Silicikum stratigraphic unit beyond the area of the Rudabánya complex, polymetallic deposit. The resampling of stored drill cores from the mapping boreholes of the Aggtelek Mts revealed sulphide enrichments and the presence of sphalerite along the Jósva Valley.

1. Introduction

The Rotaqua Kft. runs an exploration at the abandoned open-cast and underground iron ore mine of Rudabánya since 2006 in cooperation with the Institute of Mineralogy and Geology of the University of Miskolc. The licence refers to base metals, iron ore and precious metals. The siderite deposit and its gossan cap are well known to contain variable copper minerals [1]. The 10–100 m scale siderite blocks are embedded in calcareous siltstone ('clay marl'), and the rims of these blocks are mineralized with barite and considerable amount of base metal sulfides [2]. The exploration aimed these bodies originally, but the ongoing evaluation of gained structural, lithological and geochemical observations during the mapping, sampling and assaying program revealed a stratiform mineralization of sphalerite and galena bound to the siliciclastic country rock of the carbonate blocks [3].

This stratiform mineralization, overprinted by all later mineralization and deformation events, may have formed as a sedimentary exhalative deposit in a restricted basin during the Early Triassic period, independent from the subsequent metasomatic sideritization. Therefore there is a possibility that this paragenesis can also be found on other localities of the same stratigraphic horizon of the Silicikum Unit containing the Rudabánya Ore Bearing Complex.

The drill cores of several mapping drillholes from the Aggtelek area are stored at the Rákóczibánya core deposit of the Hungarian Geological Institute. As these were not drilled for ore exploration, there was no assay of base metals, and no record of observed sphalerite or galena. The aim of our study was to search for mineralized intervals in drillholes transecting the Lower Triassic part of the Silicikum.

2. Geological setting

The name Silicikum refers to an alpine Triassic succession distributed in the Aggtelek-Rudabánya Mts in Hungary and in adjacent mountainous areas in Slovakia [4]. It starts with Permian evaporite (anhydrite and black shale, Perkupa Evaporite F). The Lower Triassic comprises a transgressive succession of littoral sandstone and siltstone (Bódvaszilas

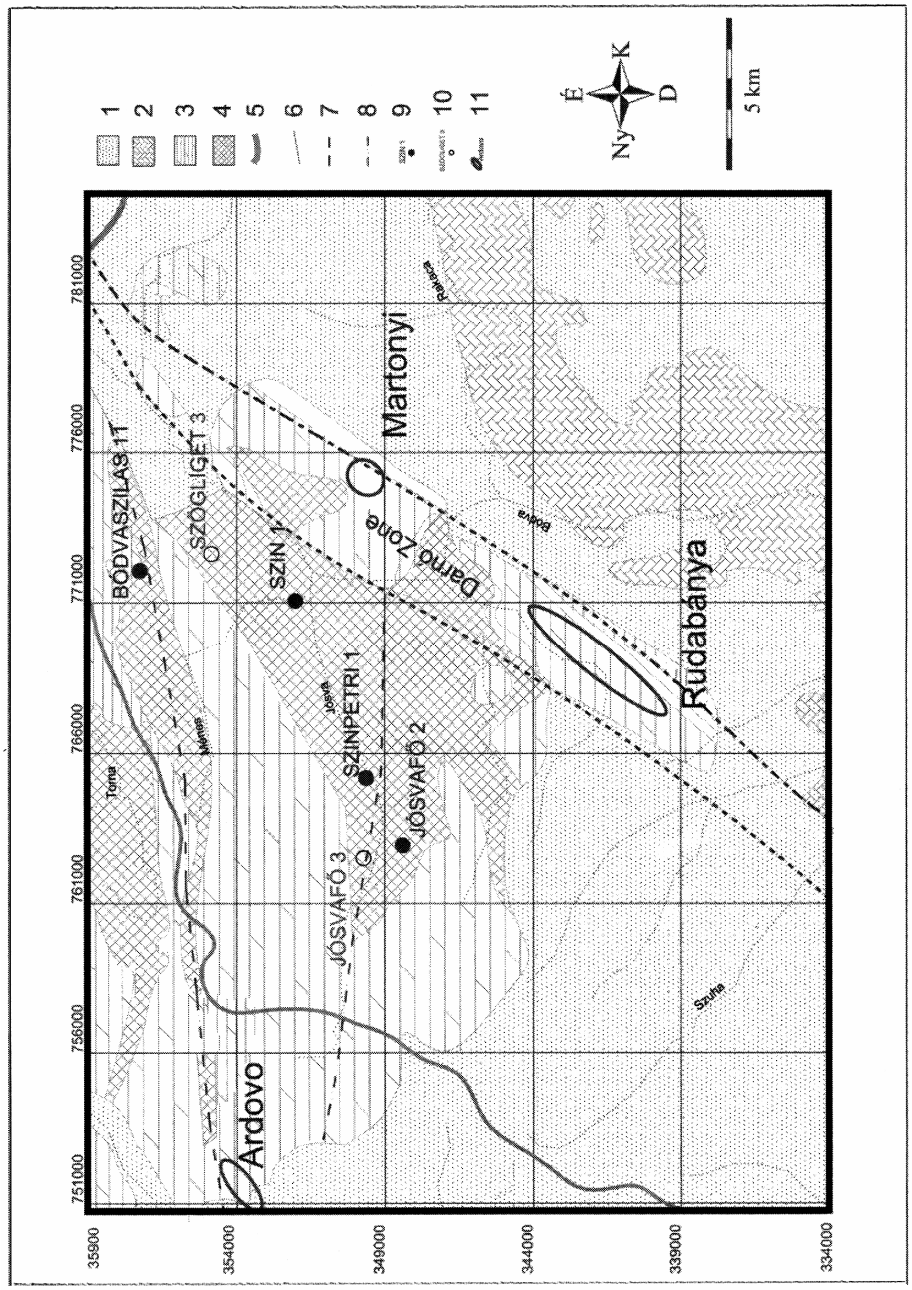

Figure 1: Simplified geological map of the Aggtelek–Rudabánya Mts. indicating the studied drillholes and known sphalerite-galena occurrences. Legends: 1. Tertiary cover; 2. Szendrő Paleozoic; 3. Silicikum, Middle and Upper Triassic carbonates; 4. Silicikum, Lower Triassic carbonates and siliciclastic rocks; 5. State border; 6. Rivers; 7. Darnó Fault Zone borders; 8. Anticline axial traces; 9. Drillhole with Zn indication; 10. Drillhole without Zn indication; 11. Sphalerite occurrences (abandoned mines)

Sandstone F), shallow water marl (Szin Marl F.) and laminar or nodular limestone (Szinpetri Limestone F). The Anisian rocks are dark, euxin facies, thick-bedded or massive limestone and dolomite (Gutenstein F) followed by light gray, platform facies limestone and dolomite (Steinalm F). In the further Middle and Upper Triassic part of the succession carbonate platforms and reefs (Wetterstein and Dachstein F) of some 100 m thickness alternating with basin facies rocks (e.g. Pötschen Limestone F, Hallstatt Limestone F. etc.) were developed.

This assemblage occurs here in the Silica Nappe. Evaporite beds acted as décollement horizon during the nappe emplacement. This basal layer also contains blocks of serpentinized basic volcanic rocks from the Meliatikum. The nappe forms km-scale gentle folds with E-W oriented axes. Synclines are characterized by karstified areas formed over thick Wetterstein Limestone and Dolomite. Anticlines expose the Lower Triassic siliciclastic rocks; the drainage system of the Jósva and Ménes Valleys follows the anticlinal crests to the east. An imbricate structure of these anticlines was indicated by some drillholes with repeated incomplete sections of the succession of the Silicikum.

The Silica Nappe is bordered by the Darnó Zone in the southeast, a some km wide strike-slip fault zone of some 10 km displacement in sinistral sense during the Miocene, but its activity spans the whole Cenozoic time [5, 6] The Rudabánya deposit is situated in this zone and the Martonyi siderite deposit with the same paragenesis cca. 15 km NE from Rudabánya is probably a displaced part of the same mineralized rock body. However there is another small zinc-lead deposit known in the Silicikum in the western continuation of the Ménes Valley Anticline in Slovakia, at Pelsőcardó [Ardovo] [7]. This small ore body is bound to Gutenstein carbonate, and after the exhaustion of sulfide resources smithsonite ore was exploited up to the first part of the 20th century.

3. Observations and results

As a first step drillholes with recorded transecting of Lower Triassic strata were chosen and displayed from the accessible store. Our study was restricted to the sulfide or any Zn-bearing mineral content of the cores, lithology was recorded at sulfide enrichments only. Neogene cover was not studied.

As experience in Rudabánya has shown, sphalerite of the stratiform mineralization is hard to distinguish from other dark, fine-grained minerals. For the detection of Zn-bearing minerals zinc-zap was used [8]. Two composites have to be sprayed on the mineral surface:

- A: 3% potassium-ferricyanide solved in water (yellow)
- B: 3% oxalic acid and 0,5% diethylaniline solved in 1% hydrochloric acid (clear)

It reacts with smithsonite, hydrocinkite, hemimorphite and sauconite, forming bright scarlet stains, with sphalerite the reaction is weaker. Fe sulfide minerals, primarily pyrite, cause dark blue color. Other minerals do not react with the zap. Cores were tested with this zap in some dm intervals or in some cases continuously.

Drillhole Szin-1 (1646 m). This is one of the deep structural exploration drillholes, located at the mouth of the Jósva Valley.

The 150–170 m interval is the lower part of the Szin Marl Formation lying over Bódvaszilas Sandstone. The greenish gray, laminar marl contains several dm-scale intervals

of crumbled material, giving blue reaction color. At 165 m white sulfate coating was formed due to the weathering of sulfide minerals during the storage of the cores.

In the Bódvaszilas Sandstone Formation down to 435 m some quartzite veins contain pyrite. The lowermost part is siltstone lying over anhydrite (Perkupa Evaporite F) with pyrite enrichment and sulfate coating. The top 5 m of the anhydrite is penetrated by quartzite veins with pyrite, giving blue reaction color.

In the 435–465 m interval stylolitic limestone was found. At the bottom of this interval a 1 dm thick sparry calcite vein was found surrounded by a net of veinlets, containing mm-thick dark veinlets of sphalerite *(Figure 2).* The reaction color was intensive red. Another vein at 440 m also reacted with red color, but it was weaker. Underlying rock was anhydrite again with pyrite nests.

The 465–1660 m interval the transected assemblage comprises alternating anhydrite, gypsum, serpentinite, metabasalt, limestone, marl, siltstone and sandstone, including the rock material of the covering formations, probably a thickened mélange in the core of the Jósva Valley Anticline. Calcite or quartzite veins, the serpentinite and the metabasalt often contains pyrite enrichments, other sulfide minerals were not found.

Drillhole Szinpetri-1 (139 m). The drillhole explored gray, compact limestone and marl with mm-scale calcite veins (Szinpetri Limestone F). Some veins also contained dark material (sulfide minerals). Three veins at 79, 83.5 and 92.5 m gave red reaction color, indicating the presence of Zn-bearing minerals; in several other cases the reaction color was blue.

Drillhole Bódvaszilas-11 (111 m). The drillhole transected alternating shale, siltstone and sandstone (Bódvaszilas Sandstone F) with cm thick sulfide rich veins in the 72–74.5 m interval, giving both red and blue reaction colors. On the bottom section, from 106 m there was dolomite with rust stains.

Drillhole Jósvafő-2 (85 m). Marl with a thin red clay bed at the bottom was transected down to 25 m, lying over anhidrite. Intensive red reaction color was observed in the anhidrite under the contact. From 42.5 m to the bottom limestone was explored with iron oxide veins only.

The drillholes Jósvafő-3 and Szögliget-3 were also tested without positive reaction.

Figure 2: Sphalerite-containing calcite vein in the Szin-1 drillhole at 463 m

4. Conclusions

Our observations proved the presence of sphalerite mineralization in four drillholes, three located along Jósva Valley and one in the Ménes Valley Anticline. However the mineralization was vein type and bound to limestone or anhidrite, resembling rather to the Pelsőcardó deposit than to the stratiform ore of Rudabánya. The lower part of the Szin Marl Formation in the drillhole Szin-1, the only drillhole transecting an undisturbed succession of the Szin Marl lying over Bódvaszilas Sandstone, proved to contain sulfide-rich intervals. Still there is a possibility, that there are local sphalerite and galena enrichments in this horizon and this may be the source of the carbonate hosted sphalerite indications.

"Acknowledgements: The present work was supported by the Rotaqua Ltd. and the TÁMOP-4.2.1.B-10/2/KONV-2010-0001 project in the framework of the New Hungarian Development Plan. The realization of this project is supported by the European Union, co-financed by the European Social Fund."

REFERENCES

[1] Koch, S.: *Magyarország ásványai*. Akadémiai Kiadó, Budapest, 1985, 562.
[2] Pantó, G.: *A rudabányai vasércvonulat földtani felépítése*. Yearbook of the Hungarian Geological Institute 44/2, 1956, 329–637.
[3] Földessy, J.–Németh, N.–Gerges, A.: *A rudabányai színesfém-ércesedés újrakutatásának előzetes földtani eredményei*. Földtani Közlöny 140/3, 2010, 281–292.
[4] Szentpétery, I.–Less, Gy. *ed.*: *Az Aggtelek–Rudabányai hegység földtana. Magyarázó az Aggtelek–Rudabányai-hegység 1988-ban megjelent 1:25000 méretarányú fedetlen földtani térképéhez.* Hungarian Geological Institute, Budapest, 2006, 92.
[5] Zelenka, T.–Baksa, Cs.–Balla, Z.–Földessy, J.–Járányi-Földessy, K.*: Mezozóos ősföldrajzi határ-e a Darnó vonal?* Földtani Közlöny 113/1, 1983, 27–37.
[6] Szentpétery, I.: *Sinistral lateral displacement in the Aggtelek–Rudabánya Mts*. (N Hungary) based on the facies distribution of Oligocene and Lower Miocene Formations. Acta Geologica Hungarica 40/3, 1997, 265–272.
[7] Balogh, K.: *Adatok Pelsőcardó környékének földtani ismeretéhez*. Tisia 4, 1940, 151–200.
[8] Hitzman, M. W.–Reynolds, N. A.–Sangster, D. F.–Allen, C. R.–Carman, C. E.: *Classification, Genesis, and Exploration Guides for Nonsulfide Zinc Deposits.* Economic Geology 98/4, 2003, 685–714.

Geosciences and Engineering, Vol. 1, No. 1 (2012), pp. 261–269.

GEOLOGICAL OBSERVATIONS IN THE CSEREHÁT, BETWEEN IROTA AND GADNA

NORBERT NÉMETH
University of Miskolc, Institute of Mineralogy and Geology
3515 Miskolc-Egyetemváros
foldnn@uni-miskolc.hu

Abstract
The easternmost outcrops of the Paleozoic succession of the Szendrő Mts are situated on the hills between Irota and Gadna. Previous explorations have found shale (phyllite) and metasandstone with high organic matter content, both suffered epizonal metamorphism; sandstone with jarosite cement in the Tertiary cover; a geomagnetic anomaly and pyrrhotite-dominated sulfide mineralization. The area is prospected for base and precious metal mineralization. In the initial stage of the prospecting geological mapping, localization and documentation of the outcrops were carried out. The results show that the area is dissected by Neogene faults with significant downthrows, also controlling the mineralization processes.

1. Introduction

The metalliferous black shale formations have a considerable potential to host economic grade mineralizations of base and precious metals, including platinum group elements [1]. 'Black shale' is a collective name for fine-grained clastic sedimentary rocks formed in restricted, reductive environments. Most of these deposits are thought to be of sedimentary-exhalative origin; the presence of organic matter and lack of oxygen enhances the precipitation of sulfide minerals [2].

One of the Paleozoic and Mezozoic formations of Northeastern Hungary corresponding to the definition of the black shale is the Irota Formation of the Szendrő Unit. In this an airborne geomagnetic survey [3] and subsequent uranium ore prospecting boreholes explored significant enrichment of pyrrhotite with traces of chalcopyrite, sphalerite and galena between Irota and Gadna at the Cserehát [4]. A new precious and base metal prospecting was initiated by the Institute of Mineralogy and Geology in cooperation with the Rotaqua Ltd. in 2010 based on these results. As a first step, the geology of the prospecting area was revised with mapping and documentation of the presently accessible outcrops, concentrated on the rock material affected by the alteration. This paper outlines the results of this mapping *(Figure 1).*

2. Geological setting

The stratigraphic structure of the Cserehát comprises an epimetamorphic Paleozoic basement (Szendrő Unit) and a sedimentary–volcanoclastic Tertiary (mainly Neogene) cover. The basement crops out in the SW part of the area, named Szendrő Mts in the geological literature (geographically a hilly country of 200–300 m a. s. l. high crests like any other parts of the Cserehát). On the eastern part the thickness of the cover exceeds 1000 m.

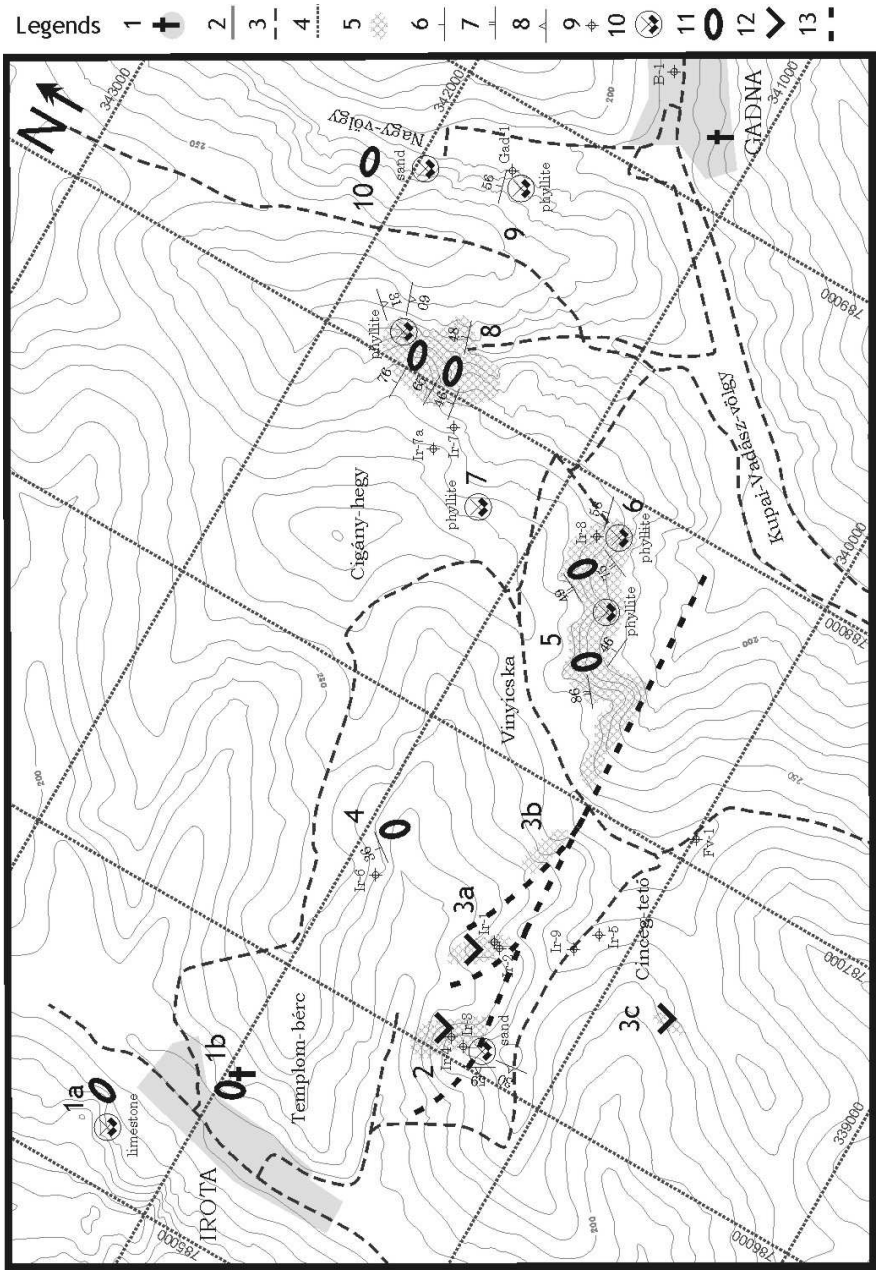

Figure 1: (opposite page): Mapped prospection area. Legends: 1. village and church; 2. contour line; 3. major road; 4. EOV grid line; 5. debris of the Irota F.; 6. dip of the first cleavage; 7. dip of the second cleavage; 8. dip of the bedding; 9. exploration borehole; 10. abandoned quarry or pit; 11. outcrops, other exposures (cliffs, cuts, gullies); 12. exploration trench; 13. supposed fault trace

The oldest known formation of the Szendrő Unit is the Irota Formation. This formation is known from surface outcrops between Irota and Gadna and some exploration boreholes at Irota (Ir-1–8), Gadna (Gad-1, B-1), Felsővadász (Fv-1) and Alsóvadász (Av-1). Its assumed age comes from the Middle Devonian fauna of the conformly overlying Szendrőlád Limestone Formation in the borehole Fv-1. It comprises gray and dark gray shale (phyllite), siltstone and pelitic sandstone with organic matter and pyrite, sometimes calcareous, containing quartz veins and silicified rock bodies [5]. The silicification, the paragenesis of quartz, siderite, montmorillonite and pyrite, the fading of the dark color of the matrix and anomalous enrichments of Ti, Mn and Ba were interpreted as indicators of a low temperature hydrothermal alteration [6]. The organic matter is often described as 'graphite', but it is rather anthracite or semianthracite. Coal seams cannot be expected in this offshore facies.

The following succession comprises dark grey, laminar, fine grained limestone and marl (Szendrőlád Limestone F), coarse grained limestone with dark and light gray bands (Rakaca Marble F), yellowish gray, fine grained limestone with sericite and chlorite layers ('cipollino', Abod Limestone F) and an assemblage very much like the Irota F, dominated by shale (Szendrő Phyllite F). This flysch-type rock lies unconformly on the limestone formations with Devonian fauna, formed probably in the Carboniferous. South Alpine and Dinaridic analogies may link this succession to the Bükk Unit, occurring S from the Cserehát, which practically starts with the closing formation here (Szilvásvárad Siltstone F. being also a flysch-type assemblage with low grade metamorphic alteration) [5].

The Irota Formation was regarded previously as the youngest member of the succession [6]. In the opinion of Koroknai [7] its lithology differs in the alteration from the Szendrő Phyllite Formation only, and the age determining limestone and marl section in the Fv-1 cores may represent an olistolith analogous to other Szendrő Mts occurrences, so the assemblage can be classified as Szendrő Phyllite.

The structural boundaries of the Cserehát are two basins, the Borsod Basin in the S and the Kanyapta (or Komarovce) Basin in the N and two strike-slip fault zones, the Darnó Zone in the NW and the Hernád Zone in the SE. Both zones were active during the Tertiary up to the recent times, although in changing sense. The outcrop areas of the Szendrő Unit formations are situated in parallel strips, striking SW–NE in the SW part, bending to an E–W strike on the E side (probably a sequence of S–SE-vergent folds) [8]. This pattern is similar to that of the Central Bükk formations in the SW continuation of the Darnó Zone, and may reflect the deformations along this structural discontinuity. On the other side the downthrow of the basement SE from Gadna is linked to the trench development along the Hernád Zone.

In the cover Miocene shallow marine, littoral, fluvial and terrestrial clastic sediments include Upper Badenian and Sarmatian rhyolite tuff horizons. Sarmatian clay, marl, silt and the 'upper tuff' closing the sequence can exceed 400 m thickness altogether [9], [10]. Similar maximal, but very variable thickness characterizes the unconformly overlying Pannonian brackish, lacustrine and fluvial sediments. A special formation of the area is the sandstone cemented with limonite and jarosite with quartzite pebbles [11].

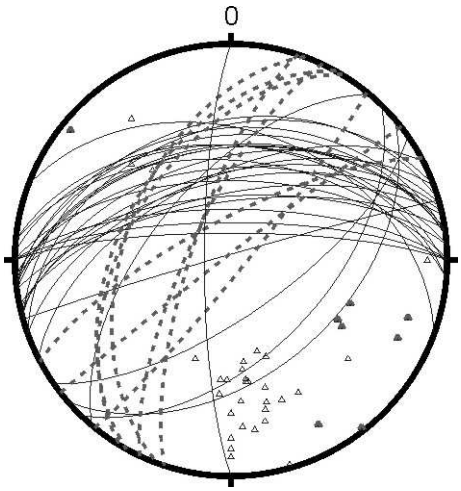

Figure 2: Stereogram of the measured dips of cleavage, equal area projection, lower hemisphere. Number of data: 38. First (slaty) cleavage: continuous lines, triangles; second (crenulation) cleavage: dashed bold lines, filled triangles

3. Mapped outcrops

Due to the low strength of the rock material and the hilly morphology, exposures are restricted to a few sites. Small outcrops of the Irota Formation were found on the steep SE side of the Vinyicska Hill only (outcrop group 5 on figure 1). Gullies, mainly in a valley descending to south on the eastern side of the Cigány Hill provide further natural exposures. Beyond these 5 small quarries were opened in this formation, three of which (in groups 6, 8 and 9) still have accessible rock faces. Cleavage orientations were measured on every appropriate outcrop *(Figure 2).* The debris of the material was found around these and in other areas too; steep slopes indicate usually that the formation is covered with 1–2 m thick debris only. Remnants of exploration trenches were also found on Cinceg Hill.

Exposure group 1. The small quarries on the W side of Irota (1a) and the road cuts to the cemetery at the church (1b) expose laminar limestone and marl with folded slaty cleavage. Cleavage surfaces are usually shiny because of mica enrichments. As the prospection was concentrated on the Irota Formation, these outcrops were not documented.

Exposure group 2. On the western peak of the Cinceg Hill a pit of cca. 10 m diameter exposes cross-bedded sandstone with pebbles. Grain size and the matrix vary with bedding; the pebbles are not well rounded. The beds are 2–3 dm thick on average. The matrix is bright yellow or yellowish brown (weathered) in fine-grained sandstone beds, but lacking from coarse-grained, pebbly beds. Yellow color may come from jarosite.

Remnants of exploration trenches and abundant debris of gray phyllite, metasandstone and quartzite were found north and east from the pit. This material is rich in limonite patches and veins, also containing hollow limonite concretions of 1–2 cm diameter.

The bedding of the sandstone dips to W on the southern side and steeply to SW on the northern side of the pit *(Figure 3).* This post-sedimentation tilting, possibly in consequence of faulting was not equal, producing differently dipping blocks. Back-tilted cross-bedding indicates WNW transport direction, so the deposited clasts originate from the east.

Exposure group 3. These locations are slope breakdowns (steep sections) without outcrops, but with abundant debris of phyllite and quartzite indicate a thin cover, while the surroundings are covered with reddish brown clay without any debris. The material is gray phyllite, metasandstone and quartzite with reddish brown limonite. The phyllite contains light and dark gray stripes, sometimes showing pencil cleavage at location 3b. The quartzite of 3c contains cm-sized vesicles with mm-sized grown-up crystals on the walls. 3a and 3b slopes follow similar NW-SE strike, 3c is a nearly N-S trending crest.

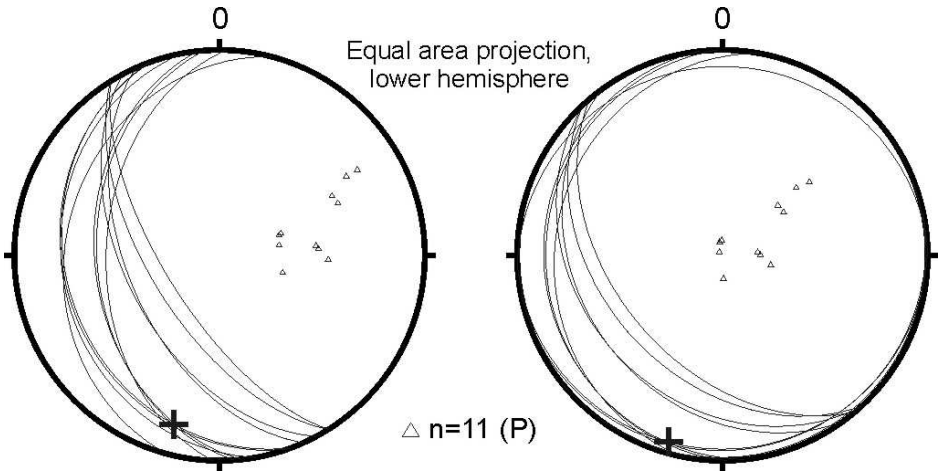

Figure 3: Measured dips of bedding and cross-bedding and dips tilted to subhorizontal bedding around 354 /00 axis by 25 . The cross indicates the intersection of bedding and cross-bedding. The data dipping to SW come from a more tilted block

Exposure 4. A shallow gully formed on a dirt road exposes the depositional base of the fluvial sand with pebbles on the phyllite with quartz veins on the 215 m level. Orientation data are uncertain because of ambiguous stability of the exposed blocks.

Exposure group 5. The steep southeastern slope of the Vinyicska Hill is covered by the debris of the Irota Formation containing abundant limonite. On a side crest there is an exploitation pit of cca. 20 m diameter, without retained rock faces. On the NE side of a small valley, however, there are small natural rocks of dark red silicified phyllite. The slaty cleavage of this rock is folded in cm-scale, forming an anastomosing secondary crenulation cleavage (similar folding of mm-scale wavelength), and a 0.5–1 dm spaced joint set was observed along these cleavage planes. The rock was strongly fractured along a 258 /80 fault plane, cemented with limonite. Green, cm-sized stains of fuchsite (Cr-bearing mica, determined by Szakáll, S.) and some mm-sized acicular gypsum were found here.

The slope angle changes suddenly above this outcrop at cca. 250 m a.s.l. On this level quartzite pebbles can be found all along the top of the phyllite-covered slope. Two soil samples were taken in 20 m distance measured across this change by hand-driven auger drilling. The sample from the lower point contained compact reddish brown clay with phyllite debris down to 80 cm, where the drilling got stuck, reaching the loose weathered top zone of the phyllite. In the upper hole the compact clay was 2.5 m thick with no phyllite debris, only sand. Below that quartzite pebbles and limonite stains were observed with variegated clay to 2.8 m, and then yellow rhyolite tuff was found down to 3.7 m, where the sampling was stopped. The compact clay forms a general cover in this area. At the crest of Vinyicska Hill, 500 m to SE from this location and 272 m. a.s.l, however yellow marl was found on the surface.

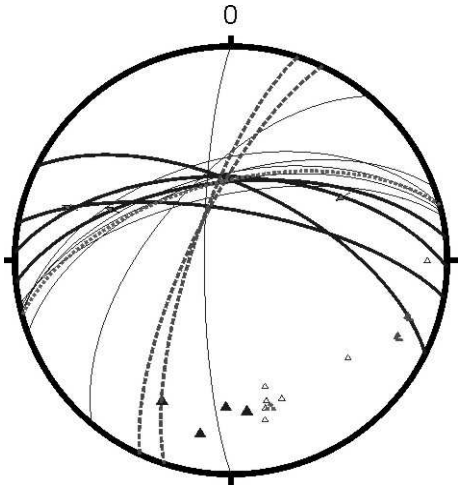

Figure 4: Stereogram of the measured orientation data from the quarry of outcrop 6, equal area projection, lower hemisphere. First (slaty) cleavage: continuous lines, triangles; second (crenulation) cleavage: dashed bold lines, triangles; faults: bold lines with arrows indicating the sense of movement; quartzite vein: dot line

Exposure 6. The quarry on Vinyicska Hill with a cca. 10 m high face exposes several faults and quartzite veins in the gray silicified phyllite. Both slaty and crenulation cleavage can be observed. Open folds of dm-scale wavelength were also observed; the axis of the folding is at the crossing of major circles on the stereogram of *Figure 4,* and it is practically the same for rotated fold limbs and crenulation cleavage surfaces. A dm-sized quartzite vein follows the general trend of the slaty cleavage, and crosscuts the short limb of a shear band fold, indicating subsequent development. The fault planes also follow roughly the slaty cleavage dipping to N, but in an undulating pattern. Poorly preserved slickenlines indicate left-oblique shear sense.

Exposure 7. A pit of similar size like the quarry of outcrop 6 is situated on the S part of the Cigány Hill. It provides no free rock surfaces, only debris and blocks. The rock material is the same as in outcrop 6.

Exposure group 8. On the lower part (below 230 m a.s.l.) of the eastern slope of Cigány Hill several gullies, a quarry with 8 m high rock face and the creek of the valley expose the gray phyllite, metasandstone and the direct covering red limonite and yellow jarosite cemented sandstone with quartzite pebbles. Globular limonite concretions are typical on the southern side of the area.

The gray phyllite and metasandstone contains here abundant quartzite veins and organic matter as in previously described outcrops. The crenulation cleavage was often observed as intersection lineation on slaty cleavage surfaces, sometimes causing pencil cleavage *(Figure 5).* Cm-scale zigzag folding is most intensive around quartzite nests in the hinges. Stretching lineation was also observed in these folds. Light gray and white bands were formed by argillitic alteration in the phyllite; the rock material was white and loose or disintegrated to powder on some sites.

Figure 5: Phyllite sample with slaty and crenulation cleavage. Left: profile wiev of the folded cleavage. Right: slaty cleavage plane with lineation caused by the crenulation

Exposure 9. A single quarry at the farm in Nagy Valley exposes laminar, dark gray phyllite which leaves black trace on white paper due to the organic matter content. This outcrop is extended by the cores of Gad-1 drillhole down to 100 m depth. Faded stripes and silicified zones with some secondary minerals indicating decomposed sulfides occur in the cores.

Exposure group 10. On the W side of the Nagy Valley a quarry and some gullies expose the sand and conglomerate beds, which are horizontal here. Dark red, 1–5 cm thick horizons are prepared out due to the limonite cementation. Such beds can be observed also around Szakácsi and in a small roadside quarry below Irota, with limonite concretions, but no jarosite.

Drillhole Fv-1. This 600 m deep hole was drilled and documented in 1988 [5] and resampled in the frames of this prospection. Paleozoic rocks were reached at 158 m below 3 m phyllite breccia with brown clay matrix (slope debris) and rhyolite tuff; the top 12 m was weathered with limonite bands along cleavage. Calcareous (marly) intervals occur down to 285 m alternating with gray phyllite with no sharp boundaries. Further downwards black phyllite, gray shale and light gray metasandstone with reddish matrix comprise the Irota Formation. A considerable part of the sulfide content was decomposed during storing of the

cores, also smashing the rock material. Secondary sulfates were formed on the core surfaces, mainly in phyllite, while the sandstone rather contained preserved disseminated sulfide grains. Pyrrhotite was detected by a magnet. Sulfides (and subsequent sulfate coatings) are unevenly distributed, concentrated in some dm thick zones. Such intervals of silicification and sulfide enrichment affect the whole Paleozoic assemblage.

4. Conclusions

The previously known rock types and signs of hydrothermal mineralization were found on the prospection area during the mapping phase. The altered Paleozoic rocks and the limonitic weathering products in the Pannonian cover are also potential locations of metal enrichments coming either from the original metal content of the black shale or from an unknown deep source.

The Paleozoic rocks have twofold cleavage. The primary slaty cleavage dips generally steeply to NNE, the secondary crenulation cleavage is subvertical, striking NE–SW. The crenulation often causes strong lineation on primary cleavage planes, plunging to NE on average. The fissures and quartzite veins follow mostly the slaty cleavage planes, but a dm-spaced joint set along crenulation cleavage is also developed. Silicification and the quartzite veins overprint the cleavage, but it is possible, that a generation of these veins was formed during the crenulation.

The variable dip and base level of the Pannonian fluvial sediments indicates Pannonian or post-Pannonian activity of the faults with a downthrow of 10–100 m magnitude. The most important structural boundary (with respect to the mineralization) is the E–W striking fault zone at the crest of Cinceg Hill, the northern edge of the geomagnetic anomaly [3] [4].

The indicators of hydrothermal alteration are not bound to this anomaly. Abundance of limonite and faded stripes or patches are typical along the fault zone, although also occurring on every other part of the area. Fuchsite was found on Vinyicska Hill, jarosite cemented sandstone on Cigány Hill. Although this fault zone was active after the alteration and sulfide mineralization, and the pyrrhotite bearing body is displaced along this zone, there is a possibility that it existed before and controlled the mineralization together with other faults, which were not reactivated.

"Acknowledgements: The present work was supported by the Rotaqua Ltd. and the TÁMOP-4.2.1.B-10/2/KONV-2010-0001 project in the framework of the New Hungarian Development Plan. The realization of this project is supported by the European Union, co-financed by the European Social Fund. The author wishes to thank to János Földessy for managing the prospection and revising this text."

REFERENCES

[1] Vine, J. W.–Tourtelot, E. B.: *Geochemistry of black shale deposits – a summary report*. Economic Geology 65, 1970, 253–272.

[2] Emsbo, P.: *Metalliferous organic-rich black shales: Are exhalative hydrothermal processes fundamental to their genesis?* Conference paper, IGC 2008 Oslo: MRD-13 Ore deposits associated with black shales: from their origin to their environmental impacts, http://www.cprm.gov.br/33IGC/1324230.html (17th May 2011)

[3] Erkel, A.–Benderné-Kelemen, O.–Szabó, Z.–Szilárd, J.–Hobot, J.–Király, E.–Lányi, J.–Szalay, I. 1967: *Komplex geofizikai kutatás a Csereháton.* Annual Report of the Hungarian Eötvös Loránd Geophysical Institute from 1965, 65–102.
[4] Csáki, F.: *A Csereháti-dombvidék paleozoos képződményeinek komplex földtani vizsgálata.* Doct. univ. theses, 1976, 111.
[5] Fülöp, J.: *Magyarország geológiája, Paleozoikum. II.* Akadémiai Kiadó, Budapest, 1994, 448.
[6] Raincsákné Kosáry, Zs.: *A Szendrői-hegység devon képződményei.* Geologica Hungarica Series Geologica 18, 1978, 7–113.
[7] Koroknai, B.: *Tektonometamorf fejlődés az Upponyi- és Szendrői-paleozoikumban.* PhD theses, ELTE, Budapest, 2004, 239.
[8] Schréter, Z. 1952: *A Szendrői szigethegység és a határos harmadkori medencerész földtani vázlata.* Annual Report of the Hungarian Geological Institute from 1948, 137–141.
[9] Alföldi, L.–Balogh, K.–Radócz, Gy.–Rónai, A.: *Magyarázó Magyarország 200 000-es földtani térképsorozatához, M-34-XXXIII lap.* Hungarian Geological Institute, Budapest, 1975, 24–27.
[10] Radócz, Gy. 1971: *A Cserehát pannóniai képződményekkel fedett területének mélyföldtani felépítése.* Annual Report of the Hungarian Geological Institute from 1969, 213–234.
[11] Jámbor, Á.: *Jarosit-kötőanyagú homokkő a Szendrői-hegység DK-i peremén.* Földtani Közlöny 90/3, 1960, 363–368.

Geosciences and Engineering, Vol. 1, No. 1 (2012), pp. 271–282.

FREQUENCY DOMAIN ELECTROMAGNETIC INVESTIGATION ON ELONGATED CONDUCTIVITY STRUCTURES

GÁBOR PETHŐ
Department of Geophysics, University of Miskolc
H-3515 Miskolc-Egyetemváros
gfpg@uni-miskolc.hu

Abstract
After a short overview of the geophysical methods applied in geothermal exploration emphasis is put on frequency domain EM methods because they are widely used in geothermal projects. The main features of magnetotellurics (MT) and controlled source audiomagnetotellurics (CSAMT) are provided and the partial differential equations describing the natural and controlled source method are also given for 2D situation. Finite difference numerical model results are also presented for 2.5D situation. It can be stated that in the course of interpretation the use of normalized impedance sections over conductivity inhomogeneities can be prosperous if the geology is far from being complex.

1. Introduction

In order to decrease geological risk in geothermal exploration and optimize the production of geothermal energy, a wide range of geophysical methods is applied in geothermal projects. There is no general recipe for the selection of the geophysical methods, however some similarities can be found between the methods and their sequence as well used in geothermal and oil exploration and also between the geophysical logs in geothermal and oil wells. At the same time there are differences as well, because after the application of geophysical methods with less resolution, emphasis is usually put on 3D seismic method in CH exploration, while in geothermal exploration this method has fewer applications in percentage due to financial reason, too. The presence of a geothermal reservoir usually results in resistivity decrease. For this reason depending on the depth and the size of the geothermal reservoir the use of different geoelectric and electromagnetic methods can be prosperous in geothermal exploration. The shape of the geothermal reservoir can usually be characterized by 3D structures. However sometimes the geometry of a reservoir can be approximated by elongated structure, where the direction of elongation coincides with the structural strike direction.

2. Geophysical methods used in geothermal exploration

Besides geological and geochemical observations the geophysical investigations must be mentioned as organic parts of the geothermal exploration. The primary aims of these surface observations are to obtain initial estimates on the size of the reservoir and the geological structure of the geothermal system. The geothermal fields occur in different rock types and generally situate in convection systems in which usually hot water rises from great depth and is trapped in the reservoirs with cap rock. For this reason the primary objective of geothermal exploration is not the identification of the rock-type of the reservoirs, but rather the localization of tectonic elements such as faults or fractures along which high heat flow can be expected.

The greatest heat flow can be experienced over geothermal fields connected to mantle plumes, rift or subduction zones. Significantly less, but greater than average heat flow can

be observed in areas where sedimentary rocks with great thickness cover fractured or faulted basement rock and the thickness of the crust is relatively small. The exploration of the geothermal system with the greatest heat flow requires the set of geophysical methods different from the one which is applied for the geothermal exploration in sedimentary basin.

The most important methods in the course of geothermal exploration are gravity, magnetic, subsurface temperature, electrical, electromagnetic and seismic method. Summaries on the geophysical methods applied in geothermal exploration were presented by [1–3].

The gravity method investigates the spatial variation of the gravity field usually on the surface. The result of gravity survey is the Bouguer anomaly map. This map is obtained after normal, free-air, Bouguer, topographic (and for airborne and marine survey Eötvös) corrections are applied to gravity field data. It is sensitive to the lateral changes in density, for this reason it can be suitable to map bedrock topography and to locate faults. By means of filtering the depth interval for the origin of gravity information can be controlled. Gravity monitoring survey (repeated gravity measurement on the same stations) can be an effective tool to observe the fluid extraction and fluid recharge in time. It can provide information on the need of reinjection too.

The spatial distribution of the magnetic field is determined by magnetic method. Airborne and ground surveys can be distinguished. Normal-field correction (taking into account the normal variation of the geomagnetic field in the function of latitude and longitude) and diurnal correction (to account for the temporal variations of the geomagnetic field during the measurement) have to be made to obtain magnetic anomaly map showing the presence of magnetic bodies. The resultant magnetization of a magnetic body is the vectorial sum of the remanent and the induced magnetization. Both depend on the type of the ferromagnetic minerals and their concentration in the rocks. The most common ferromagnetic minerals are titanomagnetite and magnetite. One of the most important applications of magnetic method is mapping near-surface effusive and intrusive rocks. The greater the depth of the magnetic body with fixed magnetization and shape is, the less its magnetic response and the longer of the wavelength of the response is. The pattern of the magnetic anomaly is influenced by the direction of the inducing magnetic field. To make magnetic data interpretation easier, reduction to pole process (the magnetic anomaly map is recomputed for the case as if it had a vertical inducing field) is applied to magnetic field data. The simultaneous use of gravity and magnetic map over sedimentary basin can provide information on the types of rock building up the basement complex. Under the depth of Curie point there are no minerals with ferromagnetic properties. From the magnetic map covering a large area the depth to the Curie point isotherm can be estimated as well.

Subsurface temperature measurements can be considered as the most direct survey for detecting and investigating area of anomalous heat flux. Earlier temperature measurements were made only in holes with a few meters of depth, nowadays temperature measurements are recommended in wells with depth of 100m at least. Even temperature measurements in shallow hole can indicate the presence of factures along which hot water is rising up. However thermal gradient surveys at depth where the effect of the annual temperature change can be negligible are more informative. In the knowledge of thermal conductivity and geothermal gradient the heat flow along the direction of borehole can be determined based on the first Fourier's law.

Electrical and electromagnetic methods are widely used in geothermal exploration, because the physical parameters measured by these methods are sensitive to the resistivity

of the formations to be investigated. These methods can be characterized with greater spatial resolution than gravity or magnetic methods. Besides information on depth, shape and size these methods may be efficiently applied to locate fractured zones filled with fluid. The higher the temperature and the salinity of the water is, the easier is to detect the presence of water. Electrical conductivity is also affected by porosity and water saturation. Conductivity increases with increasing porosity and increasing water saturation. The detectability of the geothermal zone depends on its depth and size and the resistivity contrast between the geothermal zone and its surroundings. These geophysical methods can be classified on the basis of their source origin. In this aspect natural and controlled source surveys can be distinguished. Self potential (SP) and magnetotelluric (MT) methods belong to the group of natural source methods. Direct current resistivity, controlled source audio magnetotelluric (CSAMT) and transient electromagnetic (or time domain electromagnetic, TEM) methods are the most important ones among controlled source surveys applied in geothermal projects. Additional classification can be made on the frequency. Geoelectrical methods are DC methods, where the exploration depth can be controlled by the alteration of the measuring array. The electromagnetic methods utilize usually a range of frequency values depending on the exploration depth. The controlled source methods can work in frequency and in time domain. The EM fields of controlled source methods can be generated by inductive or conductive way. Besides frequency range it is the transmitter-receiver distance which has to be adjusted to the exploration depth.

Seismic methods applied in geothermal exploration can be passive or active. Geothermal fields are frequently characterized by increased micro earthquake activity. In the course of the exploration period passive seismic method can be used if there are seismically active fracture zones in the prospect area. To obtain sufficient number of observations the microseismic surveys may take some weeks. The objective of the survey is to delineate the anomalous area of Poisson's ratio. Besides the spatial identification of each earthquake centre the determination of compressional and shear wave velocities (from which the Poisson' ratio can be concluded) is also needed. The calculated Poisson's ratio values are referred along the straight line travel paths between epicenter and seismograph. The zones with increased Poisson's ratio can be correlated to the part of the reservoir with high permeability. Another application of microseismicity can be to monitor fluid injection into the reservoir (or extraction from it) resulting in induced seismicity. Active seismic methods apply artificial sources (i.e. explosive charge or vibroseis). Depending on the geology seismic refraction or seismic reflection survey is used. The physical condition of developing seismic refracted wave (head wave) is the increasing velocity with depth. The aim of this survey is to determine the relief of the refractor(s). If we make a comparison between exploration geophysical methods, it can be stated that seismic reflection method can be characterized with the highest resolution. This is the most expensive (geophysical) exploration method. The physical condition of having elastic wave reflection from an interface is that acoustic impedance difference should be between the formations in contact. The objective of seismic reflection survey is to map subsurface interfaces (including the depth, dip and strike of bedding and lateral changes in the reflectors) and to define stratigraphic variations as well. In geothermal exploration detailed seismic survey is recommended to map fault systems.

Geophysical measurements are also carried out in boreholes. The set of these measurements are called well logging. It is not included in the geophysical exploration methods (because they are considered as surface methods). The purpose of the open hole measurements can be the in-situ determination of the important physical parameters as

porosity, permeability, temperature and to provide technical parameters for drilling engineers (i.e. caliper log for cementing). Additional parameters and indirectly technical assistance are provided by production logging and logging aiming at well inspection.

3. Frequency domain electromagnetic (FEM) methods

In the magnetotelluric (MT) method natural EM fields with variable direction, frequency and strength are used to investigate the resistivity distribution of the earth [4]. Sources of MT fields above 1Hz are thunderstorms, from which lightning radiates EM fields propagating at great distances. Sources of MT fields below 1Hz are EM fields due to the interaction between current systems in magnetosphere and the solar activity. Independent of the natural EM field's origin these fields can be considered at the surface of the earth as plane waves. Only a small amount of their energy penetrates and propagating vertically downward into the earth. The attenuation of the vertically propagating EM fields depends on the subsurface conductivity and the frequency. At interfaces some part of the energy is reflected back to the surface, while the other part of the EM fields is propagating downward after refraction. At the surface the superposition of the incident (primary) and the reflected EM fields can be measured. The ratio of electric and magnetic field components perpendicular to each other is the impedance which is used to define apparent resistivity. In exploration mainly the apparent resistivity frequency sounding curve and its phase frequency sounding curve are applied. The latter is the same as the phase frequency sounding curve of the impedance. In the interpretation of sophisticated geology the tipper and the polar diagrams of impedance tensor elements are used. Over geological situation complicated than horizontally stratified half-pace the impedance is not scalar quantity. For elongated and arbitrary (3D) situation the polar diagrams for the elements of impedance tensor are derived from the measurements usually at many frequencies, because the strike direction may change with depth. Except for near lateral conductivity changes the vertical magnetic field component can usually be assumed zero. The relation between the vertical and horizontal magnetic field components at any frequency can be expressed by means of tipper. The main advantage of the MT method is that exploration from shallow to very great depth (including lower crust) can be made. The depth of investigation of MT is much greater than in case of any controlled-source method. The shortcomings of the MT method are the difficulty of data acquisition in electrically noisy areas and the time needed for MT measurements to obtain data at all frequencies.

To overcome the natural signal strength problem in MT and to control the source polarization the controlled source audio-frequency magnetotellurics (CSAMT) with grounded electric dipole source was proposed by [5]. Similarly to magnetotellurics, the orthogonal electric and magnetic components are measured and the plane wave approximation is used to calculate scalar apparent resistivity. In general, controlled source frequency domain electromagnetic (FEM) methods apply either magnetic or electric dipole sources [6]. In both cases they can work in different zones defined by the product of wave number and transmitter-receiver separation. From the interpretation point of view the ideal situation is to measure in the far-field regime for all frequencies at any transmitter-receiver separation (r). Assuming horizontal electric dipole (HED) source field (just like in case of magnetic dipole source) we can separate three zones over the surface of the homogeneous half-space. In the far field zone the horizontal E, H components decay as $1/r^3$ and the penetration depth depends on frequency and resistivity. It is also called plane-wave zone,

because the basic resistivity MT definition can be applied. The next zone is the transition zone in which the electric field varies as $1/r^3$ and the magnetic field decays as $1/r^2$ to $1/r^3$ and both depend upon frequency. The third zone is the near-field zone, in which the horizontal E and H are independent of the frequency, E decays as $1/r^3$ and H as $1/r^2$. In the near-field zone the penetration depth can be controlled only by the geometry of the EM array opposite to the transition zone, where besides the geometry the frequency is also an influencing factor. For homogeneous earth the far field assumption fulfils when $r_{min}>6\delta$, where δ denotes skin depth. Measurements are made in the transition zone if they are carried out at smaller frequencies or with less separation characterizing the far field zone and $r_{min}>0.2\delta$. These zone limits were given by [7]. In these two regimes the EM fields depend on frequency and resistivity. However, decreasing frequency information can be obtained with approaching near field zone. The main advantages of CSAMT method over MT are a better signal to noise ratio, and the control of source polarization with respect structural strike. At the same time it has to be noted that certain source effects can cause some difficulties in the interpretation of controlled source EM data.

Both methods have a lot of geothermal applications all over the world. The increasing number of MT and CSAMT applications is proved by papers as well. [8] presented electromagnetic studies in geothermal regions among the first. Mainly audio MT is preferred by [2]. A lot of papers in this subject can be found in Geophysics and Geothermics. [9] showed the advantage of the combination of these two methods for a geothermal area in New Mexico. Special issue was presented by Elsevier in the Journal of Applied Geophysics with the title Electrical and Electromagnetic Studies in Geothermally Active Regions in 2006. In [10] emphasis is put on EM imaging of geoelectric structures of geothermal fields and some new developments in EM methods of geothermal exploration are also given.

4. Partial differential equations of FEM for elongated conductivity structures

If the investigated conductivity structure is elongated and the source field is EM plane wave, the problem to be solved is a pure 2D one. If the EM source which can be treated mathematically as a point source, we encounter a 2D model exited by a 3D source. This situation is called a 2.5D problem. For these two situations the partial differential equations are presented and the similarities and differences between them are also given. In the course of EM investigation on elongated conductivity structures exited by electric dipole source special emphasis has to be put on two modes. Distinction is made between TE mode, when the electric source field is parallel to the structural strike, and TM mode, when the electric source field is perpendicular to it.

In MT and CSAMT equations $e^{i\varpi t}$ time dependent EM field variation is assumed and let x coincide with the strike direction. The basic relationships governing the electromagnetic phenomenon are the Maxwell's equations. There is no difference in the form of the next Maxwell's equation, i.e.:

$$\mathrm{rot}\vec{E} = -\partial\vec{B}/\partial t \tag{1}$$

$\vec{j}_s = Id\vec{s}\delta(\vec{r})$ makes possible a point source approximation. This source term equals zero for MT on the right side of the following equation, which is the other Maxwell's equation:

$$rot\vec{H} = \vec{j} + \vec{j}_s \tag{2}$$

Taking into account that the partial derivative of the EM components with respect *x* equals zero for MT, the component equations of (1) and (2) can be written as:

$$\left(\frac{\partial E_z}{\partial y} - \frac{\partial E_y}{\partial_z}\right) = -i\varpi\mu H_x \tag{3}$$

$$\frac{\partial E_x}{\partial z} = -i\varpi\mu H_y \tag{4}$$

$$\frac{\partial E_x}{\partial y} = i\varpi\mu H_z \tag{5}$$

$$\left(\frac{\partial H_z}{\partial y} - \frac{\partial H_y}{\partial z}\right) = \sigma E_x \tag{6}$$

$$\frac{\partial H_x}{\partial z} = \sigma E_y \tag{7}$$

$$-\frac{\partial H_x}{\partial y} = \sigma E_z \tag{8}$$

If equations (4), (5), (6) are taken into one set of equations, only E_x, H_y, H_z components, and similarly in (3), (7), (8) only H_x, E_y, E_z can be found. The conclusion is as follows: in case of 2D situation independently of the angle of incident the plane waves the EM fields can be divided into two parts, which can be treated separately. The first mode is called TE mode, the second is the TM mode. To present the 2D MT equations for homogeneous case in the first group the value of magnetic field component from equations (4), (5) into equation (6) and in the second group the value of electric field component from equations (7), (8) into equation(3) have to be substituted. In this way the most comprehensive form for the TE mode is:

$$\frac{\partial^2 E_x}{\partial y^2} + \frac{\partial^2 E_x}{\partial z^2} = i\varpi\mu\sigma E_x \tag{9}$$

After the operations mentioned above for the TM mode a similar differential equation can be derived:

$$\frac{\partial^2 H_x}{\partial y^2} + \frac{\partial^2 H_x}{\partial z^2} = i\varpi\mu\sigma H_x \tag{10}$$

These equations can be solved with either finite difference (FD) or finite element (FE) method. In spite of the formal similarity of the TE and TM mode the solutions of the two modes are different due to the inner boundary conditions.

In case of magnetic source [11] recommended that the solution of the original 3D problem could be replaced by the series of solutions of 2D problem in the k_x wave number domain. To follow this procedure the Maxwell's equations (1) and (2) are Fourier-transformed. The way of transformation can be expressed as:

$$\tilde{F}(k_x, y, z) = \int_{-\infty}^{\infty} F(x, y, z) e^{-ik_x x} dx \tag{11}$$

In course of the transformation the Fourier transform of the partial derivative of the EM field components with respect x – which is proportional the Fourier transform of the component itself – is also needed.

Opposite MT assuming source term in equation (2) for the Fourier transforms of the Maxwell's component equation can be written as:

$$\partial\tilde{E}_z / \partial y - \partial\tilde{E}_y / \partial z = -i\varpi\mu\tilde{H}_x \tag{12}$$

$$\partial\tilde{E}_x / \partial z - i k_x \tilde{E}_z = -i\varpi\mu\tilde{H}_y \tag{13}$$

$$i k_x \tilde{E}_y - \partial\tilde{E}_x / \partial y = -i\varpi\mu\tilde{H}_z \tag{14}$$

$$\partial\tilde{H}_z / \partial y - \partial\tilde{H}_y / \partial z = \sigma\tilde{E}_x + \tilde{j}_{sx} \tag{15}$$

$$\partial\tilde{H}_x / \partial z - i k_x \tilde{H}_z = \sigma\tilde{E}_y + \tilde{j}_{sy} \tag{16}$$

$$i k_x \tilde{H}_y - \partial\tilde{H}_x / \partial y = \sigma\tilde{E}_z \tag{17}$$

Equation (12) is the only one which resembles MT TM mode and equation (15) resembles MT TE mode. As the other equations have EM fields components belonging to both modes, for this reason the two modes cannot be separated. Here TE mode denotes the situation when the direction of electric dipole source is parallel to the strike, and TM mode corresponds to the case when it is perpendicular to it as it can be seen in Fig.1. In the next the most comprehensive form for the two modes will be given. The aim of this is that instead of having three EM components, it is more comfortable to work with two EM components for each mode. Introducing the following notation as $k^2 = -i\varpi\mu\sigma$,

$\zeta^M = \sigma\left(1-\frac{k_x^2}{k^2}\right)$, $\zeta^E = i\varpi\mu\left(1-\frac{k_x^2}{k^2}\right)$, $\upsilon^M = i\varpi\mu$, $\upsilon^E = \sigma$ a partial differential equation system can be derived for the two polarizations. From equations (12)-(17), without going into details for TE mode:

$$-\frac{\partial}{\partial y}\left(\frac{1}{\zeta^M}\frac{\partial \tilde{H}_x}{\partial y}\right)-\frac{\partial}{\partial z}\left(\frac{1}{\zeta^M}\frac{\partial \tilde{H}_x}{\partial z}\right)-ik_x\frac{\partial \xi}{\partial y}\frac{\partial \tilde{E}_x}{\partial z}+ik_x\frac{\partial \xi}{\partial z}\frac{\partial \tilde{E}_x}{\partial y}+\upsilon^M\tilde{H}_x=0 \tag{18}$$

$$-\frac{\partial}{\partial y}\left(\frac{1}{\zeta^E}\frac{\partial \tilde{E}_x}{\partial y}\right)-\frac{\partial}{\partial z}\left(\frac{1}{\zeta^E}\frac{\partial \tilde{E}_x}{\partial z}\right)+ik_x\frac{\partial \xi}{\partial y}\frac{\partial \tilde{H}_x}{\partial z}-ik_x\frac{\partial \xi}{\partial z}\frac{\partial \tilde{H}_x}{\partial y}+\upsilon^E\tilde{E}_x=-\tilde{j}_{sx} \tag{19}$$

Similar coupled differential equations can be written for TM mode:

$$-\frac{\partial}{\partial y}\left(\frac{1}{\zeta^M}\frac{\partial \tilde{H}_x}{\partial y}\right)-\frac{\partial}{\partial z}\left(\frac{1}{\zeta^M}\frac{\partial \tilde{H}_x}{\partial z}\right)-ik_x\frac{\partial \xi}{\partial y}\frac{\partial \tilde{E}_x}{\partial z}+ik_x\frac{\partial \xi}{\partial z}\frac{\partial \tilde{E}_x}{\partial y}+\upsilon^M\tilde{H}_x=-\frac{\partial}{\partial z}\left(\frac{\tilde{j}_{sy}}{\zeta^M}\right) \tag{20}$$

$$-\frac{\partial}{\partial y}\left(\frac{1}{\zeta^E}\frac{\partial \tilde{E}_x}{\partial y}\right)-\frac{\partial}{\partial z}\left(\frac{1}{\zeta^E}\frac{\partial \tilde{E}_x}{\partial z}\right)+ik_x\frac{\partial \xi}{\partial y}\frac{\partial \tilde{H}_x}{\partial z}-ik_x\frac{\partial \xi}{\partial z}\frac{\partial \tilde{H}_x}{\partial y}+\upsilon^E\tilde{E}_x=ik_x\frac{\partial}{\partial y}\left(\xi\,\tilde{j}_{sy}\right) \tag{21}$$

In these equations the value of $\xi=\left(k_x{}^2-k^2\right)^{-1}$. Just like in case of MT either FD or FE method can be applied, however the 2D problem has to be solved for a lot of discrete wave number values here. In the knowledge of strike directional field components in function of wave number inverse Fourier transformation has to be applied to gain spatial solution. In order to get rid of the effect of transmitter-receiver distance on the EM field components the use of impedance can be recommended. For example in TE mode it can be determined as:

$$\left|Z_{TE}\right|=\frac{\left|E_x\right|}{\left|H_y\right|}=\frac{\left|\int_0^{k_{x\,max}}\tilde{E}_x dk_x\right|}{\left|\int_0^{k_{x\,max}}\left[\frac{\frac{\partial \tilde{E}_x}{\partial z}}{(k_x^2/k^2-1)i\varpi\mu}-\frac{ik_x}{k_x^2-k^2}\frac{\partial \tilde{H}_x}{\partial y}\right]dk_x\right|} \tag{22}$$

It is more complicated than in MT, where it can be calculated as:

$$\left|Z_{xy}\right|=\frac{\left|E_x\right|}{\left|H_y\right|}=\frac{\varpi\mu\left|E_x\right|}{\left|\frac{\partial E_x}{\partial z}\right|} \tag{23}$$

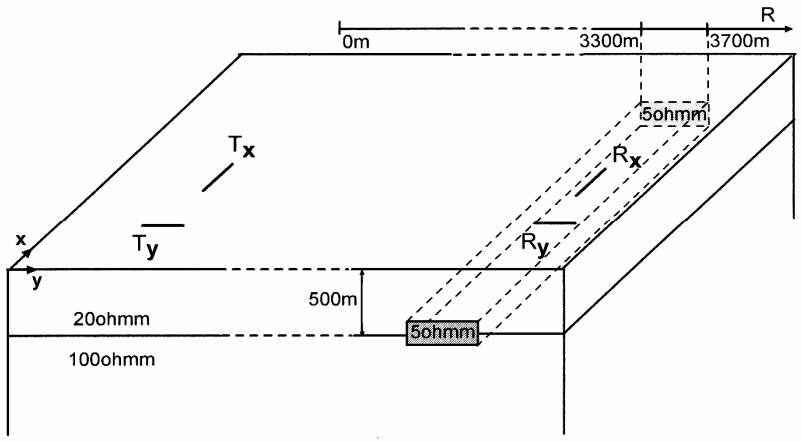

Figure 1: TE and TM mode for controlled source FEM and the investigated model

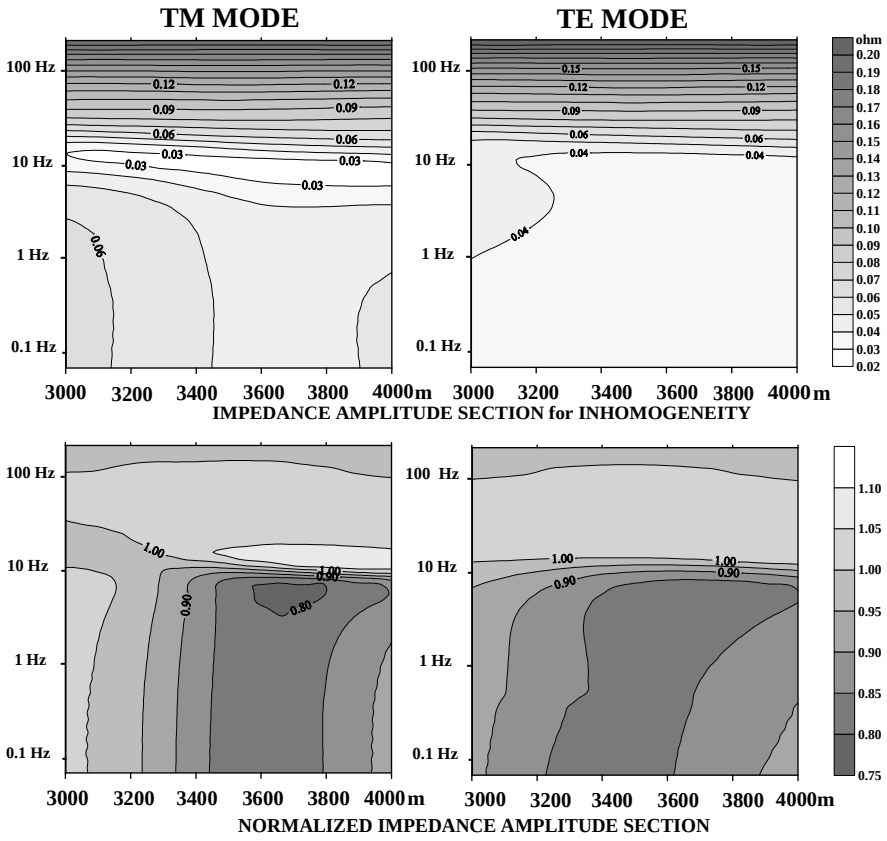

Figure 2: Impedance amplitude sections for TE and TM mode

5. Results of numerical modeling of 2.5D FEM

In the next paragraph some results of numerical modeling are presented. Differential equations of the 3. paragraph were finite differenced and block-tridiagonal LU decomposition was used to solve the resulting linear set of equations for suitable number of wave numbers. To get spatial solution numerical inverse Fourier transformation was applied.

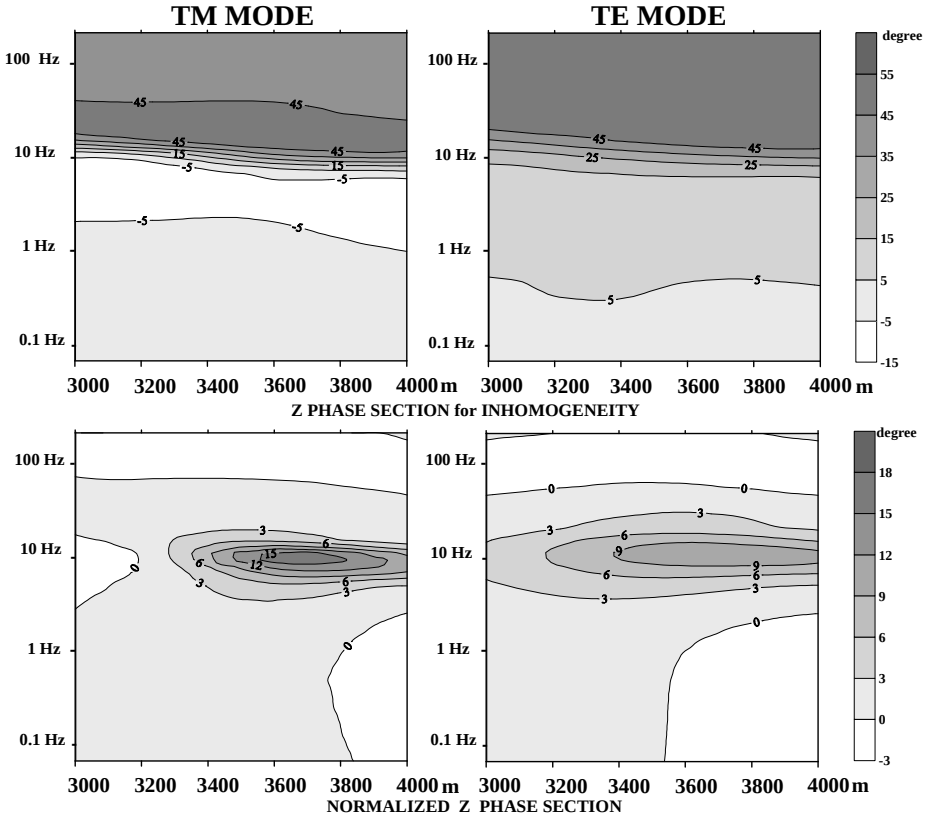

Figure 3: Impedance phase sections for TE and TM mode

In the upper part of *Figure 2* and *Figure 3* the impedance amplitude and phase distribution is given for the conductivity structure of *Figure 1*. The horizontal axis is the transmitter-receiver distance, frequency is plotted along the vertical axis of the sections. In order to enhance the response of conductive inhomogeneity, normalized impedance amplitude and normalized impedance phase sections are determined for TE (T_x–R_x array in *Figure 1*) and TM (T_y–R_y array in the same figure) mode. The EM responses over the two-layer half-space of *Figure 1*. were taken as reference values for the normalization. The result of normalization can be seen in the lower part of *Figure 2* and *Figure 3*. The method seems to be promising, however, if there is conductivity inhomogeneity under the source, the effect of source overprint can suppress the response due to the inhomogeneity under the

receiver [12]. Shadow effect also can be recognized in these situations. The shadow effect for the hosted conductive body under the receiver develops because of the stronger attenuation of the diffusive EM fields in the conductive inhomogeneity compared with its surroundings. On the basis of impedance amplitude and impedance phase sections horizontal delineation can not yield good result for the side of the elongated block away from the source (in this example at 3700m). Here the shadow effect distorts the frequency sounding curves over the side far away from the transmitter. Other geophysical methods (without source effect) or using transmitter from the opposite side may help in the interpretation.

6. Summary

The application of geophysical method cannot be abandoned in the course of geothermal exploration. After reviewing the geophysical methods used in geothermal projects the main features of MT and CSAMT were provided. Basic formalism was given for elongated conductivity structures. Results of numerical forward modeling for 2.5D FEM were also presented. Inversion should be the exact solution to determine the shape, size, depth and the conductivity of the inhomogeneity within the host rocks. However, for a relatively not sophisticated conductivity situation the normalized impedance amplitude and normalized impedance phase sections can be suggested for the two modes as a simple way of inhomogeneity imaging. The method seems to be promising in the shortage of source effects.

List of Symbols

$\vec{E}$	the electric field vector (V/m)	$\vec{j}$	the current density vector (A/m^2)
$\vec{H}$	the magnetic field vector (A/m)	$\vec{j}_s$	the applied current source (A/m^2)
$\vec{B}$	the magnetix flux density (Wb/m^2)	F	EM component (V/m or A/m)
ε	the dielectric constant (F/m)	k_x	wave number in the strike direction (1/m)
σ	the conductivity (mho/m or S/m)	$\tilde{F}$	the Fourier-transform of the F EM component (V/m or A/m)
μ	the magnetic permeability (H/m)	k	he complex wave number (1/m)
r	transmitter-receiver separation, distance (m)	ζ^M	TM impedance (S/m)
δ	skin depth (m)	ζ^E	TE impedance (Hm^{-1}s^{-1})
t	time (s)	υ^M	TM admittance (Hm^{-1}s^{-1})
ϖ	the angular frequency of the EM field (Hz)	υ^E	TE admittance (S/m)
I	transmitter current (A)	ξ	derived parameter (m^2)
$d\vec{s}$	elementary dipole length (m)	Z	impedance (ohm)
$\delta(r)$	Dirac-delta function		
i	$\sqrt{-1}$		

"Acknowledgement: This work was carried out as part of the TÁMOP-4.2.1.B-10/2/KONV-2010-0001 project in the framework of the New Hungary Development Plan. The realization of this project is supported by the European Union, co-financed by the European Social Fund."

REFERENCES

[1] Keller, G., V.: *Exploration for geothermal energy*. In: Developments in Geophysical exploration Methods-2, Edited by Fitch A. A., Applied Science Publisher Ltd., 1981, 107–149.
[2] Wright, P. M.–Ward, S. H.–Ross, H. P.–West, R. C.: *State-of-the-art geophysical exploration for geothermal resources.* Geophysics, 50, 1985, 2666–2699.
[3] Manzella, A.: *Geophysical Methods in Geothermal Exploration*. 70th EAGE Conference & Exhibition, Rome, 9th workshop, 12 June 2008.
[4] Vozoff, K.: *The magnetotelluric method*. In: Nabighian, M.N. (Ed.), Electromagnetic Methods in Applied Geophysics, 2., Society of Exploration Geophysicists, 1991, 641–707.
[5] Goldstein, M., A.–Strangway, D., W.: *Audio-frequency magnetotellurics with a grounded electric dipole source*. Geophysics, 40, 1975, 669–683.
[6] Zonge, K., L.–Hughes, L., J.: *Controlled source audiomagnetotellurics*. In: Nabighian M. N., (Ed.): Electromagnetic methods in applied geophysics, 2B, Application, Soc. Expl. Geophys., 1991, 713–809.
[7] Kaufman, A., A.–Keller, G., V.: *Frequency and transient soundings*. Elsevier Science Publishers, 1983.
[8] Berktold, A.: *Electromagnetic studies in geothermal regions*. Geophysical Surveys, 6, 1983, 173–200.
[9] Wannamaker, P. E.: *Tenzor CSAMT survey over the Sulphur Springs thermal area, Valles Caldera, New Mexio, U.S.A., Part II: Implications for CSAMT methodology*. Geophysics, 62, 1997, 466–476.
[10] Spichak, V.–Manzella, A.: *Electromagnetic sounding of geothermal zones*. Journal of Applied Geophysics 68, 2009, 459–478.
[11] Stoyer, C. H.–Greenfield, R. J.: *Numerical solutions of the response of a two-dimensional earth to an oscillating magnetic dipole source*. Geophysics, 41, 1976, 519–530.
[12] Pethő, G.: *FEM source effect investigation with 2.5D numerical modeling*. 15th European Meeting of Environmental and Engineering Geophysics, Dublin, Near Surface Proceedings &Exhibitors'Cataloge, 2009, 59.

Geosciences and Engineering, Vol. 1, No. 1 (2012), pp. 283–291.

CALCULATION OF GEARBOX TORQUES CONSIDERING INERTIAL EFFECTS

GÁBOR TAKÁCS–GÁBOR LADÁNYI
Petroleum Engineering Department, University of Miskolc
Department of Geotechnical Equipments, University of Miskolc
3515 Miskolc-Egyetemvaros, Hungary
gtakacs@kfgi.uni-miskolc.hu; gtblaga@uni-miskolc.hu

Abstract
When gearbox torques on sucker-rod pumping units are calculated the general approach is to neglect any inertial effects and to find the torques resulting from the polished rod load and the counterweights only. This is the standard procedure in most of the cases when low-slip electric motors are used to drive the installation because the angular velocity of the crankshaft is constant. However, considerable inertial torques can be expected if high or ultra-high slip motors are used and crankshaft acceleration is not zero.

Most of the inertial torques are results of the gearbox's variable rotational speed and they can very substantially affect the net torque, consequently the power requirements of pumping. Therefore, it is of utmost importance that inertial affects be correctly accounted for when the power flow in rod pumping systems is analyzed or optimized. The paper provides a thorough description of the different torques that can develop on the pumping unit's gearbox with an emphasis on inertial effects. Inertial torques are classified and computation models are derived for calculating their different components; these are illustrated by presenting example problems.

1. Introduction

In a sucker-rod pumping unit the prime mover's rotary movement is transmitted through the V-belts to the crankshaft, i.e. the slow-speed shaft of the speed reducer. It is here where the energy input to the system by the prime mover is converted into useful power to lift well fluids to the surface. The power required at the crankshaft is primarily determined by the loads acting at the polished rod, which vary greatly during the pumping cycle. The effect at the crankshaft of the polished rod loads is torque, which is defined as force acting on a lever arm. Thus in order to analyze the operational conditions of surface pumping equipment, it is essential to accurately predict the torques occurring at the crankshaft.

In the pumping cycle, great forces are required to move the polished rod during the upstroke period, whereas no outside force is needed during the downstroke, since the rod string descends due to its own weight. This implies that the prime mover has to do all its useful work during only a portion of the cycle. Thus a relatively large capacity motor and speed reducer are required, which are completely unloaded on the downstroke. Such an operational pattern would mean a very ineffective operation. To improve the energy efficiency of the pumping system, some means of counterbalancing is applied to the pumping unit which can take the form of beam or rotary counterweights or an air cylinder. The use of the proper amount of counterbalance can significantly decrease the instantaneous torque requirements during the upstroke and allows the use of smaller speed reducers and prime movers.

In addition to the torques resulting from polished rod loads and those required to turn the counterweights inertial torques can also occur on the gearbox. Inertial torques are the result of the energy stored in and released from the oscillating masses of the pumping unit structure and may arise in those parts of the unit which do not move with a constant angular velocity. Even when the crankshaft turns at a constant rate, some components of the system, like the horsehead and the walking beam have varying velocities and inertial torque in these parts cannot be neglected. Inertial torques in moving parts (cranks, counterweights etc.) produced by an uneven crankshaft rotational speed can also be significant and must be properly accounted for.

Generally three kinds of torques can be distinguished on pumping unit gear reducers:

1. Rod Torque is the result of polished rod loads and can be calculated based on the unit's kinematic parameters.
2. Counterbalance Torque is a sinusoidal torque vs. crank angle, and is required to move the counterweights at a constant angular velocity.
3. Inertial Torques represent the energy stored in and released from the accelerating/decelerating parts of the pumping unit.

The net torque loading on the speed reducer is the sum of the above components. This is the torque that the power input by the prime mover must overcome. In the following, detailed methods of calculating the components of net crankshaft torque are presented.

2. Rod Torque

The torque required to overcome the polished rod load is often called rod torque and is found with the use of the torque factor concept. Torque factors represent imaginary lever arms which, when multiplied with the polished rod load valid at the same crank position, give the resultant crankshaft torque. Rod torque, therefore, is calculated from the following formula:

$$T_r(\theta) = TF(\theta)\left[F(\theta) - SU\right] \tag{1}$$

where:

$T_r(\theta)$ = rod torque at crank angle θ, in-lbs

$TF(\theta)$ = torque factor at crank angle θ, in

$F(\theta)$ = polished rod load at crank angle θ, lbs

SU = structural unbalance, lbs.

Structural unbalance, *SU*, is one of the characteristic parameters of the pumping unit. It is defined as the force required at the polished rod to keep the walking beam in a horizontal position with the pitmans disconnected from the cranks. Depending on its direction, this force is considered to be positive when acting downwards and negative when acting upwards, its value is supplied by the manufacturer. The pumping unit manufacturer should also provide the basic kinematic parameters for every 15 degree of crank angle: the position of rods and the torque factor, as recommended in the API specification for pumping units [1].

3. Counterbalance Torque

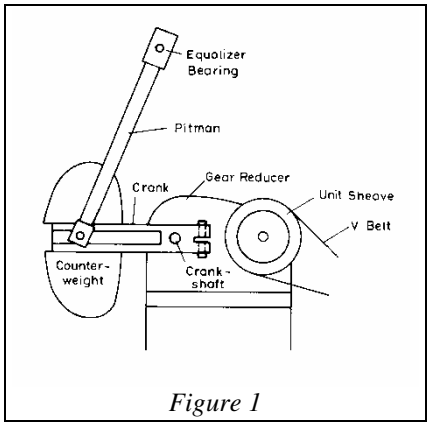

Figure 1

In the majority of cases rotary counterweights attached to the crank(s) are used to counterbalance the pumping unit. The usual arrangement on a conventional unit is shown in *Figure 1*. The counterweights impose a mechanical moment about the crankshaft, which equals the weight of the counterweights multiplied by the distance between their center of gravity and the crankshaft. Since the lever arm continuously changes as the crank rotates during the pumping cycle, the torque required to turn the counterweights about the crankshaft varies with the crank angle. It is easy to see that counterbalance torque opposes rod torque in direction and varies as a sinusoidal function of the crank angle as given here:

$$T_{CB}(\theta) = -T_{CBmax} \sin\theta \tag{2}$$

where:

$T_{CB}(\theta)$ = counterbalance torque, in-lbs

T_{CBmax} = maximum moment of counterweights, cranks, and crank pins, in-lbs

θ = crank angle, degrees

In case of a conventional geometry pumping unit, the maximum moment of the rotary counterweights, crank pins and cranks, *M* is measured while the cranks are horizontal. This is due to the fact that the counterweights' center of gravity usually falls on the centerline of the cranks. Other than conventional geometries employ phased counterweight positions, where the counterweights' center of gravity leads or lags the crank's motion. Therefore, the phase angle between the crank and the counterweight arm must be included into the above formula, and the following expressions can be derived:

$$T_{CB}(\theta) = -T_{CBmax} \sin(\theta + \tau) \qquad \text{for Mark II units} \tag{3}$$

$$T_{CB}(\theta) = -T_{CBmax} \sin(\theta - \tau) \qquad \text{for Torqmaster units} \tag{4}$$

where:

$T_{CB}(\theta)$ = counterbalance torque, in-lbs

T_{CBmax} = maximum moment of counterweights, cranks, and crank pins, in-lbs

θ = crank angle, degrees

τ = phase angle (offset) between the crank's and the counterweight arm's center line, degrees

3.1. Maximum counterbalance moment

The calculation of counterbalance torque over the pumping cycle is only possible if the maximum moment, T_{CBmax}, about the crankshaft caused by the cranks, crank pins, and counterweights is known. Typical arrangement of these components is shown in *Figure 2* from which is can be concluded that the maximum moment is composed of: (a) the moment of the cranks plus crank pins and (b) the moment of the counterweights plus auxiliary weights.

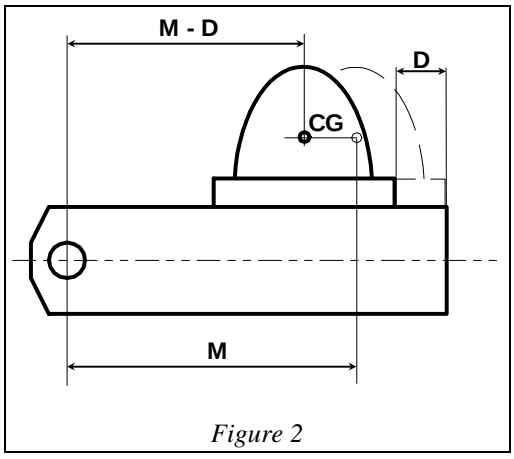

Figure 2

The combined moment of the cranks plus the crank pins is supplied by the manufacturer along with the following data on counterweights and auxiliary weights:

- Weight per piece,
- Lever arm *M* of the counterweight's center of gravity (CG) when at the outmost position on the crank.

The only unknown required for the calculation of the counterweight's moment about the crankshaft is the actual position of the center of gravity; this is found from the distance *D* of the counterweight measured from the long end of the crank. The maximum counterbalance moment can thus be found from the next formula:

$$T_{CBmax} = T_{crank} + (M - D)[NW + n\,w] \tag{5}$$

where:

T_{crank} = moment of the cranks, in-lbs
M = maximum lever arm of counterweights, in
D = distance of counterweight from long end of crank, in
N = number of counterweights on crank,
n = number of auxiliary weights on crank,
W = weight of each counterweight, lbs
w = weight of each auxiliary weight, lbs

Table 1

Crank Type = 6468C				
Moment of Cranks = 134,370 in lbs				
Counterweight		**Aux. Weight**		**M**
Type	**Weight**	**Type**	**Weight**	
	lbs/piece		**lbs/piece**	**in**
2RO	1,708	2S	612	42.20
3CRO	1,327	3BS	572	45.26
5ARO	913	5AS	366	49.77
5CRO	662	5C	327	50.96
6RO	504	6	190	52.51
7RO	315	7	140	54.16

When deriving this formula it was supposed that counterweights are installed in pairs and on the same position on both sides of the crank; auxiliary weights are fixed to counterweights in such a way that their centers of gravity overlap. Table 1 contains the necessary parameters for a given crank type from a major manufacturer.

Example 1: Find the maximum counterbalance moment on the gearbox for a conventional pumping unit if 6468C cranks and four 3CRO counterweights are used at a position of D = 12 in from the long end of the crank.

Solution: From Table 1 the moment of the cranks is 134,370 in lbs, maximum lever arm of the 3CRO counterweight is M = 45.26 in, and each counterweight weighs 1,327 lbs. Maximum counterbalance moment from Eq. 5 is found as:

T_{CBmax} = 134,370+(45.26–12) (4 1,327) = 310,914 in lbs.

4. Inertial Torques

In the preceding, the crankshaft was assumed to rotate with a constant angular velocity, which meant that inertial effects of the rotating masses could be disregarded. In the majority of pumping installations, this assumption is fully justified since the prime mover usually employed does not allow for significant speed variations. The API Spec. 11E [1] suggests that up to a speed variation of 15% over the average pumping speed, neglecting inertial effects does not introduce errors greater than 10% in torque calculations. High-slip electric motors however produce much greater speed variations during the pumping cycle and actual torques can considerably be affected by inertia. Since these motors are gaining popularity in the oil field, it is useful to discuss the role of inertia in crankshaft torque calculations.

The physics background of inertial torque calculations is the relation of the torque acting on a body that rotates around one of its axes and the body's angular acceleration. The relevant formula is very similar to Newton's Second Law:

$$T = I\frac{d^2\alpha}{dt^2} \tag{6}$$

As seen torque T causes angular acceleration $d^2\alpha/dt^2$ depending on the body's mass moment of inertia, I. This parameter is a measure of rotational inertia and is found from the mass distribution of the given body. After dividing the body into infinitesimal dm masses whose distances from the axis of rotation are denoted by r the mass moment of inertia is defined by the following integral:

$$I = \int_m r^2 dm \tag{7}$$

Inertial torques in the different parts of the pumping unit, therefore can be calculated if the parts' mass moments of inertia and their accelerations around the same axis are known.

4.1. Articulating torque

The first kind of possible inertial torques in sucker-rod pumping units is called the articulating torque. This represents the energy stored in and released from the oscillating parts of the pumping unit structure: (a) the walking beam, (b) the horsehead, (c) the

equalizer and (d) the pitmans. It is important to note that these inertial effects exist even for a constant prime mover speed since the mentioned structural parts move with varying accelerations during the pumping cycle [2].

In order to find the instantaneous values of articulating torque, the torque about the saddle bearing required to accelerate the structural parts listed previously is computed first:

$$T' = I_b \frac{d^2\theta_b}{dt^2} \tag{8}$$

where:

I_b = total moment of inertia of the components involved, lb ft^2

θ_b = angle between the centerline of walking beam and the line connecting the crankshaft and the center (saddle) bearing, radians.

This torque can be converted to an equivalent force acting at the polished rod by:

$$F = \frac{T'}{A} = \frac{I_b}{A} \frac{d^2\theta_b}{dt^2} \tag{9}$$

The gearbox torque can now be found by multiplying the polished rod load with by the pumping unit's torque factor; thus the final formula for articulating torque is the following:

$$T_{ia}(\theta) = 12\, TF(\theta) \frac{I_b}{A} \frac{d^2\theta_b}{dt^2} \tag{10}$$

where:

$T_{ia}(\theta)$ = articulating inertial torque on the gearbox at crank angle θ, in lbs

$TF(\theta)$ = torque factor at crank angle θ, in

A = distance between the saddle bearing and the polished rod, in

I_b = mass moment of inertia of the beam, horsehead, equalizer, bearings and pitmans, referred to the saddle bearing, lb ft^2

$d^2\theta_b/dt^2$ = angular acceleration of the beam, 1/s^2

During the polished rod's upstroke articulating torque increases the net torque on the gear reducer for positive beam accelerations due to the inertia of the parts driven. For negative accelerations when the beam and the connected parts are decelerating articulating torque helps the system by releasing the kinetic energy stored. On the downstroke the role of beam acceleration is the opposite because the torque factors become negative.

The mass moment of inertia of the structural parts is usually supplied by the manufacturer; lightweight structural parts (beam, horse-head etc.) are beneficial in reducing the torsional load on the unit. The walking beam's acceleration pattern can be derived from the variation of the crankshaft speed using the kinematic model of the pumping unit, e.g. Svinos' [3] method.

4.2. Rotary inertial torque

The other kind of inertial torque is called rotary inertial torque and has a greater importance than articulating torque. It only exists when the angular speed of the crankshaft varies over the pumping cycle; at higher speeds, energy is stored in the rotating parts but

inertial energy is returned into the system when the unit slows down. When calculating the gearbox torques the following rotating masses have to be considered:

- The cranks with crank pins,
- The counterweights and auxiliary weights, and
- The slow-speed shaft and gear of the speed reducer.

Since all these components rotate around the crankshaft, their combined moment of inertia can be found from simple addition of the individual moments. Using the net moment of inertia of the rotating system, the rotary inertial torque on the gearbox is found from the next formula:

$$T_{ir}(\theta) = 12\, I_s \frac{d^2\theta}{dt^2} \tag{11}$$

where:

$T_{ir}(\theta)$ = rotary inertial torque on the crankshaft at crank angle θ, in lbs,
I_s = mass moment of inertia of the cranks, counterweights and slow-speed gearing referred to the crankshaft, lb ft^2
$d^2\theta/dt^2$ = angular acceleration of the crankshaft, 1/s^2.

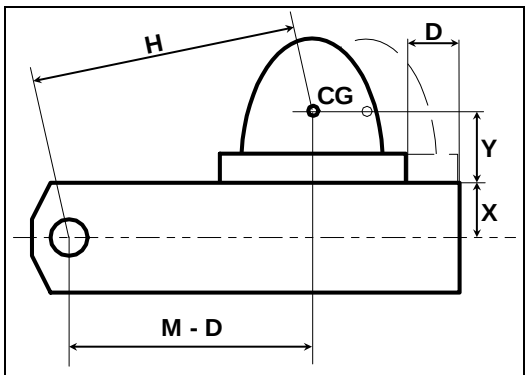

Figure 3

As seen rotary inertial torque changes with the angular acceleration of the crankshaft which can be derived from the angular velocity of the crankshaft. Crankshaft velocity, in turn, is directly measured with a generating tachometer or, as is the usual case, is inferred from electronic dynamometer measurements that record polished rod position and load vs. time. Angular velocity is found from position data and acceleration is the result of differentiation in respect to time.

The individual components of the net mass moment of inertia, I_s, are calculated as detailed in the following. Data on cranks and the slow-speed gearing is supplied by the manufacturer; only the actual moment of inertia of the counterweight system must be found.

Figure 3 shows the principle of calculating the mass moment of inertia of the counterweight components. If the moment of inertia of the counterweight about its center of gravity (CG) is known then it can be referred to the crankshaft by using the Huygens–Steiner Theorem as follows:

$$I_{CW} = I_{CG} + m_{CB}\left(\frac{H}{12}\right)^2 \tag{12}$$

where:

I_{CG} = mass moment of inertia of the counterweight about its center of gravity, lb ft^2,
m_{CB} = weight of the counterweight, lbs and
H = distance between the crankshaft and the CG of the counterweight, in.

The distance *H* changes with the position of the counterweight on the crank and is easily found from:

$$H = \sqrt{(X + Y)^2 + (M - D)^2} \tag{13}$$

where:

X, Y = dimensions of the crank and counterweight, in
M = maximum lever arm of counterweights, in
D = distance of counterweight from long end of crank, in

Sample data on the crank's moment of inertia and different counterweights are given in *Table 2* for a 160D gearbox. The next example illustrates the calculation of net rotary moment of inertia.

Table 2

Crank Type = 6468C					
Moment of Inertia = 22,282 lb ft^2					
X = 10 in					
Counterweight			**Aux. Weight**		
Type	**Moment**	**Y**	**Type**	**Moment**	**Y**
	lb ft^2	**in**		**lb ft^2**	**in**
2RO	2,458	14.2	2S	756	14.2
3CRO	1,384	13.3	3BS	562	13.3
5ARO	707	13.4	5A	272	13.4
5CRO	430	11.8	5C	220	11.8
6RO	229	9.9	6	83	9.9
7RO	114	8.6	7	51	8.6

Example 2: Find the combined moment of inertia of the cranks, counterweights and slow-speed gear about the crankshaft if a 160D gearbox is used with the same counterweights as given in the previous example.

Solution: The moment of inertia of the 160D gearbox from manufacturer data, see *Table 2*:

I_g = 318 lb ft^2.

The inertia of one crank, from Table 2 is 22,282 lb ft^2 so two cranks have:

I_{cr} = 2 22,282 = 44,564 lb ft^2.

The distance *H* is found from Eq. 13 by using *X* = 10 in and *Y* = 13.3 in from *Table 2*; and *M* = 45.26 in from *Table 1:*

$H = [(10+13.1)^2+(45.26–12)^2]^{0.5}$ = 40.49 in.

Since the moment of inertia of the counterweight about its center of gravity is 1,384 lb ft^2 as found from *Table 2,* and its weight is 1,327 lbs from *Table 1,* the moment about the crankshaft of four counterweights from Eq. 12 is:

$I_{CW} = 4\ [1{,}384+1{,}327\ (40.49/12)^2] = 65{,}967$ lb ft^2.

The net moment of inertia is the sum of individual inertias:

$I_s = 318+44{,}564+65{,}967 = 110{,}849$ lb ft^2.

5. Conclusions

The main conclusions of the paper can be summed up as follows.

- Inertial torques can substantially affect the net torque acting on the gearbox as well as the power requirement of pumping.
- The different torques that develop on the pumping unit's gearbox were described and the effects of inertial torques were illustrated.

"Acknowledgement: This work was carried out as part of the TÁMOP-4.2.1.B-10/2/KONV-2010-0001 project in the framework of the New Hungarian Development Plan. The realization of this project is supported by the European Union, co-financed by the European Social Fund."

REFERENCES

[1] *Specification for Pumping Units.* API Spec. 11E, 18th Edition, American Petroleum Institute, Washington, DC 2008.

[2] Gibbs, S. G.: *Computing Gearbox Torque and Motor Loading for Beam Pumping Units with Consideration of Inertia Effects.* JPT September 1975 1153–9.

[3] Svinos, J. G.: *Exact Kinematic Analysis of Pumping Units.* Paper SPE 12201 presented at the 58th Annual Technical Conference and Exhibition of the SPE, San Francisco, California, Dec. 5–8, 1983.

Geosciences and Engineering, Vol. 1, No. 1 (2012), pp. 293–302.

NODAL ANALYSIS OF A GEOTHERMAL WELL PRODUCED BY AN ESP PUMP

ZOLTÁN TURZO–GÁBOR TAKÁCS
Petroleum Engineering Department, University of Miskolc
3515 Miskolc-Egyetemvaros, Hungary
gtakacs@kfgi.uni-miskolc.hu; turzoz@kfgi.uni-miskolc.hu

Abstract
The paper describes how the operation of geothermal wells produced by ESP installations can be analyzed by NODAL techniques. After a detailed explanation of the use of NODAL Analysis to find the stable liquid production rate of the well-ESP pump system, an example case is presented. Different scenarios are investigated and calculation results include, in addition to the stabilized liquid rate, the distribution of pressure and temperature in the geothermal system. Results show how the behavior of the system changes with different electrical driving frequencies, pump setting depths and flowline insulation set-ups. The paper indicates the ways to increase the energy output of geothermal wells produced by ESP installations.

1. Introduction

System analysis methods and procedures used in solving production problems in the petroleum industry were named "Nodal Analysis" by K. E. Brown and the term has generally been accepted. This methodology of course can be applied to other, e.g. geothermal wells as well. An artificially lifted geothermal well's production system comprises the following main components: the reservoir, the perforations, the producing well including the artificial lift equipment, the surface flowline and the surface gas-liquid separator. In order to produce fluids to the surface, all components of this interconnected and interacting system must work together. The components all have their own specific performance relationships, but each in turn also depends upon and influences the other elements; the proper description of system performance, therefore requires accurate modeling of each component's behaviour.

Electrical submersible pumps are often used to lift high to extremely high water rates from geothermal wells. This paper applies Nodal analysis principles and procedures to model the operation of geothermal wells produced by ESP installations. Nodal principles as well as their practical applications are detailed and example cases are presented to show how well rates and outflow temperatures can be calculated.

2. The Production System

System analysis (NODAL) principles can readily be applied to the analysis of geothermal wells produced by ESP pumps. [1–4]. The production system of an ESP installation is shown with the appropriate node points in *Figure 1*. Although ideal operational conditions for ESP pumps require negligible or no gas production, in the following the specific features of the system are discussed for a generalized case when a considerable amount of free gas enters the wellbore.

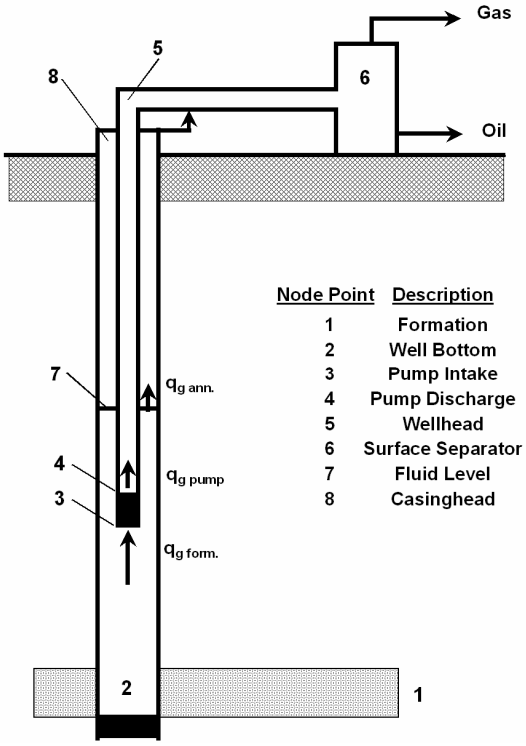

Figure 1: The production system of a geothermal well produced by an ESP pump

Well fluids entering through the sandface rise in the casing string up to the intake of the ESP pump (Node 3), where the flowing pressure equals the pump intake pressure (*PIP*). In this section of the well (in the casing string) two-phase vertical or inclined flow occurs whose free gas content is determined by the pressure conditions and the composition of the incoming wellstream. Before entering the pump, due to natural and/or forced (performed by a downhole separator) separation, the free gas stream, $q_{g\ form}$, present at Node 3 splits and part of it, $q_{g\ ann}$, rises in the annulus to the casinghead, the rest being ingested by the ESP pump.

The operation of the ESP pump, compared to the ideal case when handling an incompressible liquid, significantly deteriorates due to the presence of free gas. Therefore its discharge pressure at Node 4 varies with the gas content of the wellstream at suction conditions. The proper description of the pump's operation as well as the calculation of the pump discharge pressure require the exact knowledge of the amount of free gas entering the pump, $q_{g\ pump}$. This gas rate, in turn, is a function of the pump intake pressure (*PIP*) since the value of *PIP* determines the amount of gas released from the wellstream. Consequently, the determination of the gas rate entering the pump, $q_{g\ pump}$, is an iterative process. Because of this condition and the complexity of calculating the head developed by the stages of the

ESP pump when pumping a multiphase mixture, hand calculations are cumbersome and computer programs are normally used.

Above Node 4 vertical or inclined multiphase flow occurs in the tubing string up to the wellhead where the produced fluids enter the flowline at Node 5, finally reaching the surface separator at Node 6. In the majority of cases wells produced by ESP systems do not have a packer and continuously vent produced gas to the surface. The annulus above the pump contains a static liquid column reaching up to the dynamic liquid level (Node 7), with a steady rate of gas bubbling through the stagnant liquid. Above the dynamic liquid level, a static gas column occupies the casing-tubing annulus with gas being vented to the flowline at the casinghead.

3. NODAL Analysis

The node points of the ESP installation being defined, application of systems analysis principles allows the calculation of the liquid rate occurring in the production system. In general the NODAL Analysis procedure consists of the following basic steps.

1. A Solution Node is selected first. This can be any node point in the system the proper selection of which facilitates the evaluation of different assumed conditions. The selection depends on the type of the problem to be solved. For example, if an analysis of the parameters governing the well's inflow performance is desired than the proper choice is the sandface. If, on the other hand, the capacity of the surface system (flowline, separator, etc.) is selected as the controlling parameter, placing the solution node at the wellhead is advised.
2. A range of liquid flow rates is selected for subsequent calculations.
3. Starting from the two endpoints of the system (Node 1 and Node 6 in *Figure 1*) and working towards the Solution Node, the flowing pressures at every node point are calculated for the first assumed liquid rate.
4. After repeating the calculations in Step 3 for each and every assumed liquid flow rate, two sets of pressure – rate values will be available at the Solution Node. These values represent the performance curves for the two subsystems created by the Solution Node.
5. According to a basic rule of System Analysis inflowing and outflowing pressures at the Solution Node must be equal. Thus the intersection of the two performance curves defines the well's liquid flow rate under the given conditions.

The application of NODAL Analysis principles and the solution described here provide the basis for analyzing of existing or planned ESP installations. The generally accepted coordinate system used for System Analysis is the rate vs. pressure coordinates although the coordinate system head vs. rate is also used.

4. Example problem

4.1. Problem statement

The previously detailed principles are illustrated by presenting an example problem. The sample case involves a geothermal well producing gaseous water by an ESP pump through a buried pipeline into the surface facilities requiring a minimum of 5 bar intake pressure. The operator's objective is to produce as much power as possible.

Table 1

Well parameters for example problem

Parameter	Value
Perforation Depth, m	2,800
Prod. Casing Size, in	9 5/8
Reservoir Pressure, bars	290
Prod. Index, m^3/d/bar	75
Reservoir Temperature, C	160
Water Salinity, ppm	150,000
Gas-liquid ratio, m^3/m^3	20

The well produces from a relatively deep formation with a high productivity, the most important input data are displayed in *Table 1*. The ESP pumps assumed are the L500 series from Centrilift. The flowline is buried and insulated with bitumen; other relevant data are given in *Table 2*.

Table 2

Flowline data

Parameter	Value
Flowline Length, m	2,000
Pipe OD, m	0.12
Burial Depth, m	1.5
Insulation Thickness, mm	2

4.2. Solution strategy

The production system of the example well is similar to the one shown in *Figure 1* and the required intake pressure at the facilities can be considered constant. The solution node is best selected at the well perforations when the following two subsystems will result: (a) the formation and the well completion (the well's IPR curve), and (b) the casing string, ESP pump, tubing string plus the surface flowline (the so called VLP curve). The performance curves of these subsystems, calculated from the two known pressures at the outer boundary of the drainage area and at the surface facilities, will intersect at those liquid producing rates that will develop under different assumed conditions.

Simultaneous calculations of pressure and temperature distributions in the producing system were carried out by using the computer program package PROSPER [5] and assuming steady-state pressure and temperature conditions.

For the calculation of the geothermal power to be extracted from the given well, three different scenarios were assumed where the following parameters were varied: (1) the setting depth of the ESP pump, (2) the surface electrical frequency used to drive the ESP installation and (3) the insulation thickness on the flowline.

1st case.
The setting depth of the ESP pump is varied and the following values are assumed: 400, 600, 800, 1000 and 1500 m. The casing annulus is open at the wellhead and contains gas above the dynamic liquid level. The installation is driven by a 50 Hz electric supply.

2nd case:
The pump is set at a depth of 500 m in the well while the driving electrical frequency is varied: 30, 40, 50, 60 and 70 Hz.

3rd case:
This case studies the effect of heat insulation of the flowline. The base case with 2 mm of bitumen (k = 0.17 W/m/K) outer insulation is further enhanced by the use of a foam insulation (k = 0.035 W/m/K) using thicknesses of 1, 3, 5, and 10 cm. The pump is installed at a depth of 500 m and the installation is driven by an electrical frequency of 50 Hz.

4.3. Calculation results

1st case
The results of the first case are displayed in *Figure 2 that* contains the performance curves of the production system at the solution node, i.e. the well bottom. Pump setting depth, as seen, has no influence on the water rate received from the well since all VLP curves intersect the IPR curve at almost the same point. Numerical results show some difference, as it apparent on *Figure 3*.

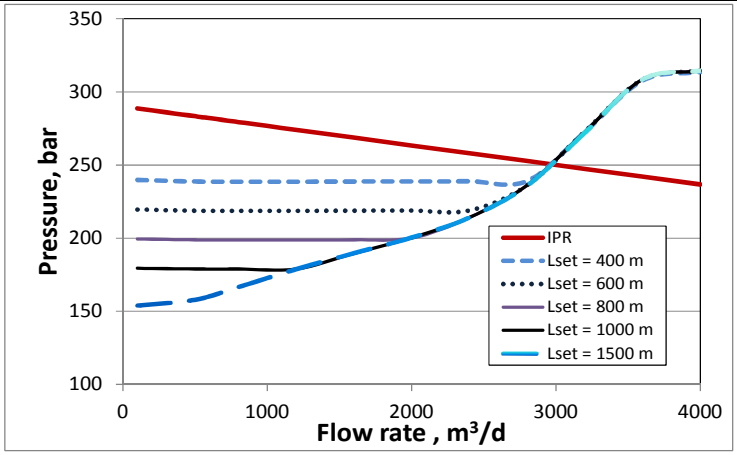

Figure 2: NODAL calculation results for the first case

Figure 3 plots the sensitivity results of the same case. It shows how the flowrate and the outflow temperature (the temperature at the end of the flowline) vary in function of the pump setting depth. As shown the maximum difference in rates is less than 20 m^3/d and in outflow temperatures is less than 2 °C. Although the highest flowrate is reached at the biggest setting depth, the highest outflow temperature is obtained at a pump setting depth of 600 m.

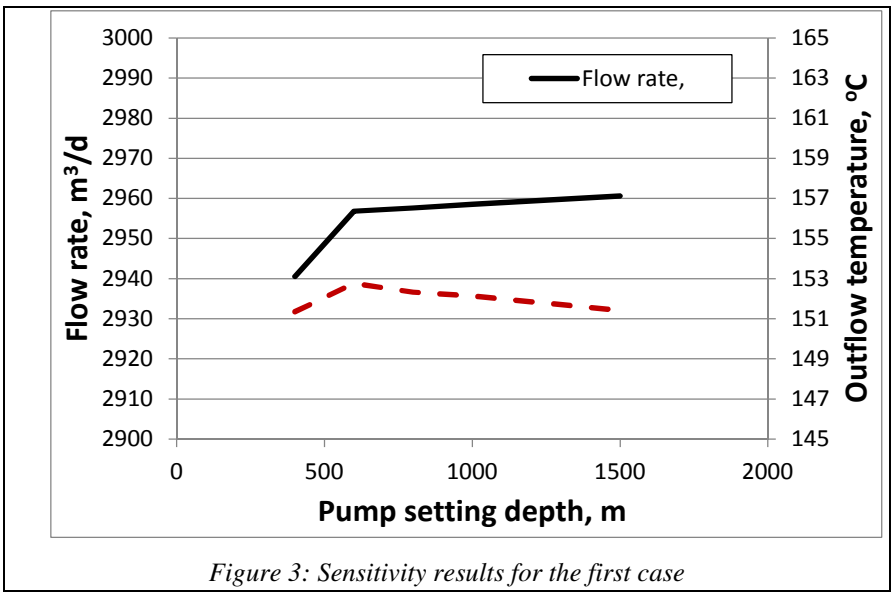

Figure 3: Sensitivity results for the first case

Based on the charts it seems that pump setting depth has negligible effect on the flow rate and the outflow temperature of an ESP pumped geothermal well. Although the differences seem to be negligible, the calculation of the geothermal power provides further insight into the problem. The difference of recoverable powers was calculated using the next equation where the reference temperature was the outflow temperature of the case with a pump setting depth of 400 m:

$$\Delta P = c\, \dot{m}\, \Delta T$$

where:

ΔP : power difference, W

c : specific heat of water, 4181 J/kg K

$\dot{m}$: mass flow rate, kg/s

ΔT : temperature difference, K (t).

Table 3

Difference in recoverable power for different pump setting depths

Pump setting depth	**Difference in recoverable power (ΔP)**
m	**kW**
400	0
600	203
800	139
1000	112
1500	8

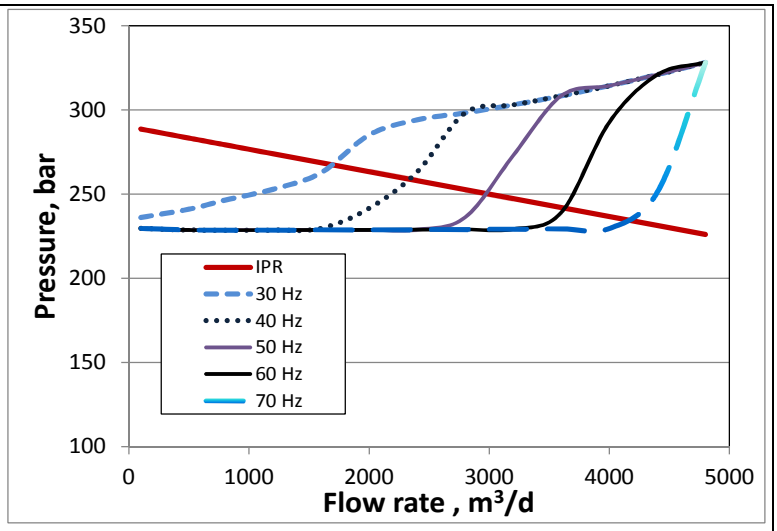

Figure 4: NODAL calculation results for the second case

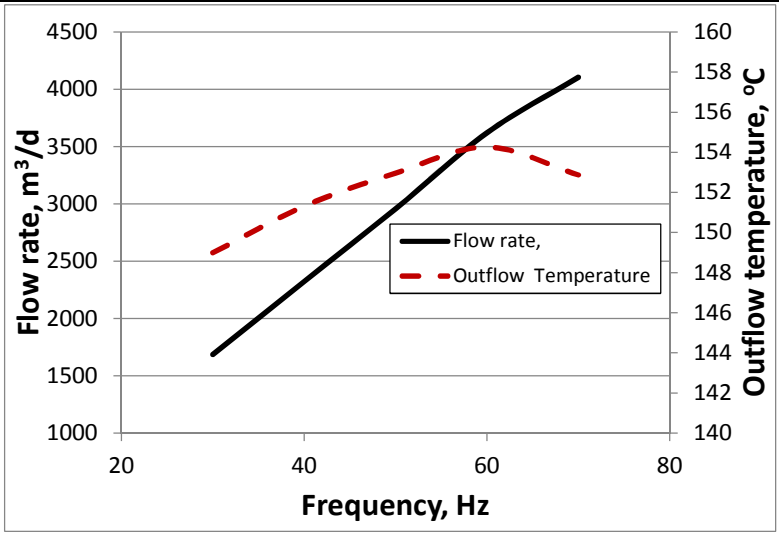

Figure 5: Sensitivity results for the second case

Table 3 shows the differences in recoverable power for the different pump setting depths. Evaluation of the results in *Table 3* shows the highest recoverable power at a pump setting depth of 600 m.

2nd case

Figure 4 contains the performance curves of the production system at the solution node. Electrical frequency, as seen, has noticeable influence on the water rate received from the well because the VLP curves intersect the IPR curve at different flow rates. Higher driving frequencies mean higher flow rates.

Figure 5 plots the sensitivity results of the same case. It shows the water flowrate and the outflow temperature in function of the electrical frequency. As shown maximum flowrate is reached at the highest driving frequency. The outflow temperature reaches its maximum value at 60 Hz, its variation is about 5 ^{o}C. On the other hand the deviation of flow rates is huge, more than 2000 m^3/d.

Table 4 shows the differences in recoverable power using the outflow temperature belonging to a frequency of 30 Hz as a reference.

Based on *Figures 4* and *5,* as well as *Table 4,* one can conclude that higher driving frequencies are desirable to increase the potential of geothermal wells placed on ESP pumps. What these data do not show is that ESP installations running at higher frequencies require higher electrical power input.

Table 4

Difference in recoverable power for different electrical frequencies

Electrical frequency	**Difference in recoverable power (ΔP)**
Hz	**kW**
30	0
40	261
50	568
60	923
70	771

To compensate for the effect just mentioned *Table 5* contains the increase in pump power for the frequencies studied and referenced to 30 Hz. The table also shows the difference between the recoverable power (calculated previously) and the required pump power increase. This value can be considered as the net power gain of the geothermal system.

Table 5

Differences in combined power for different electrical frequencies

Electrical frequency	**Increase in pump power (ΔP_p)**	**ΔP-ΔP_p**
Hz	**kW**	**kW**
30	0	0
40	94	167
50	247	321
60	474	449
70	809	-38

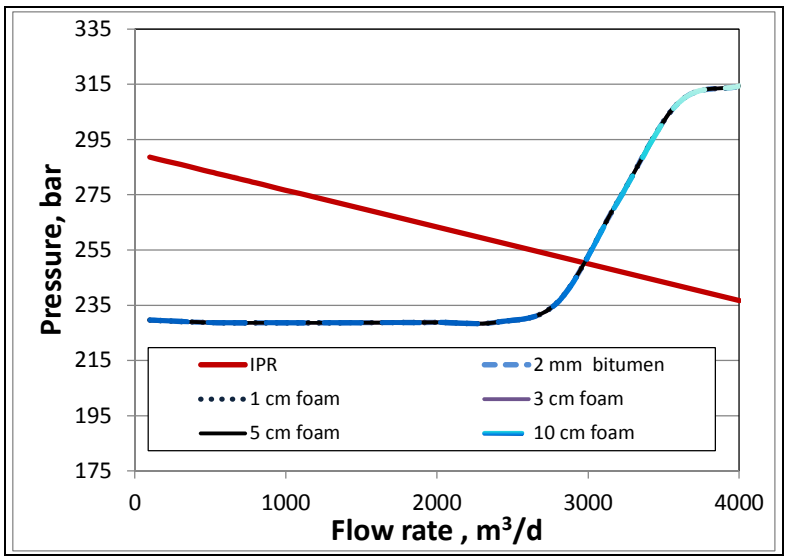

Figure 6: NODAL calculation results for the third case

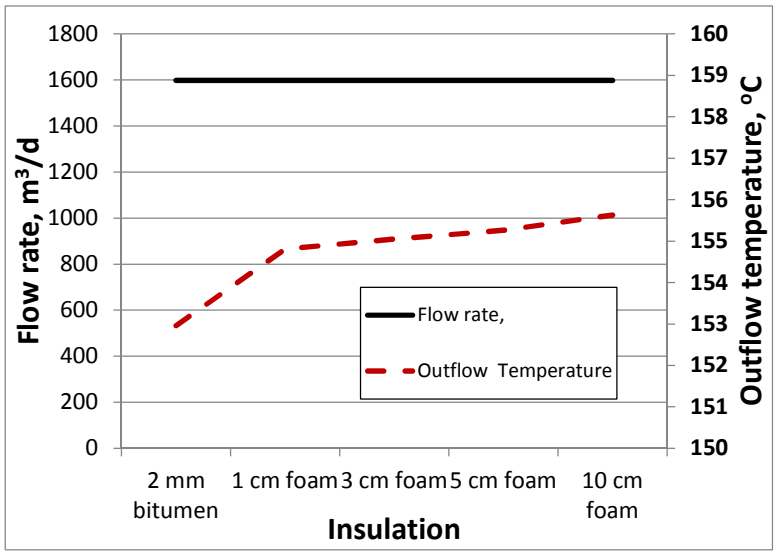

Figure 7: Sensitivity results for the third case

As seen *Table 5* presents a tendency similar to that of Table 4: usually higher operating frequencies result in higher recoverable power, but to a point. Net power, in function of electrical frequency, increases to a maximum value then decreases, i.e. there is an optimum electrical frequency, in this case it's 60 Hz.

3rd case

Figure 6 contains the results of third case where the heat insulation of the flowline has negligible effect on the water flow rate obtained from the well. As shown in *Figure 7,* water flow rate is independent of pipeline insulation scenarios; while the variation of outflow temperature is almost negligible, about 3 ^{o}C.

5. Conclusions

The paper illustrated the use of NODAL Analysis methods for modeling the operation of a geothermal well producing water by an ESP pump. The example calculations presented allow one to draw the following conclusions:

- Operating at a constant electrical frequency of 50 Hz, there is a maximum in recoverable geothermal power at a given pump setting depth.
- If the ESP pump is set at a given depth in the well, changing the electrical frequency driving the ESP installation changes the net power received in such a way that there is a definite optimum operating frequency where net power is at a maximum.
- The effect of heat insulation on the flowline does not bring about any noticeable changes in well performance while producing from a constant depth and using a constant electrical frequency.

"Acknowledgement: This work was carried out as part of the TÁMOP-4.2.1.B-10/2/KONV-2010-0001 project in the framework of the New Hungarian Development Plan. The realization of this project is supported by the European Union, co-financed by the European Social Fund."

REFERENCES

[1] Grupping, A. W.: *Pressure-Production Diagram Matches Submersible Pump Performance to that of Well.* OGJ Nov. 29, 1982. 69–75.

[2] Brown, K. E.: *The Technology of Artificial Lift Methods.* Vol. 4. PennWell Books, Tulsa Oklahoma, 1984.

[3] Wilson, B. L.: *Understanding the Basics of Electrical Submersible Pump Performance.* Paper SPE 14050 presented at the International Meeting on Petroleum Engineering held in Beijing, China. March 17–20, 1986.

[4] Takács, G.: *Electrical Submersible Pumps Manual*. Gulf Professional Publishing, an Imprint of Elsevier. Burlington, Mass., U.S.A. 2009.

[5] *PROSPER User Manual* Version 11.5, Petroleum Experts Limited, Edinburgh Scotland, April 2010.

Geosciences and Engineering, Vol. 1, No. 2 (2012), pp. 303–314.

THE EFFECTS OF WEATHER CHANGES ON NATURAL GAS CONSUMPTION

LÁSZLÓ TIHANYI[1]–ISTVÁN SZUNYOG[2]
Petroleum and Natural Gas Institute, University of Miskolc
H-3515 Miskolc-Egyetemváros, Hungary
[1]tihanyil@kfgi.uni-miskolc.hu, [2]szunyogi@kfgi.uni-miskolc.hu

Abstract
The number of heating degree days (HDD) is a connective parameter which relates natural gas demands to weather conditions. It provides a useful means for reliably planning domestic heating gas supply (monthly or annual) and estimating climate risks due to changeable weather conditions. Like many other European states, Hungary is heavily dependent on natural gas import; therefore, weather risk assessment is an essential issue for the effective and sustainable energy management of the country. Relying on the statistical analysis of annual and monthly degree days (over extensive time spans), the authors give an international comparison of climate risks and their influences on gas supply.

1. The basic characteristics of natural gas consumption

By using basic datasets that determine the main factors of national gas demand in Hungary, *Figure 1* illustrates temporal changes of the country's gas supply. As it is obvious from the figure, gross domestic consumption is subject to considerable seasonal fluctuation. Gas consumption in the coldest winter month is 2–3 times larger than the energy amount used in the hottest summer month. Yet, domestic production temporally varies within a relatively limited range; it might as well be regarded as approximately stabile.

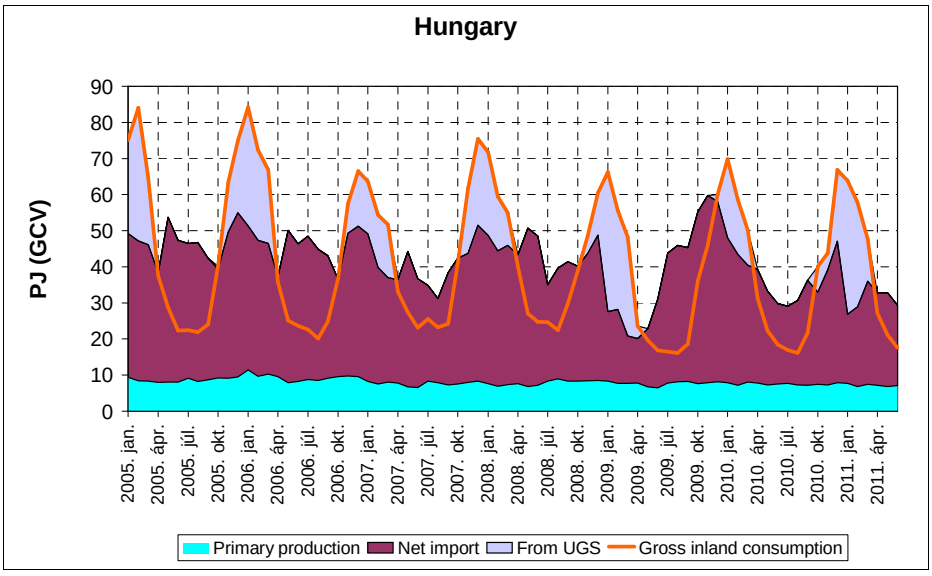

Figure 1: Natural gas demand data as a function of time
Source: EUROSTAT, 2011

Considering the first half of the recorded period, gas import has been leveled; but from 2009 on, changes become hectic. This is primarily due to external reasons: the 2009 "gas dispute" between Russia and Ukraine, resulting in considerable price fluctuations of Russian natural gas, and the still ongoing European financial-economic crisis both had their impact on the performance of energy sector. The effects of external changes and basic seasonal irregularities may be compensated with the common use of high capacity underground storages. According to the 2010 data Hungary is proprietor of a total of 3.4 billion m^3 underground storage capacity.

In the case of France, as shown in *Figure 2,* seasonal fluctuation of domestic gas demand is even more palpable. Heating gas consumption in the coldest winter month might 5–6 times exceed the amount of gas used in the hottest summer month.

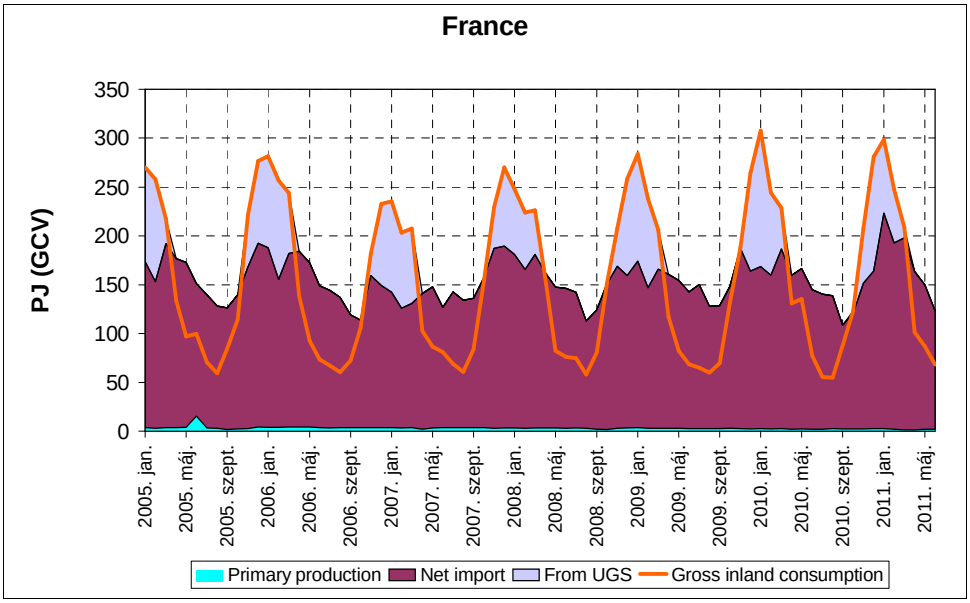

Figure 2: Natural gas demand data as a function of time
Source: EUROSTAT, 2011

Figure 3 displays the import dependency level of European countries on natural gas. In most countries this market indicator tends to reach or already equals to 100%. Poland and Romania might be called exceptional, with their indicator levels lower in 2009 than in 1990. Hungary is becoming increasingly dependent on import in natural gas, though in 2009, the indicator level still stayed below 80%. As for contrast Ireland, Poland and Portugal needed no natural gas import in 1990, whereas by 2009 they became almost 100% import-dependent.

The mentioned examples lead us to the conclusion that the energy sector does require exact parameters that are closely related to the seasonal factor of natural gas consumption, and a method which helps to reliably estimate the deviation between ordinary and extreme weather conditions.

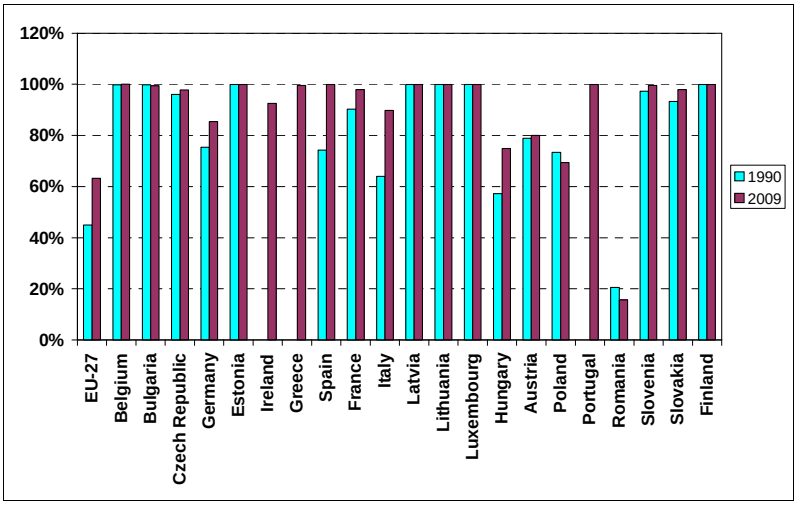

Figure 3: Natural gas import dependency of EU States in 2009
Source: EUROSTAT, 2011

2. Annual heating degree days – Background literature

Determining heating degree days is not only an important for meteorology and weather-related risk-assessment practice, but it is also a key issue for the energy industry. Although the method is commonly used in forecasting, little literature is available concerning the theoretical backgrounds. Most publications come from the field of energy management (mostly of the building sector). We can find a detailed description of the HDD method and base temperature calculations in CIBSE TM 41 Degree Days Application and Theory, published by the Chartered Institution of Building Service Engineers in 2006 (CIBSE, 2006).

Heating degree days look back on a long history. The first theory was worked out by Sir Richard Strachey as early as 1878. At that time the base temperature was established as low as 5.6 °C (with respect to agricultural purposes). Based on Strachey's work the Meteorological Office of England published a comprehensive mathematical formula in 1928. The first application of the method to building energy management was developed by AGA (American Gas Association) in 1920. It was statistically calculated that household fuel consumption, in proportion to heating degree days gives a base temperature of 18.3 °C. The underlying theoretical principle became integrated into Dufton's method in 1934, who calculated with a base temperature of 15.5 °C. This reference value is still taken to be valid in the relevant UK standards. During the 1940s CIBSE (Chartered Institution of Building Service Engineers) issued a number of publications on heating degree days method. On the basis of McVicker's technique, Knight and Cornell proposed in 1958 to split between night and day base temperatures of intermittently occupied buildings. This 'split day method' was adopted by Holmes in 1980, who also integrated thermal capacity and variable heating gain effects into his calculations. Regression and cumulative sum difference technique was introduced into building energy management by Harris (1989). The most important HDD methods are summarized in *Table 1*.

Table 1

Heating degree days (HDD) calculation methods

Degree-day calculation method	Required data	Recommended applications and comments
Mean degree-hours	Hourly outdoor dry bulb temperatures	In-house data collection systems with automated calculation procedures. The most accurate method.
Meteorological equations	Daily outdoor maximum and minimum temperatures	Automated procedures more complex than degree-hours. The standard UK method for published degree-days.
Mean daily temperature	Mean daily temperatures	Where available data is limited to mean daily temperature. Accepted standard method in USA and Germany.
Hitchin's formula	Mean monthly temperature Monthly standard deviation (not essential)	Mean monthly temperature can easily be obtained. Ideal for use in energy estimating where other data is not available. Can be used for base temperature conversions.

Source: CIBSE TM41, 2006.

The US organization of ASHRAE (American Society of Heating, Refrigerating and Air-Conditioning Engineers) considers the heating degree days calculation to be the simplest and most easily applicable method for conducting energy supply survey on buildings – in case the heating, cooling and air conditioning systems are run with constant efficiency. The procedure operates with the difference between the daily mean temperature and the reference temperature. Summing these values for all the days when the daily mean temperatures are lower than the base temperature, the annual heating degree days can be found. With a balance point temperature of 18.3 °C, the procedure will be the same for calculating annual cooling degree days as well (ASHRAE, 2005).

According to the EUROSTAT-method HDDs are defined as:
HDD = 18 °C–T_m if T_m is lower than or equal to the "heating threshold" (15 °C)
HDD = 0 if T_m is higher than 15 °C,
where T_m is the mean $((T_{min}+T_{max})/2)$ outdoor temperature over a period of one day. Calculations are executed on a daily basis, added up to a calendar month - and subsequently to a year.

In its prognosis for natural gas supply and consumption up to 2015, the National Institute of Economic and Industry Research of Australia applies a specific method, called of Effective Degree Days (EDD). This method not only uses actual daily temperatures for the calculations, but also considers the effect of wind, sunshine and other seasonal factors. Here the base average temperature is 18 °C. The reference period lasts from 6 a.m. of a given day until 6 a.m. of the next day, which is an exact equivalent of the 'heating day' unit used in Hungary (NIEIR, 2007).

3. Annual heating degree days

Heating degree days are a measure derived from daily mean temperature to characterize the annual or seasonal "weather rigorousity". If we take it metaphorically, annual degree days make an integral – proportional to the total quantity of "coldness". Degree days do not necessarily reach their peak value in the particular year when the lowest daily mean average value has been recorded. Long-lasting periods of cold, with daily mean temperatures of 7–8 °C below zero might significantly increase the number of annual heating degree days.

The EUROSTAT Database records annual and monthly HDD values for each of the EU states from 1980 until now. These data are used in our further examinations. For compatibility reasons countries like Cyprus, Malta, Croatia and Turkey are left out from the following comparable analysis.

Table 2 shows the results obtained from the statistical analysis of annual HDDs over the period of 1980–2009. The table indicates average values and various HDDs assigned to different probability levels. In the last two rows of the table the highest and lowest HDDs of the period under survey are to be found.

Table 2

Statistical analysis of annual HDDs – results

	P = 0,95	**P = 0,9**	**Average**	**P = 0,1**	**P = 0,05**	**Max.**	**Min.**
Belgium	3249	3156	2830	2504	2412	3348	2437
Bulgaria	2945	2881	2654	2428	2364	2965	2357
Czech Republic	3960	3866	3533	3200	3105	4125	3096
Denmark	3957	3843	3438	3034	2920	4062	2988
Germany	3636	3540	3199	2858	2761	3806	2782
Estonia	4958	4833	4393	3954	3829	5223	3873
Ireland	3216	3140	2871	2603	2526	3436	2552
Greece	1824	1784	1642	1500	1460	1874	1434
Spain	2087	2031	1831	1632	1576	2133	1482
France	2785	2713	2459	2205	2133	2854	2176
Italy	2224	2163	1949	1735	1674	2340	1695
Latvia	4750	4633	4220	3806	3689	5019	3725
Lithuania	4584	4466	4048	3630	3512	4818	3543
Luxembourg	3611	3512	3164	2815	2716	3675	2738
Hungary	3236	3159	2886	2613	2535	3267	2495
Netherlands	3321	3218	2854	2490	2387	3446	2424
Austria	3916	3833	3540	3248	3165	3984	3164
Poland	4037	3935	3574	3213	3111	4144	3092
Portugal	1520	1467	1278	1089	1036	1533	891
Romania	3456	3375	3092	2808	2728	3509	2750
Slovenia	3390	3309	3024	2739	2658	3407	2583
Slovakia	3793	3710	3416	3122	3038	3924	3007
Finland	6359	6230	5774	5317	5188	6651	5219
Sweden	5965	5838	5387	4936	4809	6254	4940
UK	3425	3349	3081	2812	2736	3538	2814

Figure 4 shows a "S-shaped" cumulative probability curve determined from the data of *Table 1*. The curve assigns 50% probability level to an average value of 2886 i.e. by this value the probability of obtaining an annual HDD number above or below the average is 50%-50%, respectively. With the help of such curves, one can assess the HDD range that will, with certain probability, include the number of heating degree days of any given year. HDD number 3159 is assigned to a probability level of 90% indicating that it is 90% probable that HDDs of some lower value will occur, while it is 10% possible that HDDs of any higher value would occur. Such analyses of historical datasets of annual heating degree days provide useful information for the energy sector, promoting weather-related risk assessment of domestic gas supply.

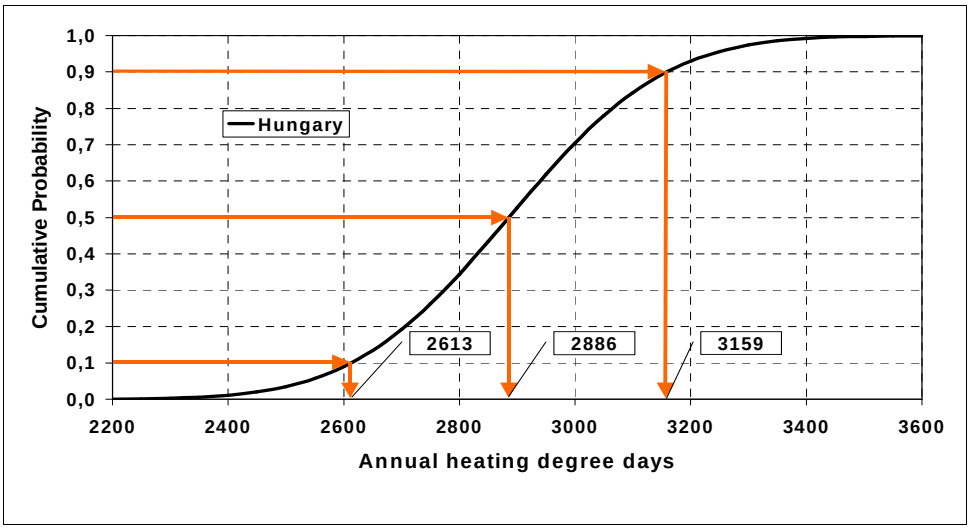

Figure 4: Cumulative probability curve of annual heating degree days
Source: EUROSTAT

On the basis of data analysis *Figure 5* indicates actual annual heating degree days in Hungary, plotted against a mean average over the time span between 1980 and 2009. Data scatter limited by 5% and 95% probability levels is also represented. The results show that annual degree days were in two cases above and in one case below the limiting values of the specified scatter range.

Another way of indicating different frequency rates is to use a "1 in 10", "1 in 20" or "1 in 50" scale. 1 in 10 means that a certain HDD value occurs once in ten years or 10 times in 100 years (on the average). 1 in 20 refers to a HDD number occurring once in twenty years or 5 times in a hundred years, respectively.

Considering weather risks and temperature effects from the aspect of energy supply, it is insufficient to examine those years which are covered by the represented scatter ranges (see *Figures 4* and *5*). *Figure 6* represents the outstanding years when extremely cold or hot periods were recorded, thus, their HDD numbers have fallen out of the statistical scatter range. On the basis of 1980–2009 data, each European country experienced extremely cold and unusually hot years as well. Such periods require the development of special preparation plans by the energy sector, in order to maintain supply security.

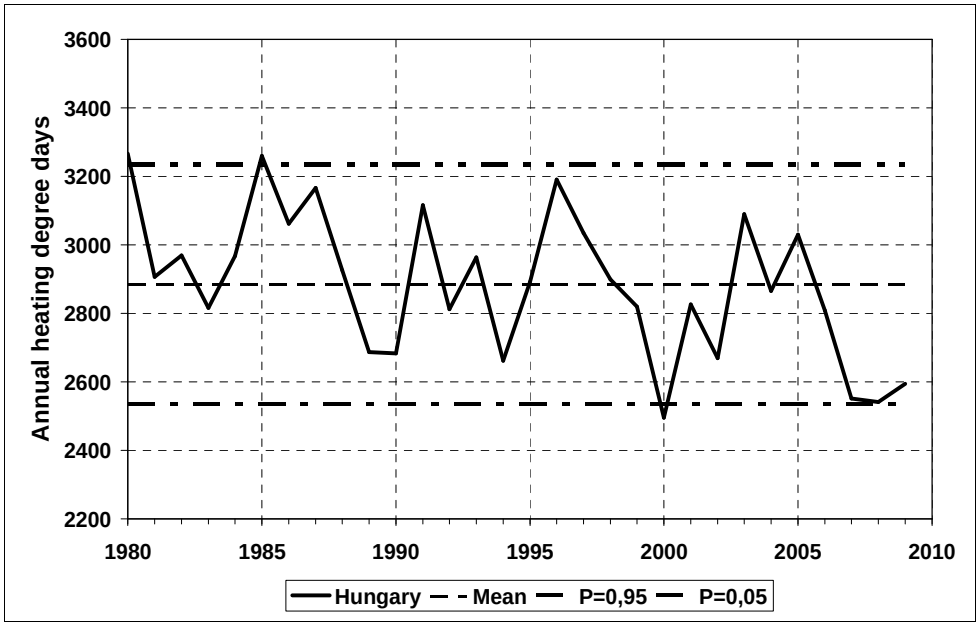

Figure 5: Actual values of annual HDD days in Hungary
Source: EUROSTAT, 2011

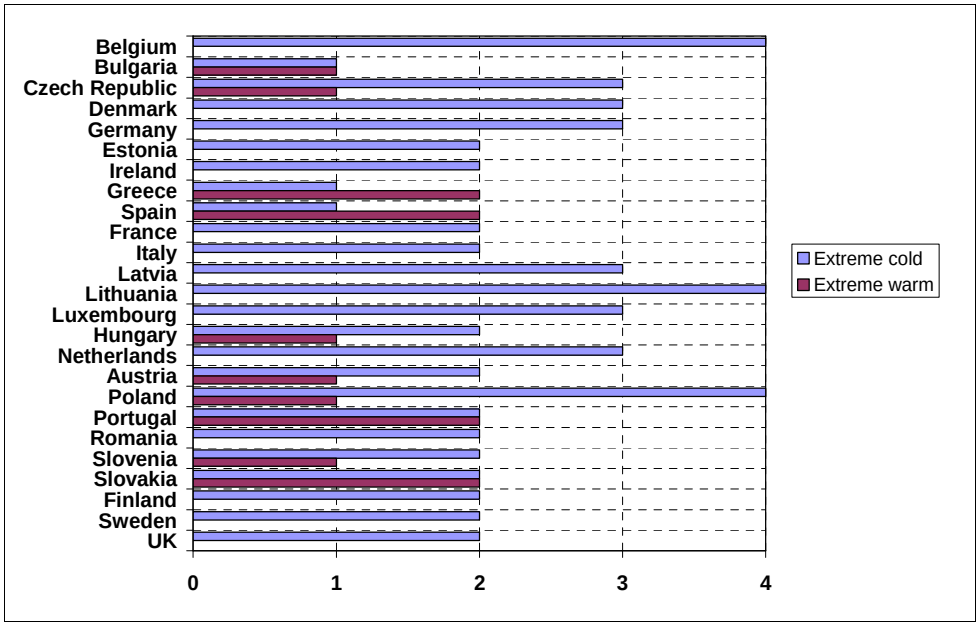

Figure 6: Frequency rate of extreme weather conditions between 1980 and 2009
Source: EUROSTAT, 2011

Figure 7 shows the statistical distribution of annual degree days obtained from the HDD data of several European countries. Average degrees for each country, together with confidence intervals specified for 10%–90% and 5%–95% probability levels are represented in the Figure. "Empty boxes" indicate real data that fall out of the confidence intervals of the given probability range.

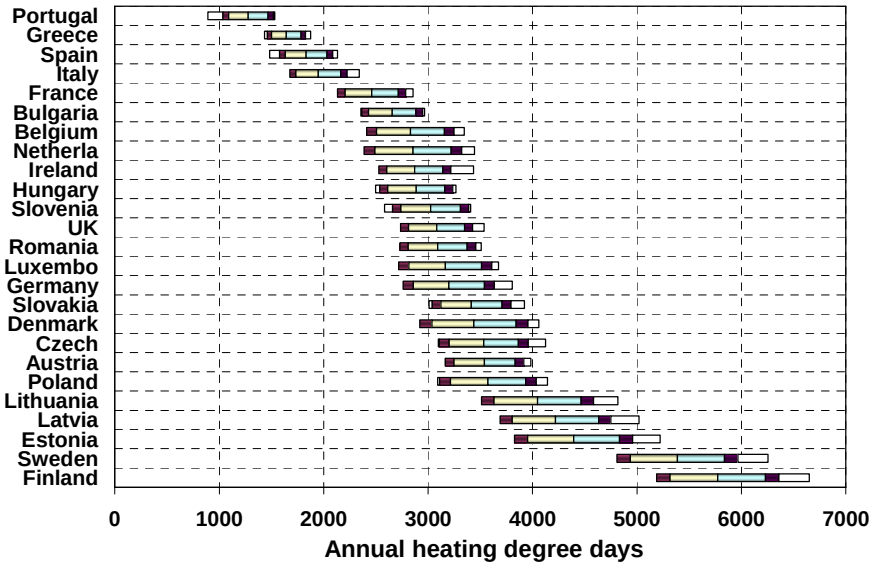

Figure 7: Annual heating degree days distribution in European countries
Source: EUROSTAT, 2011

One can observe that average HDD values and probability-related scatter ranges are the least extensive in the case of Southern European countries. Parallel with decreasing latitude and growing distance from the sea, the average HDD numbers of the countries increase and the probability-related confidence intervals become more extensive. On the other hand it is remarkable, that the United Kingdom and Ireland are ranked among the Eastern European states in the HDD order of EU members.

Further information can be obtained by comparing the limit values of the 5% to 95% annual HDD scatter ranges with the historical data of HDD averages of the given countries. As derives from *Figure 8,* the variance of annual HDDs fall into a (min.) 11%–(max.) 19% average value range for each country. Interestingly the most serious fluctuation is shown by Portugal – the country which, as it can be seen from *Figure 7,* has the lowest historical annual HDD rates amongst the countries under survey. Let us note, that this indicator might as well be taken as a "rule of thumb". It helps to simply but reliably assess the range of uncertainty assigned to 5%–95% probability levels calculated from historical averages of annual heating degree days.

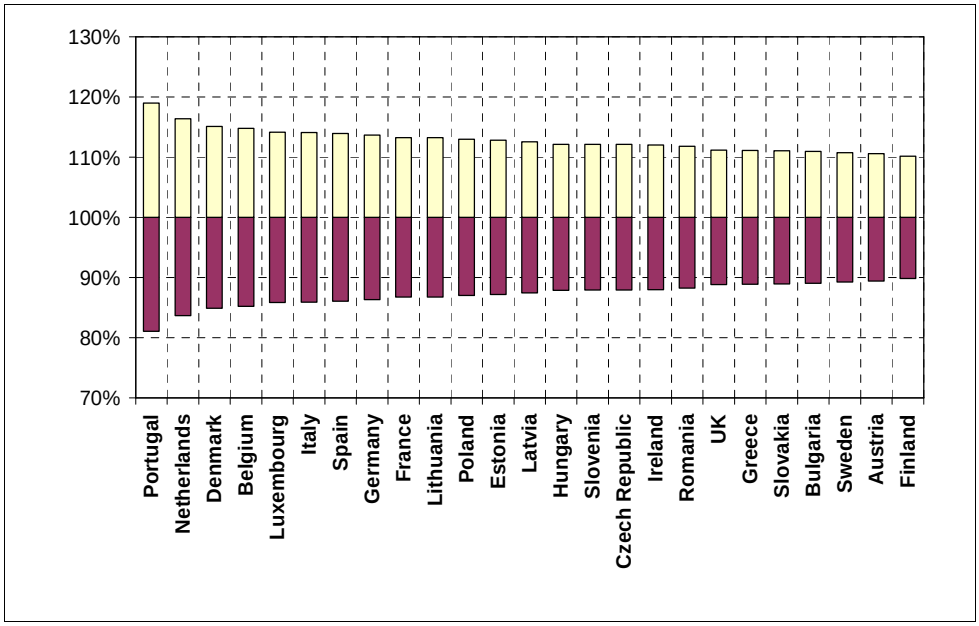

Figure 8: Scatter range of annual heating degree days
Source: EUROSTAT, 2011

4. Monthly heating degree days

Figure 9 shows the results obtained from the statistical analysis of Hungary's monthly degree days on the basis of historical data between 1980 and 2010. Average degree day values are represented for each month, together with confidence intervals specified for 10%–90% and 5%–95% probability levels. "Empty boxes" illustrate real data (minimum and maximum values) that fall out of the confidence intervals of the given probability ranges. One can easily diagnose that average values are higher and the probability-related scatter range is more extensive for January than for December. It is also notable that one has to calculate with four "cold months" in the spring season, whereas in the autumn period only three "cold months" are included.

Figure 10 illustrates the deviations of actual monthly degree days from the mean averages over the recorded time span. Certain periods on the diagram observably show serious monthly anomalies (both in positive and negative direction). Other seasonal terms, like the winter of 2006/2007, can be characterized with massive, one-directional deviations. This particular period was remarkable of having generally milder winter months than usual.

From an energy management point of view winter conditions are the most favorable if they are evenly partitioned between months below and months above the mean average – which is optimal for efficient energy supply. Considering weather conditions we can also find distinctive periods of interest between 2000 and 2010. As Figure 10 shows, during the extended winter season of 2007/2008 three months were colder than the average (from September to December, 2007), followed by four temperate months, exceeding the mean average.

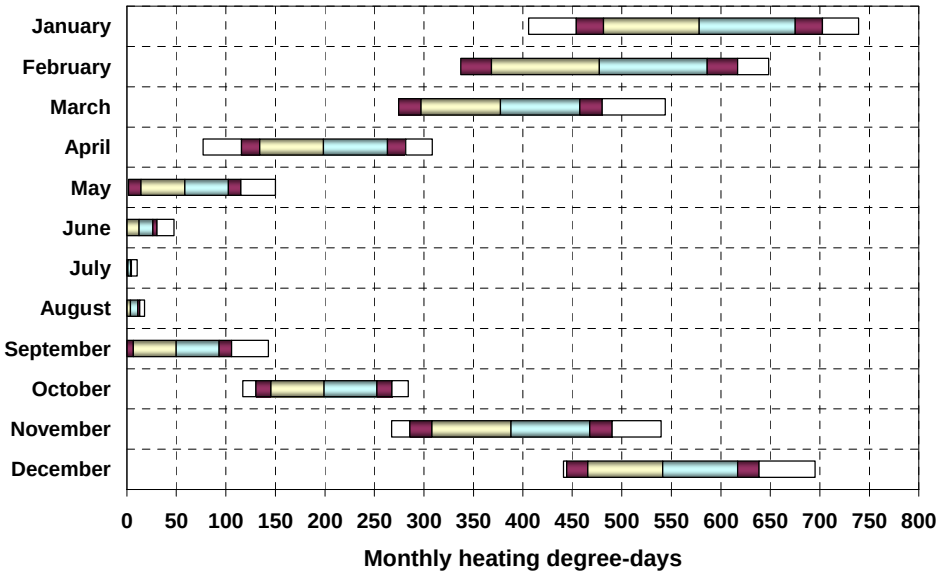

Figure 9: Variation of monthly degree days in Hungary
Source: EUROSTAT, 2011

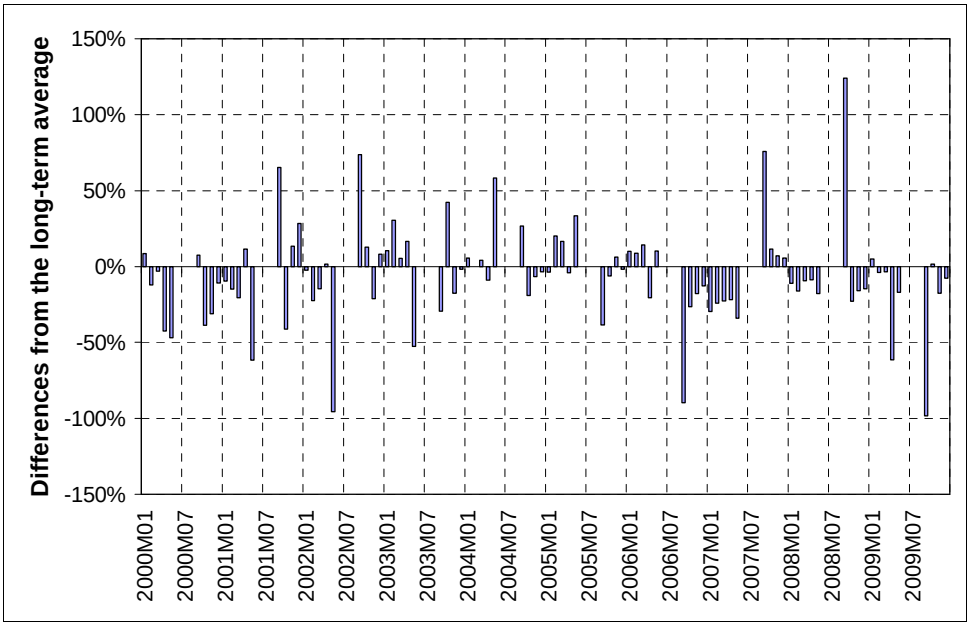

Figure 10: Deviations of monthly HDDs (Hungary)
Source: EUROSTAT, 2011

Generally the fluctuation of temperature data might exceed ±50% in certain months. This feature calls our attention to the fact that monthly degree days can significantly deviate from the mean average – especially if compared to annual heating degree days. Yet, we should take into account that milder periods tend to immediately precede or follow "strict" winter days. This will lead to the consolidation of values for the total sum of the winter season and result in an annual HDD number variation less than about ±15–20%.

5. Summary

By comparing the EUROSTAT data over 1980–2009 for most European countries, we tried to analyze the statistical distribution of annual heating degree days, with the aim of defining the specific characteristics of certain regional blocks. In the following section we summarize the results of this comparative analysis:

- Annual and monthly heating degree days provide an essential tool for planning heating energy supply and for successfully managing weather-related risks.
- On the basis of analyzing historical annual heating degree day datasets (available in EUROSTAT database) it is possible to determine all the statistical parameters that are required to reliably calculate the confidence interval associated with any arbitrarily chosen probability range.
- In the case of the surveyed countries the confidence interval assigned to 5%–95% probability levels perfectly characterizes the range of weather changes that needs to be taken into account when planning supply safety.
- The mentioned variation range might as well be expressed as the percent rate of the historical average of annual heating degree days. Considering European countries those annual heating degree day values that occur with 5%–95% frequency are likely to change within a range of min. ±11% and max. ±19% of the historical average of annual heating degree days. This value provides an easily manageable "rule of thumb" for planning, prediction and preparation in the energy industry.

"Acknowledgement: This work was carried out as part of the TÁMOP-4.2.1.B-10/2/KONV-2010-0001 project in the framework of the New Hungarian Development Plan. The realization of this project was supported by the European Union, co-financed by the European Social Fund."

REFERENCES

[1] Ashrae (American Society of Heating, Refrigerating and Air-Conditioning Engineers): *Handbook – Fundamentals* (SI) (chapter 32.), Atlanta, USA, 2005.
[2] Assessment Report of Directive 2004/67/EC on Security of Gas Supply, Commission Staff Working Document, Brussels, (2009) http://eur-lex.europa.eu/LexUriServ/LexUriServ.do?uri=SEC:2009:0978:FIN:EN:PDF
[3] Cibse (Chartered Institution of Building Services Engineers): *Technical Manual 41: Degree-days: theory and application*, London, 2006.
[4] Gas Ten Year Statement, National Grid, December, 2011, www.nationalgrid.com
[5] Gikas, A.–Keenan, R.: *Statistical aspects of the energy economy in 2004*. EUROSTAT Statistics in focus. Environment and Energy, 5/2006

[6] Gikas, A.–Keenan, R.: *Statistical aspects of the energy economy in 2005*. EUROSTAT Statistics in focus. Environment and Energy, 13/2006
[7] Nemry, F.–Uihlein, A.: E*nvironmental Improvement Potentials of Residential Building*s. (IMPRO-Building), JRC Scientific and Technical Reports, 2008.
[8] Nieir (National Institute of Economic and Industry Research): *Natural gas forecasts and customer number forecasts for the Mutinet distribution region to 2015*. Clifton Hill, Victoria, Australia, 2007.
[9] Risk assessment for the purpose of EU Regulation 994/2010 on security of gas supply, (2011) http://www.decc.gov.uk/assets/decc/11/meeting-energy-demand/energy-security/3428-risk-assessment-eu-reg-sec-supply.pdf
[10] Tihanyi, L.–Szunyog, I.: *Időjárási kockázatok a földgáz-kereskedelemben*. Magyar Energetika, 3, 7–11., 2008.
[11] Vida, M. (főszerk.): *Gáztechnikai Kézikönyv.* Műszaki Könyvkiadó, Budapest, 1991.

Geosciences and Engineering, Vol. 1, No. 1 (2012), pp. 315–319.

GEOTHERMAL ENERGY PRODUCTION AND UTILIZATION IN HUNGARY

ANIKÓ NÓRA TÓTH
Petroleum and Natural Gas Institute, University of Miskolc
H3515 Miskolc-Egyetemváros, Hungary
toth.aniko@uni-miskolc.hu

Abstract
The utilization of geothermal energy has a long tradition in Hungary. When the present economic recession in the country ends in the near future, geothermal energy will surely play an increasing role in the energy supply. The paper shortly reviews the history of geothermal power use and discusses the present state of geothermal energy production in the country. Present power statistics as well as future plans are detailed.

1. Introduction

Natural conditions in Hungary are very favorable for geothermal energy production and utilization. The anomalously high terrestrial heat flow (~0.09 W/m^2), the high geothermal gradient (~0.05 ^{c}o/m) and the vast expanses of deep aquifers form an important low-enthalpy geothermal resource. Surface manifestations have been known since ancient times: thermal springs of Budapest had been used in the Roman Empire and also later in the medieval Hungarian Kingdom. The artificial exploration of thermal waters began with the activities of V. Zsigmondy, the legendary drilling engineer, who in 1877 drilled Europe's deepest well (971 m) in Budapest. Between the two World Wars, while prospecting for oil, huge thermal water reservoirs were discovered. Based on data of this exploration, Boldizsár (1944, 1956) recognized the high heat flux and geothermal gradient in the Pannonian Basin. He also constructed the world's first regional heat flow map of Hungary (Boldizsár, 1958). During the 50's and 60's hundreds of geothermal wells were drilled, mainly for agricultural utilization. The peak of geothermal activity was at the late 70's: a total of 525 geothermal wells were registered, the best 30 of them had a production temperature of more than 90 ^{o}C. Total thermal power capacity of these wells was 1540 MW, but utilization was seasonal and the efficiency was rather low. Today the utilization of geothermal energy has decreased substantially while the technical level and the efficiency of utilization have increased.

2. Geological Background

The Pannonian basin is encircled by the Carpathian Mountains. The Earth's crust here is relatively thin (~25 km) due to sub-crustal erosion. The thinned crust had sunk isostatically and the basin thus formed is filled by mostly tertiary sediments. Pannonian sediments are multilayered, composed of sandy, shaly and silty beds. Lower Pannonian sediments are mostly impermeable; the upper Pannonian and Quaternary formations contain vast porous, permeable sand and sandstone beds. The latter formed the upper Pannonian aquifer which is the most important thermal water resource in Hungary.

The individual sandy layers have various thicknesses between 1 and 30 m. Their horizontal extension is not too large, but the sand lenses are interconnected forming a hydraulically unified system. This upper Pannonian aquifer has an area of 40 000 km^2, an

average thickness of 200–300 m, a bulk porosity of 20–30%, and a permeability of 500-1,500 mD. The hot water reservoir has an almost uniform hydrostatic pressure distribution, local recharge or discharge can slightly modify this pattern.

Another type of geothermal reservoirs are the carbonate rocks of Triassic age having a secondary porosity. These can be fractured or karstified rock masses with continuous recharge and important convection. About 20% of the Hungarian geothermal wells produce from such carbonate rock formations (Bobok et al., 1984).

The existence of high enthalpy reservoirs was proved by a dramatic outburst of steam from the well Fábiánsebestyén in the Southeast of Hungary in 1985. From an exploratory borehole over-pressured steam had blown out at a pressure of 360 bars and a temperature of 170 ^{o}C. The mass flow rate was approximately 80 kg/s. The reservoir is a fractured dolomite formation at the depth of 3700 m. The duration of the blow-out was 47 days, and the wellhead pressure as well as the flow rate remained constant. The well was finally killed and the borehole cemented. At the present feasibility studies are going on to determine the dimensions and the geothermal potential of the reservoir. Existence of other deep, high-enthalpy reservoirs in the South-Eastern part of Hungary seems to be possible.

3. Production and Utilization

Most Hungarian geothermal wells produce hot water from the upper Pannonian reservoir system. A smaller part of them taps the deep karstic aquifer. Up to the present a total of 858 wells have been drilled that produce thermal water warmer than 30 ^{o}C. Out of this number, 148 wells are abandoned and 171 are temporarily closed.

A typical geothermal well in Hungary might have a depth between 1,000 and 2,100 m. The well completion is typical. A 13 3/8 in (349 mm) conductor casing is set at a depth of 50 m, in a 17 ½ in (444,5 mm) hole. It is followed by a surface casing of 9 5/8 in (244,5 mm) at 500–1,800 m in a 12 ¼ in (311.1 mm) hole.

Finally a 7 in (177,8 mm) liner runs in a 8 ½ in (215.9 mm) hole to a depth of 1,000–2,100 m with its top at 30–50 m above the shoe of the surface casing. Each string is cemented in such a manner that the casing-hole annulus is totally filled.

Typical mass flow rates of the upper Pannonian wells can range between 20 and 30 kg/s.

Most Hungarian geothermal wells operate without any artificial production method. Reservoirs are driven by both compaction and dissolved gas. Submersible pumps are installed in only a few wells, in which the reservoir pressure has been depleted substantially.

Balneology use was the earliest way to utilize thermal waters. Worldwide-known spas are in Budapest, Bük, Hajdúszoboszló, Harkány, Hévíz, Sárvár, Zalakaros and many other places. Altogether 214 thermal wells and 120 natural springs produce water for sport and therapeutically purposes (Ottlik, 1988).

Agricultural use is the most important branch of geothermal energy utilization in Hungary. Greenhouses of more than 500,000 m^2, plastic tunnels and soil heating is supplied with the heat of thermal water. Technical level of these geothermal heating systems can be very different. There are well designed and controlled sophisticated systems, where a dozen of geothermal wells supply a cascade of sub-systems: greenhouses, plastic tunnels and soil heating are connected in series (e.g. Szentes). In other cases a single well provides thermal water directly to greenhouses and the discharged, still relatively hot water causes a low efficiency and sometimes environmental problems.

Animal husbandries are heated by thermal water in more than 50 cases at chicken, turkey, calf and pig farms. Low-temperature released waters supply fish ponds near Szentes and Győr. The estimated thermal power applied in the field of agricultural utilization is about 120 MW.

District and space heating by geothermal energy was started near balneology centers. The first examples are some apartment houses and the Budapest Zoo in between the two World Wars. In the late 50's district heating projects were started in Southeast Hungary e.g. Szeged, Szentes, Makó, Hódmezővásárhely. At the present 9,000 flats in nine cities are heated by thermal water, the estimated total thermal power is more than 38,7 MW. Simultaneously thermal water is used as domestic water in the same district. The thermal power of the domestic water supply is about 12 MW.

It is a little known fact that since 1969, thermal water is used in the secondary oil production technology in the Algyő oilfield. Presently 7,000 m^3/s of hot water is reinjected to the oil reservoir for oil displacement. The utilized geothermal power during this secondary oil recovery technology is 15 MW.

Another application is that gathering pipes are heated by thermal water in the heavy oil producing oilfield Sávoly in the Southwest of Hungary.

There is an unusual utilization of geothermal energy in the oilfield Nagylengyel. An artificial gas cap is formed above the depleted part of the oil reservoir. Natural gas with a high content of CO_2 (~81%) is produced, transported and reinjected to develop a gas cap in the formation. The technology operates without compressors, compressor power is replaced by the thermal lift between the production and reinjection wells. The higher the extracted geothermal heat from the produced gas, the stronger the thermal lift and the higher the gas mass flow rate, while the extracted heat is utilized too. In this case the fluid carrying the geothermal energy is the CO_2 gas.

Some important data of Hungarian geothermal wells are summarized in Table 1. Wells are grouped on the basis of utilization and the ranges of wellhead temperature. In order to estimate the total thermal capacities some practical approximations had to be made, as the flow rates of individual wells were not always measured. They were obtained from well completion measurements at different times thus their compatibility is questionable.

The estimated thermal capacity of any well was obtained from:

$$P = \dot{m}c\left(T_{wh} - T_s\right)$$

where $\dot{m}$ is the mass flow rate, c is the heat capacity of the water, T_{wh} is the wellhead temperature, T_s the yearly average temperature at the surface of 10,5 ^oC.

These values are summarized for several temperature ranges and types of utilization. Averages are obtained by dividing the total amount by the number of wells.

The total available thermal capacity of Hungarian geothermal wells was found to be approximately 1,201 MW. Since the utilized temperature difference is substantially lower than (T_{wh}–T_s), the effectively utilized thermal capacity can be estimated at a level of 325 MW only. This gives an assumed load factor of 27%.

4. Environmental Impact of Geothermal Energy Production

Any geothermal activity needs to deal with the significant impacts on the surrounding physical, biological and socio-economic environment. The major concerns are: reservoir pressure decrease, pollution of fresh groundwater and the waterways on the surface thermal effects, emission of dissolved gases, ground subsidence and noise.

Hungarian geothermal reservoirs may be sedimentary, sandy or karstified limestone aquifers. Reservoir pressure decreasing occurs mainly in the sandstone aquifers. Some fields have been exploited more than seventy years, thus the piesometric head of the reservoir has subsided almost 70 m in the Hajdúszoboszló field, the production can be sustained by artificial lifting methods only. The supply of the carbonate aquifers in Western Hungary seems to be unexhausted .

The freshwater aquifers are located above the geothermal reservoirs. Thus the drilling operations can be hazardous. During normal drilling situations downhole drilling fluids are usually the greatest potential threat to the environment. In the case of oil-based mud the cuttings also present a problem. There is a variety of chemicals that are toxic e.g. chromates. During the well completion operations acid jobs can be hazardous.

Nevertheless a blow out can be the greatest environmental hazard while drilling. The most serious blow out of a geothermal well occurred in Fabiánsebestyén, Eastern Hungary in 1985. The mass flow rate was 80 kg/s having an extreme high salinity and the small creek Kórógy lost all kinds of life. The noise level during the outburst reached the 125 dB.

The salinity of the Hungarian geothermal brines is comparable to that of seawater. The water of the upper Pannonian aquifer contains mainly sodium or calcium carbonate, the brine in the lower Pannonian formations contains mainly sodium chloride. The environmental impact of the released thermal waters can be serious. The wells of Bükkszék spa produce more than 1 m^3/min of very saline water, its solved solids are 24.000 mg/l. This means that 14.000 t/year are polluting the small Tarna River.

Thermal waters contain dissolved gases, mainly methane, nitrogen, carbon dioxide and hydrogen sulphide. Methane is separated from the water and utilized in auxiliary equipment. The H_2S is more harmful because of its acid, corrosive nature. This may lead to perforation of the casing and damaging of the cement sheet as well. Fortunately H_2S is present only in a few Hungarian geothermal wells (e.g. Mezőkövesd).

Most problems of environmental pollution can be avoided by means of reinjection of the heat-depleted thermal water to the aquifer. The reinjection is very useful for some other reasons too. The pressure support of the reservoir can be provided, the enthalpy of the rock matrix becomes exploitable and the surface ground subsidence can also be avoided.

Reinjection is a routine technology in the petroleum industry. It is relatively simple to inject hydraulically into karstic carbonate aquifers, but short circuiting the injected fluid to the production wells introduces a serious risk. It is a more complex procedure into a sandstone reservoir as the necessary injection pressure can substantially increase within a relatively short time. The permeability is decreased because of formation damage. It can occur because of clay swelling, pore space blocking by fine particles or precipitation of dissolved solids due to the mixing of injected water and the formation water or due to temperature changes. There are many efforts ongoing to solve these problems: theoretical analyses, numerical simulation, laboratory and in-situ experiments. Successful industrial experiments were carried out in the city Hódmezővárhely. The most important experiences are: a suitable choice of place and depth of the injection well, correctly designed and

completed well, good hydraulic performance, very slow transient performance processes (pressure, temperature, flow rate).

Some Hungarian thermal water contains toxic materials: arsenic, beryllium, chromium, organic materials (pesticides) and pathogenic organisms, bacteria. If released to the natural waterways, toxic materials and the relative warm waste waters harm the wildlife of these waters.

5. Summary

The Hungarian economy is starting to develop after some years of stagnation. There is no question that geothermal energy will continue to be an important resource base of this process. Environmental advantages of geothermal energy seem to be especially important, because CO_2 emissions in Hungary must be decreased by 4 million metric tons per year (Kyoto Protocol?).

Since 1995, three important projects have been started.

Feasibility studies are in the making to determine the conditions of electric power generation in the Southeast of Hungary, at the Békés basin. This is the site where high enthalpy geopressurized water has been found in Fábiánsebestyén and Nagyszénás. There seem to be serious technical problems due to the high pressure (360 bars at the wellhead) and the strongly saline water.

Two small-scale electric power generation plants are being planned using the organic Rankine cycle with 100 ^{o}C water in the Southern and South-Western parts of the country. These projects aim at a complex utilization: the small modular prefabricated power plant may be the attractive element of the system. Direct heat utilization for district heating and greenhouses can make the project economically viable.

"Acknowledgement: This work was carried out as part of the TÁMOP-4.2.1.B-10/2/KONV-2010-0001 project in the framework of the New Hungarian Development Plan. The realization of this project is supported by the European Union, co-financed by the European Social Fund."

REFERENCES

[1] Bobok, E.–Navratil, L.–Takács, G.: *Present Status of Geothermal Resource Assessment in Hungary.* Geothermal Resources Council. Trans. Vol. 8. 403–7., 1984.

[2] Bobok, E.–Tóth, A.: *Temperature Distribution in a Double Function Production Reinjection Geothermal Well.* Geothermal Resources Council. Trans. Vol. 24. 555–559., 2000.

[3] Boldizsár, T.: *Terrestial Heat Flow in Hungary.* Geophisica Pura e Applicata. Milano, Italy, Vol. 34, 66–70., 1956.

[4] Tóth, A.: *Geothermal Resources of Hungary at a Glance*. Proceedings of the 24th New Zealand Geothermal Workshop. 2002.

[4] Ottlik, P.: *Geothermal Experience in Hungary.* Geothermics. Vol. 17, 531–35., 1988.

Geosciences and Engineering, Vol. 1, No. 2 (2012), pp. 321–327.

HEAT LOSSES IN A GEOTHERMAL RESERVOIR

ANIKÓ NÓRA TÓTH
Petroleum and Natural Gas Institute, University of Miskolc
H3515 Miskolc-Egyetemváros, Hungary
toth.aniko@uni-miskolc.hu

Abstract
The petroleum industry has always participated in the utilization of favourable geothermal conditions in the country. Most of the Hungarian geothermal wells were drilled by the MOL Ltd. as CH prospect holes. Accordingly the field of geothermics belonged to the petroleum engineering, although marginally. It was therefore a surprise to hear of the decision of MOL Ltd. to build a geothermal power plant of about 2–5 MW. The site selected for the geothermal project is near the western border of a Hungarian oilfield, close to the Slovenian border. The location of the planned geothermal power plant was chosen after an analysis of suitable wells owned by the MOL Rt. The decision was made on the basis of different reservoir data. The existence of a reservoir of the necessary size, temperature, permeability, productivity and water chemistry data was proved. The wells provide enough information to understand the character of the reservoir and will be the production wells used by the planned power plant. Before the drilling operations and the discharge tests, the temperature of the outflowing water can be prognosticated. This is made possible by applying recently elaborated simulation methods (Bobok–Tóth, 2003; Tóth, 2004).

1. The selected site and wells

The site of the planned geothermal power plant was chosen after an analysis of the suitable wells of the MOL Rt. The wells Ortaháza Ny-3 and Ortaháza Ny-5 are suitable to investigate the behavior of the reservoir and will be the producing wells of the planned power plant. The Ortaháza Ny-3 well has a depth of 3200 m and a 7" string (178 mm) to 2028 m. It is completed as an open hole from the 7" casing shoe to the bottom. The well completion is shown in *Figure 1*. There are two perforated sections at 1930–1934 m, and 2589–2595 m. The Triassic formation is reached at 2851 m. The Ortaháza Ny-5 well was drilled to 2930 m. It has a 7" (178 mm) string to 2892 m. Below the casing an open hole section can be found. The Triassic formation starts at 2917 m. At this depth the undisturbed reservoir temperature is 141 ^{o}C. During the well test 128 ^{o}C was measured at the depth of 2879 m, but this value is necessarily lower than the previous because the circulated drilling mud cooled down the surrounding rock. The flow rate was 96 m^3/day (1,11 l/s) through a choke of 20 mm diameter. The well is temporarily closed by a cement plug at the interval of 1869–1919 m, under the plug the wellbore is filled by drilling mud.

According to the preliminary ideas both wells will be drilled further 300 m. Thus Triassic formation will be drilled through its full thickness to get inflow surface as much as possible. Thus the flow rate of the well can increase. The well Or-Ny-5 will be the production, Or-Ny-3 the reinjection well. A submersible pump will be run in the 9 5/6" casing of the production well, after cutting the upper section of the 7" casing. Thus the designed flow rate of 50 l/s can be attained. First a one-day discharge test is carried out. If this short-term test is successful a six-month long-term discharge test comes after it. Within the well test the wellhead pressure, the flow rate, the outflowing water temperature the dynamic fluid level and the chemical components will be measured. At the reinjection well injection tests will be made.

Before the drilling operations and the discharge tests the temperature of the outflowing water can be prognosticated. It is possible to use by applying recently elaborated simulation methods (Bobok–Tóth, 2003; Tóth, 2004). This calculation is introduced in the following.

2. Calculation of the temperature distribution

The first solution of this problem was developed by Boldizsár (1958). This version is a simplified solution of the original Boldizsár's work. The Bessel functions of the exact solution are replaced by a transient heat conduction function. A cylindrical coordinate system is chosen in accordance the geometry of the well. The z-axis of it is the symmetry axis of the well and is directed downward. The origin is at the surface as it is shown in *Figure 1*.

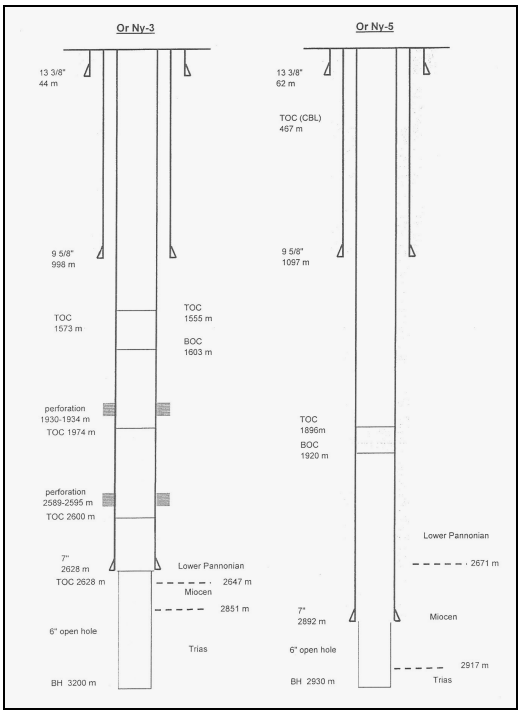

Figure 1: Schematic drawings of the wells

The balance equation of the internal energy is written for a control surface Bobok–Tóth, (2003). Let it be a cylinder coaxial with the well. Consider an infinitesimal length of it, bounded by horizontal planes in an arbitrary depth, a distance dz from each other. Its radius is R_∞, the distance of the location of the undisturbed geothermal temperature from the borehole axis.

The control surface is shown in *Figure 2.* Two sub-systems can be distinguished within it. One is the upflowing hot water in the tubing; the other is the well and the surrounding rock around it. Between the upflowing water and the tubing wall a surface heat transfer is

the dominant phenomenon, across the tubing interval surface of the radius of R_{1B}. Across the elements of the well structure and the surrounding rock a radially outward heat conduction is developed.

The overall heat resistance of the wellbore consists of the following elements. Across the tubing wall between the outer radius R_{1K} and the inner radius R_{1B} radial heat conduction occurs. The annular space between the tubing and casing is filled mostly by muddy water. Sometimes it is filled by foamy cement or other heat insulating material. In the first case natural convection, in the latter radial conduction is the way of the heat transfer. Across the casing wall and the cement sheet radial conduction can be found.

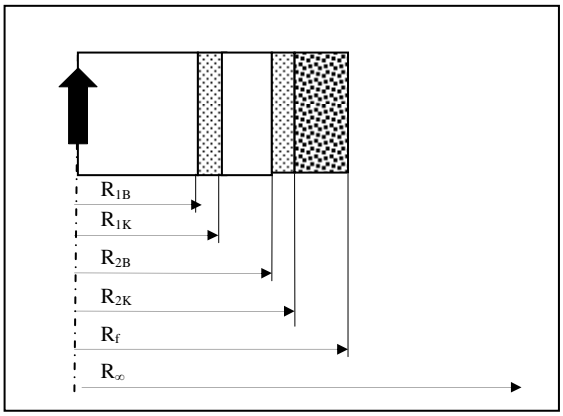

Figure 2: Control surface element

Some approximate assumptions are made before the solution of the energy equation. The upward flow in the tubing is considered to be a steady, fully turbulent flow. The flowing fluid is incompressible. It is well known that the greater Reynolds-number the more uniform the velocity profile. In the fully rough turbulent region the velocity profile can be replaced by the cross-sectional average velocity. Because of the turbulent mixing the radial temperature distribution can be also considered uniform. The temperature drop in the thermal boundary layer close to the wall can be replaced by a finite temperature jump. The vertical heat conduction in the water is neglected. The temperature distribution of the surrounding rock around the well is considered axi-symmetric. The model is adequate as long as the heat transfer around the well is conductive.

The balance equation of the internal energy is written first for the upflowing water (Bobok–Tóth, 2003). The decrease of energy content of the water is equal to the transferred heat across the wellbore. The overall heat flux is calculated by an overall heat transfer coefficient U_{1B}. Thus

$$\dot{m}cdT = 2\pi R_{1B} U_{1B} (T - T_F) dz \tag{1}$$

The radial heat flux across the wellbore is equal to the heat flux in the surrounding rock

$$2\pi R_{1B} U_{1B} (T - T_F) = 2\pi k_k \frac{T_F - T_p}{\ln \frac{R_\infty}{R_F}} \tag{2}$$

The quantity $\ln \frac{R_\infty}{R_F}$ is the increasing function of the time. R_∞ is the radius of the contour of the heated region around the well, where the undisturbed geothermal temperature is

$$T_\infty = T_0 + \gamma z \tag{3}$$

T_0 is the annual mean value of the surface temperature.

The geothermal gradient is γ = 0,0406 $^oC/m$. Since the surrounding rock around the wellbore is heated by the upflowing hot water the value of $\ln \frac{R_\infty}{R_F}$ increases monotonically with time. The radius of the contour of the heated region decreases along the depth, because the bottomhole temperature of the water and the rock is equal (Tóth, 2005). In the model its integral mean is taken, as the function of the Fourier-number and the overall heat transfer coefficient.

$$\ln \frac{R_\infty}{R_F} = f(Fo, U_{1B}) \tag{4}$$

This so-called transient heat conduction function is a dimensionless quantity. The Fourier-number is the similarity invariant of the transient heat conduction:

$$Fo = \frac{k_\infty}{\rho_k c_k} \frac{t}{R_F^2} \tag{5}$$

Equations (1) and (2) lead to a differential equation to determine the temperature distribution along the depth in the well:

$$\frac{dT}{dz} = \frac{2\pi R_{1B} U_{1B} k_k (T - T_0 - \gamma z)}{\dot{m} c (k_k + f R_{1B} U_{1B})} \tag{6}$$

Those parameters independent of depth are embedded into one quantity

$$A = \frac{\dot{m} c (k_k + f \cdot R_{1B} U_{1B})}{2\pi R_{1B} U_{1B} \cdot k_k} \tag{7}$$

In this case Eq.(6) can be written in the simple form

$$A \frac{dT}{dz} = T - T_0 - \gamma z \tag{8}$$

Its general solution is

$$T = T_0 + \gamma(z + A) - \gamma A e^{\frac{z-H}{A}} \tag{9}$$

By integrating the differential equation (8) at one step between the surface and the bottom of the well we make an obvious approximation. As the well geometry and the surrounding rock quality changes with the depth it can be divided into many suitable chosen sections along the depth. Some differences occur in the boundary conditions only.

The coefficient A has different values within each interval. The lowest section is denoted by 1, the subsequent sections are 2, 3 … etc. The outflowing water temperature for the i-th interval is equal to the inflowing water temperature for the (i+1)-th interval. This boundary condition can be formulated easily.

For the first the lowest interval the temperature distribution can be obtained as

$$T^{(1)} = T_0 + \gamma(z + A_1) - \gamma A_1 e^{\frac{z-H}{A_1}} \tag{10}$$

where A_1 refers for the first interval.

The temperature distribution along the depth can be calculated for the second section as

$$T^{(2)} = T_0 + \gamma(z + A_2) + \left[T_{out}^{(1)} - T_0 - \gamma(H_2 + A_2)\right] e^{\frac{z-H_2}{A_2}} \tag{11}$$

For the third interval the temperature distribution is

$$T^{(3)} = T_0 + \gamma(z + A_3) + \left[T_{out}^{(2)} - T_0 - \gamma(H_3 + A_3)\right] e^{\frac{z-H_3}{A_3}} \tag{12}$$

Finally we get the temperature at the wellhead as

$$T_{out}^{(3)} = T_0 + \gamma A_3 + \left[T_{out}^{(2)} - T_0 - \gamma(H_3 + A_3)\right] e^{-\frac{H_3}{A_3}} \tag{13}$$

The three sections of the temperature distribution function obtain a continuous curve. Only the derivative has a jump at depths of H_1 and H_2.

3. Calculated result

Calculated results and the outflowing water temperatures are shown in *Figure 3*. It can be recognized that as the heated region around the borehole is developed with the time, the temperature at the wellhead increases and heat losses of the water decrease. The mass flow rate is the parameter of the curves. If the mass flow rate is smaller, the wellhead temperature decreases.

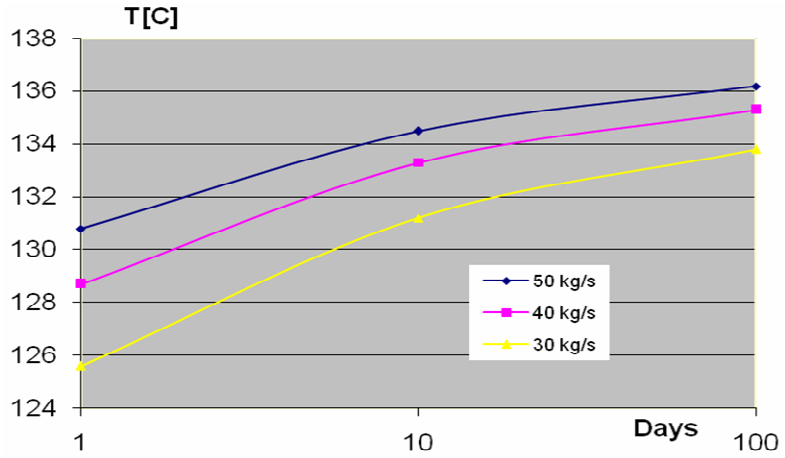

Figure 3: Wellhead temperatures vs. time

The strong influence of the mass flow rate on the temperature distribution can be recognized in both diagrams. The trend is the same in all cases. The results of the discharge test will probably modify this picture slightly.

4. Summary

A simulation procedure was introduced to determine the temperature distribution in hot water producing geothermal wells. Some factors influencing the temperature distribution have constant values such as bottomhole depth, the thermal conductivity of the rock, the completion of the well and the geothermal gradient. A different group of variables depends on the performance of the well, thus can be recognized analyzing the temperature distributions. The decreasing of the flow rate induced an important decrease of the temperature. In the initial days of the discharge test the water temperature increases until it reaches a stabilized steady value, this is the standard temperature for the operation of the power plant.

List of Symbols

T : bottomhole temperature [°C]
T_0 : surface temperature [°C]
T_{out}: outflowing temperature [°C]
T_∞ : undisturbed rock temperature [°C]
f : transient heat conductivity function [–]
m : flow rate [kg/s]
c : specific heat capacity [J/kgK]
R : diameter [m]
U : overall heat transfer coefficient [W/m^{2}K]
K : heat conductivity [W/mK]

"Acknowledgement: This work was carried out as part of the TÁMOP-4.2.1.B-10/2/KONV-2010-0001 project in the framework of the New Hungarian Development Plan. The realization of this project is supported by the European Union, co-financed by the European Social Fund."

REFERENCES

[1] Boldizsár, T.: *The Distribution of Temperature in Flowing Wells*. American Journal of Science, Vol. 256, 294–298., 1958.
[2] Bobok, E.–Tóth, A.: *Geothermal Energy Production and its Environmental Impact in Hungary Multiple Integrated Uses of Geothermal Resources.* Reykjavik, Iceland. 2003.
[3] Tóth, A.: *Geothermal Resources of Hungary at a Glance*. Proceedings of the 24th New Zealand Geothermal Workshop. 2002.
[4] Tóth, A.: *Heated Region Around Boreholes*. Proceedings World Geothermal Congress 2005 Antalya, Turkey.

Geosciences and Engineering, Vol. 1, No. 1 (2012), pp. 329–336.

DESCRIPTION OF THE PRODUCTION CONDITIONS OF A GEOTHERMAL WELL USING NODAL ANALYSIS TECHNIQUES

GÁBOR TAKÁCS–ZOLTÁN TURZÓ
Petroleum Engineering Department, University of Miskolc
3515 Miskolc Egyetemvaros, Hungary
gtakacs@kfgi.uni-miskolc.hu; turzoz@kfgi.uni-miskolc.hu

Abstract
The paper describes the basics of NODAL analysis as used in petroleum engineering practice. The application of this technique to the description of the behavior of geothermal wells is illustrated. The operation of the geothermal well is fully explained and the description of each component's behaviour is detailed including inflow performance as well as well completion effects, vertical or inclined flow of geothermal fluids in well tubing and flow in flowlines. Calculation of pressure and temperature distributions in these system components is executed as required for a complete Nodal Analysis.

Nodal Analysis principles are applied to the operation of an example geothermal well producing water by natural flow. Using several scenarios for the annular configuration of the well water rates and outflow temperatures are calculated. Calculation results provide the different ways the components of the geothermal system cooperate and allow one to optimize well conditions in order to reach maximum water rates and/or water temperatures.

1. Introduction

Geothermal fluids found in an underground reservoir move through a complex system to reach their destinations on the surface. The production system comprises the following main components: the reservoir, the perforations, the producing well, the surface flowline and the surface gas-liquid separator. This is an interconnected and interacting system of the basic components that all have their own specific performance relationships, but each in turn also depends upon and influences the other elements. In order to produce fluids to the surface, all components of the system must work together.

The outlines of this principle were first given by Gilbert [1], the father of production engineering, in the 1950s. He described the interaction of the reservoir, the well and the wellhead choke and proposed a system-oriented solution for determining the production rate of a flowing well. The practical use of Gilbert's ideas was limited, mainly due to the limitations of the methods available in his time for modeling the performance of the system's elements. During the last decades however research into the behaviour of the individual hydraulic elements of oil and gas wells has been very intensive. Because of this progress there exist today several different theories, calculation and design procedures that reliably model the performance of each element of a production system. Good examples for this are the numerous correlations available for calculating pressure traverses in vertical and horizontal pipes.

The wide selection of available calculation models and the advent of computers, which eased the burden of the necessary calculations, led to the re-appearance of Gilbert's ideas in the early 1980s [2, 3]. The new contributions aim at the numerical simulation of the production system's hydraulic behavior, but also enable the optimization of the system to produce the desired flow rate most economically. Although most of the investigators study

the production system only, the basic concepts have already been identified by Szilas [4] for the integration of these achievements into the description of a whole field's behaviour.

The systems analysis methods and procedures mentioned above were named "Nodal Analysis" by K. E. Brown and the term has generally been accepted.

2. The Production System

The production system of any producing well comprises part of the reservoir, the system transporting well fluids to the surface and the surface separation equipment. A more detailed classification of the system's components would include:

- The part of the formation between the boundary of the drainage area and the wellbore,
- the well's completion, i.e. the perforations, gravel pack etc.,
- the vertical or inclined tubing string,
- any downhole restrictions placed in the tubing, like downhole safety valves, etc.,
- artificial lift equipment, if required for lifting well fluids to the surface,
- the production choke usually placed at the wellhead,
- the flowline with its additional equipment and
- the separator where primary separation of well fluids is made.

All the above components have their own performance relationships that describe their behaviour under different flow conditions. The formation is characterized by the laws of flow in porous media, whereas in most of the other components single or multi-phase flow in pipes takes place. Accordingly a proper description of the total system's behaviour cannot be achieved without a thorough investigation of each component's performance. The different calculation models developed for the characterization of the system's components, therefore, provide a firm foundation for systems analysis.

Consider a simple flowing well with only some of the components described above. The schematic drawing of this simplified case is shown in *Figure 1*. Fluids in the formation flow to the well from as far as the boundary of the drainage area, 1. After entering the well through the sandface, vertical flow in the tubing starts at the well bottom, 2. In the tubing string vertical or inclined tubing flow takes place up to the wellhead, 3. A surface choke bean is installed at 4 which is also the intake point to the flowline. Horizontal or inclined flow in the flowline leads into the separator, 5.

The points in the flowing well's production system designated by the numbers in *Figure 1* constitute the "nodes" of the systems analysis theory. They separate the different components of the system: the formation, the tubing string, the flowline, etc. Between any two node points, flowing pressure decreases in the direction of the flow and the pressure drop can be calculated based on the characteristics of the given component. By this way the performance of any component is established as the variation of the flow rate with the pressure drop across the given component. This task is accomplished through the application of the different pressure drop calculation models valid for the different kinds of hydraulic components.

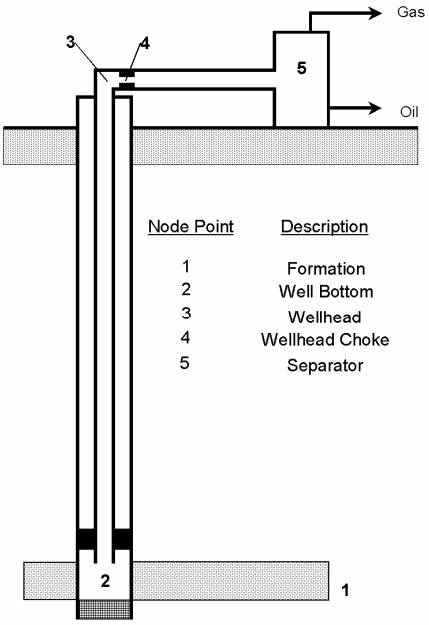

Figure 1: The production system of a flowing well with node points

Two node points deserve special considerations: the boundary of the drainage area (point 1) and the separator (point 5). These points constitute the two endpoints of the production system and their pressures are considered constant for longer periods of time. Formation pressure at the outer boundary of the drainage area of the well, of course, changes with the depletion of the reservoir but for production engineering purposes involving short- and medium-time periods, this change can be disregarded. Separator pressure at the same time, is usually set for the whole life of the field and is held constant. Thus the two endpoint pressures the average reservoir pressure and the separator pressure can duly be considered constant values for the purposes of systems analysis.

Since any fluid producing well's production system can be divided into its components by using appropriately placed nodes, systems analysis methods can widely be used in practice. This approach has found its use in solving the everyday design and analysis problems of production engineers.

3. Basic principles

One of the many objectives of systems analysis is the determination of the flow rate of a given production system. The solution of this problem is illustrated here through the example of a flowing well.

As discussed before, in connection with *Figure 1,* a well can be considered a series-connected hydraulic system made up of its components, which are bracketed by the

appropriately placed nodes. Evaluation of the total system's performance permits the following conclusions to be made:

* Mass flow rate throughout the system is constant, although phase conditions change with changes in pressure and temperature.
* Pressure decreases in the direction of flow because of the energy losses occurring in the various system components.
* At node points, input pressure to the next component must equal the output pressure of the previous component.
* System parameters being constant for considerable periods of time are:
  * the endpoint pressures at the separator and in the reservoir,
  * the wellbore and surface geometry data (pipe diameters, lengths etc.) and
  * the composition of the fluid entering the well bottom.

Taking into account these specific features of the production system, a procedure can be devised to find the flow rate at which the system will produce. This starts with dividing the system into two subsystems at an appropriately selected node called the "solution node". The next step is to find pressure vs. rate curves for each subsystem. These functions are constructed started from the node points with known pressures at the separator and at the well bottom. The intersection of the two curves gives the cooperation of the subsystems and thus the desired rate.

It is easy to understand that the described procedure will give the same result if solution s started from a different node position. This way systems (NODAL) analysis allows a flexibility to study different situations.

3.1. Application to geothermal wells

The systems analysis principles outlined above can readily be applied to the analysis of geothermal wells producing hot water. This is facilitated by the fact that a continuous single or multiphase flow takes place in the tubing string.

The methods of analysis are similar to those applied to flowing wells. The first important task is the proper selection of the solution node where the system is divided into two subsystems. The selection depends on the type of the problem to be solved. For example if an analysis of the parameters governing the well's inflow performance is desired than the proper choice is the sandface. If, on the other hand, the capacity of the surface system (flowline, separator etc.) is selected as the controlling parameter, placing the solution node at the wellhead is advised.

The solution node being selected, description of the two subsystem's behaviour follows. Starting from the points with the known constant pressures (at the separator and at the well's drainage boundary), flowing pressures in the different hydraulic elements of the production system are calculated. The resulting two performance curves describe the behaviour of the two subsystems and their common solution will give the well's production rate under the conditions studied.

4. Example problem

4.1. Problem statement

Illustration of NODAL Analysis principles detailed previously is done by presenting an example problem. It involves a flowing geothermal well producing gasless water through a buried pipeline into a user's facilities requiring a minimum of 5 bar intake pressure. The operator's objective is to produce as much water as possible at a suitable temperature.

The well produces from a relatively deep formation with a high productivity, the most important input data are displayed in *Table 1*. The flowline is buried and insulated with bitumen; other relevant data are given in *Table 2*.

Table 1

Well parameters for example problem

Parameter	Value
Perforation Depth, m	2,800
Prod. Casing Size, in	9 5/8
Reservoir Pressure, bars	290
Prod. Index, m^3/d/bar	75
Reservoir Temperature, C	160
Water Salinity, ppm	150,000

Table 2

Flowline data

Parameter	Value
Flowline Length, m	2,000
Pipe OD, m	0.12
Burial Depth, m	1.5
Insulation Thickness, mm	2

4.2. Solution strategy

The production system of the example well is similar to the one shown in *Figure 1* and the required intake pressure at the facilities can be considered constant. The solution node is best selected at the well perforations when the following two subsystems will result: (a) the formation and the well completion and (b) the tubing string plus the surface flowline. The performance curves of these subsystems, calculated from the known pressures at the radius of the drainage area and at the required facilities will intersect at those liquid producing rates that will develop under different assumed conditions.

Simultaneous calculations of pressure and temperature distributions in the producing system were carried out by using the computer program package PROSPER [5] and assuming steady-state pressure and temperature conditions. Within the constraints of the well's casing size the well was assumed to be equipped with either of the following tubing

sizes: 3 ½", 4", 4 ½", 5" and 5 ½"; they were run to the depth of the perforations where a packer was set.
Since the flowing temperature of water in the well depends on the material occupying the well's annulus three different scenarios were assumed:

1. The annulus is filled with saltwater to a depth of 1,000 m measured from the surface.
2. The annulus is empty, containing only low pressure air.
3. With an empty annulus the tubing is heat insulated with 3 cm of insulation (k = 0.034 W/m/K).

4.3. Calculation results

The results of NODAL calculations for Scenario 1 are displayed in *Figure 2* that contains the performance curves of the production system at the solution node, i.e. the well bottom. The intersections of the IPR curve, representing the inflow to the well, and the VLP curves denote those water rates that develop in the given system, Tubing size, as seen, has a profound influence on the water rate received from the well; greater tubing sizes allow the production of greater rates with the maximum reached when producing through the casing string.

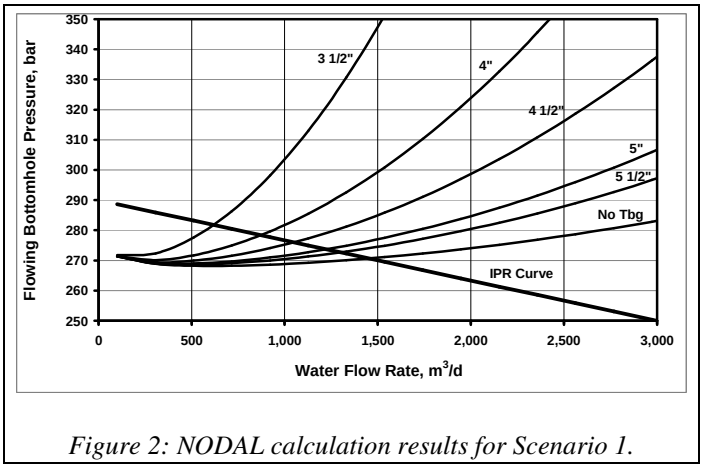

Figure 2: NODAL calculation results for Scenario 1.

Condensed results of calculations performed for all three scenarios are given in *Figure 3* where temperatures calculated at the end of the flowline are also displayed. As seen, water rates increase with the increase of the flow conduit size for each case and the effect of heat insulation in the annulus on well productivity is quite negligible. Temperature conditions, on the other hand, change more substantially with annular insulation; the better the insulation the higher the outflow temperature.

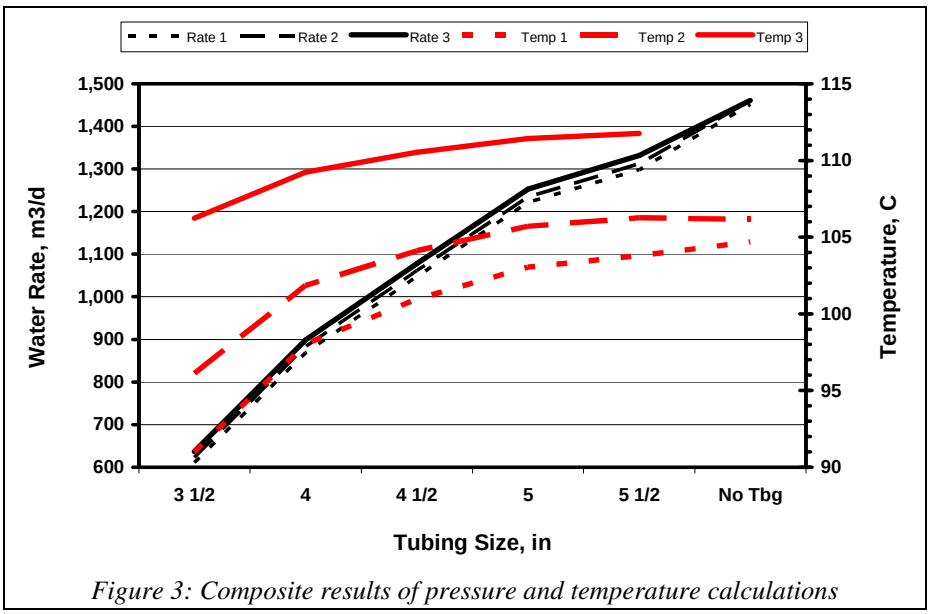

Figure 3: Composite results of pressure and temperature calculations

Figure 3 allows one to study the water rates and outflow temperatures possible with different annular configurations and to select the case when producing rates and/or water temperatures are suitable for the intended use of geothermal resources.

5. Conclusions

The paper illustrated how NODAL Analysis methods can be utilized in the modeling of geothermal well operations. Basic principles and practical recommendations were discussed and the calculation of well production rates and outflow temperatures was presented.
The most important conclusions based on the example case are:

Water rates rapidly increase with increased tubing sizes but do not significantly change with different annulus heat insulation scenarios.

Outflow temperatures, on the other hand, heavily depend on the actual degree of heat insulation in the well's annulus.

The proper flow conduit diameter and annular heat insulation can be selected for maximizing the water flow rate or the outflow temperature.

"Acknowledgement: This work was carried out as part of the TÁMOP-4.2.1.B-10/2/KONV-2010-0001 project in the framework of the New Hungarian Development Plan. The realization of this project is supported by the European Union, co-financed by the European Social Fund."

REFERENCES

[1] Gilbert, W. E.: *Flowing and Gas-Lift Well Performance.* API Drilling and Production Practice. 126-57, 1954.
[2] Proano, E. A.–Mach, J. M.-Brown, K. E.: *Systems Analysis as Applied to Producing Wells.* Congreso Panamericano de Ingeniera del Petroleo, Mexico City, March 1979.
[3] Mach, J. M.–Proano, E. A.–Brown, K. E.: *A Nodal Approach for Applying Systems Analysis to the Flowing and Artificial Oil and Gas Wells.* Society of Petroleum Engineers Paper No. 8025, 1979.
[4] Szilas, A. P.: *Field-Integrated Production System Cuts Costs.* OGJ June 13, 1983, 125–28.
[5] *PROSPER User Manual* Version 11.5, Petroleum Experts Limited, Edinburgh Scotland, April 2010.

Geosciences and Engineering, Vol. 1, No. 2 (2012), pp. 337–342.

EXAMINATION OF AN OPTIMIZED REPLACEABLE CUTTING TOOTH OF EXCAVATOR

ZOLTÁN VIRÁG[1]–SÁNDOR SZIRBIK[2]
[1]Department of Geotechnical Equipment, University of Miskolc
[2]Department of Mechanics, University of Miskolc
3515 Miskolc-Egyetemváros, Hungary
[1]gtbvir@uni-miskolc.hu ; [2]Sandor.Szirbik@uni-miskolc.hu

Abstract
This paper briefly outlines the design of replaceable cutting teeth, which are attached to a holder with detachable joint [1]. The description of the rock cutting process is very complex. Thus the investigation of the effect of lateral forces is complicated through cutting tests. We have to use accordingly numerical analysis to examine some segment of the cutting process. Our main objective is to present a finite element analysis of cutting teeth in which the linear increase of the lateral force is taken into consideration. The finite element analysis is a powerful technique, which is enabled to obtain the stress and displacement distribution in cutting teeth. The simulation results have shown that the maximum stresses decrease if the lateral force increases. The geometry of the optimized cutting teeth will be safe under the given loading conditions.

1. Introduction

An important and complex issue in mining is the rock cutting mechanization. The high cutting tooth wear and the high specific power demand are the long-standing problem of mining technique. New cutting tooth was designed in order to eliminate problems. Rock cutting tests were carried out, where winning experiments on the large sample from the mine were made using chisels modeling the in-plant winning chisels (cutting teeth), with cutting parameters close to reality [2].

To determine the geometric configuration of the cutting teeth and the cutting edges the knowledge of the mining technology is inevitable. The measurement data of cutting is collected and registered by a computer aided measurement system. On rock samples we recorded 165 measurement cycles. In each measurement cycle the following data and cutting characteristics were recorded: cutting direction, form, depth, average chip area, average cutting force F_V, average pressing force F_R and average lateral force F_O. As a result of the measurements a new cutting geometry was developed [2]. The experiments prove that it should pay attention to the wears and the geometry of cutting teeth because of the increasing of the cutting, pressing and lateral force. Considering the laboratory cutting test results a FEM was created for further investigations.

2. Mathematical procedure

In this section we give a brief introduction to displacement-based finite element methods. We remark that several books have given the basic concepts of finite element analysis. Although we have other alternatives, the principle of minimum potential energy is taken here as a starting point. First consider an elastic body V bounded by a surface A. The surface can be divided into two parts denoted by A_p and A_u. We shall assume that A_p is the union of those surface patches on which loads are imposed and A_u is the union of those

surface patches on which displacements are prescribed. The total potential energy of the e-th element after finite element discretization can be defined as

$$\Pi_P^e = \frac{1}{2}\int_{V^e} \boldsymbol{\varepsilon}^{eT}\boldsymbol{\sigma}^e dV - \int_{V^e} \mathbf{u}^{eT}\rho\mathbf{k}^e dV - \int_{A_p^e} \mathbf{u}^{eT}\mathbf{p}^e dA \tag{1}$$

where σ^e, ε^e and u^e are stress, strain and displacement vectors, respectively. Using approximation $u^e = Nq^e$, constitutive equation $\sigma^e = C\varepsilon^e$ and strain–displacement relation $\varepsilon^e = Bq^e$ we have

$$\Pi_P^e = \frac{1}{2}\mathbf{q}^{eT}\underbrace{\int_{V^e} \mathbf{B}^T\mathbf{C}\mathbf{B}\, dV}_{K^e}\mathbf{q}^e - \mathbf{q}^{eT}\underbrace{\left(\int_{V^e} \mathbf{N}^T\rho\mathbf{k}^e dV + \int_{A_p^e} \mathbf{N}^T\mathbf{p}^e dA\right)}_{f^e} \tag{2}$$

where N is the shape function matrix, B is the strain-displacement matrix, C is the matrix of elastic coefficients for an isotropic material and the nodal displacement vector is denoted by q. The total potential energy of the elastic body is

$$\Pi_P = \sum_{e=1}^{n}\Pi_P^e = \frac{1}{2}\mathbf{q}^T\mathbf{K}\mathbf{q} - \mathbf{q}^T\mathbf{f} \tag{3}$$

where n is the number of finite elements of the body, The first order variation of equation (3) assumes the form

$$\delta\Pi_P = \delta\mathbf{q}^T\mathbf{K}\mathbf{q} - \delta\mathbf{q}^T\mathbf{f} = 0 \tag{4}$$

Finally the finite element approach leads to an algebraic equation system as follows:

$$\mathbf{K}\mathbf{q} = \mathbf{f} \tag{5}$$

where K is the stiffness matrix, f is the vector of loads. This equation system can be solved for unknown nodal displacement using commercial FEM software. More detailed descriptions of finite element procedures can be found in Bathe's book [3].

3. Model description

In order to investigate the distribution of stresses in the cutting tooth, we set up a finite element model. Consider the solid model shown in *Figure 1,* consisting of a holder, a part from the cutting edge and an optimized cutting tooth. The cutting tooth is jointed into the holder as a removable piece. The holder is actually a steel rectangular structural tube, and of course it is possible the remaining parts of structure are made of a different kind of steel.

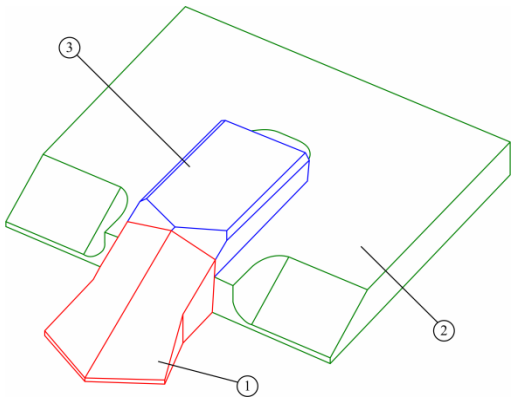

Figure 1: 3D assembly of solid models: the cutting tooth (1), the cutting edge (2) and the holder (3)

Because of the detachable contact joint we should describe five contact pairs between the appropriate surfaces of the tooth and holder in the finite element model. The contact pair consists of the two contact surfaces. One of them in the pair is selected to be the contactor surface on the tooth and the other contact surface to be the target surface on the holder. For simplicity the contact surfaces of holder are regarded as stationary, rigid surfaces. It follows that these surfaces are used in our model to simplify the contact searching instead of modeling the holder as a solid structure. We assume that the coefficient of friction is equal to zero between the contact surfaces. Under these conditions we should solve this contact problem by using finite element technique. Further details of contact problems are presented in [4, 5].

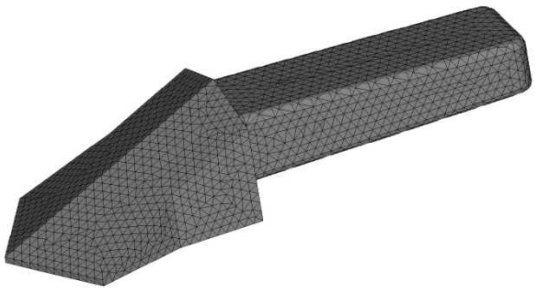

Figure 2: Geometrical model of cutting tooth for finite element analysis

The finite element mesh of cutting tooth is of free type using 10-node tetrahedral elements and so this solid structure is divided into 25 937 finite elements. The geometrical model of tooth is illustrated in *Figure 2*.

The mechanical properties of steel used in linear elastic finite element analysis are also taken: Young's modulus (E) is 2.1×10^5 MPa and Poisson's ratio (ν) is 0.3. This material behaviour is assumed to be linear elastic until the effective stress reaches proportional limit and in this region the stress-strain relation is represented by Hooke's law.

The aim of previous works [1, 2] is to simulate the cutting load from real cutting conditions on the surface, which is cross-hatched and painted with yellow color in *Figure 3*. The resultant force from the pressure on the surface consists of three components: cutting force F_V, lateral force F_O and a pressing force F_R, as see in *Figure 3*. These forces were determined by means of laboratory cutting experiments [1]. We assume that now the values of the resultant of cutting and lateral forces are 100 kN, and pressing force is always 100 kN. In order to investigate the rock cutting action for cutting forces in different directions we have to define various direction angles.

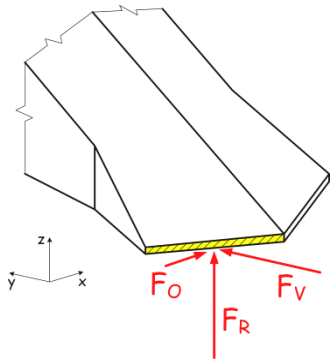

Figure 3: Cutting, lateral and pressing force

The direction angle α, which is measured in degrees positive clockwise between the direction of cutting force and the y axis of the global coordinate system, specifies the magnitudes of lateral and cutting forces. Thus $F_R = F = 100$ kN, $F_V = F \cos \alpha$ and $F_O = F \sin \alpha$ are imposed on the appropriate surface as specified loads.

4. Results of finite element analyses

In the preceding section a contact problem is proposed to determine the stress and displacement distribution in the tooth. The given problem is solved in ADINA [5]. To preserve the integrity of the teeth, the maximum stresses should be kept under the proportional limit of the material. The finite element analysis helps accordingly to qualify the strength of the new cutting tooth. The program computes effective stress (also called equivalent or von Mises stress) at each arbitrary point from the stress components using the formula

$$\sigma_{red} = \sqrt{\frac{1}{2}\left[(\sigma_x - \sigma_y)^2 + (\sigma_x - \sigma_z)^2 + (\sigma_y - \sigma_z)^2 + 6(\tau_{xy}^2 + \tau_{xz}^2 + \tau_{yz}^2)\right]} \qquad (6)$$

As appeared from the numerical simulation the maximum effective stress is about 900 MPa in the case of $\alpha = 0°$ and it occurs in front of the tooth (see *Figure 4*). However the stresses decrease quickly below 60 MPa in the remaining part and so in the shank of the tooth.

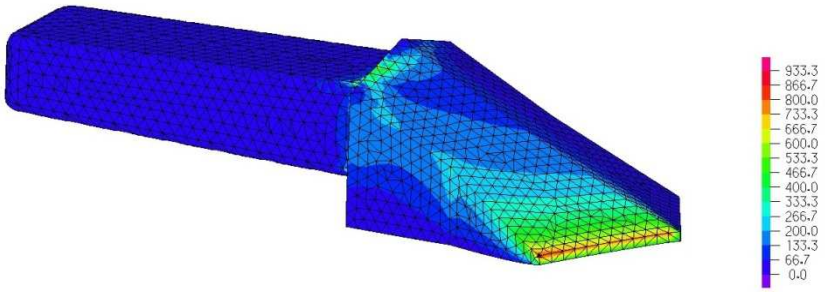

Figure 4: Effective stress distribution in the tooth

The maximum displacement occurs also in front of the tooth, where the loading condition is imposed. The maximum value of deformation is 0.426 mm. In the remaining part displacements decrease also quickly.

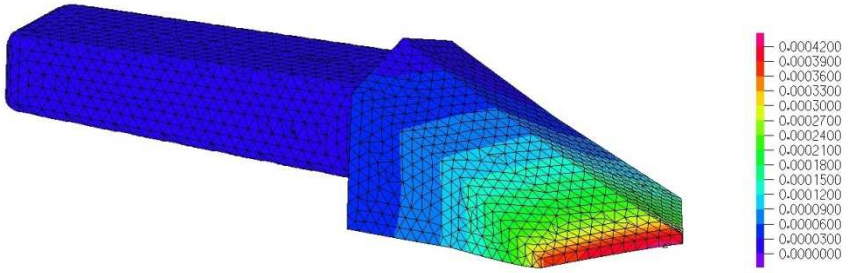

Figure 5: Displacement distribution in the tooth

The corresponding results after changing the direction angle have been tabulated in *Table 1,* where the maximum effective stress is denoted by σ_{max} and the maximum displacement by u_{max} and as mentioned previously, the angle α is measured in degrees.

Table 1

Maximum values of numerical results

α [degree]	σ_{max} [MPa]	u_{max} [mm]
0°	933.3	0.426
10°	884.9	0.389
20°	850.3	0.422
30°	829.3	0.532

The simulation results show differences in the values of displacements. However the stresses decrease if the angle increases. We remark that these results show good analogy with those obtained in the previous study [6], where the whole stucture is modeled as a solid structure. Finally the theoretical optimized cutting tooth is realized.

5. Conclusions

It is established that the development of cutting teeth could be improved by using finite element analysis. This technique is applicable to compare different types of teeth easily. It leads to an assessment of the effect of the main parameters on the behaviour of the geometric configuration of the cutting teeth. Consequently the results of finite element analysis show that the head of cutting tooth is the most critical point and so we conclude that high strength steel will be adequate because of the extreme loads. The obtained results can be useful in practice.

List of Symbols

A Surface	K Stiffness matrix	ε Strain vector
B Strain-displacement matrix	q Nodal displacement vector	ν Poisson's ratio
C Matrix of elastic coefficients	u Displacement	σ Normal stress
E Modulus of elasticity	u Displacement vector	σ Stress vector
f Vector of loads	V Volume	$\prod_p$ Potential energy
F Force	α Angle	τ Shearing stress

"Acknowledgment. This work was carried out as part of the TÁMOP-4.2.1.B-10/2/KONV-2010-0001 project in the framework of the New Hungarian Development Plan. The realization of this project is supported by the European Union, co-financed by the European Social Fund."

REFERENCES

[1] Ladányi, G.–Sümegi, I.–Virág, Z.: *Meríték- és bontófogfejlesztések első fázisának eredményei a Mátrai Erőmű ZRt. bányáiban üzemelő merítéklétrás kotróknál*. 43. Bányagépészeti és Bányavillamossági Konferencia kiadványa, 2010, 135–148.
[2] Ladányi, G.–Sümegi, I.–Virág, Z.: *Laboratory rock cutting tests on rock samples from Visonta South Mine*. Annals of the University of Petroşani, Mechanical Engineering, 9, 2007, 209–218.
[3] Bathe, K. J.: *Finite Element Procedures*. Prentice-Hall, Inc., New Jersey, 1996.
[4] Wriggers, P.: *Computational Contact Mechanics*. Spinger-Verlag, Berlin–Heidelberg, 2006.
[5] ADINA *theory and modeling guide*. Report ARD 10-5, ADINA R&D, Inc; 2010.
[6] Virág, Z.–Szirbik, S.: *Merítéklétrás kotró technológiájához optimált cserélhető bontófog vizsgálata.* LXII. évfolyam, 2011/11, III. kötet, 48–51.

University of Miskolc, Department of Research Management and International Relations
Responsible for publication: Prof. Dr. Mihály Dobróka prorector
Miskolc-Egyetemváros
Editor: László Kis
Published by the Miskolc University Press under leadership of Erzsébet Burmeister
Responsible for duplication: Erzsébet Pásztor
Number of copies printed: 200
Put to the Press on 2012
TU – 2012 – 397 – ME ISSN 2063-6997